



AD-A228 707



ELECTRICAL ENGINEERING DEPARTMENT  
SCHOOL OF ENGINEERING AND APPLIED SCIENCE  
405 HILGARD AVENUE  
LOS ANGELES, CALIFORNIA 90024-1594

September 22, 1990

Mr. Ulsh  
U.S. Army Research Office  
AMXRO-IP-Library  
P.O. Box 12211  
Research Triangle Park, NC 27709-2211

SUBJECT: Final Report for Grant DAAL 03-86-k-0090

Dear Mr. Ulsh:

This is the final report for the U.S. Army Research Office Grant DAAL 03-86-k-0090. According to the reporting instructions (ARO Form 18, page 5) technical material which was already reported will not be included here.

The thrust of the research under this grant has been to develop the methodology for the modeling and design antenna arrays and microstrip discontinuities for microwave circuit applications. I believe that certain outstanding results have been obtained during this period and these are highlighted in what follows:

H-Y. Yang's Ph.D. thesis involves several key contributions in the subject areas of modeling *microstrip discontinuities*, *microstrip transitions*, and the *synthesis* of microstrip dipole arrays. This work has generated several journal publications within which one finds a fundamental contribution to the understanding of the above mentioned subjects. The analysis and the generated computer programs serve as practical tools for the design of microstrip circuits and microstrip dipole arrays. The methodology was substantiated in each case with an experiment. The journal publication "Design of Transversely Fed EMC Microstrip Dipole Arrays Including Mutual Coupling" IEEE Transactions on Antennas and Propagation, Vol. 38, No.2, February 1990 is only one of many examples from Yang's excellent Ph.D. thesis work. This is a seminal paper since it is the first publication where a full *synthesis* procedure is developed for the design of transversely fed electromagnetically coupled dipoles. The solution is complete as it accounts for all substrate effects and mutual coupling. It demonstrates

DISTRIBUTION STATEMENT A

Approved for public release

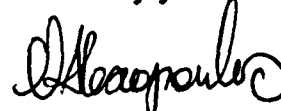
Distribution Unlimited

90 10 23 024

that mutual coupling contributes 25% of the total value of the array input active admittance and it therefore can not be neglected. The design procedure evolved into the fabrication of a microstrip dipole array. The experimental results show very good agreement with theory.

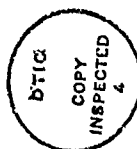
An evolution of Yang's work has led to the understanding of microstrip discontinuity effects. In particular the theory has been extended to model microstrip bends, T-junctions, four ports, etc. In each case the algorithms account for a precise description of energy loss at discontinuities due to radiation loss and surface wave loss. These models have also been substantiated with experiment. The models are now extended to provide precise designs for microstrip corporate feeds. This will lead to the design of two dimensional transversely fed electromagnetically coupled dipole arrays.

Sincerely yours,



N.G. Alexopoulos  
Professor

NGA:jh  
Enclosure



Accession For	
NTIS	DTIC
DTIC	DTIC
Unannounced	Justified
By	
Distribution	
Availability	
Dist	Availability
A-1	

# REPORT DOCUMENTATION PAGE

Form Approved  
OMB No. 0704-0188

Public reporting burden for this collection of information is estimated to average 1 hour per response, including the time for reviewing instructions, searching existing data sources, gathering and maintaining the data needed, and completing and reviewing the collection of information. Send comments regarding this burden estimate or any other aspect of this collection of information, including suggestions for reducing this burden, to Washington Headquarters Services, Directorate for Information Operations and Reports, 1215 Jefferson Davis Highway, Suite 1204, Arlington, VA 22202-4302, and to the Office of Management and Budget, Paperwork Reduction Project (0704-0188), Washington, DC 20503.

1. AGENCY USE ONLY (Leave blank)		2. REPORT DATE 1990		3. REPORT TYPE AND DATES COVERED Final 1 Jul 86 - 30 Sep 90	
4. TITLE AND SUBTITLE On the Modeling & Experimentation of Electromagnetically Coupled Microstrip Dipole Arrays in a Substrate-Superstrate				5. FUNDING NUMBERS DAAL03-86-K-0090	
6. AUTHOR(S) N. G. Alexopoulos					
7. PERFORMING ORGANIZATION NAME(S) AND ADDRESS(ES) University of California Department of Electrical Engineering Los Angeles, CA 90024-2594				8. PERFORMING ORGANIZATION REPORT NUMBER	
9. SPONSORING/MONITORING AGENCY NAME(S) AND ADDRESS(ES) U. S. Army Research Office P. O. Box 12211 Research Triangle Park, NC 27709-2211				10. SPONSORING/MONITORING AGENCY REPORT NUMBER ARO 23678.15-EL	
11. SUPPLEMENTARY NOTES The view, opinions and/or findings contained in this report are those of the author(s) and should not be construed as an official Department of the Army position, policy, or decision, unless so designated by other documentation.					
12a. DISTRIBUTION/AVAILABILITY STATEMENT Approved for public release; distribution unlimited.				12b. DISTRIBUTION CODE	
<p>→ The thrust of the research under this grant has been to develop the methodology for</p> <p>13. the modeling and design antenna arrays and microstrip discontinuities for microwave circuit applications. <i>The</i></p> <p>H-Y. Yang's Ph.D. thesis involves several key contributions in the subject areas of modeling <i>microstrip discontinuities</i>, <i>microstrip transitions</i>, and the <i>synthesis</i> of microstrip dipole arrays. This work has generated several journal publications within which one finds a fundamental contribution to the understanding of the above mentioned subjects. The analysis and the generated computer programs serve as practical tools for the design of microstrip circuits and microstrip dipole arrays. <i>the</i></p> <p>An evolution of <i>Yang's</i> work has led to the understanding of microstrip discontinuity effects. In particular the theory has been extended to model microstrip bends, T-junctions, four ports, etc. In each case the algorithms account for a precise description of energy loss at discontinuities due to radiation loss and surface wave loss. These models have also been substantiated with experiment. The models are now extended to provide precise designs for microstrip corporate feeds. This will lead to the design of two dimensional transversely fed electromagnetically coupled dipole arrays. <i>Keywords</i></p>					
14. SUBJECT TERMS Antenna Arrays, Microstrip Discontinuities, Microwave Circuit Applications, Microstrip Dipole Arrays, <i>Microstrip Circuits</i>				15. NUMBER OF PAGES	
				16. PRICE CODE <i>(RH)</i>	
17. SECURITY CLASSIFICATION OF REPORT UNCLASSIFIED	18. SECURITY CLASSIFICATION OF THIS PAGE UNCLASSIFIED	19. SECURITY CLASSIFICATION OF ABSTRACT UNCLASSIFIED	20. LIMITATION OF ABSTRACT UL		

# **Design of Transversely Fed EMC Microstrip Dipole Arrays Including Mutual Coupling**

**Hung-Yu Yang**  
**Nicolaos G. Alexopoulos**  
**Philippe M. Lepeltier**  
**George J. Stern**

Reprinted from  
**IEEE TRANSACTIONS ON ANTENNAS AND PROPAGATION**  
Vol. 38, No. 2, February 1990

# Design of Transversely Fed EMC Microstrip Dipole Arrays Including Mutual Coupling

HUNG-YU YANG, MEMBER, IEEE, NICOLAOS G. ALEXOPOULOS, FELLOW, IEEE, PHILIPPE M. LEPELTIER, AND GEORGE J. STERN, SENIOR MEMBER, IEEE

**Abstract**—Design techniques and procedures for microstrip dipole arrays transversely fed by proximity coupled microstrip lines are presented. Two design equations, which include the effects of mutual coupling, are developed and the corresponding design curves are obtained by a rigorous integral equation solution. A seven-element standing wave linear array is designed to illustrate the developed design procedures. The design data are checked by a complete integral equation solution of the array with good agreement. The measurements of radiation pattern and input impedance are found in good agreement with the design goal.

## I. INTRODUCTION

OLTMAN INTRODUCED a class of electromagnetically coupled (EMC) dipole antennas [1], [2]. The advantages of EMC dipoles are greater bandwidth, higher efficiency and an easier match to the feed lines, when compared to classically fed printed antennas. Based on the transmission line circuit model, Oltman and Huebner [2] built an EMC dipole array with radiating elements parallel (collinear) to the feedlines. Later, Elliott and Stern developed a rigorous design theory to include the effects of mutual coupling which successfully predicted the array performance [3], [4]. An efficient way to obtain the design curves was reported later [5]–[7] based on solving a Pocklington type integral equation using the method of moments. The EMC collinear dipole is ideally suited to a corporate feed, and elements of this type can be arranged in circular as well as rectangular grids.

Another dipole antenna of the Oltman type is the EMC transverse dipole, as shown in Fig. 1, where a dipole is oriented transverse to an embedded microstripline. A string of these dipoles above a common microstripline becomes a linear array. Depending on dipole spacing, one can obtain standing wave arrays or traveling wave arrays. A family of these linear arrays becomes a planar array. Current excitation on the dipole is governed by the amount of offset and the dipole length. If the dipole straddles symmetrically, no excitation of the dipole occurs. Weak coupling from line to dipole can be achieved through a slight lateral displacement of

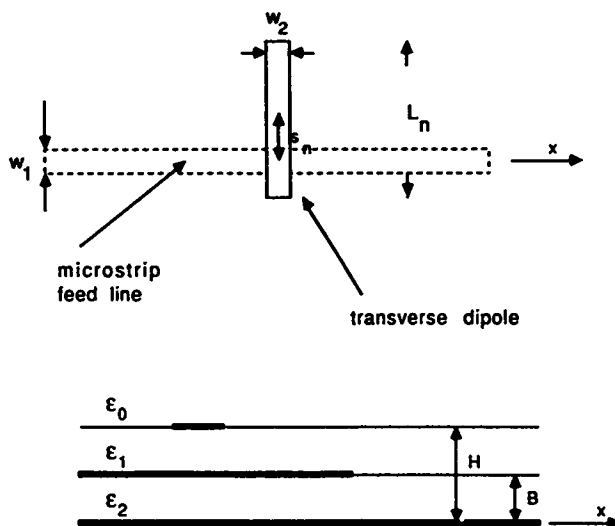


Fig. 1. The electromagnetically coupled transverse dipole.

the dipole from its centered position. Because of this weak coupling, large arrays are feasible [8].

Both theoretical and experimental studies of the EMC transverse dipole have been reported recently [9], [10]. In this paper, a design technique which includes mutual coupling is developed for the EMC transverse dipole arrays. Two design equations will be introduced in Section II. The methods for generating design curves will be discussed in Section III. A design example will be given in Section IV together with the experimental results. A numerical verification of the design obtained by solving the boundary value problem of the whole array system will also be provided.

## II. TWO DESIGN EQUATIONS

For the transverse EMC dipole under consideration, it can be shown from image theory that the scattering off the dipole is symmetric. In other words, the forward and backward scattering coefficients are the same. Therefore, in terms of the transmission line equivalent circuit, the dipole can be approximated as a shunt element with respect to the feed [11]. Each dipole in the array environment can then be modeled as a two-port network as shown in Fig. 2, and the whole system is a linear bilateral network. Therefore, one can write

$$I_n = \sum_{m=1}^N V_n Y_{mn} \quad (1)$$

as a set of equations connecting the transmission line mode

Manuscript received May 5, 1988; revised March 15, 1989. This work was supported by U.S. Army Research Office Grant DAAL03-86-K-0090.

H. Y. Yang was with the Electrical Engineering Department, University of California, Los Angeles, CA. He is now with Phraxos Research and Development, Inc., Santa Monica, CA 90405.

N. G. Alexopoulos is with the Electrical Engineering Department, University of California, Los Angeles, CA 90024.

P. Lepeltier is with Institut National Des Sciences Appliquees De Rennes, 35043 Rennes, Cedex, France.

G. J. Stern is with the Missile Systems Group, Hughes Aircraft Company, Canoga Park, CA 91304.

IEEE Log Number 8931320.

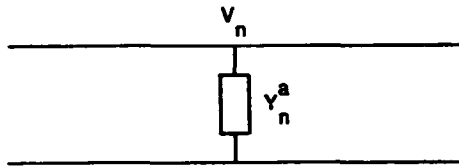


Fig. 2. Equivalent circuit of a dipole seen by the transverse microstripline.

voltages and currents at each reference port. The active admittance of each dipole seen by the feed line can be defined from (1) by

$$Y_n^a = \frac{I_n}{V_n} = Y_{nn} + Y_n^b \quad (2)$$

where

$$Y_n^b = \sum_{m=1}^N \left( \frac{V_m}{V_n} \right) Y_{mn}, \quad (3)$$

with the prime on  $\Sigma$  indicating the term  $n = m$  is excluded.  $Y_{nn}$  is the self-admittance and  $Y_n^b$  is referred to as the mutual admittance due to the mutual coupling between each dipole. Since a linear system is assumed, the current in each dipole can be written as

$$\frac{I_n^{\text{rad}}}{V_n} = \frac{I_{nn}}{V_n} + \sum_{m=1}^N \frac{I_{mn}}{V_n} \quad (4)$$

where  $I_{nn}$  is the current of the  $n$ th dipole for a given mode voltage in the absence of other dipoles and  $I_{mn}$  is the current of the  $n$ th dipole due to the current in the  $m$ th dipole. The isolated dipole current  $I_{nn}$  is a function of mode voltage, dipole length, and dipole offset which can further be expressed as

$$\frac{I_{nn}}{V_n} = \frac{Y_{nn}}{f_n(s_n, l_n)}, \quad (5)$$

where  $f_n(s_n, l_n)$  is a coefficient function relating the isolated dipole current to its self-admittance.

The two design equations can be summarized from the above derivations by

$$\frac{I_n^{\text{rad}}}{V_n} = \frac{Y_{nn}}{f_n} + \sum_{m=1}^N \frac{I_{mn}}{V_n} \quad (6)$$

and

$$Y_n^a = Y_{nn} + \sum_{m=1}^N \frac{V_m}{V_n} Y_{mn}. \quad (7)$$

It is noted that, for the EMC transverse dipole, the current phase variation in an isolated dipole is quite large, typically  $5^\circ$  to  $10^\circ$ ; while, in contrast, the current due to mutual coupling has a small phase variation. Therefore, in the design, the coefficient function is not suitable for relating mutual current ( $I_{mn}$ ) and mutual admittance ( $Y_{mn}$ ). One can use the mutual current term ( $I_{mn}$ ) directly in (6).

The fundamental design problem is now obvious. For a given design goal (radiating current in each dipole  $I_n^{\text{rad}}$ ) one wishes to find a set of  $(s_n, l_n)$  such that not only is (6) satisfied, but also the active admittance seen by each feed line is what was prescribed. The definition of the radiating current in each dipole may depend on the design goal. For example, if one wishes to design a specific pattern in the  $H$ -plane (perpendicular to the dipole), the  $I^{\text{rad}}$  should be defined as the current collapsed in the feed line. In other words,

$$I_n^{\text{rad}} = \int_0^{l_n} I_n(y) dy. \quad (8)$$

In the two design equations ((6) and (7)),  $Y_{nn}$ ,  $f_n$ ,  $I_{mn}/V_n$  and  $Y_{mn}$  can be determined by the method of moments. This issue will be discussed in the next section.

Suppose that all four functions are known. Further computations are still required to find the dipole lengths and offsets. Since only relative currents in the dipoles are meaningful, one can arbitrarily choose a dipole, say the  $m$ th, with length  $l_n$  and offset  $s_n$ . For the moment, assume that no mutual coupling exists and that the left-hand side of (6) can be determined according to the design goal (desired currents in the dipoles). One now can use the first design equation (6) to find  $N-1$  dipole lengths and offsets. This procedure requires that a two-variable nonlinear equation be solved  $N-1$  times. To avoid the stability and solvability problem of this nonlinear equation, the conjugate gradient method [12] can be used to provide optimized solutions. Even if the above procedures are completed, a few iterations of changing the dipole length or offset of the first selected dipole are required to provide the prescribed input impedance. Now the design data is what one should obtain if no mutual coupling exists. To include the effect of mutual coupling, one can use the present design data to compute the mutual admittance and mutual currents and go back to the two design equations repeating the above iterations. The whole procedure is iterated until convergence of the design data is found.

### III. DISCUSSION OF THE METHOD OF MOMENTS SOLUTION

In order to make an accurate design possible, information about the interaction between dipoles as well as dipole coupling to the feed line is required. The method of moments provides a rigorous and accurate solution. Integral equations for the EMC transverse dipole can be written as

$$E_x(x, y) = \iint G_{xx} J_x^{(1)}(x', y') dx' dy' + \iint G_{xy} J_y^{(2)}(x', y') dx' dy' \quad (9)$$

and

$$E_y(x, y) = \iint G_{yx} J_x^{(1)}(x', y') dx' dy' + \iint G_{yy} J_y^{(2)}(x', y') dx' dy' \quad (10)$$

where  $J_x^{(1)}(x', y')$  is the current in the microstripline and  $J_y^{(2)}(x', y')$  is the current in the dipole. The functions  $G_{xx}$ ,  $G_{xy}$ ,  $G_{yx}$  and  $G_{yy}$  are the dyadic Green's function components. A nice way of modeling the feed line is to use a finite but long

microstripline with a  $\delta$ -gap generator placed far from the line-dipole coupling region [5], [6]. When the combination of piecewise sinusoidal and Maxwell current basis functions is used in the method of moments [5], [6] followed by the Galerkin procedure, the matrix equations

$$[Z_{mn}][I_n] = [E_n] \quad (11)$$

can be obtained. The excitation column vector  $E$  has components  $E_k = -1$  when the  $\delta$  gap source is located at the center of the  $k$ th basis function, and  $E_n = 0$  anywhere else. The impedance matrix elements are in the form of

$$Z_{mn} = \int_0^{\pi/2} \int_0^\infty [(k^2 - \lambda_x^2)f(\lambda) + \lambda_x^2 h(\lambda)] J_n(\lambda_x, \lambda_y) \cdot J_m(\lambda_x, \lambda_y) \cos(\lambda_x \Delta x) \cos(\lambda_y \Delta y) d\lambda d\phi \quad (12)$$

when the  $m$ th and the  $n$ th basis functions are both on the dipole or on the line, and

$$Z_{mn} = \int_0^{\pi/2} \int_0^\infty \lambda_x \lambda_y [f(\lambda) - h(\lambda)] J_n(\lambda_x, \lambda_y) \cdot J_m(\lambda_x, \lambda_y) \sin(\lambda_x \Delta x) \sin(\lambda_y \Delta y) d\lambda d\phi, \quad (13)$$

otherwise. The functions  $J_n(\lambda_x, \lambda_y)$  and  $J_m(\lambda_x, \lambda_y)$  are the Fourier transforms of the expansion and testing functions, respectively.  $(\Delta x, \Delta y)$  is the displacement vector of two basis function centers, while  $\lambda_x$  and  $\lambda_y$  are defined as

$$\lambda_x = \lambda \cos \phi \quad (14)$$

and

$$\lambda_y = \lambda \sin \phi. \quad (15)$$

The functions  $f(\lambda)$  and  $h(\lambda)$  are given explicitly in [13], [14]. The unknown currents in the feed line or the dipole can be obtained by matrix inversion. As a result, one can use the unimode transmission line theory to deduce the circuit information from the method of moments solution for the current in the feed line. This procedure involves finding the current maximum, minimum, and their positions. Detailed procedures for this are shown in [5]. It is noted that in order to find the dipole equivalent admittance, the dipole can be placed a half-electrical wavelength from the line end such that the stub admittance will not be included in the input admittance observed by the feed line. An example of the input impedance calculation for an isolated dipole together with the experimental verification [9] is shown in Fig. 3. In the calculation, 19 basis functions are used in the dipole and 100 basis functions are used in the feed line of  $1.5 \lambda_0$  long. The comparison shows rather good agreement.

One of the features of using a  $\delta$  gap source is that the mode voltage of the line changes with change of the dipole length or offset (load); therefore, care must be taken to find this mode voltage, since as shown in (6), dipole current is proportional to the mode voltage and only their ratio is useful in the design.

Another feature of using the moment method in the array design is that the information about the currents in the dipoles can be obtained from the numerical process. This aspect is

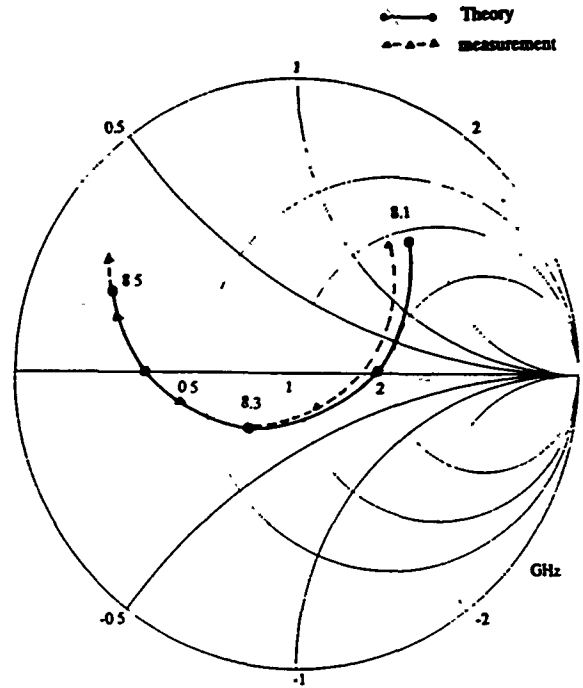


Fig. 3. Comparison between theoretical and experimental results for the input impedance of an EMC transverse dipole.  $\epsilon_1 = 2.17$ ,  $\epsilon_2 = 2.17$ ,  $H = 1.6$  mm,  $B = 0.8$  mm,  $w_1 = 1$  mm,  $w_2 = 2.2$  mm,  $\Delta x = 0$ ,  $\Delta s = 4.5$  mm and  $L = 12.4$  mm.

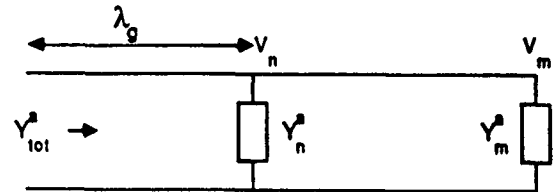


Fig. 4. Equivalent circuit of two parallel dipoles seen by a transverse microstripline.

particularly helpful, since one can use the dipole current directly to design for the desired excitation instead of using the equivalent circuit of the dipoles. This will be discussed further in the next section. Other issues in this array design are how the mutual coupling information can be separated from that of the self-term and how this can be achieved without involving the whole system at the same time. In order to solve these problems, certain assumptions are necessary. It is assumed that the self-admittance and self-current to mode voltage ratio will be the same with or without the presence of other dipoles, and that the mutual coupling between any two dipoles is unaffected by the rest. These two assumptions are good if mutual coupling is not too strong [11], which is usually true for practical arrays.

A method of computing mutual coupling of dipoles individually fed by a microstripline has been discussed in [7]. One of the features of the array considered here is that the dipoles are series fed by transverse microstriplines. The computation of mutual coupling in this case requires a different approach from [7]. To find the mutual coupling information, one can consider two dipoles fed by a microstripline and follow a numerical method similar to that for an isolated dipole except for the additional computation of dipole to dipole reaction. The equivalent circuit for these two dipoles is shown in Fig. 4. An

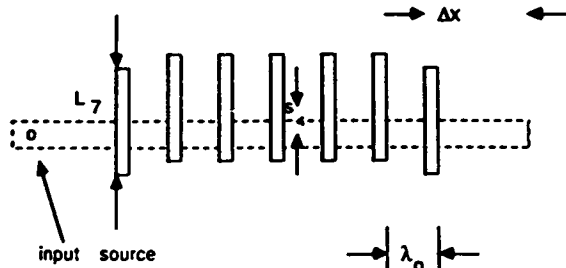


Fig. 5. A seven-element linear standing wave array. Elements are separated by a guide wavelength.

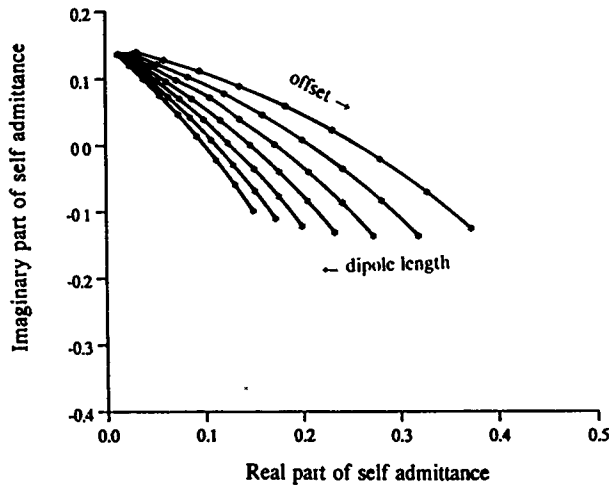


Fig. 6. Self-admittance of the dipole versus offset  $s$  and length  $L$ .  $s = 0.32 + 0.12(k-1)$  mm,  $k = 1, 2, 3, \dots, 9$ .  $L = 11.91 + 0.025(n-1)$  mm,  $n = 1, 2, 3, \dots, 7$ .

asymptotic extraction technique together with point source approximation has been developed in [15] to compute efficiently and accurately the reaction of two dipoles. After the matrix inversion, the solution for the current in the line and dipoles provides the total active admittance as well as active currents of the dipoles. For the  $n$ th and  $m$ th dipole with resonant spacing, the method of moments allows one to compute the total active admittance

$$\begin{aligned} Y_{tot}^a &= Y_n^a + Y_m^a \\ &= Y_{nn} + Y_{mm} \mp 2Y_{mn}. \end{aligned} \quad (16)$$

The minus or plus signs depend on whether the dipole spacing is an odd or even integer multiple of a half-guide wavelength. From (16), if the self-admittance of each dipole is known, the mutual admittance can be determined. The active currents in the dipole  $I_n^a$  and  $I_m^a$  can also be obtained numerically and can be described as

$$\frac{I_n^a}{V_n} = \frac{I_{nn}}{V_n} + \frac{I_{mn}}{V_n} \quad (17)$$

and

$$\frac{I_m^a}{V_m} = \frac{I_{mm}}{V_m} + \frac{I_{mn}}{V_m}. \quad (18)$$

From (17) and (18) together with knowledge of the current excited in an isolated dipole, the mutual current ( $I_{mn}$ ) can be obtained.

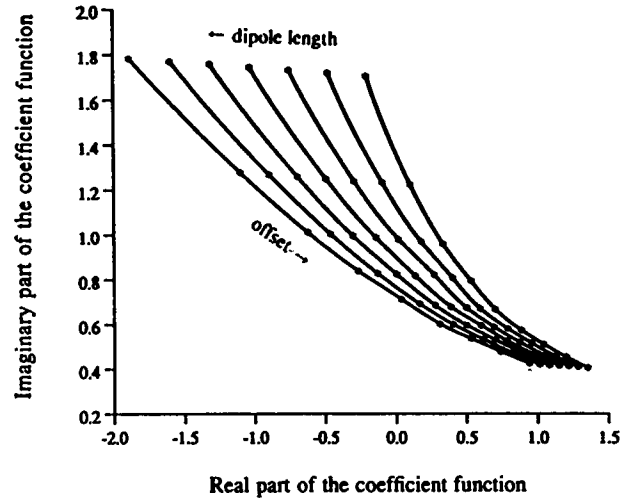


Fig. 7. Coefficient function of the dipole versus offset  $s$  and length  $L$ .  $s = 0.32 + 0.12(k-1)$  mm,  $k = 1, 2, 3, \dots, 9$ .  $L = 11.91 + 0.025(n-1)$  mm,  $n = 1, 2, 3, \dots, 7$ .

#### IV. A DESIGN EXAMPLE

The previous discussion of the design theory applies either to a linear or a planar array. Here, a seven-element standing-wave linear array will be designed to illustrate the design technique. The geometry is shown in Fig. 5. A sum pattern in the  $H$ -plane with a  $-20$  dB sidelobe level was prescribed for this array. The printed dipoles are series fed by a  $50 \Omega$  microstripline embedded in the middle of a substrate of thickness 62 mil and permittivity 2.35. The design frequency is 8.5 GHz and element spacing is chosen to be one guide wavelength. All dipoles have the same width of 1 mm and the offsets and lengths are to be found. The design curves for the self-admittance  $Y_{nn}$  and the coefficient function  $f_n$  as a function of offset and length obtained from the method of moments solution are shown in Figs. 6 and 7, respectively. It is found that, for the EMC transverse dipole, many basis functions are required to obtain adequate convergence. To obtain each data point, 19 expansion modes are used in each dipole, and piecewise sinusoidal modes of size of 0.04 guide wavelength are used in the line. It is observed from Fig. 7 that for different dipole offsets and lengths, the phase of  $f_n$  is not a constant. This implies that even for resonant spacing, to have in-phase excitation, the dipole cannot be self-resonant. To obtain a perfect match, the stub length  $\Delta x$  in Fig. 5 can be suitably adjusted to tune out the total active susceptance.

The sampled data are used to construct the database such that for a given offset and length the function value can be obtained through a two-dimensional interpolation routine. Mutual coupling between two dipoles is a function of dipole lengths and offsets for a fixed spacing. It is found that mutual coupling is not sensitive to a small change in dipole length. Also from the results for no mutual coupling, it is found that the lengths of all the dipoles are different by less than 0.2%. Therefore, in the mutual coupling computation, the dipole lengths are held fixed. The mutual admittance and mutual current as a function of offsets for one guide wavelength spacing and fixed dipole length are shown in Figs. 8 and 9, respectively. A similar procedure can be followed for a two



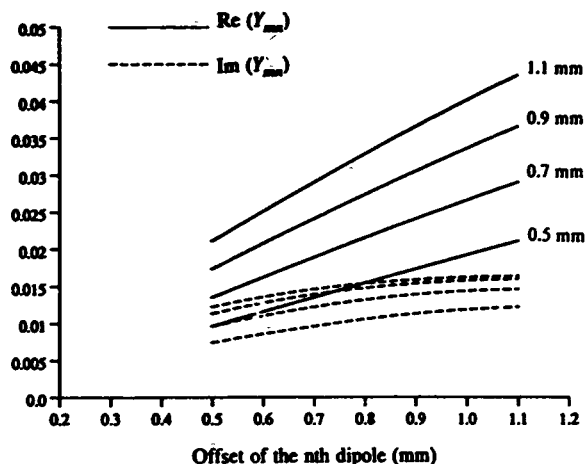


Fig. 8. Mutual admittance of two dipoles versus their offsets. Element spacing is one guide wavelength and  $L = 11.98$  mm.

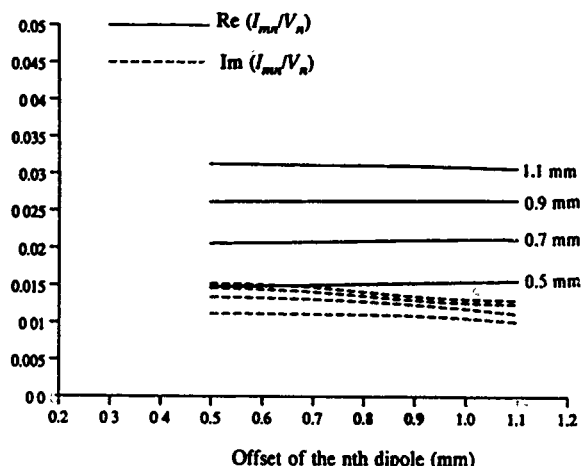


Fig. 9. Mutual current of two dipoles versus their offsets. Element spacing is one guide wavelength and  $L = 11.98$  mm.

wavelength spacing, and so on. As a result, the interpolation or extrapolation method can provide the mutual coupling information for any dipole spacing.

The design data after a few iterations, including the self- and mutual admittances are shown in Table I. The element spacing is 23.6 mm and  $\Delta x = 9.68$  mm. It is seen that the mutual admittance is more than 25% of the total active admittance. Therefore, it is concluded that even at one wavelength spacing, the effect of mutual coupling should not be ignored. To provide a confident check of the design data, the method of moments is applied to the seven-element linear array. The results of active admittance and current in each dipole are shown in Table II together with the results from the synthesis technique. It is observed that the current amplitudes agree within 1 to 2% and the phases agree within  $\pm 1^\circ$ . The admittance comparison is also good.

The antenna array was built on a 12-in square Duroid board as shown in Fig. 10. The measured return loss from the feed line is shown in Fig. 11. The bandwidth of this array is about 4.2%. At the designed resonant frequency (8.5 GHz), the measured VSWR is about 1.1. The agreement between the theory and measurement confirms the importance of the

effects of mutual coupling. Both the desired and measured radiation patterns in the  $H$ -plane are shown in Fig. 12. The measured pattern is found to be in good agreement with the design criteria. The asymmetry of the sidelobes is due to the fact that the array is not symmetrically located with respect to the edges of the finite array and therefore space and surface wave diffraction at the edges contributes nonuniformly to the radiation pattern. Another contributing factor may be the limited accuracy of the photo-etching process in producing identical microstrip dipoles and highly accurate interdipole spacing.

## V. CONCLUSION

A synthesis method for the design of transversely fed EMC microstrip dipole arrays has been presented. By using a network representation, two design equations, which include the effect of mutual coupling, are developed. An iterative procedure using the conjugate gradient method has been applied to solve the design equations. The design curves are obtained numerically by the method of moments. The method of computing mutual coupling is also described. It is found that

TABLE I  
DESIGN DATA FOR A SEVEN-ELEMENT LINEAR ARRAY

No.	Offset in mm	Dipole Length in mm	$Y_{in}$	$Y_{mutual}$
1	0.5151	11.982	$0.0536 + j 0.1040$	$0.014 + j 0.010$
2	0.6884	12.000	$0.0805 + j 0.0674$	$0.038 + j 0.023$
3	0.8925	11.983	$0.1422 + j 0.0093$	$0.056 + j 0.029$
4	0.9500	11.973	$0.1674 - j 0.0096$	$0.064 + j 0.031$
5	0.8925	11.983	$0.1422 + j 0.0093$	$0.056 + j 0.029$
6	0.6884	12.000	$0.0805 + j 0.0674$	$0.038 + j 0.023$
7	0.5151	11.982	$0.0536 + j 0.1040$	$0.014 + j 0.010$

$Y_{in} = 0.996 + j0.02$  (result from iterations)

$Y_{in} = 1.000 - j0.04$  (result from IES)

TABLE II  
DESIGN CHECK THROUGH AN INTEGRAL EQUATION SOLUTION

No.	Desired Current	IES Current
1	$1.0000 < 0.0$	$1.0000 < 0.0$
2	$1.2751 < 0.0$	$1.2961 < -0.7$
3	$1.6810 < 0.0$	$1.6703 < -0.9$
4	$1.8351 < 0.0$	$1.8222 < 0.3$
5	$1.6810 < 0.0$	$1.6730 < -0.7$
6	$1.2751 < 0.0$	$1.2971 < -0.3$
7	$1.0000 < 0.0$	$0.9940 < 0.7$

The unit of the phase of current is in degrees

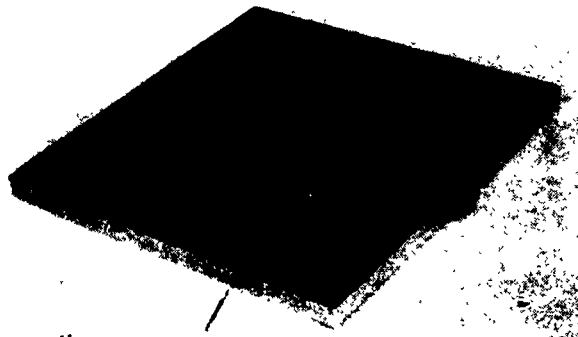


Fig. 10. A 12-in square microstrip dipole array.

to obtain a satisfactory design, one needs to include the mutual admittance as well as the mutual current in the design equations. The design of a seven-element standing wave linear array is presented. The design data obtained from the synthesis procedure are implemented in a numerical experiment, namely, solving the boundary value problem of the whole array system. The input admittance and radiating currents from this integral equation solution are found to be in good agreement with the design goal. The measurements of the

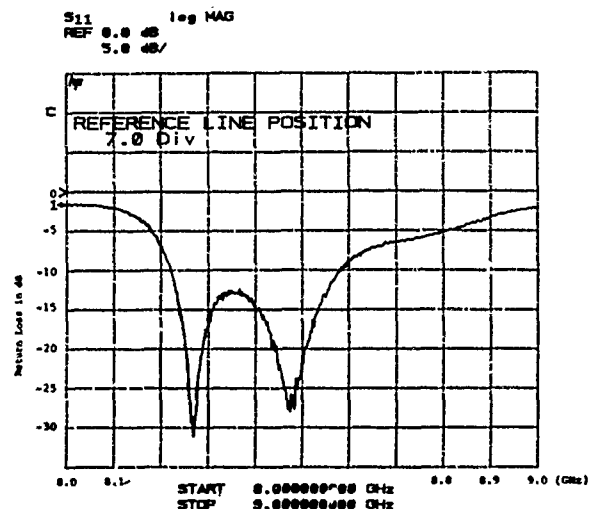


Fig. 11. Measured return loss of the designed antenna array.

radiation pattern and input admittance also compare very well with the design criteria.

#### ACKNOWLEDGMENT

The authors would like to thank Professor R. S. Elliott for his comments and discussion during this research. The authors

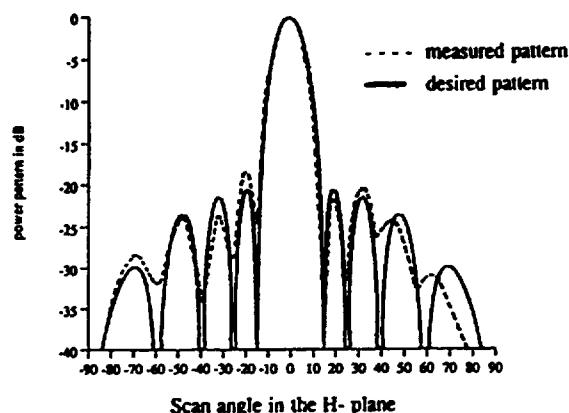


Fig. 12. Comparison between the desired and measured antenna.

would also like to thank Dr. J. A. Castaneda of Phraxos Research and Development, Inc. for his help with the measurements.

#### REFERENCES

- [1] H. G. Oltman, "Electromagnetically coupled microstrip dipole antenna elements," presented at the 8th European Microwave Conf., Paris, France, Sept. 1978.
- [2] H. G. Oltman and D. A. Huebner, "Electromagnetically coupled microstrip dipoles," *IEEE Trans. Antennas Propagat.*, vol. AP-29, no. 1, pp. 151-157, Jan. 1981.
- [3] R. S. Elliott and G. J. Stern, "The design of microstrip dipole arrays including mutual coupling, Part I: Theory," *IEEE Trans. Antennas Propagat.*, vol. AP-29, no. 9, pp. 757-760, Sept. 1981.
- [4] G. J. Stern and R. S. Elliott, "The design of microstrip dipole arrays including mutual coupling, Part II: Experiment," *IEEE Trans. Antennas Propagat.*, vol. AP-29, no. 9, pp. 761-765, Sept. 1981.
- [5] P. B. Katehi and N. G. Alexopoulos, "On the modeling of electromagnetic coupled microstrip antennas—The printed strip dipole," *IEEE Trans. Antennas Propagat.*, vol. AP-32, no. 11, pp. 1179-1186, Nov. 1984.
- [6] D. R. Jackson and N. G. Alexopoulos, "Analysis of planar strip geometries in a substrate-superstrate configuration," *IEEE Trans. Antennas Propagat.*, vol. AP-34, no. 12, pp. 1430-1438, Dec. 1986.
- [7] P. B. Katehi, "A generalized method for the evaluation of mutual coupling in microstrip arrays," *IEEE Trans. Antennas Propagat.*, vol. AP-35, no. 2, pp. 125-133, Feb. 1987.
- [8] R. S. Elliott, private communication.
- [9] P. Lepeltier, J. M. Floc'h, and J. Citerne, "Complete and rigorous analysis of the electromagnetically coupled transverse microstrip dipole," *Electron. Lett.*, vol. 23, no. 16, pp. 822-824, July 1987.
- [10] P. Lepeltier, J. M. Floc'h, J. Citerne, and D. Martin, "On the excitation microstrip line parasitic radiation observed in printed antennas—The EMC dipole," in *IEEE Antennas Propagat. Soc. Int. Symp. Dig.*, June 1987, pp. 814-818.
- [11] R. S. Elliott, *Antenna Theory and Design*. Englewood Cliffs, NJ: Prentice-Hall, 1981.
- [12] M. Aoki, *Introduction to Optimization Techniques*. New York: Macmillan, 1971.
- [13] N. G. Alexopoulos and D. R. Jackson, "Fundamental superstrate (cover) effects on printed circuit antennas," *IEEE Trans. Antennas Propagat.*, vol. AP-32, pp. 807-816, Aug. 1984.
- [14] H. Y. Yang and N. G. Alexopoulos, "Basic blocks for high-frequency interconnects—Theory and experiment," *IEEE Trans. Microwave Theory Tech.*, vol. 36, no. 8, pp. 1258-1264, Aug. 1988.
- [15] D. R. Jackson and N. G. Alexopoulos, "An asymptotic extraction technique for evaluating Sommerfeld-type integrals," *IEEE Trans. Antennas Propagat.*, vol. AP-34, no. 12, pp. 1467-1470, Dec. 1986.

#### Hung-Yu Yang (S'87-M'88)



He received the B.S. degree in electrical engineering from the National Taiwan University in 1982 and the M.S. and Ph.D. degrees in electrical engineering from the University of California, Los Angeles, in 1985 and 1988, respectively.

His research included the areas of millimeter wave printed circuit antennas, printed antenna design and the modeling of millimeter wave integrated circuit discontinuities. Currently, he is a Research Engineer with the Phraxos Research and Development, Inc., Santa Monica, CA. He is involved in the development of computer codes for frequency selective surfaces, computer-aided design of high-frequency integrated circuit discontinuities, the synthesis of microstrip arrays and the scattering from antennas.



Nikolaos G. Alexopoulos (S'68-M'69-SM'82-F'87) graduated from the 8th Gymnasium of Athens, Greece, and received the B.S.E.E., M.S.E.E., and Ph.D. degrees from the University of Michigan, Ann Arbor, in 1964, 1967, and 1968, respectively.

Currently he is Professor and Chairman of the Electrical Engineering Department at the University of California, Los Angeles. He is also a Consultant with Northrop Corporation's Advanced Systems Division. His current research interests are in electromagnetic theory as it applies to the modeling of integrated-circuit components and printed circuit antennas for microwave and millimeter-wave applications, substrate materials and their effect on integrated-circuit structures and printed antennas, integrated-circuit antenna arrays, and antenna scattering studies. He is also interested in the interaction of electromagnetic waves with materials and, in particular, active media.

Dr. Alexopoulos is the Editor of the *Electromagnetics Journal* and *Alta Frequenza* and is on the Editorial Boards of the *IEEE TRANSACTIONS ON MICROWAVE THEORY AND TECHNIQUES* and the *International Journal on Electromagnetics Theory*. He served as the 1974 Chairman of the IEEE APS Chapter. He is the co-recipient (Honorable Mention) of the 1983 APS R.W.P. King Best Paper Award.

#### Philippe M. Lepeltier



He received the "Diplôme d'Ingénieur," "Diplôme d'Etudes Approfondies" and the Ph.D. degree in electrical engineering from the National Institute of Applied Science, Rennes, France, in 1983, 1983, and 1986, respectively.

He was with the Electrical Engineering Department of the University of California, Los Angeles, for part of 1987. He is currently a Research Engineer at Alcatel Espace, Rennes, Cedex, France. His research interests are microstrip antennas, corrugated horns and multiple-beam, dual-band primary feeds for reflector antennas.

George J. Stern (S'58-M'61-M'69-SM'84), for a photograph and biography please see page 1271 of the November 1985 issue of this TRANSACTIONS.

# A FULL-WAVE ANALYSIS OF SHIELDED MICROSTRIP LINE-TO-LINE TRANSITIONS<sup>†</sup>

T.S. Horng, H.Y. Yang, and N.G. Alexopoulos

Electrical Engineering Department, University of California, Los Angeles  
Los Angeles, CA 90024

## Abstract

A rigorous procedure is used to analyze several microstrip line-to-line transitions in a shielded multi-layer structure. The transitions studied include edge-coupled lines, overlay-coupled lines and coupled-to-single lines. A power conservation check based on a rigorous Poynting vector analysis is also used to determine the accuracy of the numerical convergence. The results of power distributions and coupling coefficients of the line-to-line transitions are studied parametrically to identify the properties and applications of each transition.

## Introduction

Proximity-coupled line-to-line transitions are important building blocks for high frequency interconnects. Applications in millimeter-wave integrated circuits include high-pass filters, multiplexers and directional couplers. Losch [1] has designed a broadband highpass filter in realization of an overlay coupled line transition based on a quasi-static formulation. A more rigorous full wave analysis for coupled line filters associated with the open structure has been discussed by Katehi [2] for an edge-coupled transition and by Yang and Alexopoulos [3] for an overlay-coupled transition. In [3] a spectral-domain approach by expanding the current in the coupled line section with a combination of entire domain and subdomain modes is used. This mode expansion mechanism seems to be the most efficient and fruitful by far. For the advantage of preventing unnecessary interaction and radiation loss, a waveguide

housing is sometimes more common and practical in the real circuit design. In this work, a full-wave moment method is used to characterize shielded microstrip line-to-line transitions.

## Method of Moments

Several different types of electromagnetically coupled lines as shown in Figs. 1-3 are investigated. The methodology applied here is in analogy to that reported in [3], however, the spectral Green's function and the numerical procedure are very much different. Since the line-offset and the width of microstrips in shielded structures are comparable to the waveguide dimensions, the transverse current component should not be neglected and complete dyadic Green's function of a multi-layer waveguide is required. The integral equation after a Galerkin's procedure can be converted into a set of linear equations, when expressed in matrix form:

$$\begin{bmatrix} [Z_{11ss}] & [Z_{11se}^{ref}] & [Z_{12ss}] & [Z_{12se}^{tra}] \\ [Z_{21ss}] & [Z_{21se}^{ref}] & [Z_{22ss}] & [Z_{22se}^{tra}] \end{bmatrix} \begin{bmatrix} [I_{1s}] \\ -\Gamma \\ [I_{2s}] \\ T \end{bmatrix} = \begin{bmatrix} [I_{11se}^{inc}] \\ [I_{21se}^{inc}] \end{bmatrix} \quad (1)$$

where each submatrix  $[Z]$ , due to the presence of both x and z directed currents, contains 4 submatrices, for example:

$$[Z_{11ss}] = \begin{bmatrix} [Z_{11ssxx}] & [Z_{11ssxz}] \\ [Z_{12ssxz}] & [Z_{11sszz}] \end{bmatrix} \quad (2)$$

and submatrix  $[I]$  and  $[I^{inc}]$  contain two submatrices as follows:

<sup>†</sup> This research was performed under U.S. Army Research Office Grant  
DAAL 03-86-k-0090

$$[I_{1s}] = \begin{bmatrix} [I_{1z}] \\ [I_{1x}] \end{bmatrix} \quad (3)$$

$$[I_{11e}^{inc}] = \begin{bmatrix} [I_{11ze}^{inc}] \\ [I_{11xe}^{inc}] \end{bmatrix} \quad (4)$$

Each element in these submatrices represents the reaction of different basis functions. For instance, the elements of  $[Z_{12xxz}]$  are the reaction between x-directed currents of subdomain mode associated with microstrip 1 and z-directed currents of subdomain mode associated with microstrip 2. These subdomain modes are basically either PWS functions or pulse functions. The entire domain modes are composed of the reflected mode, transmitted mode, and incident mode which are distinguished with abbreviation *ref*, *tra*, and *inc*, respectively. The computation of each element requires both infinite summation and integration in spectral domain and their expressions are in the general form of:

$$Z_{ijss\hat{u}_1\hat{u}_2}^{kl} = \sum_{n=-\infty}^{\infty} \int_{-\infty}^{\infty} \hat{G}_{ij\hat{u}_1\hat{u}_2}(\alpha_n, \beta) \hat{J}_{i\hat{u}_1}(\alpha_n) \hat{J}_{j\hat{u}_2}(\alpha_n) \hat{f}_{i\hat{u}_1}^k(\beta) \hat{f}_{j\hat{u}_2}^l(\beta)^* d\beta \quad (5)$$

and

$$Z_{ijse\hat{u}_1\hat{u}_2}^{kp} = \sum_{n=-\infty}^{\infty} \int_{-\infty}^{\infty} \hat{G}_{ij\hat{u}_1\hat{u}_2}(\alpha_n, \beta) \hat{J}_{i\hat{u}_1}(\alpha_n) \hat{J}_{j\hat{u}_2}(\alpha_n) \hat{f}_{i\hat{u}_1}^k(\beta) \hat{f}_{j\hat{u}_2}^p(\beta)^* d\beta \quad (6)$$

where  $\hat{G}_{ij\hat{u}_1\hat{u}_2}$  is the spectral-domain dyadic Green's function. Superscript *p* identifies different entire domain modes.  $\hat{J}_{i\hat{u}_1}$  is the Fourier transform of transverse dependence and  $\hat{f}_{i\hat{u}_1}^k$ ,  $\hat{J}_{i\hat{u}_1}$  are Fourier transform of longitudinal dependence with respect to subdomain and entire domain modes, respectively.

### Power Conservation Check

For shielded microstrip transitions, the convergence of the moment method solution is very sensitive to the type and number of expansion functions chosen. Power conservation provides a nice way of checking the accuracy of the solution. According to the configurations shown in Figs. 1-3, the incident power should be equal to the summation of reflected power, transmitted power and some loss coupled to the multi-layered waveguide modes. With proper waveguide dimension, the loss coupled to the waveguide modes can be removed and the expression of power conservation can be simply written as

$$|\Gamma|^2 + \frac{Z_{e2}}{Z_{e1}} |T|^2 = 1 \quad (7)$$

where  $Z_{e1}$  and  $Z_{e2}$  are the characteristic impedance of feed line and parasitic coupled line respectively. A frequency-dependent method of computing the characteristic impedance of both single and coupled microstrip transmission lines described in [4, 5] can be used to determine the accuracy of the numerical results given in this work. In the present computations of the transition problems, entire domain modes of 3 guided wavelength and 9 to 18 subdomain modes are used in each microstrip line. The convergence has been checked within 1% accuracy. The power conservation is also checked with good consistency. An example of this check is shown in Table I.

### Numerical Results and Discussions

From Figs. 5 - 11, the maximum coupling occurs around  $ovl = \frac{1}{4}\lambda_{go}$  ( $\lambda_{go}$  is the wavelength of the odd-mode guided in the coupled line section) with a wide frequency-insensitive range. This implies that the transitions are broad-band and are very useful in many MMIC applications. Besides, from Figs. 5 - 8, the coupling efficiency is better in overlay line-to-line transition than in edge coupled line-to-line transition. This indicates the former will be a promising element in realization of millimeter wave high-pass filter.

Figs. 9 - 10 show the results for the case of an overlay coupled-to-single microstrip transition. It is seen that the even-mode coupling depends less on the line-offset of parasitic coupled line, as compared with single-line coupling. It is also noted that the even-mode of coupled lines can couple energy to a centered parasitic microstrip line while the odd-mode can not. This may find applications in a phase detector.

The frequency response of an overlay-coupled microstrip transition is shown in Figs. 11 - 12. The geometrical parameters are specially designed in the coupled section where the line-width is much larger than the spacing between two lines. It is seen that, in a wide frequency range, the coupling coefficient is almost independent of frequency. In addition, it is possible to couple more than 95% of the total power through the discontinuity. This geometry (so called

ovl	$ \Gamma ^2 + \frac{\pi \epsilon_2}{\pi \epsilon_1}  \Gamma ^2$	ovl	$ \Gamma ^2 + \frac{\pi \epsilon_2}{\pi \epsilon_1}  \Gamma ^2$
-0.05	1.000	0.13	0.997
-0.03	1.000	0.15	0.999
-0.01	1.001	0.17	1.004
0.01	1.003	0.19	1.003
0.03	1.004	0.21	1.002
0.05	1.003	0.23	1.001
0.07	1.001	0.25	1.000
0.09	1.001	0.27	1.000
0.11	0.999	0.29	0.999

Table 1. Power conservation check for the configuration of Fig. 2. Both  $|\Gamma|^2$  and  $|\Gamma|^2$  are the same as those in Figs. 7 and 8.

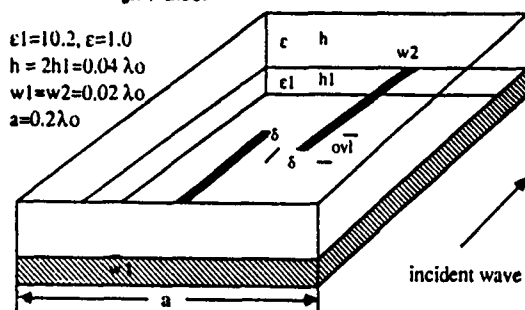


Fig. 1 Edge coupled line-to-line transition

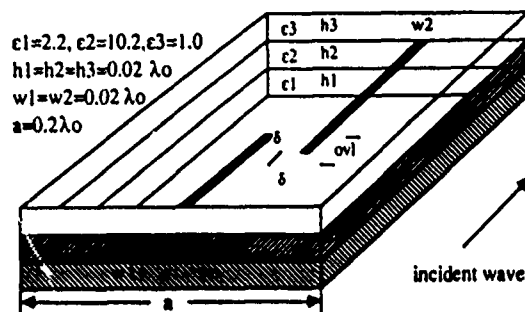


Fig. 2 Overlay coupled line-to-line transition

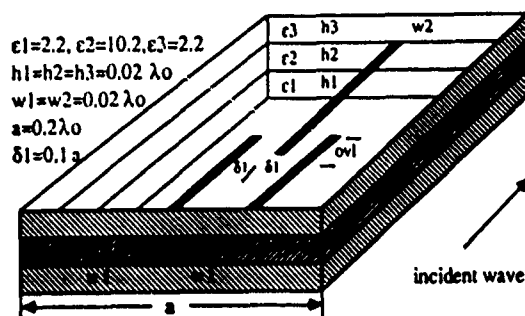


Fig. 3 Overlay coupled-to-single line transition

suspended stripline) may be very useful due to these two excellent characteristics.

## Conclusions

In this work, a full-wave analysis is proposed to develop a generalized dynamic model for several types of shielded microstrip line-to-line transitions. The results obtained from the method of moments are checked within 1% accuracy by power conservation. The results presented also show excellent properties in some transitions and may find promising applications in MMIC coupler and filter design.

## References

- [1] L.E. Losch, "Design Procedure for inhomogeneous coupled line sections," IEEE Trans. on Microwave Theory and Techniques, Vol. MTT-36, pp. 1186-1190, July 1988.
- [2] P.B. Katehi, "Radiation losses in MM-wave open microstrip filters," Electromagnetics, vol.7, pp. 137-152, 1987.
- [3] H.Y. Yang and N.G. Alexopoulos, "Basic building blocks for high frequency interconnects: theory and experiment," IEEE Trans. on Microwave Theory and Techniques, Vol. MTT-36, pp.1258-1264, Aug. 1988.
- [4] M.K. Krage and G.I. Haddad, "Frequency-dependent characteristics of microstrip transmission lines," IEEE Trans. on Microwave Theory and Techniques, Vol. MTT-20, pp. 678-686, Oct. 1972.
- [5] A. Nakatani and N.G. Alexopoulos, "Toward a generalized algorithm for the modeling of dispersive properties of integrated circuit structures on anisotropic substrates," IEEE Trans. on Microwave Theory and Techniques, Vol. MTT-33, pp. 1436-1441, Dec. 1985.

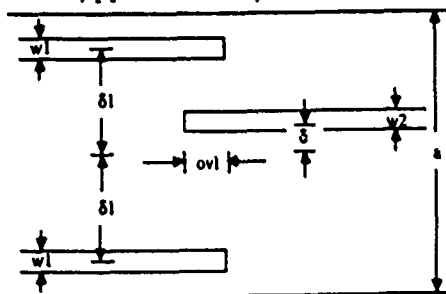


Fig. 4 Top view for Fig. 3

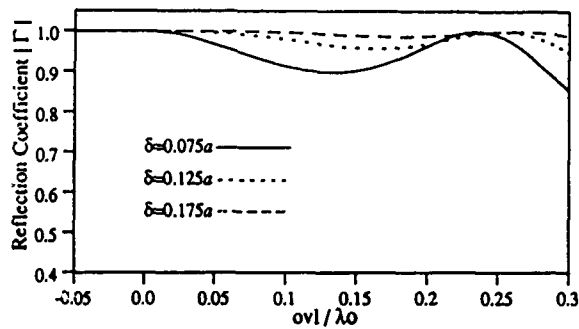


Fig. 5  $|\Gamma|$  versus overlap for the configuration of Fig. 2.1

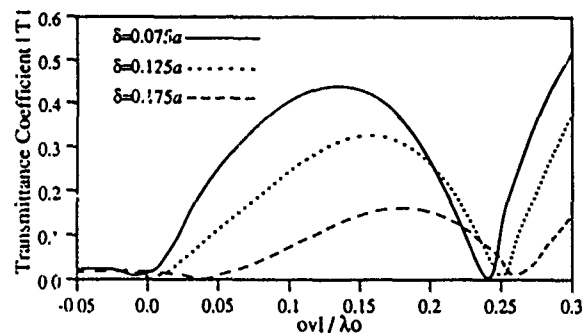


Fig. 6  $|T|$  versus overlap for the configuration of Fig. 2.1

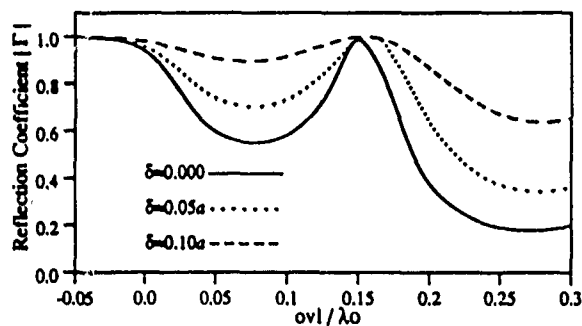


Fig. 7  $|\Gamma|$  versus overlap for the configuration of Fig. 2.2

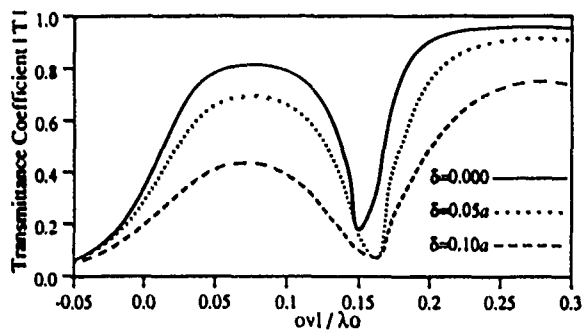


Fig. 8  $|T|$  versus overlap for the configuration of Fig. 2.2

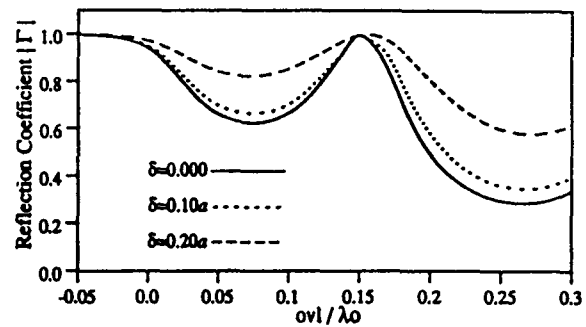


Fig. 9  $|\Gamma|$  versus overlap for even-mode excitation (configuration Fig. 2.3)

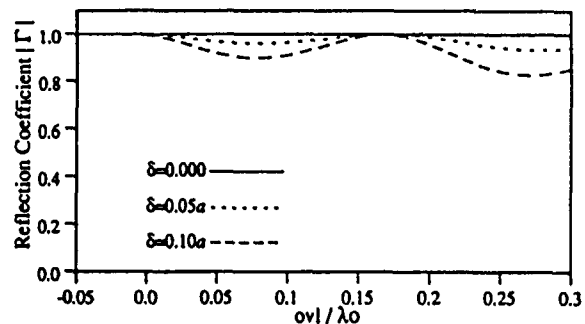


Fig. 10  $|\Gamma|$  versus overlap for odd-mode excitation (configuration Fig. 2.3)

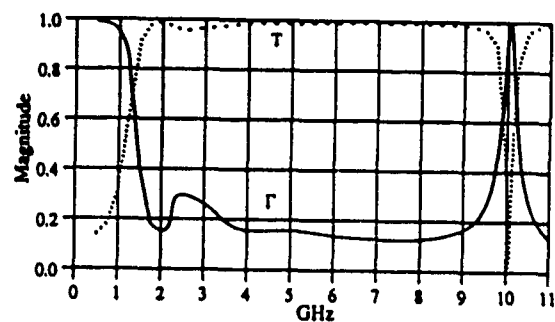


Fig. 11 Magnitude of  $\Gamma$  and  $T$  versus frequency.

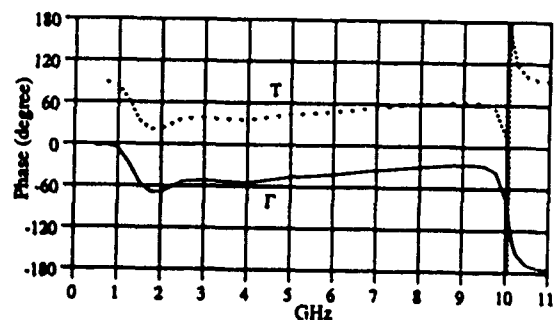


Fig. 12 Phase of  $\Gamma$  and  $T$  versus frequency.  
Geometrical parameters:  $\epsilon_1 = \epsilon_3 = 1, \epsilon_2 = 10.2$ ,  
 $h_1 = h_3 = 70\text{mil}, h_2 = 10\text{mil}, w_1 = w_2 = 50\text{mil}$ ,  
 $\delta_1 = \delta_2 = 0, \text{ovl} = 185\text{mil}, a = 500\text{mil}$

**UNIVERSITY OF CALIFORNIA**

**Los Angeles**

**Frequency Dependent Modeling  
of  
Passive Integrated Circuit Components**

**A dissertation submitted in partial satisfaction of the  
requirements for the degree Doctor of Philosophy  
in Electrical Engineering**


**by**


**Hung-Yu Yang**

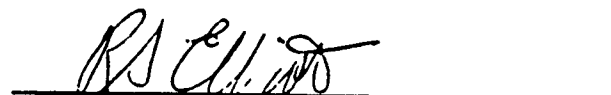
**1988**

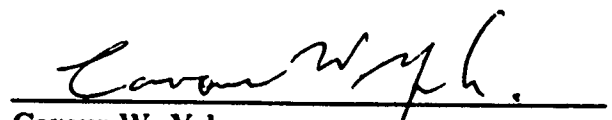


The dissertation of Hung-Yu Yang is approved.

  
Nathaniel Grossman

  
Paul M. Davis

  
Robert S. Elliott

  
Cavour W. Yeh

  
Nicolaos G. Alexopoulos, Committee Chair

University of California, Los Angeles

1988

## DEDICATION

To my parents and my wife Ding-hwa

## Contents

List of figures.....	viii
List of tables .....	xv
Acknowledgements .....	xvi
Vita .....	xvii
Publications.....	xvii
Abstract .....	xix
<b>I Introduction.....</b>	<b>1</b>
1.1 Integrated circuit modeling.....	1
1.2 Printed antenna modeling .....	4
<b>II Integral equation formulation and Green's function.....</b>	<b>7</b>
2.1 Green's function for an electric Hertzian dipole.....	7
2.2 Green's function for a magnetic Hertzian dipole.....	14
<b>III MIC discontinuities I -</b>	
<b>Microstrip open-end and gap discontinuities</b>	
<b>in a two-layer configuration .....</b>	<b>19</b>
3.1 Introduction .....	19
3.2 The method of moments and matrix formulation.....	22
3.3 Numerical technique.....	28
3.4 Results.....	33
<b>IV MIC discontinuities II -</b>	
<b>Slot line short-end discontinuities.....</b>	<b>43</b>
4.1 Introduction .....	43

4.2	Integral Equation.....	46
4.3	Results.....	46
<b>V</b>	<b>A dynamic model for microstrip-slotline transition .....</b>	<b>51</b>
5.1	Introduction .....	51
5.2	Theory.....	52
5.2.1	Green's function formulation .....	52
5.2.1	The choice of expansion modes .....	55
5.2.3	The method of moments and matrix formulation.....	57
5.2.4	Some aspects of the numerical analysis.....	57
5.3	Numerical results.....	58
<b>VI</b>	<b>Proximity coupled microstrip transition</b>	
	<b>in double layer integrated circuits .....</b>	<b>62</b>
6.1	Introduction .....	62
6.2	Analysis.....	65
6.2.1	EMC collinear microstriplines.....	65
6.2.2	EMC transverse microstriplines .....	66
6.3	Results.....	68
<b>VII</b>	<b>Radiation characteristics of printed slot antennas.....</b>	<b>77</b>
7.1	Introduction .....	77
7.2	Substrate effects on printed slot properties.....	77
7.3	A center fed printed slot.....	85
<b>VIII</b>	<b>Printed antenna feeding structures.....</b>	<b>90</b>
8.1	Introduction .....	90
8.2	A microstrip fed slot.....	91

8.3	A slot line fed dipole.....	97
8.4	An EMC transverse dipole.....	101
8.5	A microstrip fed slot coupled dipole .....	104
<b>IV</b>	<b>Design of transverse fed EMC dipole arrays</b>	
	<b>including mutual coupling.....</b>	<b>108</b>
9.1	Introduction .....	108
9.2	Two design equations .....	110
9.3	Discussion of the method of moments solution .....	114
9.4	A design example.....	118
<b>X</b>	<b>Conclusions.....</b>	<b>127</b>
	<b>References .....</b>	<b>130</b>
	<b>Appendix A .....</b>	<b>138</b>
	<b>Appendix B.....</b>	<b>140</b>
	<b>Appendix C .....</b>	<b>142</b>
	<b>Appendix D .....</b>	<b>144</b>
	<b>Appendix E.....</b>	<b>145</b>

## List of Figures

Fig. 2.1	An electric Hertzian dipole in the superstrate .....	8
Fig. 2.2	An electric Hertzian dipole in the substrate .....	8
Fig. 2.3	A magnetic Hertzian dipole in a substrate-superstrate configuration .....	16
Fig. 3.1	An open-end microstrip line in a two layer structure.....	20
Fig. 3.2	Microstrip gap in a two-layer structure .....	20
Fig. 3.3	Equivalent circuit of a microstrip gap.....	23
Fig. 3.4	Top view of a microstrip gap discontinuity .....	23
Fig. 3.5	Layout of the expansion modes in a microstrip gap.....	25
Fig. 3.6	Convergence test for open-end capacitance $\epsilon_1 = 9.6, b = 0.02\lambda_0$ and $w/b = 1$ .....	38
Fig. 3.7	Convergence test for open-end conductance $\epsilon_1 = 9.6, b = 0.02\lambda_0$ and $w/b = 1$ .....	38
Fig. 3.8	Convergence test for open-end capacitance $\epsilon_1 = 9.6, b = 0.02\lambda_0$ .....	39
Fig. 3.9	Excess length of an open-end microstrip line versus microstrip width $\epsilon_1 = 9.6, b = 0.01\lambda_0$ .....	39
Fig. 3.10	Energy loss at microstrip open-end versus frequency $\epsilon_1 = 9.6, b = 0.3\text{mm}, w = b$ and $t = b$ .....	40
Fig. 3.11	Excess length of an open-end microstrip line versus frequency $\epsilon_1 = 9.6, b = 0.3\text{mm}, w = b$ and $t = b$ .....	40

Fig. 3.12	Excess length of an open-end microstrip line versus frequency $b = t = h/2$ , $h = 0.3$ mm and $w/h = 1$ .....	41
Fig. 3.13	Gap capacitance versus gap spacing $\epsilon_1 = 8.875$ , $\epsilon_2 = 1$ , $b = 0.508$ mm and $w = b$ .....	41
Fig. 3.14	Gap conductances versus frequency $\epsilon_1 = 9.6$ , $b = 0.3$ mm, $w = b$ , $t = b$ and $s = 0.3762 b$ .....	42
Fig. 3.15	Normalized gap capacitance versus frequency $b = t = h/2$ , $h = 0.3$ mm and $w/h = 1$ and $s = 0.2 h$ .....	42
Fig. 4.1	A basic slot line structure.....	45
Fig. 4.2	A short-end slot line discontinuity.....	45
Fig. 4.3	A short-end slot line sandwich .....	45
Fig. 4.4	Power losses at slot line short end versus frequency $\epsilon_1 = 12$ and $h = 121$ mil.....	49
Fig. 4.5	Normalized slot line short-end reactance versus frequency $\epsilon_1 = 12$ and $h = 121$ mil.....	49
Fig. 4.6	Power losses at slot line short end versus frequency Comparison between slot line and sandwiched slot line $\epsilon_1 = 12$ $h = d = 121$ mil and $w/h = 0.5$ .....	50
Fig. 4.7	Normalized slot line short-end reactance versus frequency. Comparison between a slot line and a slot line sandwich $\epsilon_1 = 12$ $h = d = 121$ mil and $w/h = 0.5$ .....	50
Fig. 5.1	Top view of microstrip-slot line transition .....	53
Fig. 5.2	Cross section of microstrip-slot line transition.....	53
Fig. 5.3	VSWR versus frequency for microstrip-slot line transition.....	60

Fig. 5.4	Smith chart plot of impedance versus frequency for microstrip-slot line transition. The reference plane is on the center of the cross section.....	61
Fig. 6.1	Proximity coupled collinear microstrip -microstrip transition .....	63
Fig. 6.2	Proximity coupled transverse microstrip -microstrip transition .....	64
Fig. 6.3	$ \Gamma $ versus overlap $l_{ol}$ for an EMC $50\Omega - 50\Omega$ collinear microstrip transition. $f = 10$ GHz, $h = 50$ mil, $b = 25$ mil .....	72
Fig. 6.4	$ \Gamma $ and $ T $ versus frequency. $l_{ol} = 0.15$ cm, $\epsilon_1 = 2.2$ and $\epsilon_2 = 10.2$ , $h = 50$ mil, $b = 25$ mil, $w_1 = 42$ mil and $w_2 = 76$ mil.....	73
Fig. 6.5	$ \Gamma $ as a function of stub length for an EMC $50\Omega - 50\Omega$ transverse microstrip transition. $f = 10$ GHz, $h = 50$ mil, $b = 25$ mil, $w_1 = 42$ mil and $w_2 = 76$ mil.....	74
Fig. 6.6	$ \Gamma $ as a function of stub length for an EMC $50\Omega - 50\Omega$ transverse microstrip transition. $f = 10$ GHz, $h = 50$ mil, $b = 25$ mil, $w_1 = 42$ mil and $w_2 = 76$ mil.....	75
Fig. 6.7	VSWR versus frequency for transverse microstrip transition. Parameters are the same as those in Fig. 6.5, except $l_{m1} = 0.81$ cm and $l_{m2} = 0.75$ cm.....	76



Fig. 7.1	A basic printed slot structure.....	78
Fig. 7.2	A magnetic Hertzian dipole in the ground plane.....	78
Fig. 7.3	Power distribution in a printed slot structure versus substrate thickness. $\epsilon_1 = 4$ and $\mu_1 = 1$ .....	83
Fig. 7.4	Power distribution in a printed slot structure versus substrate thickness. $\epsilon_1 = 12.5$ and $\mu_1 = 1$ .....	83
Fig. 7.5	Power distribution in a printed slot structure versus substrate thickness. $\epsilon_1 = 1$ and $\mu_1 = 4$ .....	84
Fig. 7.6	Slot radiation efficiency versus substrate thickness .....	84
Fig. 7.7	A center-fed printed slot.....	86
Fig. 7.8	Input admittance of a center-fed printed slot versus slot length. $b = 0.02\lambda_0$ and $0.1\lambda_0$ .....	88
Fig. 7.9	Input admittance of a center-fed printed slot versus slot length. $\epsilon_1 = 2.2$ and $0.1\lambda_0$ .....	88
Fig. 7.10	Input admittance of a center-fed printed slot versus slot length. $\epsilon_1 = 2.2$ and $1\lambda_0$ .....	89
Fig. 8.1	A microstrip fed slot.....	93
Fig. 8.2	Normalized resistance of a $50\Omega$ microstrip fed slot. $h = 0.02\lambda_0$ and $w = 0.01\lambda_0$ .....	94
Fig. 8.3	Normalized reactance of a $50\Omega$ microstrip fed slot. $h = 0.02\lambda_0$ and $w = 0.01\lambda_0$ .....	94
Fig. 8.4	Smith chart plot of the impedance of a microstrip fed slot versus offset. $\epsilon_1 = 2.2$ , $h = 0.02\lambda_0$ , $w_s = 0.01\lambda_0$ and $w_m = 3.125h$ .....	95

Fig. 8.5	Input impedance of a stub-tuned slot fed by a microstrip line. $\epsilon_1 = 2.2$ , $d = 2.032$ mm, $w_m = 6.35$ mm, $w_s = 1.016$ mm, $L = 40$ mm and stub length = 2.2 mm .....96
Fig. 8.6	A slot line fed printed dipole.....98
Fig. 8.7	Normalized admittance of a slot line fed dipole versus dipole length. $\epsilon_1 = 12.8$ and $0.2\lambda_0$ , $w_s = 0.01\lambda_0$ and $w_m = h$ .....99
Fig. 8.8	Normalized admittance of a slot line fed dipole versus frequency. $\epsilon_1 = 12$ , $h = 0.121$ in, $w_s = 0.562 h$ , $w_m = h$ and $L = 1.6$ cm.....100
Fig. 8.9	Normalized admittance of a slot line fed dipole versus frequency. $\epsilon_1 = 2.54$ , $\epsilon_2 = 12$ , $h_1 = h_2 = 121$ mil, $w_s = 0.562 h$ , $w_m = h$ and $L = 3$ cm.....100
Fig. 8.10	The electromagnetically coupled transverse dipole .....102
Fig. 8.11	Comparison between theoretical and experimental results for the input impedance of an EMC transverse dipole. $\epsilon_1 = 2.17$ , $\epsilon_2 = 2.17$ , $h_1 = h_2 = 0.8$ mm, $w_1 = 1$ mm, $w_2 = 2.2$ mm, $\Delta x = 0$ , $\Delta y = 4.5$ mm and $L = 12.4$ mm .....103
Fig. 8.12	A microstrip fed slot coupled dipole .....106
Fig. 8.13	Normalized impedance of microstrip fed slot coupled dipole versus dipole length. $f = 3$ GHz, $\epsilon_1 = 2.54$ , $\epsilon_2 = 2.54$ , $h_1 = h_2 = 1.6$ mm, $w_s = 1$ mm, $w_m = 4.45$ mm, $w_d = h$ .....107
Fig. 9.1	The electromagnetically coupled transverse dipole .....109
Fig. 9.2	A seven element linear standing wave array.

	Elements are spaced by a guided wave length.....	119
Fig. 9.3	Self admittance of the dipole versus offset and length .....	122
Fig. 9.4	Coefficient function of the dipole versus offset and length ....	122
Fig. 9.5	Mutual admittance of two dipoles versus their offsets. Element spacing is one guided wavelength and $L = 12.70$ mm.....	123
Fig. 9.6	Mutual current of two dipoles versus their offsets. Element spacing is one guided wavelength and $L = 12.70$ mm.....	123
Fig. 9.7	Measured return loss of the designed antenna array.....	125
Fig. 9.8	Comparison between the desired and measured antenna pattern in the H- plane.....	126
Fig. E.1	Integration contour of Eq. E.3, branch point is at $j\lambda_y$ .....	147
Fig. E.2	Integration contour of Eq. E.4 .....	147

## **List of Tables**

Table I	Design data of a seven element linear array .....	124
Table II	Design check through an integral equation solution.....	124

## ACKNOWLEDGMENTS

The author would like to express his sincerely gratitude to his adviser Professor N. G. Alexopoulos for his constant guidance, encouragement and support during this research. The author also thanks Professor R. S. Elliott for his valuable comments and suggestions. A debt of gratitude is also due to Professors P. M. Davis, R. S. Elliott, N. Grossman and C. W. Yeh for serving in the committee.

The author additionally thanks the U.S. Army Research Office and TRW Company for providing funding for this research.

The author also likes to express his appreciation to Dr. D. R. Jackson at Houston University for his helpful discussions during this research. Appreciation is extended to Dr. P. Lepeltier at I.N.S.A. in France for providing the experimental results. Mr. O. Forham's help for experiment is also appreciated.

The author would also like to thank his student colleagues for their friendship; among them, Dr. Y. U. Kim should be specially mentioned.

Finally, but never the least, the author would like to thank his parents for their support and his wife Ding-hwa for her love and patience.

## VITA

October 25, 1960	Born, Taipei, Taiwan, R.O.C.
1978-1982	B.S., National Taiwan University, Taipei, R.O.C.
1982-1984	Navy Electronics Officer, Taiwan, R.O.C..
1984-1985	M.S., University of California, Los Angeles
1985-1988	Research Assistant, University of California, Los Angeles

## PUBLICATIONS AND PRESENTATIONS

- H-Y. Yang and N.G. Alexopoulos, "Uniaxial and biaxial substrate effects on finline characteristics," IEEE Trans. on Microwave Theory and Technique, Vol. MTT-35, no. 1, pp. 24-29, Jan. 1987.
- H-Y. Yang and N.G. Alexopoulos, "Gain enhancement methods for printed circuit antennas through multiple superstrates," IEEE Trans. on Antennas and Propagation, Vol. AP-35, no. 7, pp.860-863, July 1987.
- H-Y. Yang and N.G. Alexopoulos, "Generation of nearly hemispherical and high gain azimuthally symmetric pattern with printed circuit antennas," IEEE Trans. on Antennas and Propagation, Vol. AP-35, no. 8, pp.972-976, August, 1987.
- H-Y. Yang and N.G. Alexopoulos, "Multi-level proximity coupled microstrip transition," Proceedings of 17th European Microwave Conference, pp. 362-367, 1987.
- H-Y. Yang and N.G. Alexopoulos, "Characterization of the finline step discontinuity on anisotropic substrates," IEEE Trans. on Microwave Theory and Technique, Vol. MTT-35, no. 11, pp. 956-963, Nov. 1987.
- H-Y. Yang and N.G. Alexopoulos, "A dynamic model for microstrip-slotline transition and related structures," IEEE Trans. on Microwave Theory and Technique, Vol. MTT-36, no. 2, pp. 286-293, Feb. 1988.

- Y. Yang and N.G. Alexopoulos, "On the theory of proximity coupled open end microstrip transition in double layer integrated circuit structures," IEEE Trans. on Microwave Theory and Technique, Vol. MTT-36, no. 8, Aug. 1988.
- H-Y. Yang and N.G. Alexopoulos, "Uniaxial and biaxial substrate effects on uniform finlines and finline step discontinuities" IEEE MTT-s International Microwave Symposium, pp.61-63, Baltimore, June 1986.
- H-Y. Yang and N.G. Alexopoulos, "A dynamic model for microstrip- slotline transition and related structures" IEEE MTT-s International Microwave Symposium, pp.773-775, Las Vegas, June 1987.
- H-Y. Yang and N.G. Alexopoulos, "Analysis of an aperture coupled dipole antenna, a microstrip fed slot and a slotline fed dipole," IEEE A-Ps International symposium, pp.921-924, Blacksburg, June 1987.
- H-Y. Yang, N.G. Alexopoulos and D.R. Jackson, "Analysis of microstrip open-end and gap discontinuities in a substrate-superstrate configuration", IEEE MTT-s International Microwave Symposium, New York, May 1988.

**ABSTRACT OF THE DISSERTATION**

**FREQUENCY DEPENDENT MODELING**

**OF**

**PASSIVE INTEGRATED CIRCUIT COMPONENTS**

**by**

**Yang Hung-Yu**

**Doctor of Philosophy in Electrical Engineering**

**University of California, Los Angeles, 1988**

**Professor Nicolaos G. Alexopoulos, Chair**

The topic of this dissertation involves a dynamic modeling of frequency dependent passive integrated circuit components. The first part of this dissertation deals with the characterization of microwave and millimeter wave discontinuities. The analytic approach is based on solving integral equations with the method of moments. In the method of moments procedure, an exact Green's function is used, which takes into account all the physical effects including radiation, surface waves and high order mode effects. In order to characterize the discontinuities, a numerical scheme is developed to model coupled semi-infinite lines. This involves using both entire domain modes and subdomain modes as the expansion functions to represent the fundamental



propagating mode and higher order evanescent modes respectively. This type of expansion mechanism is numerically efficient and particularly useful in coupled line modeling.

Microstrip open-end and gap discontinuities in layered integrated circuits are studied with emphasis on the material, radiation and surface wave effects. The analysis is modified to study slotline short-end discontinuities in sandwich structures. The advantage of using a slot line sandwich is also discussed. With the understanding of the simplest discontinuities in microstrip and slotline circuits, the study is further extended to the line-to-line transition which becomes increasingly important in monolithic circuits. Three types of circuit transitions are investigated: microstrip-slotline transition, proximity coupled collinear and transverse microstrip-microstrip transition. The applications of these transitions are described and the validity of the developed theory is verified by experiments.

The second part of this dissertation involves the study of printed circuit antennas which are special cases of integrated circuit discontinuities. The numerical method for integrated circuit discontinuities can be applied directly to the printed circuit antenna structures. Four potential printed antenna architectures for millimeter wave monolithic phased array applications are discussed. These include a microstrip fed slot antenna, a slotline fed dipole antenna, an EMC transverse dipole antenna and a microstrip fed slot coupled dipole antenna. The features of each architecture are described.

Design techniques and procedures for microstrip dipole arrays transversely fed by proximity coupled microstrip lines are also presented. Two design

equations which include the effects of mutual coupling are developed. The corresponding design curves are obtained by a rigorous integral equation solution. A seven element standing wave linear array is designed to illustrate the developed procedures. The data is checked by a complete integral equation solution of the array with excellent agreement. The antenna pattern and input impedance are also compared with the measurement with good agreement.

## **Chapter I**

### **Introduction**

#### **1.1. Integrated Circuit Modeling**

Integrated circuit structures have been used for numerous electronics applications due to the features of low cost, light weight, easy fabrication and reproducibility [1], [2]. The basic structure is composed of a grounded substrate with various circuit components integrated on the air-dielectric interface. In solid state electronics, bipolar or field effect transistors usually require semiconductor layers on top of the substrate [3]. This type of geometry is usually referred to as a layered structure. For frequencies below 1 GHz, passive components, which include signal transmission path (wire), inductance, capacitance etc, have been well understood using lumped circuit concepts. However, in the current state of the art, various applications require the operating frequency of the device to go beyond the microwave wave or millimeter wave range [4] – [7]. Microwave and millimeter wave integrated circuits, in the current trend, have become increasingly important for both commercial and military applications. When the operating frequency is high enough such that the device dimension is comparable to a wavelength, the circuit components are electromagnetically coupled (EMC) together and the design concept needs to be completely reformulated. In the past decade, numerous works have contributed to the investigation of the electromagnetic phenomena of microwave integrated circuits (MICs) and microwave

monolithic integrated circuits (MMICs). However, most of the published works are confined to the characteristics of wave guiding structures. For this reason, many discontinuity problems are not well understood and remain to be solved [7] – [14]. From the design point of view, with the increasing complexity of integrated circuits, accurate computer aided design (CAD) tools are needed to determine precisely the circuit performance. Therefore, currently and in the near future, developing accurate and efficient CAD algorithms should be a primary concern for the microwave society [15]. The early researches on discontinuities problems were mainly based on the electrostatic approximation due to its simplicity [16] – [18]. This approximation (or so called quasi-static approach) is known to be valid in the frequency transition from low frequencies to the microwave range.

A full wave spectral domain approach (SDA) for analyzing MIC discontinuities was proposed in the early 1980s by Jansen [19]. Since this SDA was originally proposed for waveguide applications, the integrated circuits are assumed surrounded by an enclosed housing. Therefore, this approach has the limitation that radiation and surface wave effects are not included [20] – [23]. Besides, in order to simulate the open structure, waveguide dimensions would usually be large which cause numerical convergence problems. Therefore, it is reasonable to conclude that the SDA is good only for waveguide discontinuity problems or for open structures with frequencies below C band, where the radiation and surface wave effects are less important.

An integral equation approach (IEA) was first proposed in 1985 by Katchi and Alexopoulos to characterize MIC and MMIC discontinuities [24]. This

approach is complete and rigorous in the sense that it simulates the physical structure and includes all the physical effects, although the applications of this method are still at the beginning stage [25] – [27] .

The first part of this dissertation will be concerned with a rigorous examination of the method of moments solution of integral equations, in terms of its accuracy, efficiency and applicability, to the characterization of MIC and MMIC discontinuities. Special numerical treatises will be developed to characterize a class of semi-infinite line transitions frequently encountered in integrated circuits. The derivation of Green's function will be provided in Chap. II. Microstrip open end and gap discontinuities in layered integrated circuits will be discussed in Chap III. Numerical techniques adopted in this dissertation will also be discussed in detail in Chap. III. It will be shown in Chap. III that the developed numerical algorithm is general enough to apply to many related structures. The analysis developed in Chap. III is extended in Chap. IV to study slotline short-end discontinuities in sandwiched structures. With enough understanding of the simplest discontinuities in microstrip and slotline circuits, the analysis can be further extended to the investigation of the important subject of line-to-line transitions in integrated circuit structures. In Chap. V a dynamic model for the microstrip-slotline transition is developed. Two types of novel transitions are analyzed in Chap. VI, namely the EMC collinear microstrip-microstrip transition and the EMC transverse microstrip-microstrip transition. The potential applications of these transitions are also described. The analysis is also confirmed by experiments.

## 1.2. Printed Antenna Modeling

Integrated or printed circuit antennas (PCA) are a natural evolution of integrated circuit components [28], [29]. The radiating elements may consist of dipoles, slots or patches. Since the invention of microstrip antennas back to the early 50s [30], extensive researches have been carried out worldwide. Mathematical modeling was initially proposed in the early 1970s with a transmission line analogy [31], [32]. Later on, a cavity method and a quasi-static approach were also applied to certain structures with some success [33] – [37]. However, for frequencies above the microwave range, the above mentioned methods will not be accurate due to their thin substrate approximation. Besides, these methods are not applicable for printed dipoles and slots, and do not include surface wave effects. A rigorous and almost exact dynamic analysis of PCA was first performed at UCLA in 1979 [38]. This approach is based on solving the Pocklington type integral equation with the method of moments. Since then, an extensive amount of work has been carried out toward the efficient and accurate evaluation of this Sommerfeld-type integral [39] – [44]. At the same time, fundamental properties of PCAs such as gain, efficiency, bandwidth and antenna patterns have also been investigated in terms of various device parameters [45] – [55]. Fundamental radiation characteristics of a printed slot will be discussed in Chap. VII. The properties of a printed dipole and a printed slot are also compared in terms of the radiation efficiency, surface wave effects and radiation resistance.

One of the crucial parts in the design of printed circuit antennas is the design of feeding structures. Microstrip lines electromagnetically coupled (EMC)

to the radiating elements has proven to be the most versatile and convenient type of feed for antenna arrays [56]. Rigorous analysis of EMC collinear dipoles has been thoroughly investigated in Katehi's and Jackson's dissertations [57], [58]. In the second part of this dissertation, several new feeding structures will be investigated by a method of moments solution of coupled integral equations. The current trend in printed circuit antenna technology is to develop an architecture which is completely monolithic. In Chap. VIII, four potential architectures for millimeter monolithic phased array applications are discussed. The features of each architecture are described. These four feeding structures are a microstrip fed slot antenna, a slotline fed dipole antenna, an EMC transverse dipole antenna and a microstrip fed slot coupled dipole antenna.

The ultimate goal in the analysis of printed circuit antennas is to provide a design technique of microstrip arrays. Looking back to the past, the only rigorous and complete design of microstrip arrays was published by Elliott and Stern in 1981 [59], [60]. In Chap. IX of this dissertation, a new type of microstrip array will be investigated. The geometry is composed of dipoles parallel to each other fed by an EMC transverse microstripline embedded in the substrate. The design of an antenna array requires the knowledge of each antenna element's size and position with respect to other elements and the feed such that the desired excitation in each antenna and therefore the desired antenna pattern can be achieved. Two design equations which are closely related to those developed by R.S. Elliott in waveguide slot array design [61] will be discussed. The corresponding design curves will be obtained numerically

through a rigorous integral equation solution. In order to show how the design technique works, a seven element standing wave linear array will be designed to have the performance of 20 dB Dolph-Chebyshev broadside sum pattern in the H- plane. The importance of the effects of mutual coupling will also be addressed.



## Chapter II

### Analysis of Hertzian Dipoles in a Layered Planar Geometry

In this chapter, the electromagnetic fields due to an electric Hertzian (infinitesimally small) or a magnetic Hertzian dipole are derived. These fields, or so called Green's function must be known before the method of moments can be applied. This Green's function for a layered planar geometry is well known as a Sommerfeld-type solution [62]. In section 2.1, the Green's function for an electric dipole is discussed. In section 2.2, the Green's function for a magnetic dipole will be developed.

#### 2.1. Green's Function for an Electric Hertzian Dipole.

For the substrate-superstrate geometry under consideration, the formulation of the Green's function for a dipole embedded in the superstrate (Fig. 2-1) or in the substrate (Fig. 2-2) is different and will be discussed separately. The case for a dipole in the superstrate will be considered first.

##### (a). An Electric Hertzian Dipole in the Superstrate

The geometry shown in Fig. 2-1 contains a substrate with permittivity  $\epsilon_1$ , permeability  $\mu_1$  and thickness  $b$ , and a superstrate with permittivity  $\epsilon_2$  and permeability  $\mu_2$ . The total thickness of the material is  $h$ . The dipole is located at  $z = z_s$  with  $b \leq z_s \leq h$  and oriented in the  $\hat{x}$  direction.

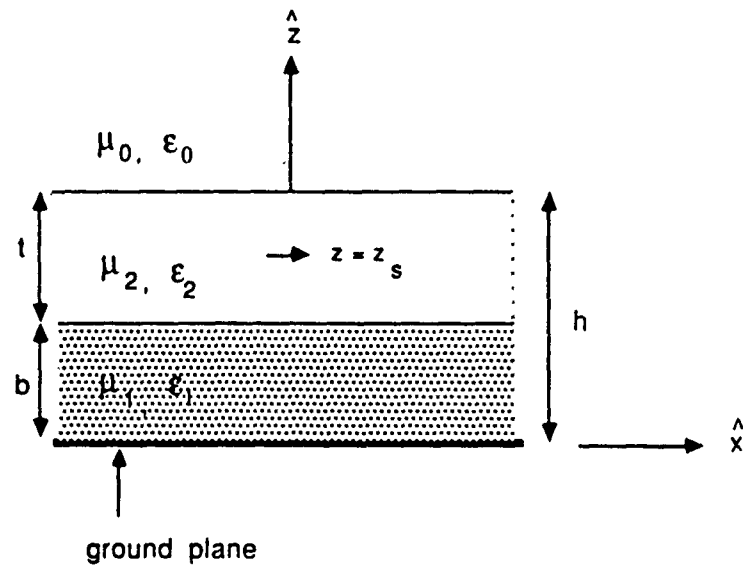


Figure 2-1. An electric Hertzian dipole in the superstrate.

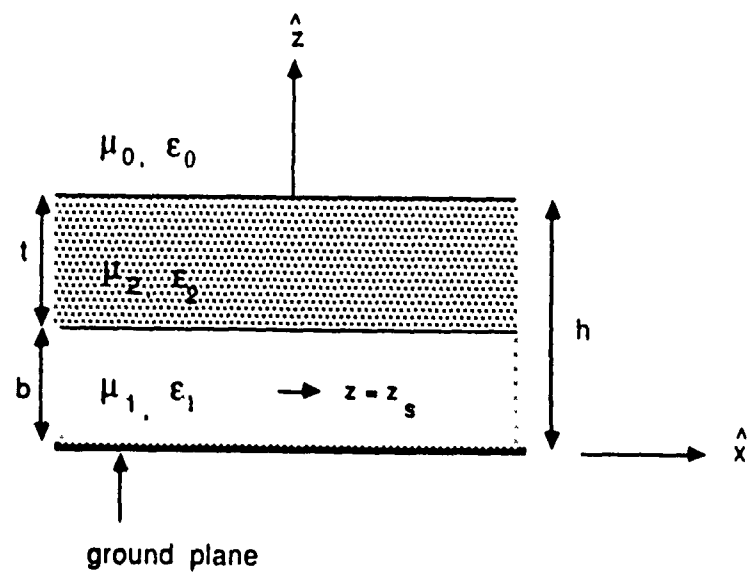


Figure 2-2. An electric Hertzian dipole in the substrate.

The electromagnetic fields in each region can be characterized in terms of the Hertz potential in the following forms:

$$E^{(i)} = k_i^2 \vec{\pi}^{(i)} + \nabla (\nabla \cdot \vec{\pi}^{(i)}) \quad (2.1)$$

and

$$H^{(i)} = j\omega\epsilon_i\epsilon_0 (\nabla \times \vec{\pi}^{(i)}) \quad (2.2)$$

with  $i$  representing the region (i). From Sommerfeld's work [62], it is known that the Hertz potential may contain only  $x$  and  $z$  components. In other words,

$$\vec{\pi}^{(i)} = \pi_x^{(i)} \hat{x} + \pi_z^{(i)} \hat{z}. \quad (2.3)$$

The nice feature of using the Hertz potential is that its components satisfy the scalar wave equations, where the solution can be obtained in a straight forward manner. Through the use of the Hertz potential, Maxwell's equations can be reformulated in the form of

$$\nabla^2 \vec{\pi}^{(i)} + k_i^2 \vec{\pi}^{(i)} = \frac{1}{-j\omega\epsilon_2\epsilon_0} \delta(x - x_s) \delta(y - y_s) \delta(z - z_s) \hat{x}. \quad (2.4)$$

The lateral electromagnetic fields in region  $i$  are related to the Hertz potential through

$$E_x^{(i)} = k_i^2 \pi_x^{(i)} + \frac{\partial}{\partial x} \left( \frac{\partial \pi_x^{(i)}}{\partial x} + \frac{\partial \pi_z^{(i)}}{\partial z} \right), \quad (2.5)$$

$$E_y^{(i)} = \frac{\partial}{\partial y} \left( \frac{\partial \pi_x^{(i)}}{\partial x} + \frac{\partial \pi_z^{(i)}}{\partial z} \right), \quad (2.6)$$

$$H_x^{(i)} = j\omega\epsilon_i\epsilon_0 \frac{\partial \pi_z^{(i)}}{\partial y}, \quad (2.7)$$

$$H_y^{(i)} = j\omega\epsilon_i\epsilon_0 \left( \frac{\partial \pi_x^{(i)}}{\partial z} - \frac{\partial \pi_z^{(i)}}{\partial x} \right). \quad (2.8)$$

With the boundary conditions that  $E_x$ ,  $E_y$ ,  $H_x$  and  $H_y$  are continuous across each interface, and with the radiation condition at  $z \rightarrow \infty$ , one is able to obtain an expression for the Hertz potential in the Fourier domain from eight equations with eight unknowns. The resulting Hertz potential in each region can be summarized as:

In region 0:  $h \leq z$

$$\pi_x^{(0)} = \frac{1}{\gamma} \int_{-\infty}^{\infty} \int_{-\infty}^{\infty} \frac{f_0(\lambda)}{D_e(\lambda)} e^{-q(z-h)} e^{-j\lambda_x(x-x_s)} e^{-j\lambda_y(y-y_s)} d\lambda_x d\lambda_y \quad (2.9)$$

and

$$\pi_z^{(0)} = \frac{1}{\gamma} \int_{-\infty}^{\infty} \int_{-\infty}^{\infty} \frac{j\lambda_x h_0(\lambda)}{D_e(\lambda) D_m(\lambda)} e^{-q(z-h)} e^{-j\lambda_x(x-x_s)} e^{-j\lambda_y(y-y_s)} d\lambda_x d\lambda_y. \quad (2.10)$$

In region 1:  $0 \leq z \leq b$

$$\pi_x^{(1)} = \frac{1}{\gamma} \int_{-\infty}^{\infty} \int_{-\infty}^{\infty} \frac{f_1(\lambda)}{D_e(\lambda)} \sinh q_1 z e^{-j\lambda_x(x-x_s)} e^{-j\lambda_y(y-y_s)} d\lambda_x d\lambda_y \quad (2.11)$$

and

$$\pi_z^{(1)} = \frac{1}{\gamma} \int_{-\infty}^{\infty} \int_{-\infty}^{\infty} \frac{j\lambda_x h_1(\lambda)}{D_e(\lambda) D_m(\lambda)} \cosh q_1 z e^{-j\lambda_x(x-x_s)} e^{-j\lambda_y(y-y_s)} d\lambda_x d\lambda_y. \quad (2.12)$$

In region 2:  $B \leq z \leq H$

$$\pi_x^{(2)} = \frac{1}{\gamma} \int_{-\infty}^{\infty} \int_{-\infty}^{\infty} \frac{f_2(\lambda)}{D_e(\lambda)} e^{-j\lambda_x(x-x_s)} e^{-j\lambda_y(y-y_s)} d\lambda_x d\lambda_y \quad (2.13)$$

and

$$\pi_z^{(2)} = \frac{1}{\gamma} \int_{-\infty}^{\infty} \int_{-\infty}^{\infty} \frac{j\lambda_x h_2(\lambda)}{D_e(\lambda) D_m(\lambda)} e^{-j\lambda_x(x-x_s)} e^{-j\lambda_y(y-y_s)} d\lambda_x d\lambda_y. \quad (2.14)$$

The functions  $f_2(\lambda)$  and  $h_2(\lambda)$  are shown in Appendix A. Other parameters are defined as follows:

$$\begin{aligned} D_e(\lambda) = & q_2 \left( q + \frac{q_1}{\mu_1 \tanh q_1 b} \right) \cosh q_2(h - b) \\ & + q_2 \left( \frac{q_2}{\mu_2} + \frac{\mu_2 q_1 q}{\mu_1 q_2 \tanh q_1 b} \right) \sinh q_2(h - b) \end{aligned} \quad (2.15)$$

and

$$\begin{aligned} D_m(\lambda) = & \frac{q_2 n_2^2}{\mu_1} (q n_1^2 + q_1 \mu_1 \tanh q_1 b) \cosh q_2(h - b) \\ & + (q_2^2 n_1^2 + \frac{\mu_1 n_2^4 q_1 q \tanh q_1 b}{\mu_2^2 q_2}) \sinh q_2(h - b) \end{aligned} \quad (2.16)$$

where

$$\lambda = \sqrt{\lambda_x^2 + \lambda_y^2}, \quad (2.17)$$

$$q = \sqrt{\lambda^2 - k_0^2}, \quad (2.18)$$

$$q_1 = \sqrt{\lambda^2 - k_1^2}, \quad (2.19)$$

$$q_2 = \sqrt{\lambda^2 - k_2^2}, \quad (2.20)$$

$$k_0 = \omega \sqrt{\mu_0 \epsilon_0} . \quad (2.21)$$

$$k_1 = k_0 \sqrt{\mu_1 \epsilon_1} , \quad (2.22)$$

$$k_2 = k_0 \sqrt{\mu_2 \epsilon_2} . \quad (2.23)$$

$$n_1 = \sqrt{\mu_1 \epsilon_1} , \quad (2.24)$$

$$n_2 = \sqrt{\mu_2 \epsilon_2} \quad (2.25)$$

and

$$\gamma = 4\pi^2 j \omega \epsilon_2 \epsilon_0 . \quad (2.26)$$

(b). An Electric Hertzian Dipole in the Substrate.

When the dipole is embedded in the substrate, as shown in Fig. 2-2, the electromagnetic fields will be different from the case when the dipole is in the superstrate, although the analytic procedure is very much the same. The dipole in this case is located at  $z = z_s$  with  $0 \leq z_s \leq b$  and oriented in the  $\hat{x}$  direction. The electromagnetic fields in each region can be characterized in terms of the Hertz potential given in Eqs. 2.1 and 2.2 which satisfy the equation

$$\nabla^2 \pi_s^{(i)} + k_i^2 \pi_s^{(i)} = \frac{1}{-j\omega \epsilon_1 \epsilon_0} \delta(x - x_s) \delta(y - y_s) \delta(z - z_s) \hat{x} \quad (2.27)$$

The lateral electromagnetic fields in region i are related to the Hertz potential through Eqs. 2.10-2.13. With the same boundary conditions as the case for

a dipole in the superstrate, the Hertz potential in each region can be summarized as:

In region 0:  $h \leq z$

$$\pi_{sx}^{(0)} = \frac{1}{\gamma'} \int_{-\infty}^{\infty} \int_{-\infty}^{\infty} \frac{f'_0(\lambda)}{D_e(\lambda)} e^{-q(z-h)} e^{-j\lambda_x(x-x_s)} e^{-j\lambda_y(y-y_s)} d\lambda_x d\lambda_y \quad (2.28)$$

and

$$\pi_{sz}^{(0)} = \frac{1}{\gamma'} \int_{-\infty}^{\infty} \int_{-\infty}^{\infty} \frac{j\lambda_x h'_0(\lambda)}{D_e(\lambda) D_m(\lambda)} e^{-q(z-h)} e^{-j\lambda_x(x-x_s)} e^{-j\lambda_y(y-y_s)} d\lambda_x d\lambda_y. \quad (2.29)$$

In region 1:  $0 \leq z \leq b$

$$\pi_{sx}^{(1)} = \frac{1}{\gamma'} \int_{-\infty}^{\infty} \int_{-\infty}^{\infty} \frac{f'_1(\lambda)}{D_e(\lambda)} e^{-j\lambda_x(x-x_s)} e^{-j\lambda_y(y-y_s)} d\lambda_x d\lambda_y \quad (2.30)$$

and

$$\pi_{sz}^{(1)} = \frac{1}{\gamma'} \int_{-\infty}^{\infty} \int_{-\infty}^{\infty} \frac{j\lambda_x h'_1(\lambda)}{D_e(\lambda) D_m(\lambda)} \cosh q_1 z e^{-j\lambda_x(x-x_s)} e^{-j\lambda_y(y-y_s)} d\lambda_x d\lambda_y. \quad (2.31)$$

In region 2:  $b \leq z \leq h$

$$\pi_{sx}^{(2)} = \frac{1}{\gamma'} \int_{-\infty}^{\infty} \int_{-\infty}^{\infty} \frac{f'_2(\lambda)}{D_e(\lambda)} e^{-j\lambda_x(x-x_s)} e^{-j\lambda_y(y-y_s)} d\lambda_x d\lambda_y \quad (2.32)$$

and

$$\pi_{sz}^{(2)} = \frac{1}{\gamma'} \int_{-\infty}^{\infty} \int_{-\infty}^{\infty} \frac{j\lambda_x h'_2(\lambda)}{D_e(\lambda) D_m(\lambda)} e^{-j\lambda_x(x-x_s)} e^{-j\lambda_y(y-y_s)} d\lambda_x d\lambda_y, \quad (2.33)$$

where

$$\gamma' = 4\pi^2 j\omega\epsilon_1\epsilon_0. \quad (2.34)$$

The functions  $f'(\lambda)$  and  $h'(\lambda)$  are shown in Appendix B. Other parameters are found in Eqs. 2.15-2.26.

## 2.2. Green's Function for a Magnetic Hertzian Dipole.

Slots in planar layered structures are also considered in this dissertation. The problem is formulated for the case where slots in a ground plane are sandwiched by two layers on both sides of the ground plane. From the Stratton-Chu solution of Maxwell's equations [61], one is able to see that the tangential electric fields in the boundary can be viewed as sources which generate electromagnetic fields inside the region of interest. These fictitious sources, usually called magnetic currents, when placed in Maxwell's equations are dual to electric currents. Maxwell's curl equations, with only magnetic current sources are

$$\nabla \times E = -J_m - j\omega\mu H \quad (2.35)$$

and

$$\nabla \times H = j\omega\epsilon E. \quad (2.36)$$

These two equations are constructed for the reason of mathematical convenience. The procedure of interchanging sources and boundary conditions is, in fact, well known in the realm of partial differential equations [64]. For the geometry under consideration, one can argue that the electromagnetic fields above the ground plane are due to magnetic currents (physically they are



electric fields) at a slot position infinitesimally close to the ground plane. The same arguments are valid for the space below the ground plane. In this situation, the ground plane is in effect closed without any apertures. Therefore, in the formulation of electromagnetic fields in a half space (either above or below the ground plane), the electromagnetic fields on the other side are irrelevant. The nice feature of this is that in the Green's function formulation, one can consider the geometry above or below the ground plane sequentially. However, if the magnetic currents in the slots are to be determined instead of being known beforehand, the fields in the whole space will be related through an additional boundary condition across the slots. This additional boundary condition will lead to an integral equation which can be solved by the method of moments.

The Green's function for a magnetic Hertzian dipole is obtained by solving Maxwell's equations with magnetic currents replaced by a delta source oriented in the  $\hat{x}$  direction. Since the source is known, only the half space as shown in Fig. 2-3 needs to be considered. Due to geometric symmetry, the formulation for the other half space is the same. The electromagnetic fields in each region can be characterized in terms of the Hertz potential in the following forms:

$$H^{(i)} = k_i^2 \vec{\pi}_m^{(i)} + \nabla (\nabla \cdot \vec{\pi}_m^{(i)}) \quad (2.37)$$

and

$$E^{(i)} = -j\omega\mu_i\mu_0 (\nabla \times \vec{\pi}_m^{(i)}) \quad (2.38)$$

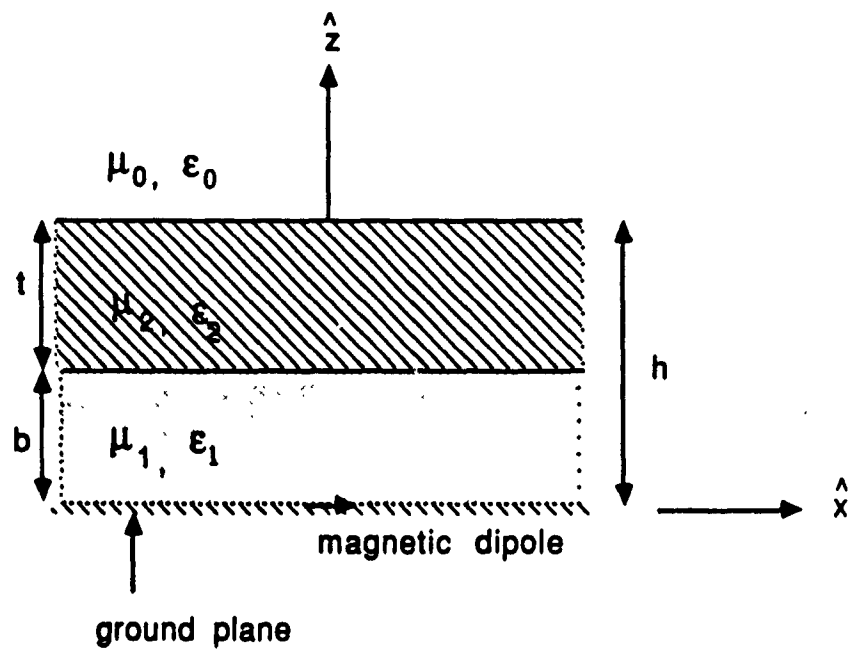


Figure 2-3. A magnetic Hertzian dipole in a substrate-superstrate configuration.

where  $i$  represents the region  $(i)$  and

$$\vec{\pi}_m^{(i)} = \pi_{mx}^{(i)} \hat{x} + \pi_{mz}^{(i)} \hat{z}. \quad (2.39)$$

Through the use of the Hertz potential, Maxwell's equations can be reformulated in the form of

$$\nabla^2 \vec{\pi}_m^{(i)} + k_i^2 \vec{\pi}_m^{(i)} = \frac{1}{-j\omega\mu_1\mu_0} \delta(x - x_s) \delta(y - y_s) \delta(z) \hat{x} \quad (2.40)$$

The lateral electromagnetic fields in region  $i$  are related to the Hertz potential through

$$H_x^{(i)} = k_i^2 \pi_{mx}^{(i)} + \frac{\partial}{\partial x} \left( \frac{\partial \pi_{mx}^{(i)}}{\partial x} + \frac{\partial \pi_{mz}^{(i)}}{\partial z} \right), \quad (2.41)$$

$$H_y^{(i)} = \frac{\partial}{\partial y} \left( \frac{\partial \pi_{mx}^{(i)}}{\partial x} + \frac{\partial \pi_{mz}^{(i)}}{\partial z} \right), \quad (2.42)$$

$$E_x^{(i)} = -j\omega\mu_1\mu_0 \frac{\partial \pi_{mz}^{(i)}}{\partial y} \quad (2.43)$$

and

$$E_y^{(i)} = -j\omega\mu_1\mu_0 \left( \frac{\partial \pi_{mx}^{(i)}}{\partial z} - \frac{\partial \pi_{mz}^{(i)}}{\partial x} \right). \quad (2.44)$$

Eq. 2.40 can be solved subject to the boundary conditions at each interface and

$z \rightarrow \infty$ . The resulting Hertz potentials in each region are:

In region 0:  $h \leq z$

$$\pi_{mx}^{(0)} = \frac{1}{\gamma_m} \int_{-\infty}^{\infty} \int_{-\infty}^{\infty} \frac{f_{m0}(\lambda)}{D_m(\lambda)} e^{-q(z-h)} e^{-j\lambda_x(x-x_s)} e^{-j\lambda_y(y-y_s)} d\lambda_x d\lambda_y \quad (2.45)$$

and

$$\pi_{mz}^{(0)} = \frac{1}{\gamma_m} \int_{-\infty}^{\infty} \int_{-\infty}^{\infty} \frac{j\lambda_x h_{m0}(\lambda)}{D_e(\lambda) D_m(\lambda)} e^{-q(z-h)} e^{-j\lambda_x(x-x_s)} e^{-j\lambda_y(y-y_s)} d\lambda_x d\lambda_y. \quad (2.46)$$

In region 1:  $0 \leq z \leq b$

$$\pi_{mx}^{(1)} = \frac{1}{\gamma_m} \int_{-\infty}^{\infty} \int_{-\infty}^{\infty} \frac{f_{m1}(\lambda)}{D_m(\lambda)} e^{-j\lambda_x(x-x_s)} e^{-j\lambda_y(y-y_s)} d\lambda_x d\lambda_y \quad (2.47)$$

and

$$\pi_{mz}^{(1)} = \frac{1}{\gamma_m} \int_{-\infty}^{\infty} \int_{-\infty}^{\infty} \frac{j\lambda_x h_{m1}(\lambda) \sinh q_1 z}{D_e(\lambda) D_m(\lambda)} e^{-j\lambda_x(x-x_s)} e^{-j\lambda_y(y-y_s)} d\lambda_x d\lambda_y. \quad (2.48)$$

In region 2:  $b \leq z \leq h$

$$\pi_{mx}^{(2)} = \frac{1}{\gamma_m} \int_{-\infty}^{\infty} \int_{-\infty}^{\infty} \frac{f_{m2}(\lambda)}{D_m(\lambda)} e^{-j\lambda_x(x-x_s)} e^{-j\lambda_y(y-y_s)} d\lambda_x d\lambda_y, \quad (2.49)$$

$$\pi_{mz}^{(2)} = \frac{1}{\gamma_m} \int_{-\infty}^{\infty} \int_{-\infty}^{\infty} \frac{j\lambda_x h_{m2}(\lambda)}{D_e(\lambda) D_m(\lambda)} e^{-j\lambda_x(x-x_s)} e^{-j\lambda_y(y-y_s)} d\lambda_x d\lambda_y. \quad (2.50)$$

where

$$\gamma_m = 4\pi^2 j\omega \mu_1 \mu_0. \quad (2.51)$$

The functions  $f_{mi}(\lambda)$  and  $h_{mi}(\lambda)$  can be found in Appendix C. Other parameters are defined in Eqs. 2.15-2.26.

## **Chapter III**

### **MIC Discontinuities I -**

#### **Microstrip Open-end and Gap Discontinuities**

#### **in a Two-layer Configuration**

### **3.1. Introduction**

Microstrip open-end and gap discontinuities are useful in the design of matching stubs and coupled filters. In recent years, layered integrated structures have found various applications in MIC and printed circuit antennas, especially for monolithic applications. Therefore, design data for open-end and gap discontinuities in layered structures would be useful. In this chapter, microstrip open-end and gap discontinuities in a substrate-superstrate configuration (Fig. 3-1 and 3-2) will be considered. The characterization of these discontinuities for a single layer has been performed quite extensively in the past. Quasi-static analysis based on solving Poisson's equation has been applied for low frequency applications [16] – [18], [65] . For higher frequencies, models based on rigorous dynamic analysis are required. A spectral-domain approach [19], [22] has been used to characterize the discontinuity problems with an enclosed waveguide housing. A dynamic method based on solving integral equations by the method of moments has recently been applied to the modeling of microstrip open-end and gap discontinuities for a single layer case [24], [25]. This analysis takes into account all the physical effects including radiation, surface waves and dominant as well as higher order mode coupling. In [24], a finite but long microstrip line with a

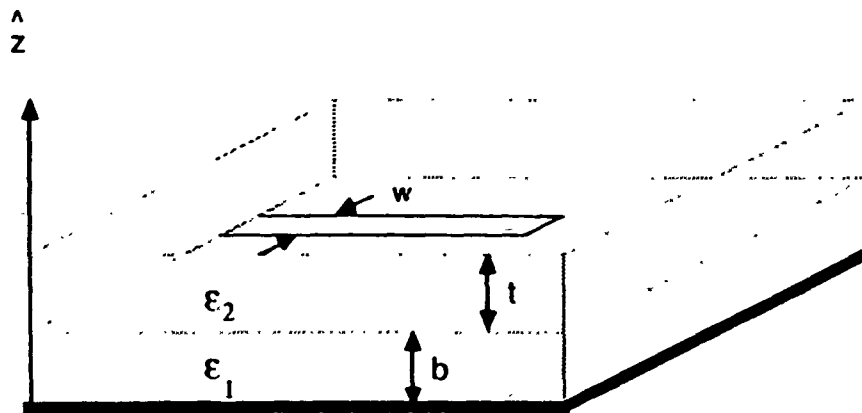


Figure 3-1. An open-end microstrip line in a two-layer structure.

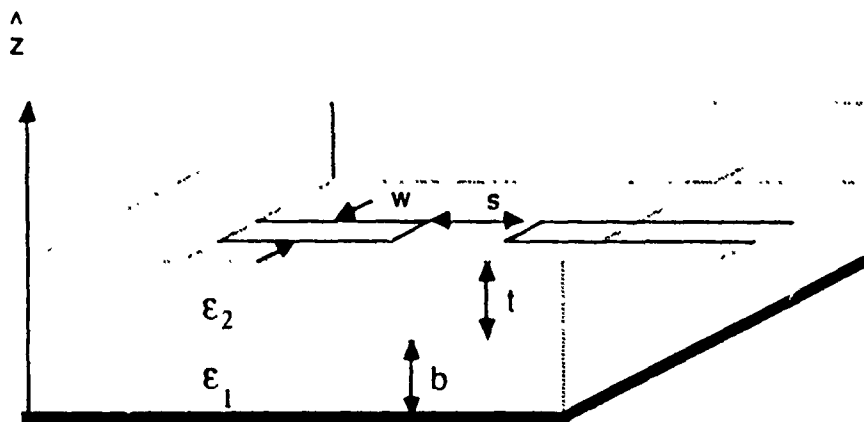


Figure 3-2. Microstrip gap in a two-layer structure.

$\delta$  gap source is used, which typically requires many basis functions and is numerically inefficient. In [25], a more efficient method, using a combination of the entire domain modes and subdomain modes, is used. However, from the discussion presented in [25], it seems that the method does not provide reliable results for the capacitance calculation. In this chapter, a revised analysis of [25] together with a detailed discussion of the convergence of the solutions is presented. Since, for the rest of this dissertation, the methodology adopted here will be repeated, the analysis will be discussed in extensive detail in this chapter.

A crucial step (and difficult) is choosing the proper basis functions to provide efficient and accurate numerical computation. In the present problem, modeling of semi-infinite lines is required. A combination of semi-infinite traveling wave modes and local subdomain modes is fruitful and can be modified easily to adapt to different geometries. The traveling wave mode corresponds to the fundamental guided wave mode of the microstrip line. The local subdomain modes are used in the vicinity of the discontinuity region to take into account the higher order mode effects. For the transverse dependence of the expansion functions, it is possible that with sufficiently high frequencies, the simple Maxwellian or pulse function used in [24], [25] may not be a good approximation when the dominant mode is not TEM-like. Therefore in this analysis, the transverse dependence of the longitudinal current is obtained by a two dimensional infinite line analysis where three modified cosine-Maxwellian functions are used. The characterization of an open-end discontinuity is through the open-end capacitance which is mainly due to the fringing

electric fields [17]. When radiation and surface wave losses are considered, a conductance should also be included in the equivalent circuit model. The gap discontinuity can be modeled as a  $\pi$  network with two capacitances (see Figs. 3-3 and 3-4). The loss mechanism can also be included by adding two conductances in Fig. 3-3. The material effects of layered structures on the radiation and surface wave loss, and the fringing fields at the discontinuities will also be discussed.

### 3.2. The Method of Moments and Matrix Formulation

The transverse current has been found in the past to be a few orders of magnitude smaller than the longitudinal current for a strip width  $< 0.1\lambda_0$  and is neglected for simplicity [8]. Under such circumstances, the integral equation for the open end case can be simplified in terms of the longitudinal electric field on the microstrip:

$$E_x(x, y, z) = \int_{-\infty}^0 \int_{-w/2}^{w/2} G_{xx}(x, y, z | x_s, y_s, z_s) J_x(x_s, y_s) dy_s dx_s \quad (3.1)$$

where  $E_x$  is the electric field due to the current at  $z = z_s$ . The Green's function  $G_{xx}$  is the value of  $E_x$  on the  $(x, y)$  of microstrip due to an  $\hat{x}$  directed delta source at  $(x_s, y_s)$ . This Green's function has been described in Chap. II. In the method of moment procedure, the unknown current distribution is expanded in terms of a set of known functions. An efficient way is to use a semi-infinite traveling wave mode to represent the fundamental guide wave mode of the microstrip line and to use subdomain modes



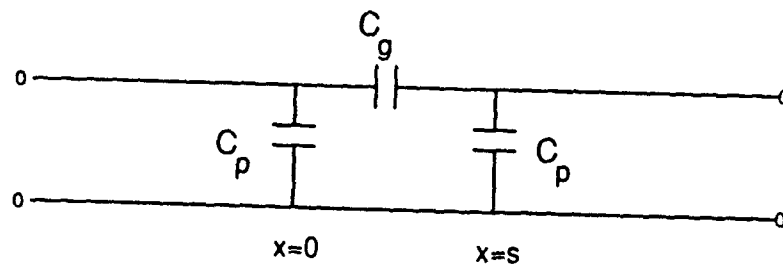


Figure 3-3. Equivalent circuit of a microstrip gap.

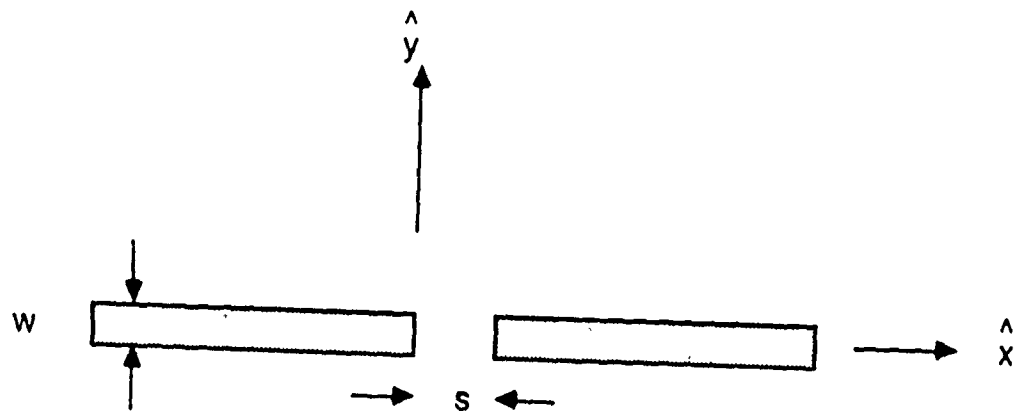


Figure 3-4. Top view of a microstrip gap discontinuity.

(piecewise sinusoidal modes) to describe the current behavior in the vicinity of the discontinuities. Since the microstrip open end is a special case of the gap discontinuity, the formulation in the following will be for the gap case. The open-end case will be discussed later. The current in the microstrip gap shown in Fig. 3-4 can be expanded as

$$J_x(x, y) = f(x) J(y) \quad (3.2)$$

with

$$f(x) = e^{-jk_m x} - \Gamma e^{jk_m x} + \sum_{n=1}^N I_{n1} f_n(x) \quad \text{for } x \leq 0, \quad (3.3)$$

$$f(x) = T e^{-jk_m(x-s)} + \sum_{n=1}^N I_{n2} g_n(x) \quad \text{for } x \geq s, \quad (3.4)$$

and

$$J(y) = \frac{a_0 + a_1 \cos(\frac{2\pi}{w}y) + a_2 \cos(\frac{4\pi}{w}y)}{\pi w \sqrt{1 - (2y/w)^2}}, \quad (3.5)$$

where  $\Gamma$  is the reflection coefficient from the discontinuity and  $T$  is the wave amplitude of the transmitted wave. The layout of the expansion modes is shown in Fig. 3-5. The parameters  $k_m$ ,  $a_0$ ,  $a_1$  and  $a_2$  are obtained through an infinite line analysis, which involves solving a characteristic equation in a matrix form [66]. The piecewise sinusoidal modes (PWS) are defined as

$$f_n(x) = \frac{\sin k_{e1}(d_1 - |x + nd_1|)}{\sin k_{e1}d_1} \quad \text{for } |x + nd_1| < d_1, \quad (3.6)$$

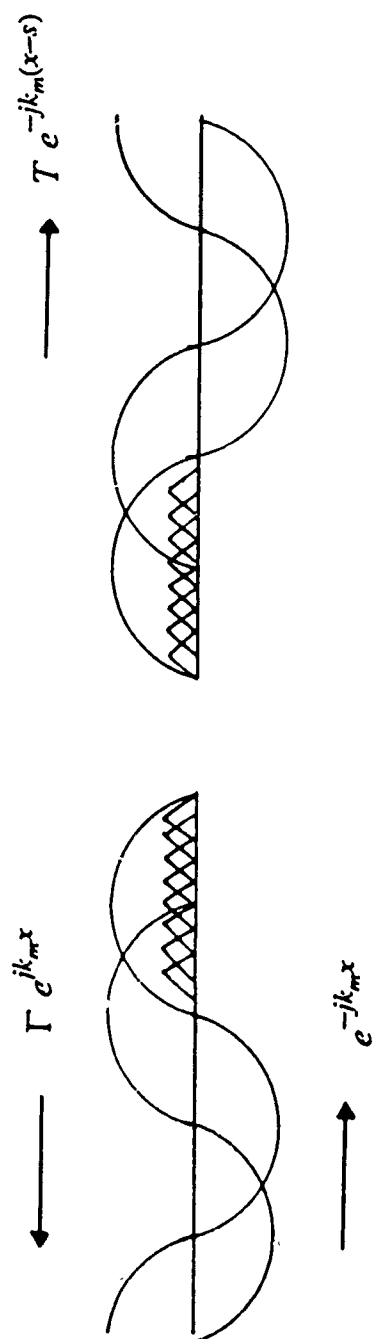


Figure 3-5. Layout of the expansion modes in a microstrip gap.

and

$$g_n(x) = \frac{\sin k_{e1}(d_1 - |x - nd_1 - s|)}{\sin k_{e1}d_1} \quad \text{for } |x - nd_1 - s| < d_1 \quad (3.7)$$

where  $d_1$  is half length of the PWS mode. The choice of  $k_{e1}$  can be quite arbitrary.

When the expansion functions are used in Eq. 3.1, followed by Galerkin's procedure [63], integral equations are converted into a set of linear equations. These  $2N + 2$  equations when expressed in matrix form are

$$\begin{bmatrix} [Z_{self}] & [Z_{tself}] & [Z_{eeact}] & [Z_{teact}] \\ [Z_{eeact}] & [Z_{teact}] & [Z_{self}] & [Z_{tself}] \end{bmatrix} \begin{bmatrix} [I_1] \\ [\Gamma] \\ [I_2] \\ [\bar{I}] \end{bmatrix} = \begin{bmatrix} [I_{inc_1}] \\ [I_{inc_2}] \end{bmatrix}. \quad (3.8)$$

The matrix elements in each submatrix can be expressed in the following form after some tedious algebraic manipulations:

$[Z_{self}]$  is an  $(N + 1) \times N$  matrix with matrix elements

$$Z_{self}^{nm} = \int_{-\infty}^{\infty} \int_{-\infty}^{\infty} \overline{G}_{xx}(\lambda_x, \lambda_y) F_1^2(\lambda_y) A_1^2(\lambda_x) \cos[\lambda_x(m - n)d_1] d\lambda_x d\lambda_y, \quad (3.9)$$

$[Z_{tself}]$  is an  $(N + 1) \times 1$  column vector with elements

$$Z_{tself}^n = \int_{-\infty}^{\infty} \int_{-\infty}^{\infty} \overline{G}_{xx}(\lambda_x, \lambda_y) F_1^2(\lambda_y) P_1(\lambda_x) A_1(\lambda_x) e^{jnd_1\lambda_x} d\lambda_x d\lambda_y, \quad (3.10)$$

$[Z_{eeact}]$  is an  $(N + 1) \times N$  matrix with matrix elements

$$Z_{teact}^{nm} = \int_{-\infty}^{\infty} \int_{-\infty}^{\infty} \overline{G}_{xx}(\lambda_x, \lambda_y) F_1^2(\lambda_y) A_1^2(\lambda_x) \cos[\lambda_x(nd_1 + md_1 - s)] d\lambda_x d\lambda_y, \quad (3.11)$$

$[Z_{teact}]$  is an  $(N+1) \times 1$  column vector with elements

$$Z_{teact}^n = \int_{-\infty}^{\infty} \int_{-\infty}^{\infty} \overline{G}_{xx}(\lambda_x, \lambda_y) F_1^2(\lambda_y) P_1(\lambda_x) A_1(\lambda_x) \cos[\lambda_x(nd_1 - s)] d\lambda_x d\lambda_y, \quad (3.12)$$

$[I_{inc_1}]$  is an  $(N+1) \times 1$  column vector with elements

$$I_{inc_1}^n = \int_{-\infty}^{\infty} \int_{-\infty}^{\infty} \overline{G}_{xx}(\lambda_x, \lambda_y) F_1^2(\lambda_y) Q_1(\lambda_x) A_1(\lambda_x) e^{jnd_1\lambda_x} d\lambda_x d\lambda_y, \quad (3.12)$$

$[I_{inc_2}]$  is an  $(N+1) \times 1$  column vector with elements

$$I_{inc_2}^n = \int_{-\infty}^{\infty} \int_{-\infty}^{\infty} \overline{G}_{xx}(\lambda_x, \lambda_y) F_1^2(\lambda_y) Q_1(\lambda_x) A_1(\lambda_x) \cos[\lambda_x(nd_1 - s)] d\lambda_x d\lambda_y, \quad (3.13)$$

where

$$A_1(\lambda_x) = 2k_{e1} \frac{(\cos k_{e1}d_1 - \cos \lambda_x d_1)}{(\lambda_x^2 - k_{e1}^2)}, \quad (3.14)$$

$$F_1(\lambda_y) = \sum_{k=0}^2 \frac{a_k}{2} [J_0(\frac{w_1}{2}\lambda_y + k\pi) + J_0(\frac{w_1}{2}\lambda_y - k\pi)], \quad (3.15)$$

$$P_1(\lambda_x) = [e^{\frac{-j\lambda_x\pi}{2k_m}} + j] \int_{-\infty}^0 \sin k_m x e^{j\lambda_x x} dx, \quad (3.16)$$

$$Q_1(\lambda_x) = [e^{\frac{-j\lambda_x\pi}{2k_m}} - j] \int_{-\infty}^0 \sin k_m x e^{j\lambda_x x} dx \quad (3.17)$$

and

$$\int_{-\infty}^0 \sin(k_m x) e^{-j\lambda_x x} dx = \frac{k_m}{\lambda_x^2 - k_m^2} + \frac{j}{2} [\delta(\lambda_x - k_m) - \delta(\lambda_x + k_m)]. \quad (3.18)$$

The function  $\overline{G}_{xx}$  is the Fourier transform of the Green's function. From Eqs. 3.9-3.13, one can see that this Green's function will play an important role in the numerical computations.

### 3.3. Numerical Techniques

Eqs. 3.9-3.13 indicate two types of integrations. One is related to the PWS and PWS modes reaction while the other is related to the traveling wave and the PWS modes reaction. The case of the PWS and PWS modes interaction will be considered first. Eq. 3.9, after being transformed into polar coordinates, can be written as

$$Z_{self}^{mn} = 4 \int_0^{\pi/2} \int_0^\infty \overline{G}_{xx}(\lambda_x, \lambda_y) F_1^2(\lambda_y) A_1^2(\lambda_x) \cos[\lambda_x(m - n)t_1] \lambda d\lambda d\phi \quad (3.19)$$

where

$$G_{xx}(\lambda_x, \lambda_y) = \frac{-jZ_0}{4\pi^2 k_0} \left[ \frac{k_2^2 - \lambda_x^2}{D_c(\lambda)} f_c(\lambda) + \frac{\lambda_x^2}{D_c(\lambda) D_m(\lambda)} g_c(\lambda) \right], \quad (3.20)$$

$$\lambda_x = \lambda \cos \phi, \quad (3.21)$$

$$\lambda_x = \lambda \sin \phi. \quad (3.22)$$

The functions  $f_c$  and  $g_c$  can be obtained from the Green's function discussed in Chapter II.

Eq. 3.19 involves a double integration. For the finite integral, a 32 points Gauss quadrature formula is used [57]. For the infinite integral, special numerical methods are required. One can break the infinite integration range into two parts  $(0, A)$  and  $(A, \infty)$  such that in the first section the integrand contains singularities or derivative singularities, while for the second section the integrand is well behaved but slowly convergent. The choice of  $A$  is quite flexible, but it should satisfy  $A > \max(k_1, k_2)$ . The first integral contains surface wave poles whenever  $D_s(\lambda)$  or  $D_m(\lambda)$  become zero. If a pole extraction technique is applied [39] in addition to the residue and Cauchy Principal value, four sections of integrations are required due to the derivative singularities at  $\lambda = k_0, k_1$  and  $k_2$ . Another way to perform the integration from 0 to  $A$  is to deform the contour off the real axis and apply the Cauchy Riemann theorem such that the integrand is well behaved [67]. This method is particularly useful in a multi-layered structure, since it is not required to know the pole position and the integration has no singularities. Both of the above mentioned methods have been used and a negligible difference has been observed.

The second integration from  $A$  to  $\infty$  is the so-called tail integration. For an asymptotic approximation, it is convenient to choose  $A$  such that

$\tanh \lambda b \cong 1$  and  $\tanh \lambda t \cong 1$ , for  $\lambda \geq A$ . If one studies the asymptotic behavior of the Green's function  $G_{xx}(\lambda_x, \lambda_y)$  (omitting the term outside the bracket of Eq. 3.20), one can find that as  $\lambda \rightarrow \infty$ ,  $G_{xx}$  converges slowly when the testing and observation points are on the same plane (same  $z$ ) and decays exponentially otherwise. This is because the Green's function contains a singularity in the space domain due to the delta source and converges slowly in the Fourier domain. The dominant and first order asymptotic behavior of  $G_{xx}$  can be summarized by the following:

Case (a):  $z = z_s = h = (b + t)$

$$G_{xx}(\lambda_x, \lambda_y) \simeq \frac{(k_{eff}^2 - \lambda_x^2)}{2q_e \varepsilon_{eff}} + O\left(\frac{c_0 - c_1 \lambda_x}{\lambda^3}\right) \quad (3.23)$$

where  $\varepsilon_{eff} = \frac{(1 + \varepsilon_2)}{2}$  and  $q_e = \sqrt{\lambda^2 - k_{eff}^2}$ .

Case (b):  $b < z = z_s < h$

$$G_{xx}(\lambda_x, \lambda_y) \simeq \frac{(k_{eff}^2 - \lambda_x^2)}{2\varepsilon_{eff} q_e} + O(c_2 e^{\lambda(z-h)}) \quad (3.24)$$

where  $\varepsilon_{eff} = \varepsilon_2$  and  $q_e = \sqrt{\lambda^2 - k_{eff}^2}$ .

Case (c):  $z = z_s = b$

$$G_{xx}(\lambda_x, \lambda_y) \simeq \frac{(k_{eff}^2 - \lambda_x^2)}{2\varepsilon_{eff} q_e} + O\left(\frac{c_3 - c_4 \lambda_x}{\lambda^3}\right) \quad (3.25)$$



where  $\varepsilon_{eff} = \frac{(\varepsilon_1 + \varepsilon_2)}{2}$  and  $q_e = \sqrt{\lambda^2 - k_{eff}^2}$ .

Case (d):  $b < z = z_s < h$

$$G_{xx}(\lambda_x, \lambda_y) \simeq \frac{(k_{eff}^2 - \lambda_x^2)}{2\varepsilon_{eff}q_e} + O(c_4 e^{\lambda(b-z)}) \quad (3.26)$$

where  $\varepsilon_{eff} = \varepsilon_1$  and  $q_e = \sqrt{\lambda^2 - k_{eff}^2}$ .

It can be seen that the dominant term of the Green's function is in the same form for all four cases, which, when transformed back to real space is  $E_x$  due to a delta current in the  $\hat{x}$  direction in a homogeneous space with an effective dielectric constant  $\varepsilon_{eff}$ . The dominant term of the integral will be computed separately. This formulation will be discussed in Appendix D. It is seen that the first order term left in Eqs. 3.23-3.26 will enable the integrand in Eq. 3.19 to converge either exponentially or in the order  $1/\lambda^3$  and can be integrated numerically in a straightforward way. It has been shown in Appendix D that if  $k_{cl}$  in the PWS modes is chosen to be the same as  $k_{eff}$ , the computations are greatly simplified. Therefore, throughout this dissertation, PWS expansion modes are chosen in this way.

The other type of integration is related to the PWS modes and traveling wave mode reaction. When Eq. 3.18 is inserted in Eq. 3.10, with suitable rearrangements, one has

$$Z_{iself}^n = \int_{-\infty}^{\infty} \frac{2k_m}{\lambda_x^2 - k_m^2} (e^{\frac{-j\lambda_x \pi}{2k_m}} + j) e^{jnd_1 \lambda_x} A_1(\lambda_x) S(\lambda_x) d\lambda_x \quad (3.27)$$

where

$$S(\lambda_x) = \int_{-\infty}^{\infty} \overline{G}_{xx}(\lambda_x, \lambda_y) F_1^2(\lambda_y) d\lambda_y. \quad (3.28)$$

At a first look, it seems that Eq. 3.27 contains poles at  $\lambda_x = \pm k_m$  which may cause trouble in the numerical integration. However, as mentioned before,  $k_m$  is obtained by an infinite line analysis where the characteristic equation is  $S(\lambda_x) = 0$ . Therefore, one would have  $S(k_m) = 0$  and the singularities in Eq. 3.27 turn out to be removable. The integration in Eq. 3.27 after being transformed into polar coordinates may be expressed as

$$Z_{\text{itself}}^n = Z_a^n(nd_1 - \frac{\pi}{2k_m}) + j Z_a^n(nd_1) \quad (3.29)$$

where

$$Z_a^n(nd_1) = \int_0^{\pi/2} \int_0^{\infty} \overline{G}_{xx}(\lambda_x, \lambda_y) F_1^2(\lambda_y) A_1(\lambda_x) \frac{4k_m}{\lambda_x^2 - k_m^2} \cos \lambda_x nd_1 \lambda d\lambda d\phi. \quad (3.30)$$

It is obvious from Eqs. 3.19 and 3.30 that the integral in Eq. 3.30 can be computed numerically in the same manner as the one occurring in Eq. 3.19 except for the tail integration. This difference is due to the fact that the traveling wave mode is semi-infinitely long so the technique used for Eq. 3.19 can not be applied. In other words, if the integration is transformed back to real space, the integration over the half-infinite microstrip line will cause other numerical convergence problems. However, due to the use of entire domain base functions, the integration in Eq. 3.30 usually converges better than the one in

Eq. 3.19 because the integrand contains the Fourier transform of the entire domain mode which decreases quickly away from the point where  $\lambda_x$  is equal to the phase constant  $k_m$ . Further details in the asymptotic analysis of Eq. 3.27 by using branch-cut integration is shown in Appendix E.

Although the above discussion is for the microstrip gap case, the open-end case is also included. From the submatrices  $[Z_{self}]$ ,  $[Z_{lself}]$  and  $[I_{inc_1}]$  in Eq. 3.8, the information of an open-end microstrip line can be obtained.

### 3.4. Results

Usually MIC discontinuities are characterized by their equivalent circuits. Therefore, in order that the characterization be meaningful, all the disturbances of the current should die out quickly as one moves away from the discontinuity. In microstrip structures, any discontinuity will generate radiating and surface waves. These waves will also propagate along with the microstrip line fundamental mode. Therefore, when radiating or surface waves are strong enough such that their interactions with the microstrip guided mode become noticeable, the computed equivalent circuits will not be accurate. This implies that, for this case, if one tries to measure the equivalent circuits, the results will be different at different reference planes.

The equivalent circuit of a microstrip open end is computed from the reflection coefficient which is obtained directly from the matrix inversion of Eq. 3-8. The convergence of the results depends on the size of the expansion functions and the region where subdomain modes are used (see Fig. 3-5). An example of a convergence check for the open-end conductance and capacitance

for the number of modes used in a fixed subdomain mode region is shown in Figs. 3-6 and 3-7. The subdomain region is chosen as 10 times the substrate thickness. It is found that with only two modes a convergent result for the conductance calculation has already occurred. However, the convergence of the capacitance value is very slow with respect to the number of expansion modes. The region where the subdomain modes are used is less important. An example of this convergence check is shown in Fig. 3-8 where the basis function size is fixed. It is found that the results are almost unchanged in a wide range. Physically, this means that the higher order modes generated by the discontinuity have already died out in the testing region. The above convergence tests are for the case that the radiating and surface waves are weakly excited. It is found that the results do not converge at all when the surface waves and radiation loss are strong, due to their interaction with the microstrip fundamental mode. For a circuit to be useful, radiation and surface wave loss should be as small as possible. With a careful convergence study, it is found that, within the useful frequency range, typically, 19 piecewise sinusoidal modes of size  $\sim 0.06$  guided wavelength (0.6 guided wavelength in total) can provide results within a few percent accuracy. The validity of the current analysis is further checked with the quasi-static method at low frequencies. Fig. 3-9 shows the comparison between this analysis and the quasi-static method for a single layer case. The substrate thickness is 1% of a free space wavelength which is thin enough to insure the accuracy of the quasi-static method. The comparison yields very good agreement.

Energy loss due to radiation and surface waves at a microstrip open end is shown in Fig. 3-10 with and without a cover layer. The microstrip line in this case is embedded between the substrate and the superstrate. It is found that with the presence of the cover layer, the loss increases with the increase of the superstrate dielectric constant due to stronger radiation and surface waves. The length extension (or capacitance) at the open end due to the fringing field for the same geometry as that in Fig. 3-10 is shown in Fig. 3-11. It is found, by adding a cover layer, the excess length to substrate thickness ratio (or end capacitance) is larger due to a stronger fringing field. In general, the excess length increases with the increase of effective dielectric constant and is insensitive to frequency except when the surface waves are strong. The excess length values for microstrip in a composite substrate are shown in Fig. 3-12. Two different material arrangements were investigated which include the case of a large permittivity on the top with a lower one on the bottom and the case of the other way around. It is found that the excess length value for the first case is significantly larger than the second one. This implies that, when the microstrip line is on the larger dielectric constant material, the fringing electric field is stronger.

For the gap case, after a matrix inversion in Eq. 3-8 is performed, the reflection coefficients  $\Gamma$  and transmission coefficient  $T$  are  $S_{11}$  and  $S_{12}$  respectively. Therefore, the admittance matrix of the gap discontinuities can be obtained by the following transformation

$$[Y] = ([U] - [S])([U] + [S])^{-1} \quad (3.31)$$

where  $[U]$  is the unitary matrix. By comparing the two-port  $\pi$  network and Fig. 3-3, one has

$$\frac{G_p + j\omega C_p}{G_0} = Y_{11} - Y_{12} \quad (3.32)$$

and

$$\frac{G_g + j\omega C_g}{G_0} = Y_{12} \quad (3.33)$$

The results for the gap discontinuity are first compared with those obtained by the quasi-static method [18] and those obtained by measurements [68] and are shown in Fig. 3-13. Since the gap capacitance is small and is sensitive to the device tolerances, the measurement is inherently difficult to perform accurately. In this analysis, the frequency is chosen to be 5 GHz. It is found that this dynamic model agrees well with the quasi-static approach. Some discrepancies for large gap spacing may be due to the fact that, in such cases, the amount of energy coupled through the gap is comparable to the energy losses due to surface waves and radiation, and this aspect is not included in the quasi-static approach. The gap conductances  $G_p$  and  $G_g$  are shown in Fig. 3-14 for the same material arrangements as those shown in Fig. 3-10. It is found that the cover layer (superstrate) will increase conductance due to stronger fringing field and more energy losses. Also since  $G_p + j\omega C_p$  represents the input admittance when a perfect magnetic wall is in the middle of the gap, it is expected that, due to image cancellation,  $G_g$  will be much larger than  $G_p$ . As shown in Fig. 3-14,  $G_g$  is about two orders larger than  $G_p$ . For a

narrower gap,  $C_g$  will be larger than  $C_p$  due to stronger end coupling. However for wide gap spacing, the input admittance seen from either side of the gap is mainly the open-end admittance, so  $C_p$  will be larger than  $C_g$ . The results for the microstrip gap on top of the superstrate are shown in Fig. 3-15. It is found that  $C_g/w$  is more frequency dependent than  $C_p/w$ , when the dispersion is strong.

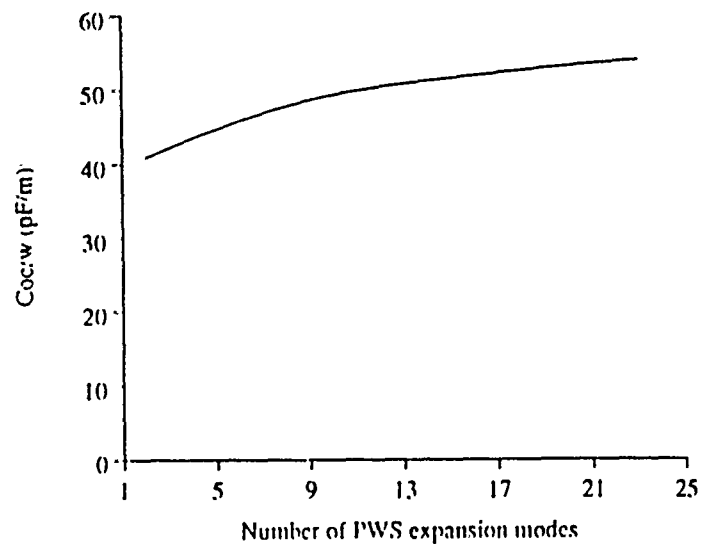


Figure 3-6. Convergence test for open-end capacitance.

$\epsilon_1 = 9.6$ ,  $h = 0.02\lambda_0$  and  $w/b = 1$ .

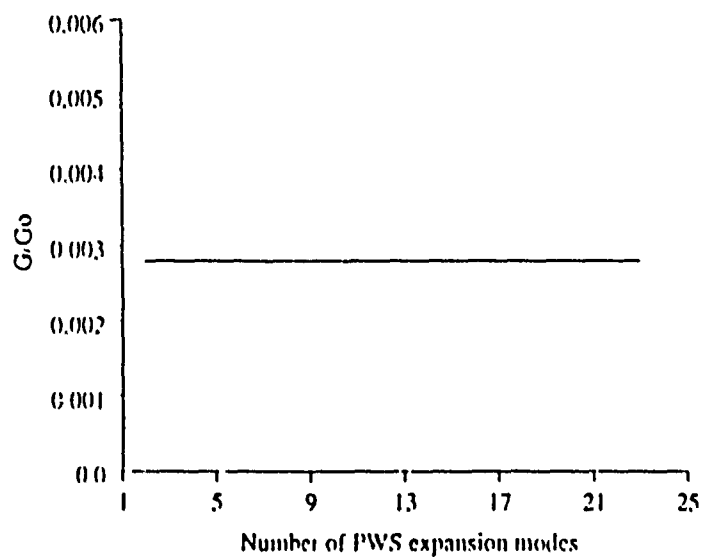


Figure 3-7. Convergence test for open-end conductance.

$\epsilon_1 = 9.6$ ,  $h = 0.02\lambda_0$  and  $w/b = 1$ .



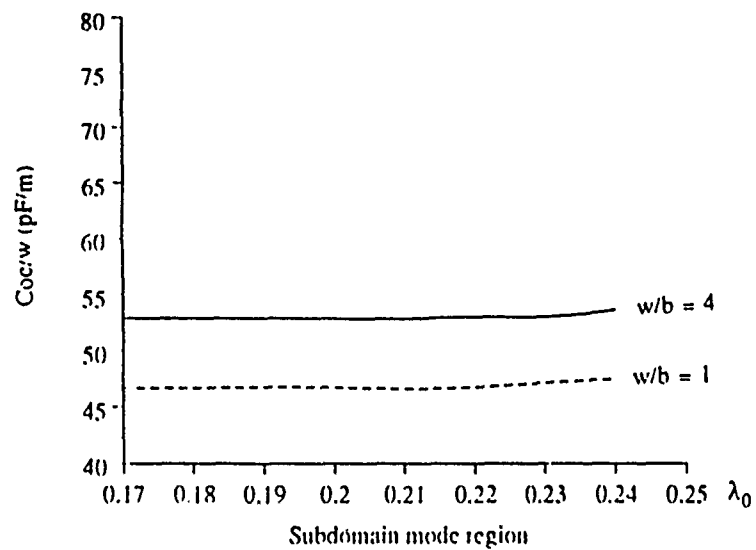


Figure 3-8 Convergence test for open-end capacitance.

$$\epsilon_1 = 9.6, b = 0.02\lambda_0.$$

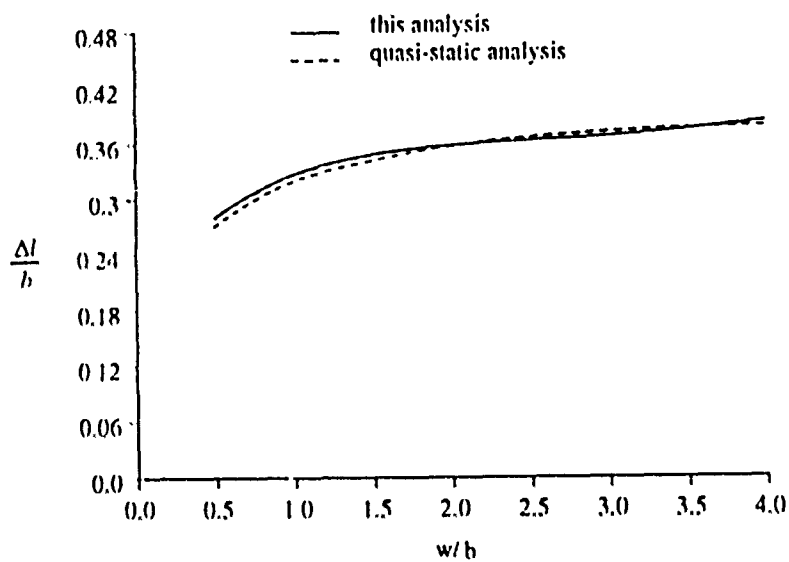


Figure 3-9. Excess length of an open-end microstrip line versus microstrip width.

$$\epsilon_r = 9.6 \text{ and } b = 0.01 \lambda_0.$$

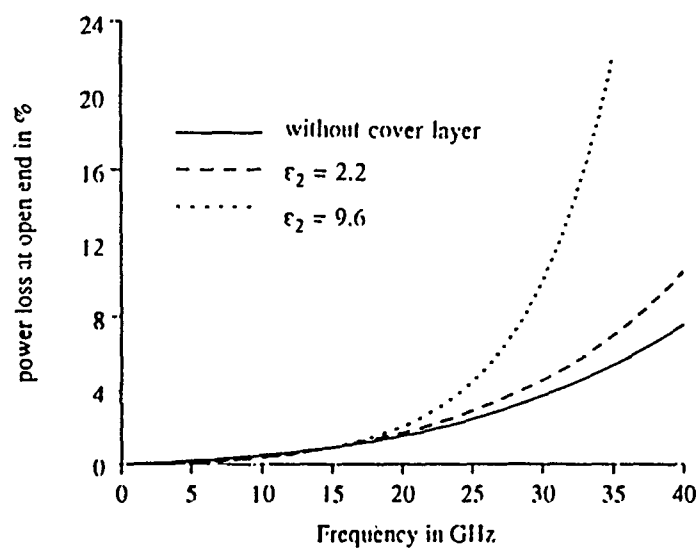


Figure 3-10. Energy loss at microstrip open end versus frequency.

$\epsilon_1 = 9.6$ ,  $b = 0.3$  mm,  $w = b$  and  $t = b$ .

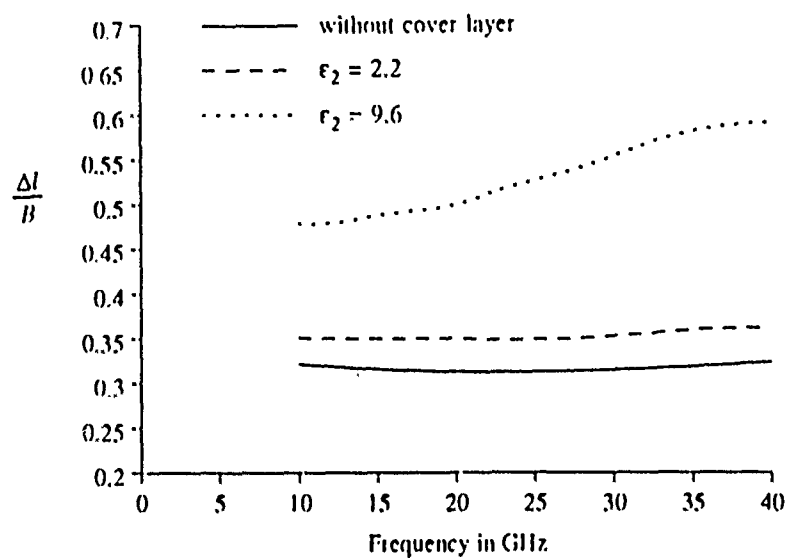


Figure 3-11. Excess length of an open-end microstrip line versus frequency.

$\epsilon_1 = 9.6$ ,  $b = 0.3$  mm,  $w = b$  and  $t = b$ .

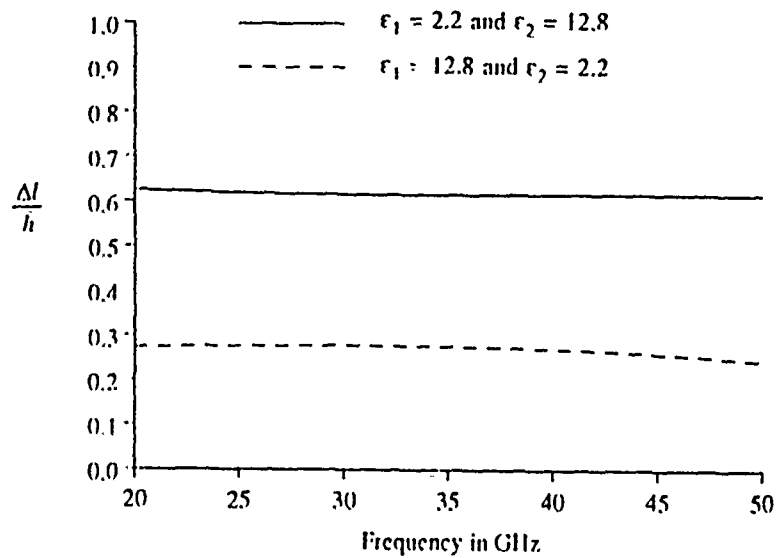


Figure 3-12. Excess length of an open-end microstrip line versus frequency.  
 $b = t = h/2$ ,  $h = 0.3$  mm and  $w/h = 1$ .

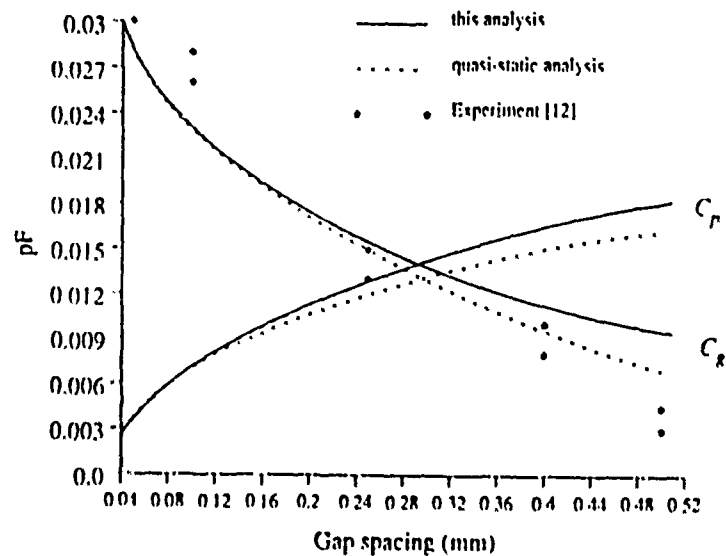


Figure 3-13. Gap capacitances versus gap spacing.  
 $\epsilon_1 = 8.875$ ,  $\epsilon_2 = 1$ ,  $b = 0.508$  mm and  $w = b$ .

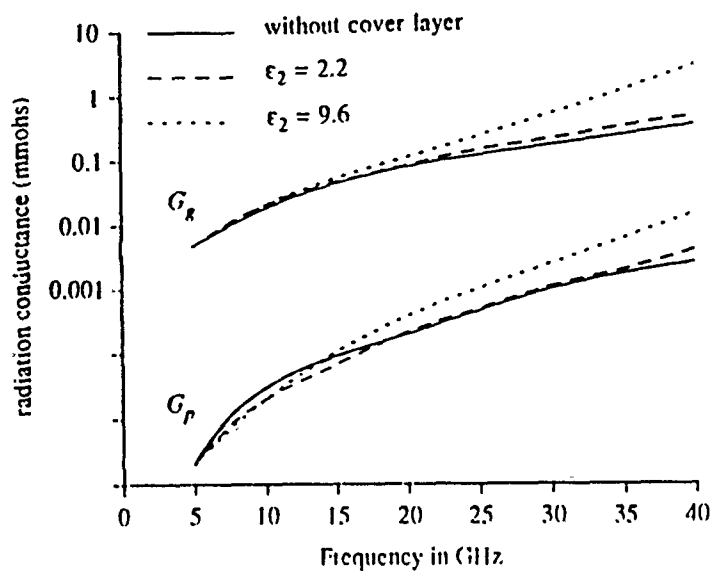


Figure 3-14. Gap conductances versus frequency.

$\epsilon_1 = 9.6$ ,  $b = 0.3$  mm,  $w = b$ ,  $t = b$  and  $s = 0.3762$  b.

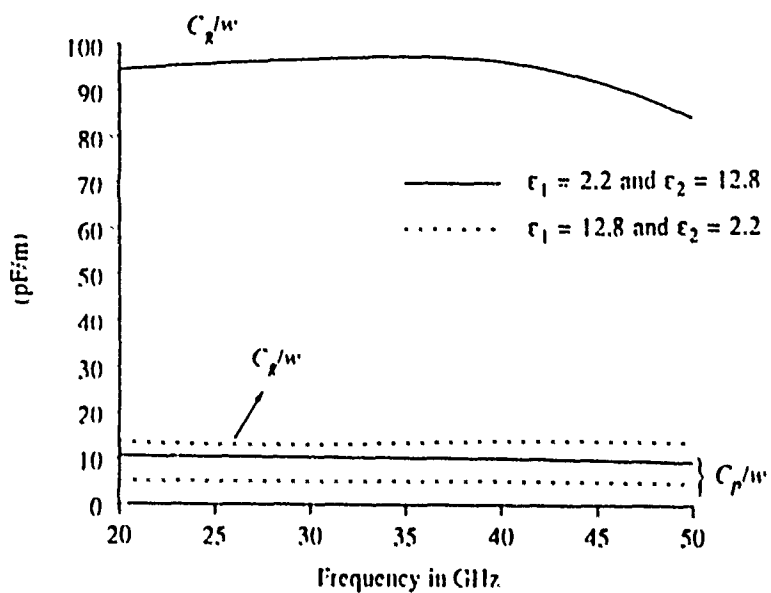


Figure 3-15. Normalized gap capacitance versus frequency.

$b = t = h / 2$ ,  $h = 0.3$  mm,  $w = h$  and  $s = 0.2$  h.

## Chapter IV

### MIC Discontinuities II-

#### Slot Line Short-end Discontinuities

#### 4.1 Introduction

Slot line was first proposed by Cohn in 1968 [69] as a waveguiding structure for MIC applications. The basic structure consists of a narrow slot in a conductive coating on one side of a substrate, the other side of the substrate being interfaced with air. The geometry of a slot line is shown in Fig. 4-1. In order that electromagnetic waves be confined in the vicinity of the slot, the permittivity of the substrate is usually high ( $> 10$ ). This slot line structure has been used in filters, couplers and circuits containing semiconductor devices [70], [13]. Since the electric field of the guide wave is approximately transverse to the wave propagation direction, the fundamental mode is TE-like. There is no cut-off frequency for this structure, since the slot separates two semi-infinite ground planes. Slot lines can also be included in microstrip circuits by etching the slot circuits in the ground plane. With the slot and microstrip combinations, many circuits have been realized; for example, hybrid branchline directional couplers [71] and microstrip bandstop filters [16]. Other discontinuities, such as the microstrip-slot transition for a two-level circuit design, and resonant slots for antenna applications, will be discussed in Chaps. V and VII respectively. The characteristics of a slot line including its propagation constant and characteristic impedance have been studied extensively [71] – [74]; however, analytic methods for slot line discontinuities are

scarce, especially in terms of including the radiation and surface waves effects. This slot line short-end discontinuity, as shown in Fig. 4-2, is the most commonly seen discontinuity in slot line circuits [74]. It can be used in the design of matching networks, filters and couplers. Since the current will flow near the end of the slotline, there is an appreciable amount of energy storage beyond the termination. The end discontinuity will cause radiation and generates surface waves. Without the image cancellation, energy storage and losses are more severe than in the microstrip line case, and this end effect has to be accounted for in accurate circuit designs.

In slot line structures, the larger the effective dielectric constant, the more the energy is confined to the vicinity of the slot. If the other side of the ground plane is covered by a dielectric material (instead of being free space), the effective dielectric constant of the slot line will increase. This offers the advantages of shorter wavelength, greater confinement of electromagnetic fields, and stronger coupling between slot line circuits [16]. The geometry of a short-end slot line sandwich is shown in Fig. 4-3. The comparison of the end effects including fringing, radiation and surface waves between a slot line and a slot line sandwich will be provided in this chapter.

The analysis of slotline discontinuities is almost a one-to-one correspondence with microstrip discontinuities. The numerical methods discussed in the previous chapter can be modified and applied to the slot line structure.

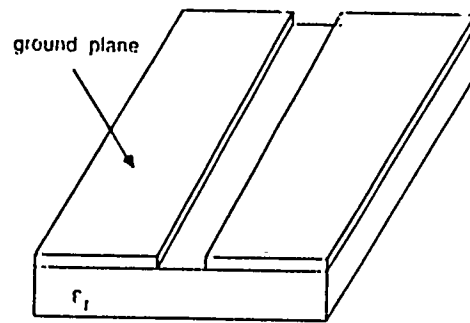


Figure 4 1 A basic slot line structure

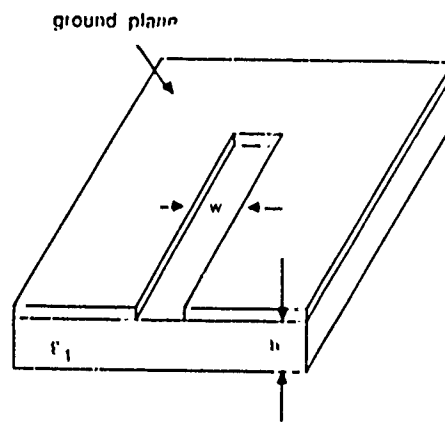


Figure 4 2 A short end slot line discontinuity

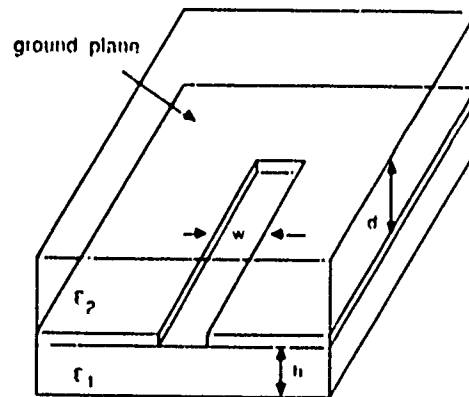


Figure 4 3 A short end slot line sandwich

## 4.2. Integral Equation

Since the one layer slot line is the case of the slot line sandwich with  $\epsilon_2 = 1$ , only the analysis for the latter case will be discussed. For the short-end slot line under consideration, an integral equation can be formulated in terms of a transverse electric field in the slender slot, viz.,

$$H_x(x, y, z = 0^+) = \int_{-\infty}^0 \int_{-w/2}^{w/2} G_{1a}(x, y | x_s, y_s) E_y(x_s, y_s) dy_s dx_s, \quad (4.1)$$

and

$$H_x(x, y, z = 0^-) = \int_{-\infty}^0 \int_{-w/2}^{w/2} G_{1b}(x, y | x_s, y_s) E_y(x_s, y_s) dy_s dx_s \quad (4.2)$$

with

$$H_x(x, y, z = 0^+) - H_x(x, y, z = 0^-) = 0 \quad (4.3)$$

on the slot line, where  $H_x$  is the magnetic field due to the electric field on the slot line. The Green's function  $G_{1a}$  can be found from Eqs. 2.47 and 2.48 of Chap. II, while  $G_{1b}$  due to symmetry is equal to  $G_{1a}$  except the sign and material parameters. Integral equation in Eq. 4.3 can be solved by the method of moments. This procedure is the same as that for the open-end microstrip line.

## 4.3. Results

From Schelkunoff's equivalence principle, the electric field in the slot is equivalent to the magnetic source in the ground plane. From image theory [61], the magnetic source and its image have the same magnitude and phase. On the other hand, in the microstrip structure, the electric current and its im-



age are  $180^\circ$  difference in phase. Therefore, the slot line circuits tend to radiate more energy than microstrip circuits. An example of radiation and surface wave losses at a slot line short-end in terms of total incident power versus frequency for three different slot widths is shown in Fig. 4-4. It is seen that the energy losses increase with the increase of slot line width or frequency. This is because, by increasing the frequency or slot width, less energy is confined near the slot. The above discussion also explains the result in Fig. 4-5 where it is shown that the normalized reactance due to fringing increases with the increase of slot width or frequency. It is seen from Fig. 4-4 that, for the substrate with  $\epsilon_1 = 12$ , when the substrate thickness is about  $0.06\lambda_0$ , more than 25% of the incident power is lost at the short end for all the three slot widths. Fig. 4-4 provides an idea of the upper frequency where a slot line circuit is still useful. It is also observed that even for a thin substrate thickness ( $0.01\lambda_0$ ), the radiation and surface wave losses are 5 to 10 % of the total incident power. This is one of the main disadvantages of this one-sided slotline structure.

By adding a cover layer on the free-space side of the slot line, the guide wavelength will decrease and more energy will be confined near the slot region. This implies that the characteristic impedance will decrease. The result is, that with a unit voltage wave incident to the slot line, the total incident power  $\frac{1}{2Z_0}$  will increase quite noticeably (typically, 5 to 16 %). On the other hand, for a unit voltage wave, the radiation and surface wave losses at the short end increase only slightly when a layer is added. Therefore, it is expected that the amount of the energy loss at the discontinuities can be reduced by using a slot

line sandwich. An example of this result is shown in Fig. 4-6. It is seen that the radiation and surface wave losses are greatly reduced. It is also seen from Fig. 4-7 that, by using the slot line sandwich, the fringing fields and normalized reactance increase due to the higher effective dielectric constant and to more energy being confined near the slot line. This implies that the coupling between slot line circuits is enhanced.

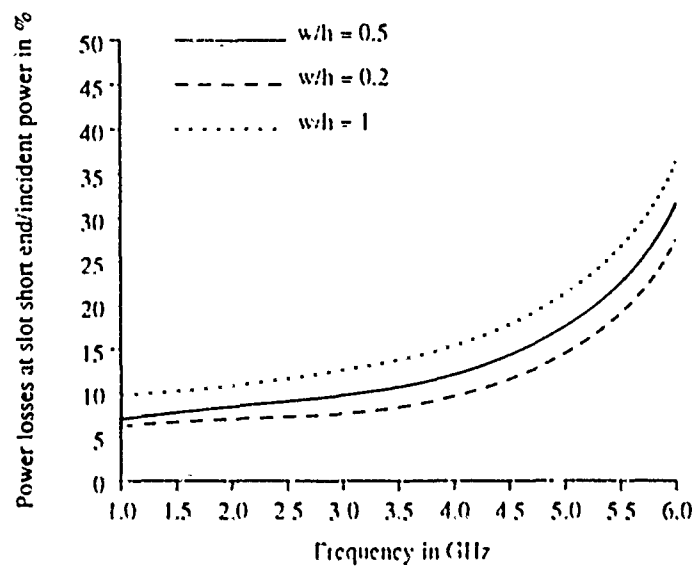


Figure 4.4. Power losses at slot line short end versus frequency  
 $\epsilon_1 = 12$  and  $h = 121$  mil.

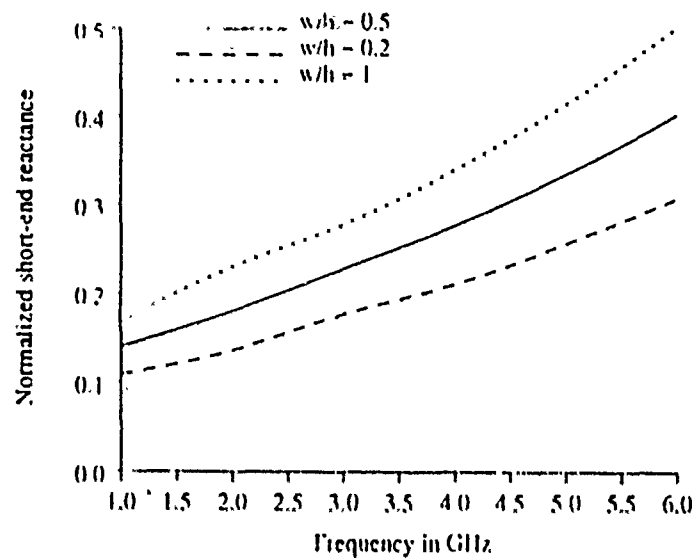


Figure 4.5. Normalized slot line short-end reactance versus frequency.  
 $\epsilon_1 = 12$  and  $h = 121$  mil

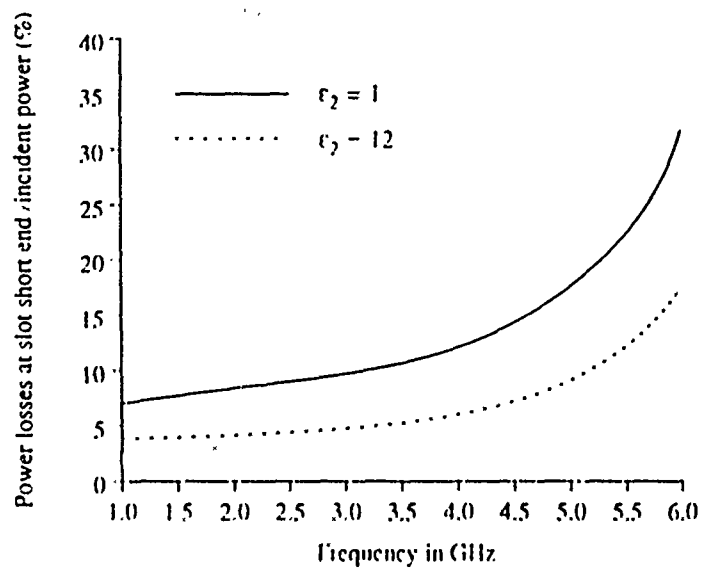


Figure 4.6 Power losses at slot line short end versus frequency.  
Comparison between slot line and sandwiched slot line.  
 $\epsilon_1 = 12$ ,  $h = d = 121$  mil, and  $w/h = 0.5$ .

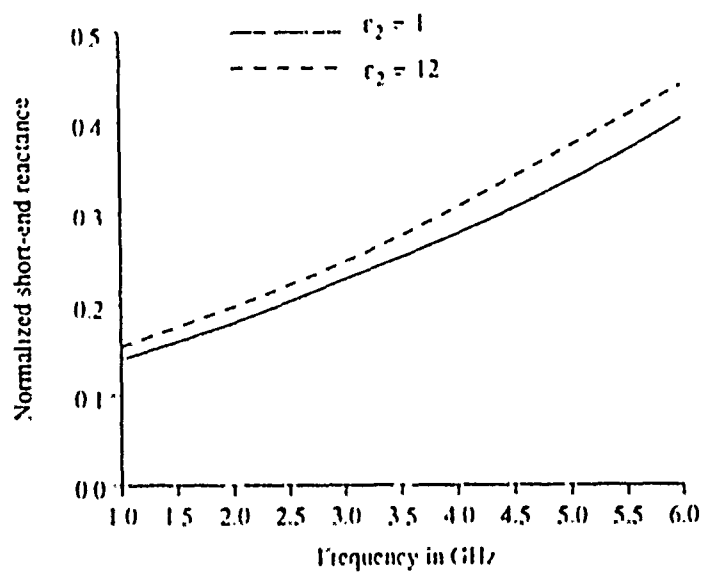


Figure 4.7. Normalized slot line short-end reactance versus frequency.  
Comparison between slot line and sandwiched slot line.  
 $\epsilon_1 = 12$ ,  $h = d = 121$  mil, and  $w/h = 0.5$ .

## Chapter V

### A Dynamic Model for a Microstrip-Slotline Transition

#### 5.1 Introduction

Based on the approach described in the Chap. III, a dynamic model for a microstrip-slotline transition and its related structures (such as a microstrip fed slot and a slotline fed printed dipole) is proposed in this chapter. The developed model, with some modifications, can be applied to other types of transitions in MIC and MMIC design. Some of these examples will be discussed in the next chapter.

In a microstrip-slotline transition, a short-circuit slotline which is etched on one side of the substrate is crossed at a right angle by an open-circuit microstrip on the opposite side. This type of transition makes a two-level circuit design possible [16]. Some experimental work has been reported [13], [75] and a transmission line circuit model has been described in [76]. In the present approach, the radiation and surface waves due to the cross-junction, the line discontinuities, and all the mutual coupling due to the dominant mode as well as higher order modes of each line are included in the method of moments solution. The VSWR and input impedance of the transition, can be determined by the current distribution on the microstripline in conjunction with transmission line theory. In the formulation procedure, certain important problems in MIC, MMIC or printed antennas design can also be solved. This aspect will be discussed in Chapter VIII.

## 5.2. Theory

### (5.2.1) Green's Function Formulation.

The microstrip to slotline transition is shown in Fig. 5-1 and the cross section is shown in Fig. 5-2, where the lines are extended a certain distance beyond the cross-junction, so that their extension may act as a tuning stub. Due to the assumption that the strip or slot is slender, the transverse vector components ( $J_y$  and  $M_{mx}$ ) on the lines are a second order effect, and are neglected for simplicity. Therefore, only the  $\hat{x}$ -directed electric surface current  $J_x$  on the strip and the  $\hat{y}$ -directed magnetic surface current  $M_{my}$  ( $\hat{x}$ -directed electric field  $E_x$ ) are considered. Under the above assumptions, the coupled integral equations can be formulated in terms of  $E_x$  and  $H_y$ . As a result, the electric  $E_x$  at  $(x, y, d)$  due to the presence of both strip and slot is

$$E_x = \iint G_{xx} J_x ds_m + \iint G_{xy} M_{my} ds_s, \quad (5.1)$$

and the difference of the magnetic field  $H_y$  at  $(x, y, 0^+)$  and at  $(x, y, 0^-)$  is

$$\Delta H_y = \iint G_{yx} J_x ds_m + \iint G_{yy} M_{my} ds_s, \quad (5.2)$$

where  $G_{xx}$  and  $G_{yx}$  are the dyadic Green's function components due to an  $\hat{x}$ -directed infinitesimal electric dipole at  $z=d$  and  $G_{xy}$  and  $G_{yy}$  are the dyadic Green's function components due to a  $\hat{y}$ -directed infinitesimal magnetic dipole at  $z=0$ .  $J_x$  is the current on the microstrip  $s_m$  while  $M_{my}$  is the magnetic current (electric field) on the slotline  $s_s$ .

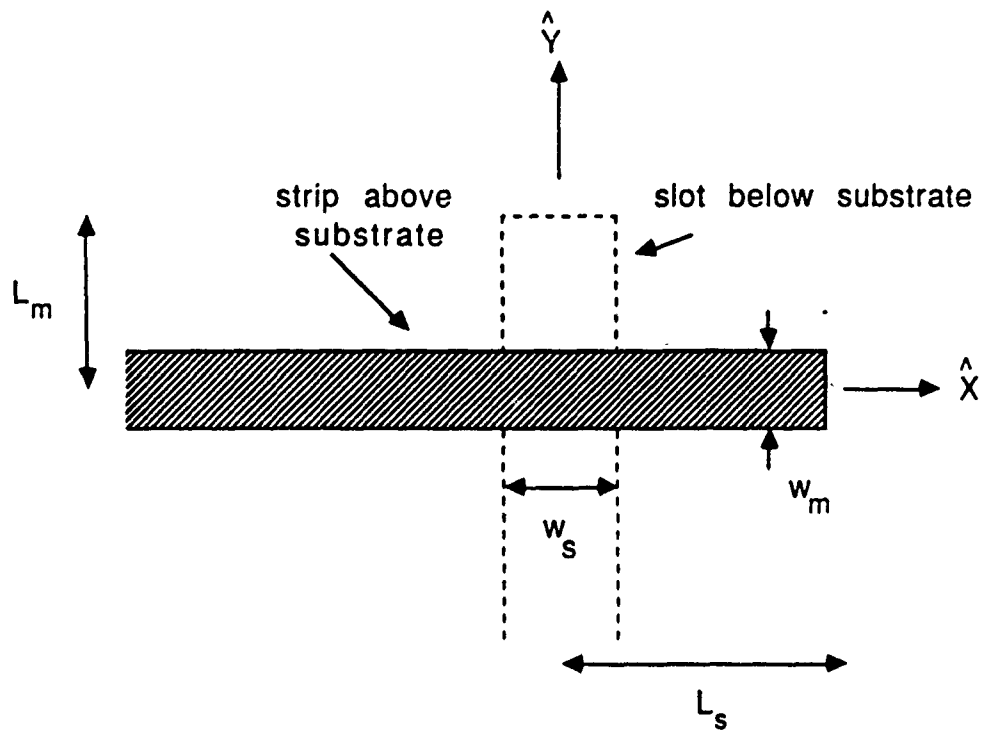


Figure 5-1. Top view of microstrip-slot line transition.

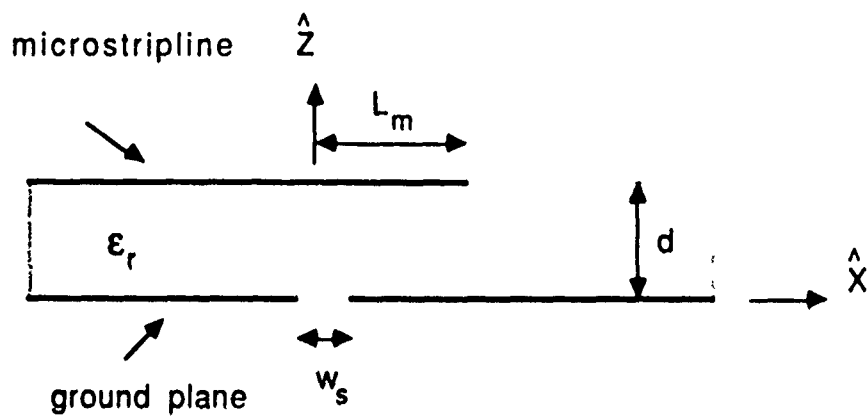


Figure 5-2. Cross section of microstrip-slot line transition.

The dyadic Green's function components  $G_{xx}$ ,  $G_{xy}$ ,  $G_{yx}$  and  $G_{yy}$  can be derived from Eqs. 2.13-2.14 and 2.47-2.48. The results can be expressed as

$$G_{xx}(x, y|x_o, y_o) = \int_{-\infty}^{\infty} \int_{-\infty}^{\infty} \bar{G}_{xx}(\lambda_x, \lambda_y) e^{j\lambda_x(x-x_o)} e^{j\lambda_y(y-y_o)}, \quad (5.3)$$

$$G_{xy}(x, y|x_o, y_o) = \int_{-\infty}^{\infty} \int_{-\infty}^{\infty} \bar{G}_{xy}(\lambda_x, \lambda_y) e^{j\lambda_x(x-x_o)} e^{j\lambda_y(y-y_o)}, \quad (5.4)$$

$$G_{yx}(x, y|x_o, y_o) = -G_{xy}(x, y|x_o, y_o) \quad (5.5)$$

and

$$G_{yy}(x, y|x_o, y_o) = \int_{-\infty}^{\infty} \int_{-\infty}^{\infty} \bar{G}_{yy}(\lambda_x, \lambda_y) e^{j\lambda_x(x-x_o)} e^{j\lambda_y(y-y_o)} \quad (5.6)$$

where

$$\bar{G}_{xx}(\lambda_x, \lambda_y) = \frac{-j Z_o}{4\pi^2 k_o \epsilon_r} \left[ \frac{k_1^2 - \lambda_x^2}{D_e(\lambda)} + \frac{\lambda_x^2 q_1 (1 - \epsilon_r) \sinh q_1 d}{D_e(\lambda) D_m(\lambda)} \right] \sinh q_1 d, \quad (5.7)$$

$$\bar{G}_{xy}(\lambda_x, \lambda_y) = \frac{-1}{4\pi^2} \left[ \frac{q_1}{D_e(\lambda)} + \frac{\lambda_x^2 (\epsilon_r - 1) \sinh(q_1 d)}{D_e(\lambda) D_m(\lambda)} \right], \quad (5.8)$$

$$\begin{aligned} \bar{G}_{yy}(\lambda_x, \lambda_y) = \frac{-j}{4\pi^2 Z_o k_o} & \left[ (k_1^2 - \lambda_y^2) \frac{q_1 \cosh q_1 d + \epsilon_r q \sinh q_1 d}{q_1 D_m(\lambda)} \right. \\ & \left. + \frac{\lambda_y^2 q_1 (1 - \epsilon_r)}{D_e(\lambda) D_m(\lambda)} + \frac{(k_o^2 - \lambda_y^2)}{q} \right], \end{aligned} \quad (5.9)$$

and with

$$D_e(\lambda) = q \sinh(q_1 d) + q_1 \cosh(q_1 d), \quad (5.10)$$



$$D_m(\lambda) = q_1 \sinh(q_1 d) + \epsilon_r q \cosh(q_1 d). \quad (5.11)$$

Other pertinent parameters have been defined in Chap. II.

### (5.2.2) The Choice of Expansion Modes.

In the method of moments procedure,  $J_x$  and  $M_{my}$  are expanded in terms of a set of known functions. For the transition under consideration, the modeling of two half infinite lines is necessary, in which several mechanisms are possible. If subsectional expansion modes are used in the two finite lines with a  $\delta$  gap source, in order to characterize the cross-junction of this resonator, two sets of wave amplitudes on each line corresponding to two different length of the parasitic line, are required. This scattering matrix formulation has been found to be very sensitive to error. A more reliable method is to simulate the physical situation where both the microstripline and the slotline are terminated by a matched load. In this scheme, subsection expansion modes are used in both lines near the cross-junction region, while entire domain travelling waves are used to represent the transmitted wave in the parasitic line (slotline) and the incident wave and the reflected wave on the feed line (microstripline). Other choices of expansion modes are also possible, such as using subsectional basis functions in the feed line and subsectional modes and traveling wave modes in the parasitic line, or the traveling wave modes starting away from the cross-junction such that the mutual coupling of traveling wave and PWS modes on different lines is negligible. These types of expansion modes have

some advantages in numerical analysis and will be discussed in the next section.

The traveling wave modes used involve microstripline and slotline propagation constants  $k_m$  and  $k_s$ . From the knowledge of  $k_m$  and  $k_s$ , the unknown current distribution on the microstripline can be expanded as

$$f(x) = I^{inc} + I^{ref} + \sum_{n=1}^N I_n f_n(x) \quad (5.12)$$

while the unknown electric field distribution in the slotline can be expanded as

$$g(y) = V^t + \sum_{n=1}^M E_n g_n(x) \quad (5.13)$$

where

$$I^{inc} = e^{-jk_m x}, \quad (5.14)$$

$$I^{ref} = -\Gamma e^{jk_m x} \quad (5.15)$$

and

$$V^t = T e^{jk_s y}. \quad (5.16)$$

Piecewise sinusoidal (PWS) modes are used as subsectional expansion modes and are defined starting from the end of each line. These modes were shown in Eqs. 3.6 and 3.7.

### (5.2.3) The Method of Moments and Matrix Formulation

The coupled integral equations can be obtained from Eqs. 5.1 and 5.2 by forcing the boundary conditions that the E- field must be zero on the microstripline and the H- field must be continuous across the slotline. When the expansion modes are substituted into Eqs. 5.1 and 5.2 followed by Galerkin's procedure, one has

$$\begin{bmatrix} [Z_{self}] & [Z_{tself}] & [T_{meact}] & [T_{tmeact}] \\ [T_{emeact}] & [T_{temact}] & [Y_{self}] & [Y_{tself}] \end{bmatrix} \begin{bmatrix} [I] \\ [E] \\ [T] \end{bmatrix} = \begin{bmatrix} [I_{inc}] \\ [V_{tra}] \end{bmatrix} \quad (5.17)$$

where the submatrices are the reaction between different expansion modes,  $[I]$  is an  $N \times 1$  column vector with elements  $I_1, I_2, \dots, I_N$ , and  $[E]$  is an  $M \times 1$  column vector with elements  $E_1, E_2, \dots, E_M$ .

### (5.2.4) Some Aspects of the Numerical Analysis.

The formulation in the last section is quite flexible and can be easily modified to other types of mode expansion mechanisms. For example, the traveling wave modes may start more than a wavelength away from the cross-junction, which modifies the Fourier transform of the traveling wave mode in the above formulation. This type of expansion has the advantage that the mutual coupling between traveling wave modes and PWS modes of the other line ( $[T_{temact}]$  and  $[T_{tmeact}]$ ) is negligible. Therefore, the computation effort in Eqs. 5.17 can be reduced. Besides, the solutions are automatically convergent in the sense of the number of expansion modes. Another type of expansion is also possible where only PWS modes are used in the feed line. This has the ad-

vantage of providing some insight into the current distribution on the feed line and of avoiding the computations of the submatrices  $[Y_{\text{itself}}]$  and  $[T_{\text{ineact}}]$  in Eq. 5.17. The above different mode expansion mechanisms may also be used to check the convergence and stability of the solution.

### 5.3. Numerical results

The results for a microstrip-slotline transition have been obtained based on the developed algorithm. The numerical analysis was performed on the IBM 3090 system. Typically, for each data set it takes about one minute and thirty seconds of computer time in contrast to a half second to obtain the propagation constant  $k_m$ , although a lot of effort has been made to reduce the computer cost. An example of a  $50\ \Omega$  microstripline to a  $80\ \Omega$  slotline transition is given. The results of the VSWR and input impedance are shown in Figs. 5-3 and 5-4 respectively. The results for the VSWR are first checked by interchanging the feed line and parasitic line. The differences in  $|\Gamma|$  are within 2%, which is consistent with the property of low loss two port networks. The complex reflection coefficient that is obtained is checked further by changing the number of modes and different mode expansion mechanisms as described in the last section. Two sets of input impedances with different numbers of expansion modes and base function size are shown in Fig. 5-4 to illustrate a convergence test example. With the particular device parameters chosen it is found that both the magnitude and phase of the reflection coefficient converge very well (2 % in  $|\Gamma|$  and  $5^\circ$  in phase ) for  $d \leq 0.036\lambda_0$ . However, for higher frequencies, the results are more unstable, and typically the results are 5-10

% accurate in  $|\Gamma|$  and 10-15 degrees in phase before higher order modes turn on. This behavior may be due to the reasons that 1), when the radiated and surface waves are not weakly excited, the transmission line theory applied to the microstripline or slotline is only an approximation and the mode expansion approach is somewhat of a brute force. 2), the transverse vector components ( $J_y$  and  $M_y$ ) which are neglected in the present investigation become more important as frequency increases. The VSWR obtained by the transmission line circuit model [76] and the measurement [75] are also shown in Fig. 5-3 to provide a comparison. In the transmission line circuit model the stub length is assumed to be measured from the center of each line and the propagation constants  $k_m$  and  $k_s$  and the excess length are obtained from the current analysis. It is seen from Figs. 5-3 and 5-4 that the present method agrees very well with the circuit model in the low frequency range. The discrepancy for higher frequencies is probably due to the higher order modes, surface waves, and radiation effects which are neglected in the circuit model. The measurements reported in [75] show a wider bandwidth than that of either the circuit model or the present analysis. It is believed that the accuracy of the device parameters, the non-ideal matched load and (especially), the coaxial to microstripline transition affected the frequency-dependent results in the measurement. Besides, the material used in [75] is Custom HiK 707-20 ( $\epsilon_r = 20$ ) which is usually very lossy especially for higher frequencies. These effects may explain the discrepancy between theory and experiment.

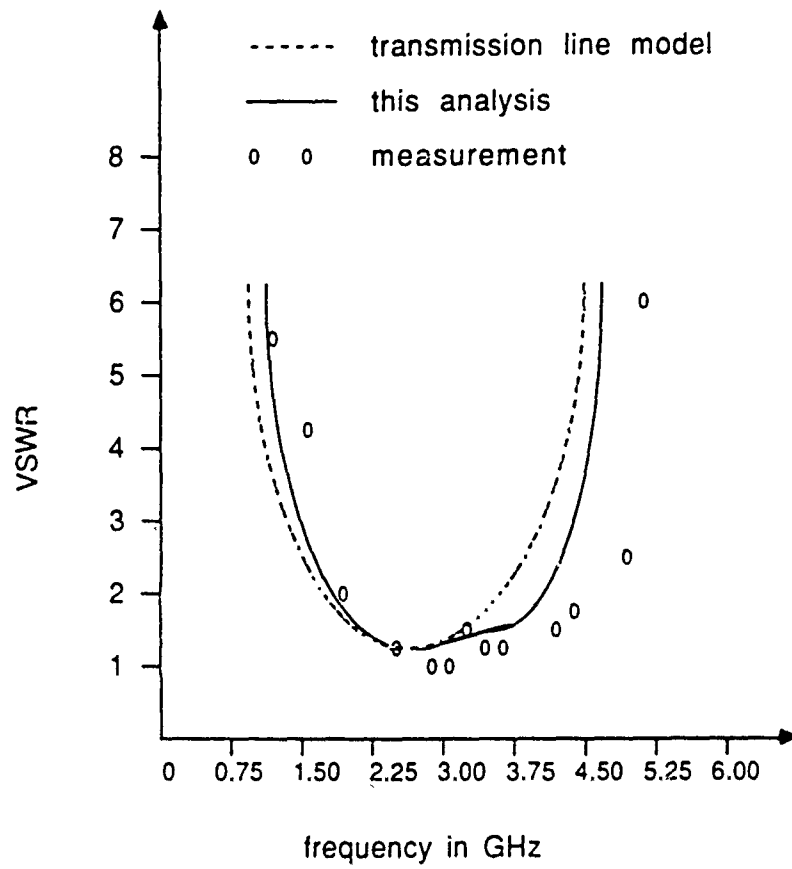


Figure 5-3. VSWR versus frequency for microstrip-slot line transition.

- ▲ ▲ ▲ transmission line circuit model
- ○ ○ present theory,  $M=N=4$  and  $h=0.03 \lambda_0$
- + + + present theory,  $M=N=7$  and  $h=0.025 \lambda_0$

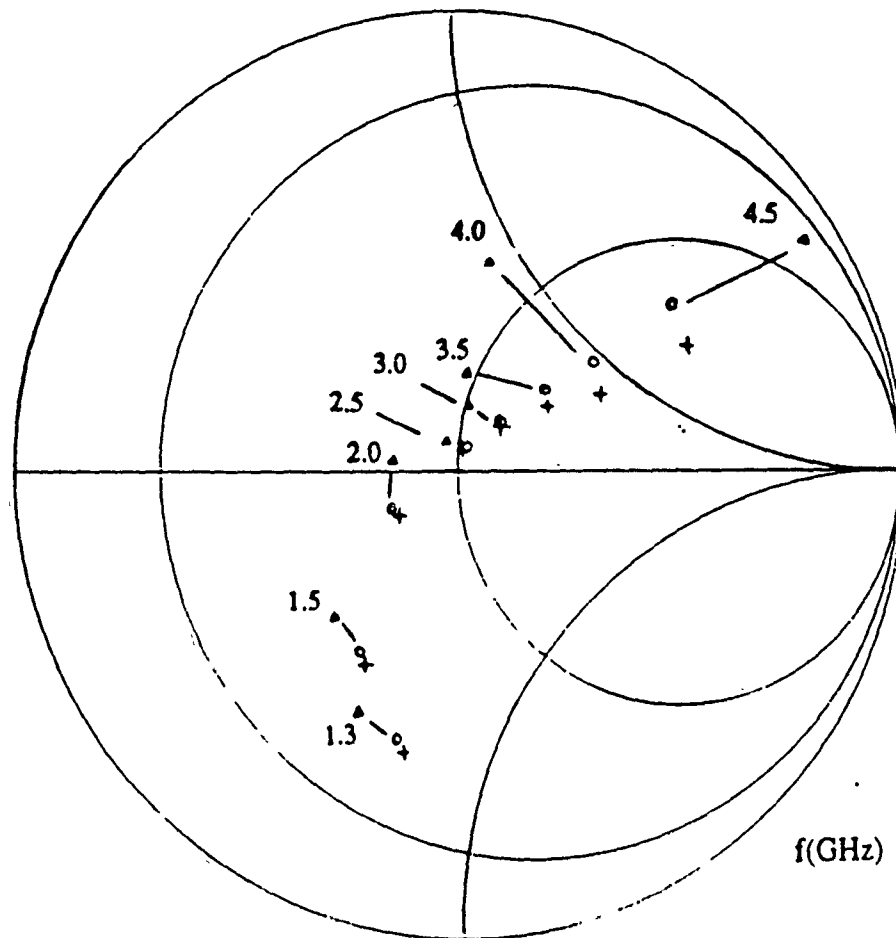


Figure 5-4. Smith chart plot of impedance versus frequency  
for microstrip-slotline transition.  
The reference plane is on the center of the cross section.

## Chapter VI

### Proximity Coupled Microstrip Transition in Double Layer Integrated Circuits.

#### 6.1. Introduction

Analytic and numerical methods described in the previous chapter are extended here to study two types of proximity coupled open end microstriplines in a double layer planar structure. These proximity coupled transitions constitute potentially important components for MIC and MMIC design. Fig. 6-1 shows two semi-infinite collinear microstriplines at different levels. This type of transition has the advantage over the end coupled lines in that the overlap distance  $l_o$  may be used to control the coupling. Also this transition provides a wider range of coupling coefficient with a reasonably large bandwidth and it therefore is useful in coupler or filter design. Fig. 6-2 shows two EMC transverse microstriplines. In this type of transition, an open-circuit microstripline printed on top of the superstrate is crossed at a right angle by another open-circuit microstripline embedded on the substrate. These two lines are extended a certain distance beyond the cross-junction to provide tuning stubs. This type of transition has the properties of broadband and good match due to the presence of the double stub. The materials in the substrate-superstrate configuration may greatly affect the coupling in the transition and this issue has also been investigated. In Section 6.2, the method of moments solution of integral equations is formulated. In Section III, the results



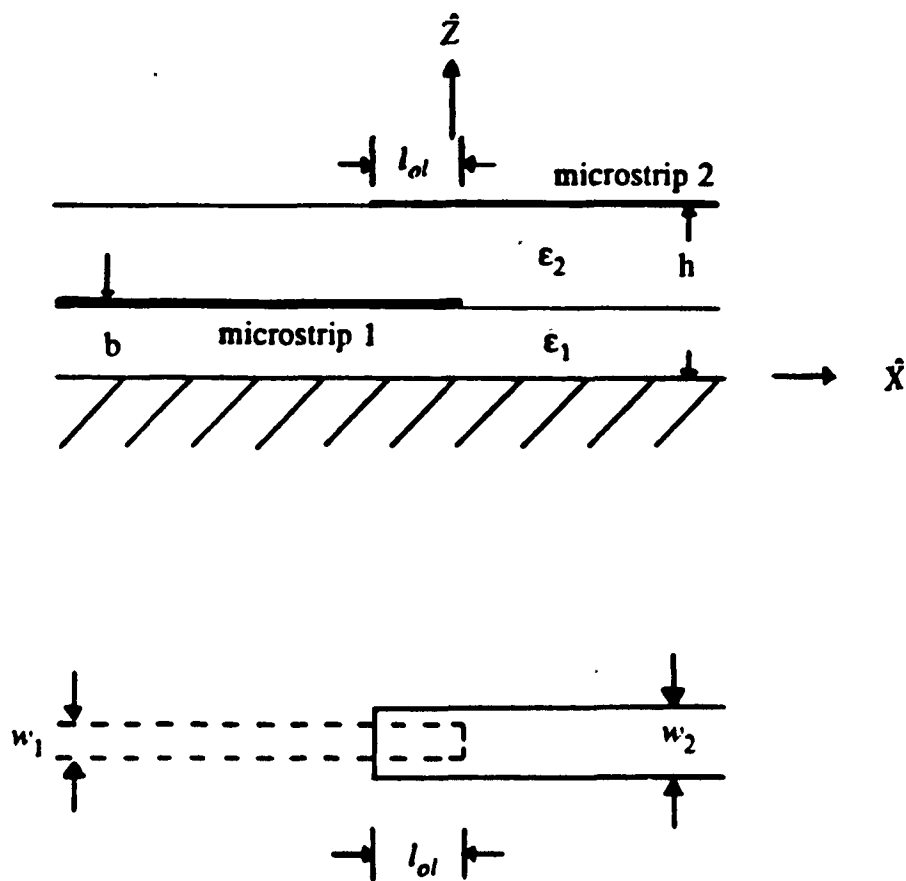


Figure 6-1. Proximity coupled collinear microstrip-microstrip transition.

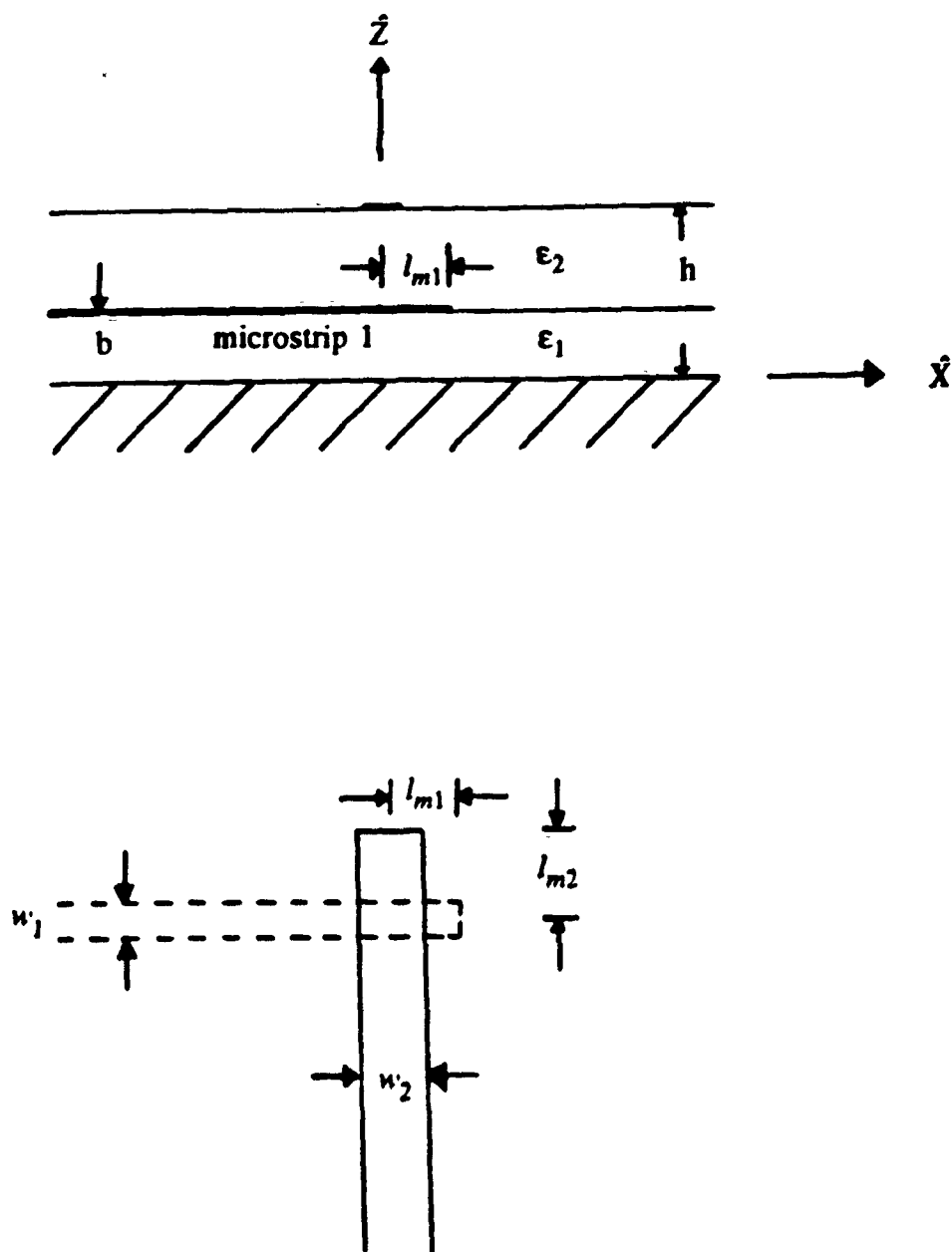


Figure 6-2. Proximity coupled transverse microstrip-microstrip transition.

from the numerical analysis are presented and some interesting properties of the above-mentioned transitions are discussed.

## 6.2. Analysis

### (6.2.1). EMC collinear microstriplines.

Integral equations for EMC collinear microstriplines are

$$E_x^{(i)} = \sum_{j=1}^2 \iint G_{ij} J_x^{(j)} ds_j, \quad (6.1)$$

where  $E_x^{(i)}$  is the electric field at microstrip  $i$ ,  $i = 1$  or  $2$ . Here microstrip 1 is at  $z = b$  while microstrip 2 is at  $z = h$ . The Green's function  $G_{ij}$  is  $E_x$  at  $(x, y)$  of microstrip  $i$  due to an  $\hat{x}$  directed delta source at  $(x_s, y_s)$  of microstrip  $j$ . This Green's function has been derived in Chap. II and can be expressed as

$$G_{ij} = \int_{-\infty}^{\infty} \int_{-\infty}^{\infty} D_{ij}(\lambda_x, \lambda_y) e^{-j\lambda_x(x-x_s)} e^{-j\lambda_y(y-y_s)} d\lambda_x d\lambda_y \quad (6.2)$$

where

$$D_{ij}(\lambda_x, \lambda_y) = \frac{-jZ_0}{4\pi^2 k_0 \epsilon_2} \left[ \frac{k_2^2 - \lambda_x^2}{D_e(\lambda)} f_{ij}(\lambda) + \frac{\lambda_x^2 q_2}{D_e(\lambda) D_m(\lambda)} g_{ij}(\lambda) \right]. \quad (6.3)$$

The function  $f_{ij}$  and  $g_{ij}$  can be identified from the Green's function described in the Chap. II. Other parameters are defined in Eqs. 2.20-2.31. When the expansion modes (similar to those in Chaps. III and V) are used in Eq. 6.1, followed by Galerkin's procedure in the same way as described in the last

chapter, integral equations are converted into a set of linear equations. These  $M + N + 2$  equations when expressed in matrix form are

$$\begin{bmatrix} [Z_{self_1}] [Z_{tself_1}] [Z_{eeact_2}] [Z_{teact_2}] \\ [Z_{eeact_1}] [Z_{teact_1}] [Z_{self_2}] [Z_{tself_2}] \end{bmatrix} \begin{bmatrix} [I_1] \\ -\Gamma \\ [I_2] \\ \bar{T} \end{bmatrix} = \begin{bmatrix} [I_{inc_1}] \\ [I_{inc_2}] \end{bmatrix}. \quad (6.4)$$

The computation of each matrix element in Eq. 6.4 requires a double infinite integration where the integrand contains the corresponding Green's function  $D_{ij}(\lambda_x, \lambda_y)$  and the Fourier transform of the current expansion functions. For example  $[Z_{eeact_2}]$  is an  $(N + 1) \times M$  matrix with matrix elements

$$Z_{eeact_2}^{nm} = \int_{-\infty}^{\infty} \int_{-\infty}^{\infty} D_1(\lambda_x, \lambda_y) F_2(\lambda_y) F_1(\lambda_y) A_1(\lambda_x) A_2(\lambda_x) \cos[\lambda_x(nd_1 + md_2 - l_{ol})] d\lambda_x d\lambda_y, \quad (6.5)$$

where  $l_{ol}$  is the microstrip overlap length, and all other parameters in Eq. 6.5 has been described in Chap. III.

#### (6.2.2). EMC transverse microstriplines.

The analysis of EMC transverse microstriplines is almost one to one in correspondence to the collinear case. In matrix formulation, if local coordinates are used, it can be easily shown that the self reaction in each microstrip is identical for the collinear and transverse cases. To be more specific, the integral equations for the transverse microstriplines are

$$E_x^{(1)} = \iint G_{xx} J_x^{(1)} ds_1 + \iint G_{xy} J_y^{(2)} ds_2 \quad (6.6)$$

and

$$E_y^{(2)} = \iint G_{yx} J_x^{(1)} ds_1 + \iint G_{yy} J_y^{(2)} ds_2 \quad (6.7)$$

where  $E_x^{(1)}$  and  $E_y^{(2)}$  are the longitudinal electric fields at microstrip 1 (at  $z = b$ ) and microstrip 2 (at  $z = h$ ), respectively. The function  $G_{xx}$  equals to  $G_{11}$ , while  $G_{yy}$  is the same as  $G_{22}$  except  $\lambda_x$  and  $\lambda_y$  are interchanged in  $D_{22}$ . Other Green's functions are

$$G_{xy} = \int_{-\infty}^{\infty} \int_{-\infty}^{\infty} D_{xy}(\lambda_x, \lambda_y) e^{-j\lambda_x(x-x_s)} e^{-j\lambda_y(y-y_s)} d\lambda_x d\lambda_y \quad (6.8)$$

and

$$G_{yx} = G_{xy} \quad (6.9)$$

where

$$D_{xy}(\lambda_x, \lambda_y) = \frac{-jZ_0}{4\pi^2 k_0 \epsilon_2} \left[ -\frac{\lambda_x \lambda_y}{D_e(\lambda)} f_{12}(\lambda) + \frac{\lambda_x \lambda_y q_2}{D_e(\lambda) D_m(\lambda)} g_{12}(\lambda) \right]. \quad (6.10)$$

The mode expansion mechanism and the method of moments procedure follow in the same manner as for the collinear case. The final matrix is in exactly the same form as Eq. 6.4. The submatrices  $[Z_{self_i}]$ ,  $[Z_{iself_i}]$  with  $i = 1$  or  $2$  and  $[I_{inc_i}]$  are identical for the collinear and transverse cases. All other submatrices can be obtained in a similar way as for the longitudinal coupling case. For example,

$$Z_{eeact_1}^{nm} = - \int_{-\infty}^{\infty} \int_{-\infty}^{\infty} D_{xy}(\lambda_x, \lambda_y) F_2(\lambda_x) F_1(\lambda_y) A_1(\lambda_x) A_2(\lambda_y) \sin[\lambda_x(nd_1 - l_{m1})] \sin[\lambda_y(md_2 - l_{m2})] d\lambda_x d\lambda_y, \quad (6.11)$$

where  $[Z_{eeact_1}]$  is an  $(M+1) \times N$  matrix, The parameters  $l_{m1}$  and  $l_{m2}$  are the stub length for microstrips 1 and 2 respectively. Sine function in Eq. 6.11 instead of a cosine in Eq. 6.5 is because the Green's function in Eq. 6.11 is an odd function of either  $\lambda_x$  or  $\lambda_y$ .

### 6.3. Results

Although the impedance matrix in Eq. 6.4 looks formidable, the computation can be simplified further based on some physical insight. For example, the Green's function and basis functions are the same in each submatrix except for a translation in reaction center. Therefore in the numerical process, these common factors need to be computed only once. Also due to reciprocity, only a fraction of the impedance elements need to be computed. In the computations for the transition problem, entire domain modes of three and a half guided wavelength long and eight to thirteen PWS modes (depending on the overlap or stub length) are used in each microstripline. The convergence has been checked for  $S_{11}(\Gamma)$ , to within 3% in magnitude and 3° in phase. The magnitude of the reflection coefficients is shown in Fig. 6-3 as a function of overlap for the collinear transition with three types of material arrangements. The corresponding microstrip width is chosen such that the microstrip lines have a 50  $\Omega$  characteristic impedance. For the case of a large dielectric constant material in the substrate and a smaller one in the superstrate, since en-

ergy is mostly confined in the substrate, less power is transmitted than that of other types of material arrangements. This behavior is observed in Fig. 6-3. From these two figures, one can see that the coupling coefficient depends on the amount of energy of an embedded microstrip stored in the superstrate. The relationship between overlap length and power distribution observed in Fig. 6-3 is not obvious. It can be explained empirically as follows. The amount of current induced in the parasitic line is mainly due to the longitudinal electric field generated by the open end feed line. This current varies sinusoidally and decreases as the observation point moves further away from the open end. Therefore, as the two microstrips are brought closer, increased coupling occurs. As the coupling gets stronger, the electric field due to the parasitic line will interact with the feed line field. Since these two microstriplines have different fundamental modes, as the overlap increases further, the coupling starts to decrease due to wave destructive interference. It is interesting to see that with a particular overlap length, very little coupling occurs. This behavior is found to be related to the superstrate thickness and dielectric constant. It is also observed that as the overlap gets larger, the reflection becomes smaller. This implies that in such a case, the guided fundamental mode is more like the coupled line mode. It is further found from Fig. 6-3, that in a certain region where coupling reaches a local maximum, the scattering matrix is insensitive to overlap length. Since the line impedance and effective dielectric constant are also frequency insensitive, in this microstrip transition, only the effective overlap length will be frequency sensitive. This implies that this transition is broadband. An example is shown in Fig. 6-4.

One can see that the scattering parameters change no more than 3% in magnitude for this particular X band computation.

For the transverse microstrip transition, the material also has a strong effect on the coupling mechanism, as shown in Figs. 6-5 and 6-6. The coupling between two transverse microstrips is further complicated by the presence of the two tuning stubs. The effect of these two stubs is very much different from those in the microstrip-slotline transition where optimum coupling occurs when both stubs are about a quarter wavelength long. For the transverse microstrip transition, the coupling is minimum when either stub is about a quarter wavelength and is maximum when both stubs are a half wavelength long. This phenomenon is due to the fact that the parasitic line, from a circuit point of view, is a shunt element to the feed line, and vice versa. Therefore, when both stubs are a half wavelength long, the circuit (looking from the cross junction) is in resonance, while when either stub is about a quarter wavelength long, the circuit is in effect shorted. For the parameters in Fig. 6-5, the guide wavelength for each microstrip is approximated as  $\lambda_{m1} = 0.547\lambda_0$  and  $\lambda_{m2} = 0.507\lambda_0$ , while in Fig. 6-6, the guide wavelength is  $\lambda_{m1} = 0.321\lambda_0$  for microstrip 1 and  $\lambda_{m2} = 0.360\lambda_0$  for microstrip 2. In Fig. 6-5, maximum coupling occurs when both stubs  $l_{m1}$  and  $l_{m2}$  are about a half guide wavelength long. In this particular case, one can see that the VSWR of this transition can be as small as 1.1. Therefore, this transition can be potentially useful in a two level circuit design.

To verify the analysis, a 3 inch by 3 inch circuit was built and tested for the case of a transverse microstrip transition. Duroid materials with permittivity



2.2 and 10.2 were the substrate and the superstrate respectively. The dimensions of the device were chosen to be the same as those in Fig. 6-5 except that stub lengths of about a half guide wavelength were used (0.75 cm and 0.81 cm for the top and bottom microstrip respectively). The circuit was made using a standard photo-etching technique and was measured on an HP-8510 network analyzer. Both computed and measured results for VSWR are shown in Fig. 6-7. The comparison shows good agreement. The ripple observed in the measurement may be due to an imperfect match at the coaxial-microstrip transitions. One can observe that the VSWR is less than 1.8 from 7 to 11 GHz. Such a broadband transition would be very useful in circuit design. This broadband property is mainly attributed to the double resonance due to the presence of double stubs. In this investigation, 50  $\Omega$  microstrip lines were used. The impedance level will affect coupling in the transition. Therefore, the results presented here may not be optimal. The choice of the impedance level may depend upon the purpose of the circuit design.

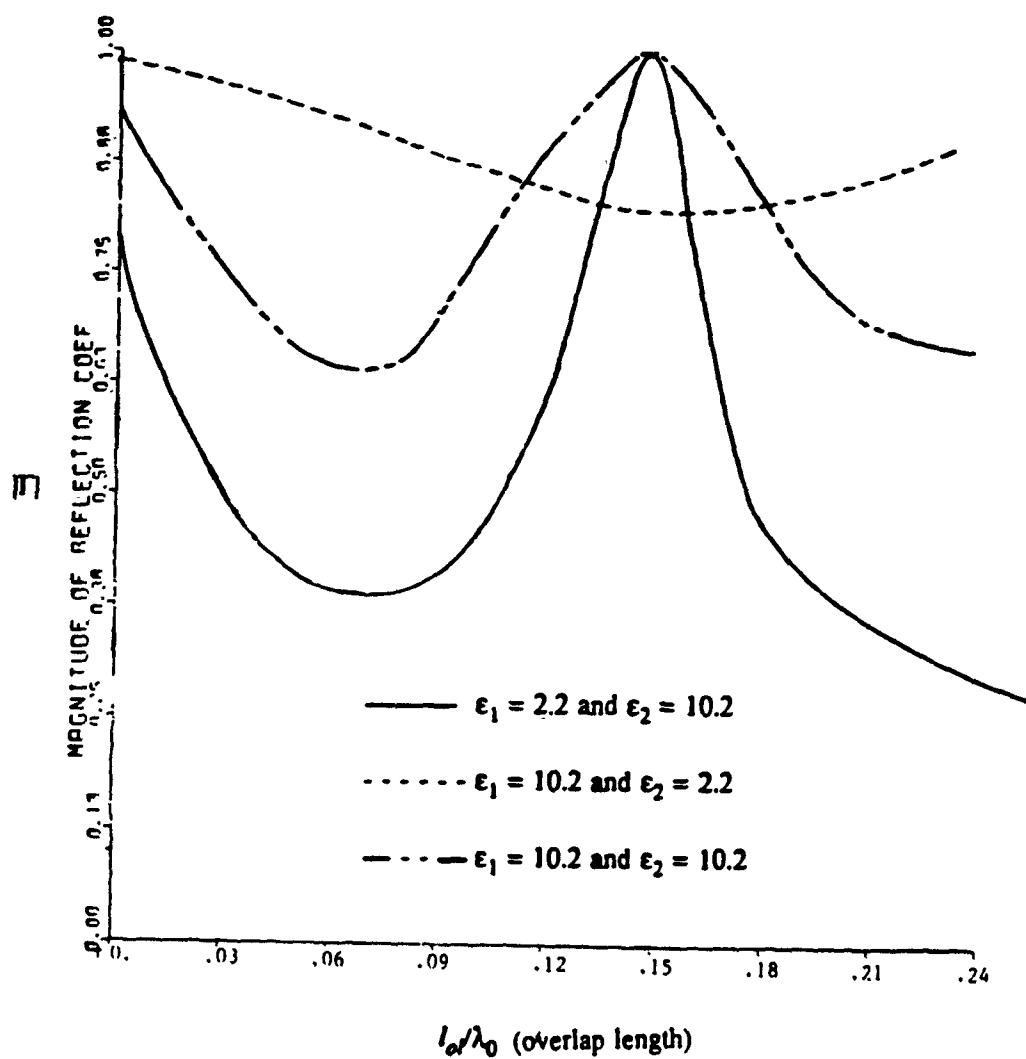


Figure 6-3.  $|\Gamma|$  versus overlap  $l_o$  for an EMC 50 $\Omega$ -50 $\Omega$  collinear microstrip transition.  $f = 10$  GHz,  $h = 50$  mil,  $b = 25$  mil.

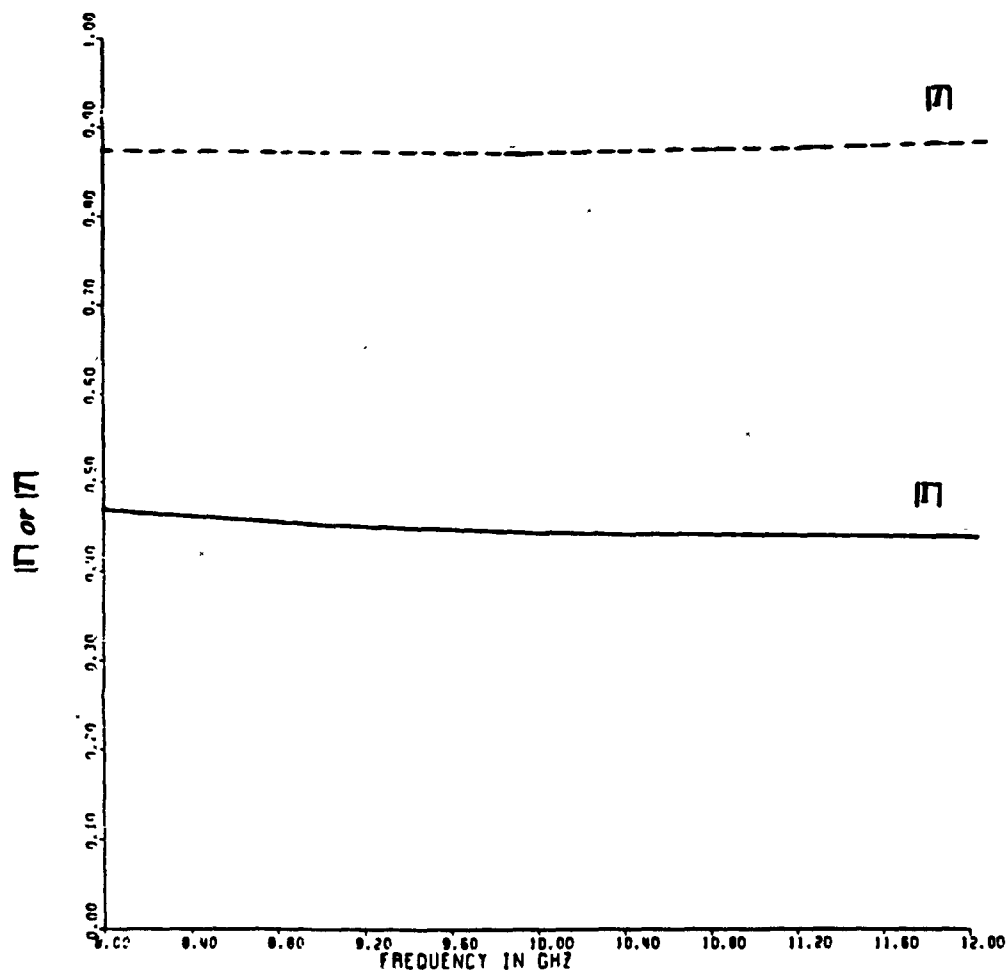


Figure 6-4.  $|\Gamma|$  and  $|T|$  versus frequency.  $l_{ol} = 0.15$  cm,  $\epsilon_1 = 2.2$  and  $\epsilon_2 = 10.2$ .

$h = 50$  mil,  $b = 25$  mil,  $w_1 = 42$  mil and  $w_2 = 76$  mil.

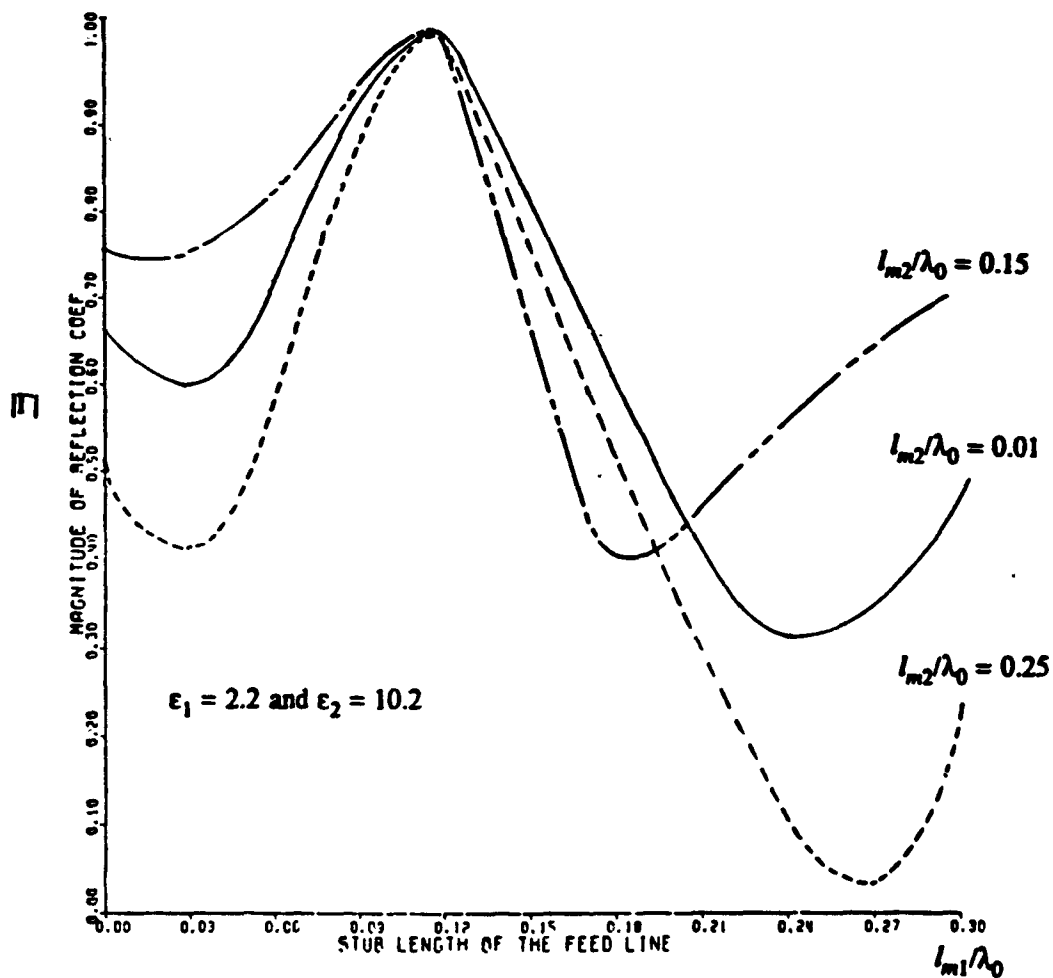


Figure 6-5.  $|\Gamma|$  as a function of stub length.

50 $\Omega$ -50 $\Omega$  transverse microstrip transition.

$f = 10$  GHz,  $h = 50$  mil,  $b = 25$  mil,  $w_1 = 42$  mil and  $w_2 = 76$  mil.

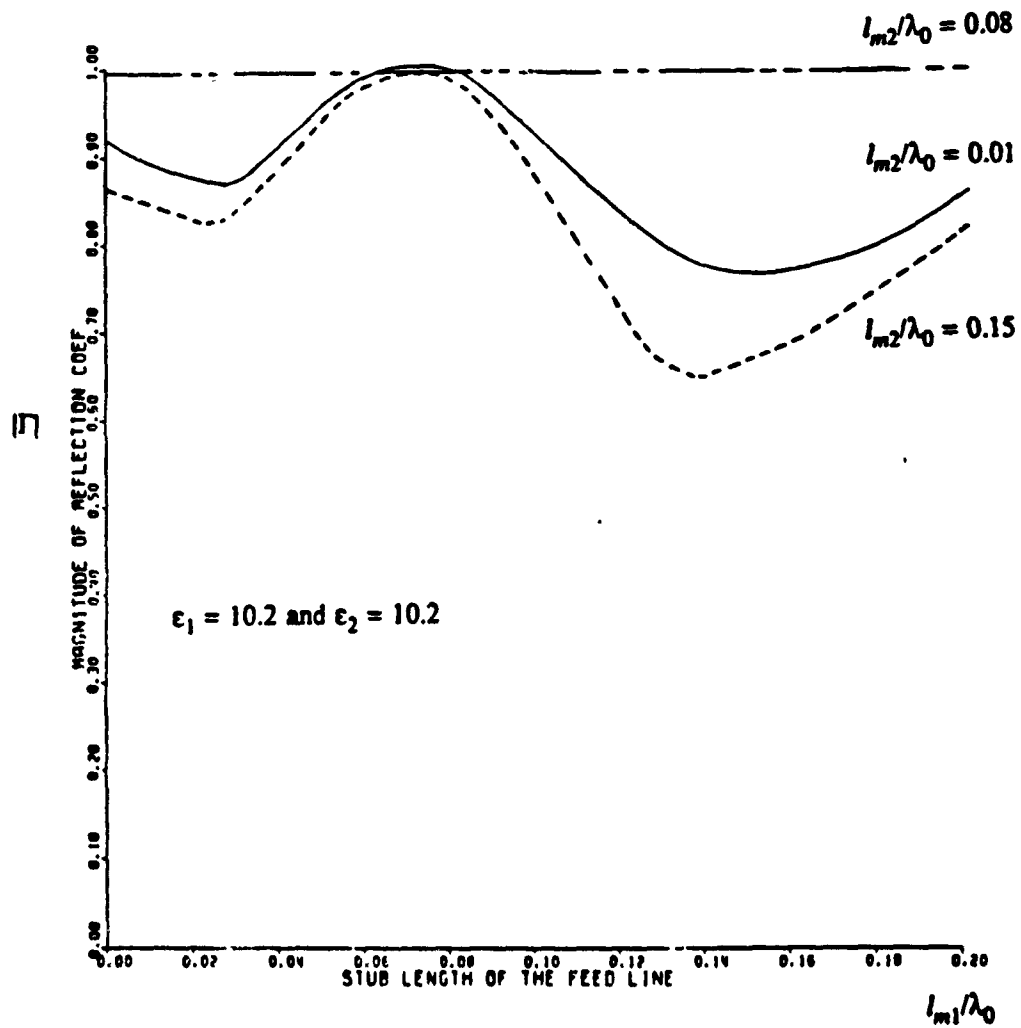


Figure 6-6.  $|\Gamma|$  as a function of stub length for a  $50\Omega$ - $50\Omega$  transverse transition.

$f = 10$  GHz,  $h = 50$  mil,  $b = 25$  mil,  $w_1 = 16$  mil and  $w_2 = 50$  mil.

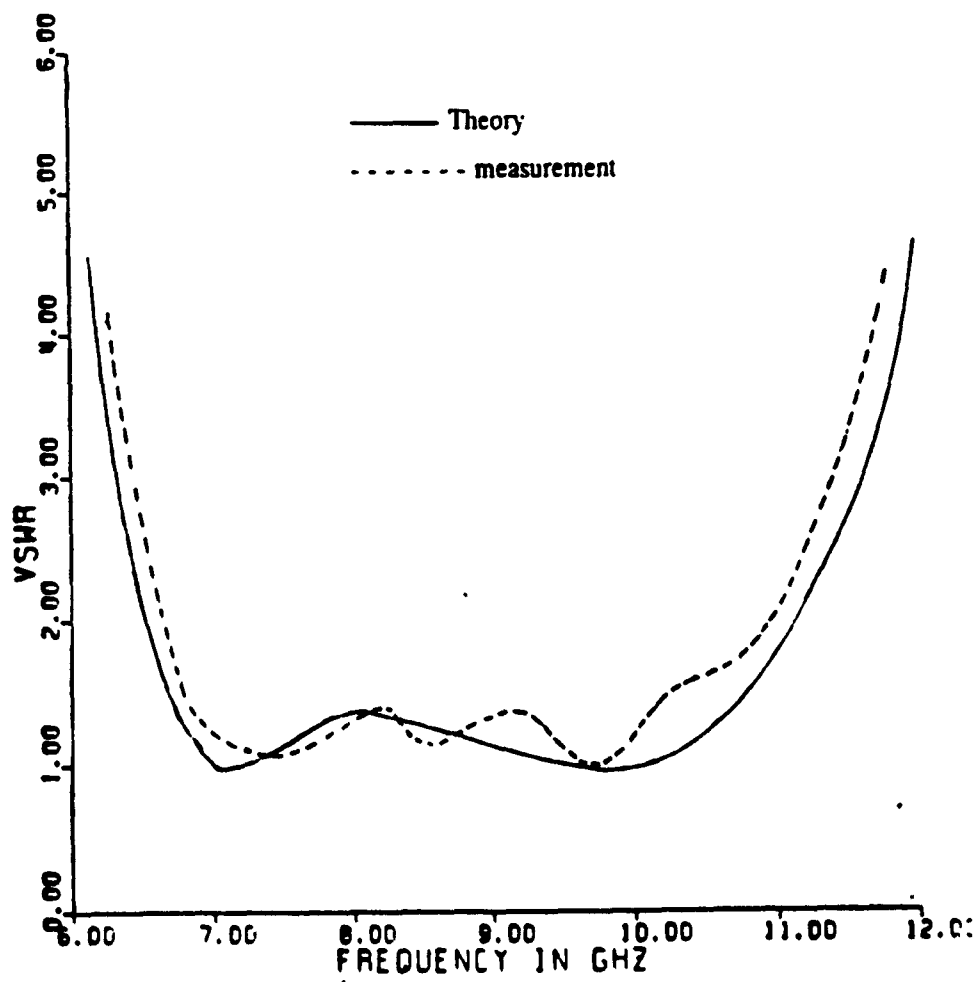


Figure 6-7. VSWR versus frequency for transverse microstrip transition.

Parameters are the same as those in Fig. 6-5, except

$l_{m1} = 0.81$  cm and  $l_{m2} = 0.75$  cm.

## Chapter VII

### Printed Slot Characteristics

#### 7.1. Introduction

The printed slot antenna is a radiating element within the category of integrated circuit antennas. The basic structure consists of a grounded substrate with a slot etched in the ground plane. The geometry is shown in Fig. 7-1. This printed slot structure has the features of producing bidirectional radiation patterns and offering an additional degree of freedom when combined with microstrip dipoles or patches [79]. The combination of printed slots and dipoles also enables the realization of circularly polarized radiation patterns [55]. In this chapter, some characteristics of printed slot antennas, such as efficiency, power distribution in each region, and the effects of materials are studied. In Section II, Green's function of an infinitesimally small magnetic dipole in the ground plane is used to study the material effects on the radiated power in either side of the ground plane and the surface wave power in the substrate. In Section III, substrate effects on the resonant length and the input admittance of a center-fed printed slot are investigated through a method of moments solution of a magnetic-type integral equation.

#### 7.2. Substrate Effects on Printed Slot Properties

The slot antenna geometry under consideration is shown in Fig. 7-2. The problem consists in its simplest forms of an  $\hat{x}$ -directed infinitesimal magnetic dipole skintight against the ground plane. The electromagnetic fields of this

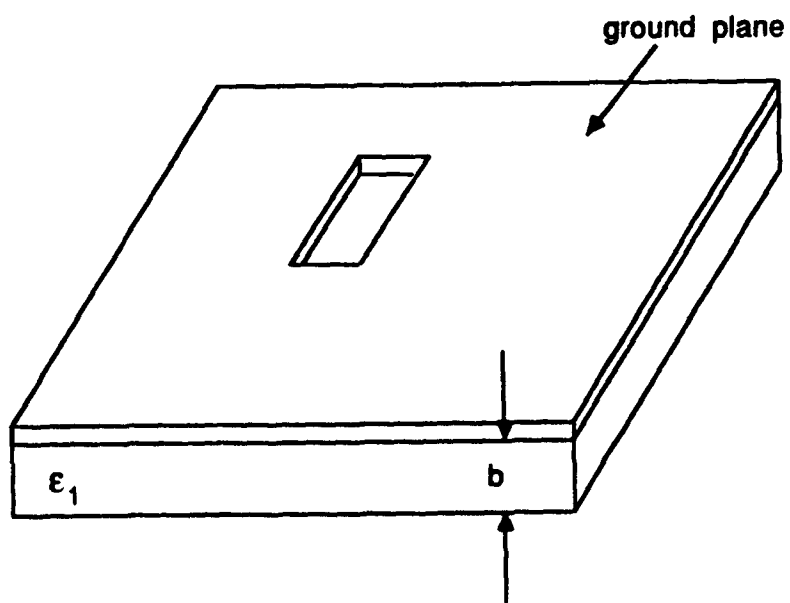


Figure 7-1. A basic printed slot structure.

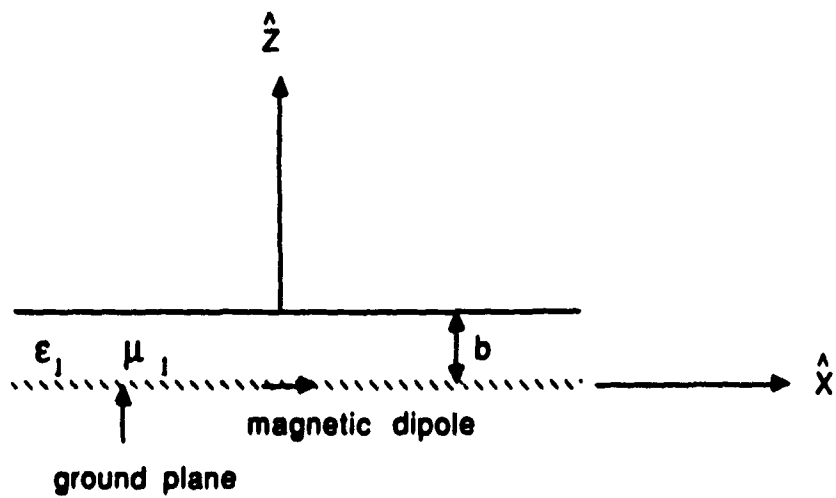


Figure 7-2. A Hertzian magnetic dipole in the ground plane.



geometry follow from the derivation of the Green function presented in Chap. II and can be described in term of a Sommerfeld-type [62] integral.

The radiating and surface waves of interest here are the electromagnetic waves in the far zone, where radiating fields are spherical waves with  $R = \sqrt{\rho^2 + z^2} \rightarrow \infty$ , and where surface waves are cylindrical waves with  $\rho \rightarrow \infty$ . The radiating fields can be obtained by the method of steepest descent [80]: while the surface waves can be found by applying the Residue and Cauchy Riemann theorems [80]. The final results for the far zone radiating fields can be summarized as

$$E_\theta = -j\omega\mu_0 \sin \phi \cos \theta k_0^2 \frac{2n_1^2}{D_m(k_0 \sin \theta)} \frac{e^{-jk_0 R}}{R}, \quad (7.1)$$

$$E_\phi = -j\omega\mu_0 \cos \phi \cos \theta k_0 M(k_0 \sin \theta) \frac{e^{-jk_0 R}}{R}, \quad (7.2)$$

$$M(\lambda = k_0 \sin \theta) = \cos \theta k_0 \frac{2n_1^2}{D_m(\lambda)} - \frac{2(1 - n_1^2) \sinh q_1 b}{D_m(\lambda) D_e(\lambda)}, \quad (7.3)$$

$$H_\theta = \frac{E_\phi}{120\pi} \quad (7.4)$$

and

$$H_\phi = -\frac{E_\theta}{120\pi}. \quad (7.5)$$

The radiating power above the substrate  $P_a$  is

$$P_a = \int_0^{2\pi} \int_0^{\pi/2} \frac{|E_\theta|^2 + |E_\phi|^2}{240\pi} R^2 \sin \theta d\theta d\phi. \quad (7.6)$$

The  $\phi$  integration is carried out analytically while  $\theta$  is computed numerically.

It can be shown by reciprocity that each surface wave mode propagates independently [49]. The surface wave modes propagate along the dielectric surface and decay exponentially toward free space. For the TM surface wave modes (transverse to  $z$ ), the total surface wave power  $P_{TM}$  is the sum of the surface wave power in region 0, ( $P_{TM0}$ ) and in region 1, ( $P_{TM1}$ ) where

$$P_{TM0} = \frac{\pi^2 \omega \mu_0}{2} \sum_{\lambda_{TM}} \left| \frac{2n_1^2 \lambda}{D'_m(\lambda)} \right|^2 \frac{k_0^2}{q}, \quad (7.7)$$

$$P_{TM1} = \frac{\pi^2 \omega \mu_1 \mu_0}{2} \sum_{\lambda_{TM}} \left| \frac{2k_1 h_m(\lambda) \lambda}{q_1 D'_m(\lambda)} \right|^2 \left[ \frac{\sinh(2q_1 b)}{4q_1} + \frac{b}{2} \right] \quad (7.8)$$

and

$$h_m(\lambda) = q_1 \cosh q_1 b + \epsilon_1 q \sinh q_1 b. \quad (7.9)$$

For the TE surface wave modes, the total surface wave power  $P_{TE}$  is the sum of surface wave power in region 0, ( $P_{TE0}$ ), and in region 1, ( $P_{TE1}$ ), where

$$P_{TE0} = \frac{\pi^2 \omega \mu_0}{2} \sum_{\lambda_{TE}} \left| \frac{2\lambda (1 - n_1^2) \sinh q_1 b}{D_m(\lambda) D'_e(\lambda)} \right|^2 \frac{1}{q} \quad (7.10)$$

and

$$P_{TE1} = \frac{\pi^2 \omega \mu_0}{2\mu_1} \sum_{i, TE} \left| \frac{2\lambda^3 k_1 (1 - n_1^2)}{q_1 D_m(\lambda) D'_m(\lambda)} \right|^2 \left| \frac{b}{2} - \frac{\sinh(2q_1 b)}{4q_1} \right|. \quad (7.11)$$

The total surface wave power,  $P_{s.w.}$  is the sum of  $P_{TM}$  and  $P_{TE}$ . The power in the free-space side of the ground plane,  $P_b$  can be obtained from the expression in Eq. 7.3 as a special case

$$P_b = \frac{k_0^4}{45} (120\pi)^2. \quad (7.12)$$

For printed slot antennas, it is important to know how the radiated powers on either side of the ground plane, and the power losses due to surface waves are affected by the substrate thickness, permittivity and/or permeability. The radiation efficiency in the upper half of the ground plane ( $z \geq 0$ ) is defined as the ratio of radiated power to total power, i.e

$$e_s = \frac{P_a}{P_a + P_{s.w.}}. \quad (7.13)$$

The powers  $P_a$ ,  $P_b$  and  $P_{s.w.}$  as a function of the substrate thickness with  $\epsilon_1 = 4$  and  $\mu_1 = 1$  are shown in Fig. 7-3, where each power component has been normalized to  $P_b$ . It is seen that, as substrate thickness increases from zero, both  $P_a$  and  $P_{s.w.}$  increase. The radiated power reaches a maximum when the first TE surface wave mode turns on. When the substrate thickness increases further, both  $P_a$  and  $P_{s.w.}$  decrease until the next surface wave mode nearly turns on. The local maximum of radiated power is due to the fact that when a surface wave mode turns on, there is a considerable amount of power

radiating along the horizon [53]. The oscillatory behavior of the surface wave variation with substrate thickness can be explained in terms of ray optics [57] and is mainly due to the constructive and destructive interference of wavefronts when rays bounce back and forth inside the substrate. In Fig. 7-4, the power distribution versus substrate thickness for  $\epsilon_1 = 12.5$  and  $\mu_1 = 1$  is shown. By comparing Fig. 7-3 and Fig. 7-4, one can see that, for a larger substrate permittivity, higher order surface wave modes turn on at smaller substrate thickness. It is also observed that materials with larger permittivity can support more surface wave power and allow more radiation. The results show that even though both radiated and surface wave power in the region  $z \geq 0$  increase with the increase of substrate permittivity, the increase of the surface wave power is more marked. The power distribution versus substrate thickness for a magnetic material  $\epsilon = 1$  and  $\mu_1 = 4$  is shown in Fig. 7-5. It is observed that for a magnetic substrate  $P_b$  is greater than  $P_a$ . Generally speaking, in printed slot structures, more power radiates in the substrate side of the ground plane ( $P_a$ ) than that in the free space side ( $P_b$ ), when the substrate is a dielectric; while the reverse is true for a magnetic material. It is also observed that the surface wave power for magnetic materials, in contrast to dielectric materials, increases even after the first TE surface wave mode turns on. The radiation efficiency versus substrate thickness is shown in Fig. 7-6. For a magnetic material, with a small substrate thickness, surface wave power increases and radiated power decreases with the increase of substrate thickness. Therefore, it is seen from Fig. 7-6 that efficiency decreases drastically versus substrate thickness for a thin substrate of magnetic material.

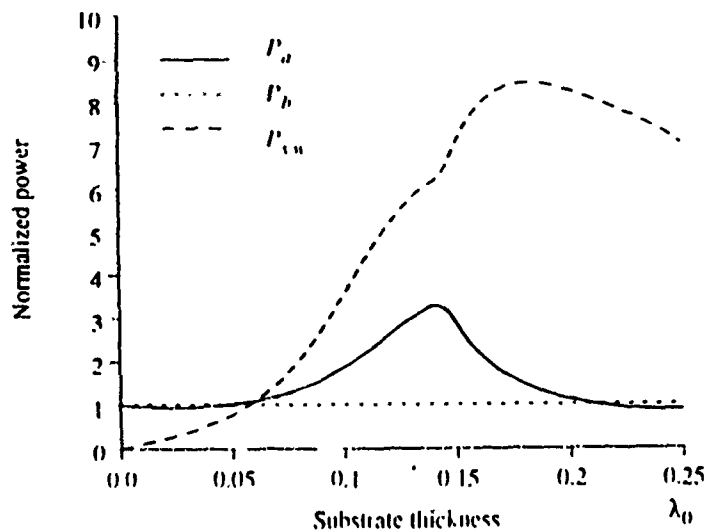


Figure 7-3. Power distribution in a printed slot structure versus substrate thickness.  $\epsilon_1 = 4$  and  $\mu_1 = 1$ .

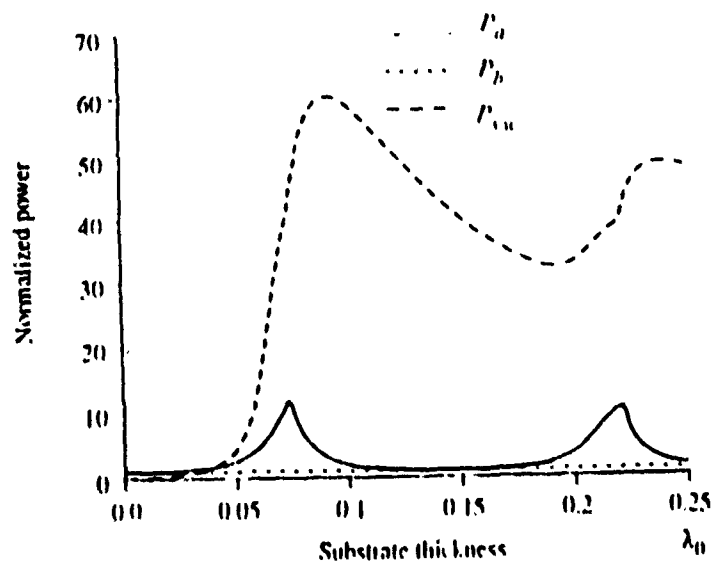


Figure 7-4. Power distribution in a printed slot structure versus substrate thickness.  $\epsilon_1 = 12.5$  and  $\mu_1 = 1$ .

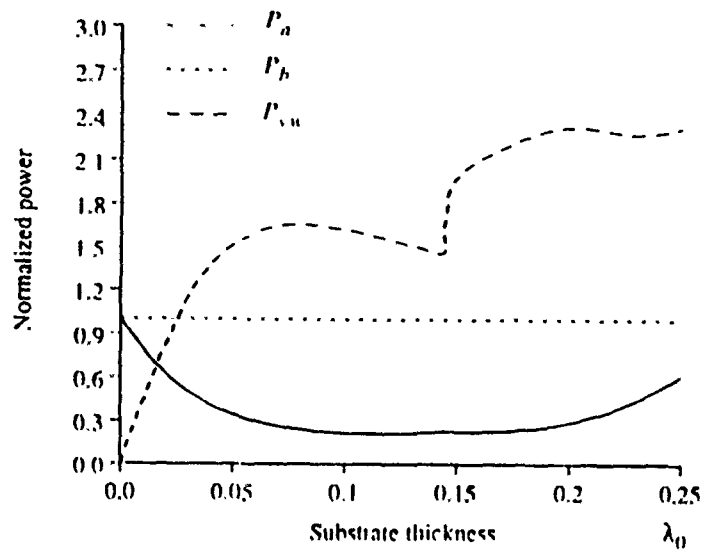


Figure 7-5. Power distribution in a printed slot structure versus substrate thickness.  $\epsilon_1 = 1$  and  $\mu_1 = 4$ .

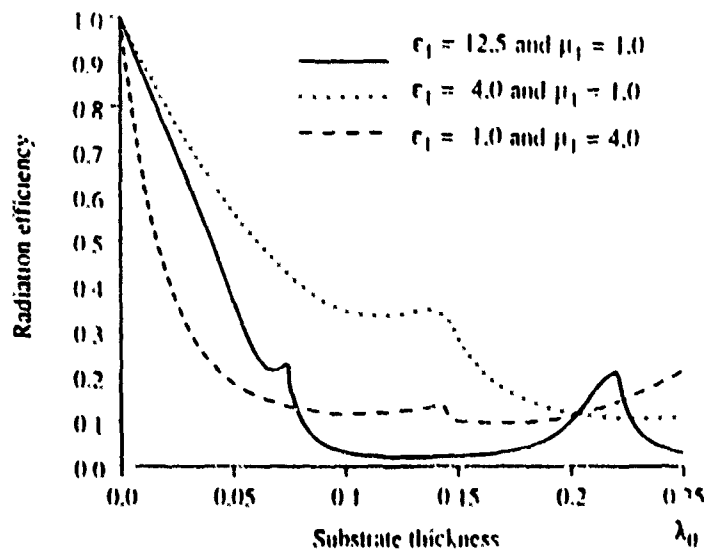


Figure 7-6. Slot radiation efficiency versus substrate thickness

For  $\mu_1 = 4$ ,  $\epsilon_1 = 1$ , less than 20% efficiency is observed when the substrate thickness is only  $0.1 \lambda_0$ .

### 7.3. A Center-fed Printed Slot

A printed slot, center-fed by an ideal  $\delta$ -gap source, is considered in this section. The geometry is shown in Fig. 7-7. A method of moments solution of integral equation is used here to study the characteristics of a slender rectangular slot. The procedure described in Chap. V for the slot can be used to obtain the following linear simultaneous equations:

$$[Y][V] = [I], \quad (7.14)$$

where  $V_1, V_2, \dots, V_N$  are the amplitudes of the expansion functions. Suppose that an odd  $N$  is used, then for a center-fed slot,

$$I_{(N+1)/2} = -1 \quad (7.15)$$

and  $I_k = 0$  for  $k \neq (N+1)/2$ . The matrix elements  $Y_{mn}$  can be formulated as

$$Y_{mn} = \int_{-\infty}^{\infty} \int_{-\infty}^{\infty} \bar{G}_m(\lambda_x, \lambda_y) J_0^2(\lambda_y w/2) A_1^2(\lambda_x) e^{j(m-n)\lambda_x d} d\lambda_x d\lambda_y \quad (7.16)$$

where

$$\bar{G}_m(\lambda_x, \lambda_y) = \frac{2}{\gamma_m} \left[ \frac{k_1^2 - \lambda_x^2}{D_m(\lambda)} f_m(\lambda) + \frac{q_1(1 - \epsilon_1)\lambda_x^2}{D_m(\lambda) D_e(\lambda)} + \frac{k_0^2 - \lambda_x^2}{q} \right], \quad (7.17)$$

$$f_m(\lambda) = \cosh q_1 b + \epsilon_1 \frac{q}{q_1} \sinh q_1 b. \quad (7.18)$$

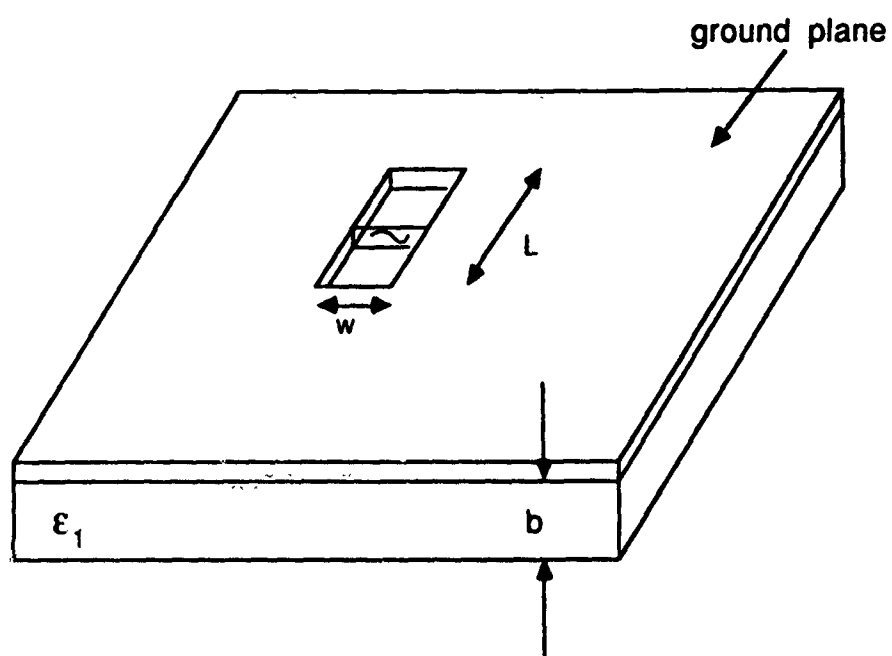


Figure 7-7. A center-fed printed slot.



and  $A_1(\lambda_x)$  is the Fourier transform of the PWS expansion mode. The method of computing Eq. 7.16 has been discussed in the previous chapters. The input admittance is defined as

$$Y_{in} = G_s + j B_s = \frac{1}{V_{(N+1)/2}} \quad (7.19)$$

Based on the above analysis, the input admittance of a center-fed slot is examined as a function of various structure parameters. In Fig. 7-8, the input admittance versus slot length is shown with two different material permittivities. It is observed from Fig. 7-8 that when the permittivity increases, the slot resonant length decreases and resonant resistance increases. The center-fed slot bandwidth (BW) can be defined [46] as

$$BW = \frac{1}{L_r} \frac{2G_r}{\left(\frac{dB}{dL}\right)_{L_r}} \quad (7.20)$$

It is found from Fig. 7-8 that with  $b = 0.02\lambda_0$  and  $w = 0.01\lambda_0$ , when  $\epsilon_1$  increases from 2.2 to 5.0, the bandwidth (BW) decreases from 21.5% to 13.2%. The input admittance versus slot length with two different substrate thickness is shown in Fig. 7-9. It is observed that increase of the substrate thickness decreases the resonant length, the resonant resistance and the bandwidth. The effect of slot width on the input admittance is shown in Fig. 7-10. It is found that the increase of slot width causes the slot resonant length and resonant resistance to decrease and the bandwidth to increase.

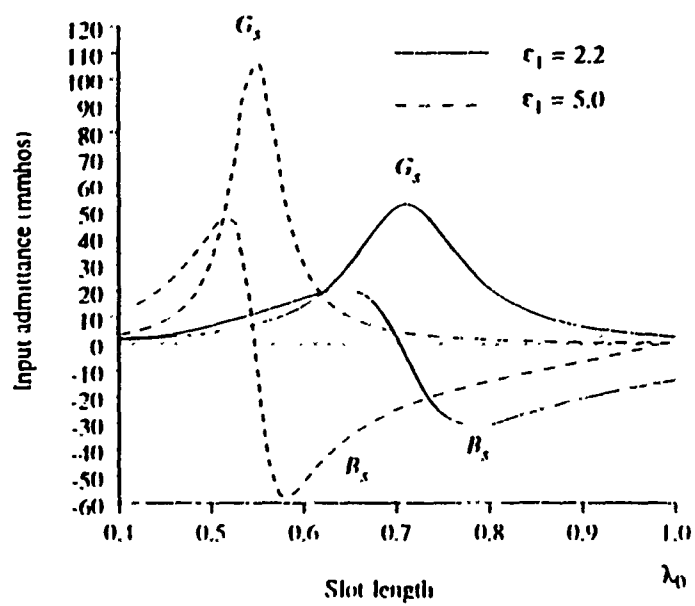


Figure 7-8. Input admittance of a center-fed printed slot versus slot length.  
 $b = 0.02\lambda_0$  and  $w = 0.01\lambda_0$ .

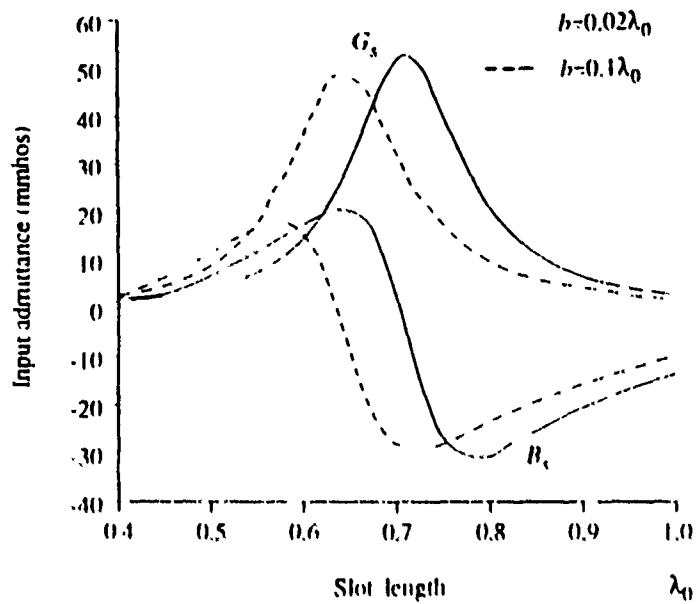


Figure 7-9. Input admittance of a center-fed printed slot versus slot length.  
 $\epsilon_1 = 2.2$  and  $w = 0.01\lambda_0$ .

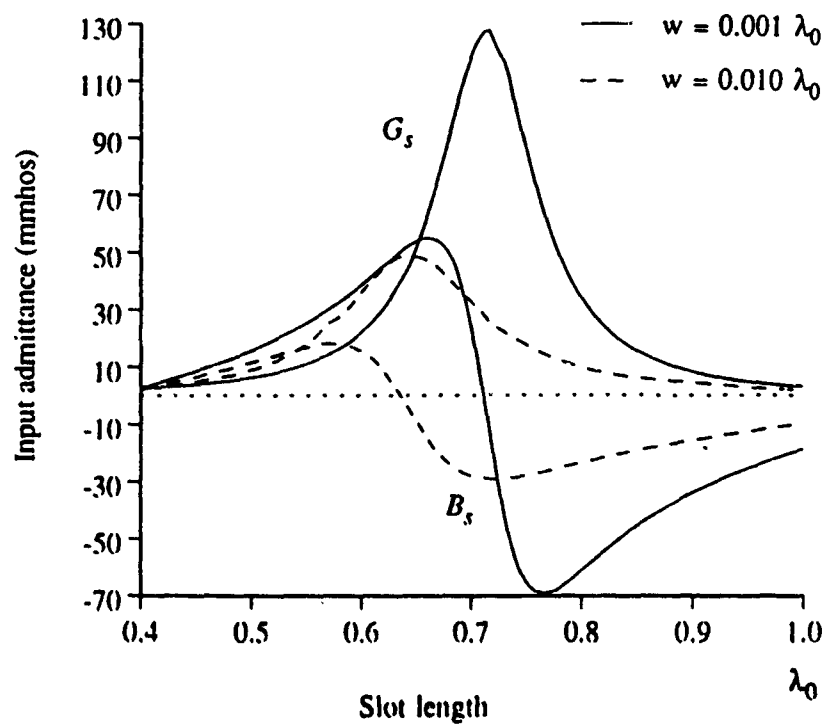


Figure 7-10. Input admittance of a center-fed printed slot versus slot length.

$\epsilon_1 = 2.2$  and  $b = 0.1\lambda_0$ .

## Chapter VIII

### Printed Antenna Feeding Structures

#### 8.1. Introduction

The design of feeding structures is one of the most important parts in the design of printed circuit antennas. Since the geometry of printed circuit antennas involves grounded substrates, the design of feeding networks usually requires integrated circuit technology. For monolithic phased array applications, the transition from feeding networks to radiating elements is the key to the success of the design. Classical feeds of printed circuit antennas contain either a microstrip transmission line in physical contact with the radiating elements or a coaxial line penetrating through the ground plane [81], [28]. In the former case, feed and antenna together form a resonator. Due to the high  $Q$  of this type of resonator, the bandwidth is very narrow. Undesired spurious radiation at the microstrip-antenna junction may also be a serious problem. The probe fed microstrip antenna is not suitable for millimeter wave or monolithic applications mainly due to the presence of the probe.

To overcome the disadvantages of classical feeds, a new feed-antenna arrangement using electromagnetic coupling (EMC) has been proposed [81], [56]. In this type of structure, there is no physical connection between feed lines and radiating elements. The microstrip line can be very close to the ground plane to reduce spurious radiation and the antenna is away from the ground plane to increase the bandwidth. GaAs substrate ( $\epsilon_1 = 12.8$ ) is very suitable for active devices, but its dielectric constant is too high for radiating

elements when efficiency and bandwidth are considered. EMC antenna structures are excellent for these monolithic phased array applications, where active devices can be printed on a GaAs substrate and antennas on a low permittivity superstrate. The architectures using EMC antennas in layered configurations seem to be the ultimate choice for monolithic phased arrays.

The EMC collinear dipole has been extensively studied in the past few years [59], [60], [42], [43]. In this chapter, four EMC antenna feeding structures are discussed. These include a microstrip fed slot, a slotline fed dipole, an EMC transverse dipole and a microstrip fed slot coupled dipole. These structures have the common feature that a string of the antenna element above a common feed line becomes a linear array. The analyses discussed in Chaps. V and VI may also be used to study the printed circuit antenna structures. The features of the four feeding structures together with numerical results will be discussed in Sections 8.2-8.5.

## **8.2. A Microstrip Fed Slot**

The radiation characteristics of a printed slot antenna were discussed in the last chapter. The features of the slot antenna as compared to the strip dipoles are that it is broadband and gives bidirectional radiation. A simple way to design its feeding structure is to use a microstrip line electromagnetically coupled to the transverse slot, as shown in Fig. 8-1. The analysis of this structure has been reported using an equivalent circuit model [82], a waveguide model [83], and via reciprocity [84]. However up to now there are no rigorous results available. In this section, a rigorous result based on solving an exact

integral equation by the method of moments is presented. The equivalent circuit of a slender rectangular slot perpendicular to the microstrip is a series element. In order to understand the property of the slot, the equivalent circuit as a function of various device parameters should be investigated. The normalized equivalent resistance and reactance as a function of slot length are shown in Figs. 8-2 and 8-3 respectively, for two different substrate dielectric constants. It is observed that for a fixed substrate thickness, the resonant length decreases and maximum coupling (resonant resistance) increases with the increase of the substrate permittivity. These phenomena are due to the fact that the increase of substrate permittivity will decrease the effective substrate thickness (effective distance between microstrip and slot) and decrease the effective length of the structure; as a result, the resonant length decreases and maximum coupling increases. It is also seen that for smaller substrate permittivity, the equivalent circuit is less sensitive to the change of the structure parameters.

Fig. 8-4 shows the Smith chart plot of the equivalent impedance of the slot as a function of offset ( $\delta$ ) for three different slot lengths. The offset  $\delta$  is defined as the distance between the center of the slot and the center of the microstrip line. It is observed that the coupling between the slot and the microstrip line decreases monotonically as offset increases. It is interesting to see that, for small offset, the impedance is insensitive to the offset change. This implies that the alignment between the slot and the microstrip line is less critical than for EMC dipoles [60], where the offset control is very important to the accuracy of a design.

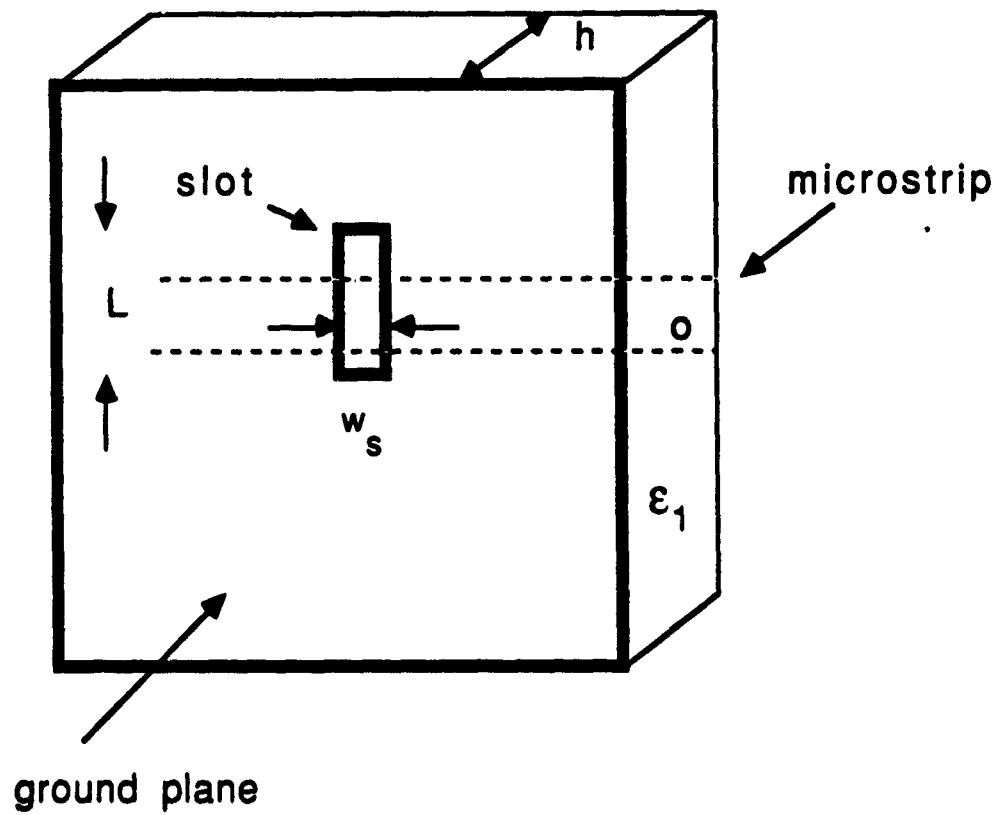


Figure 8-1. A microstrip fed slot.

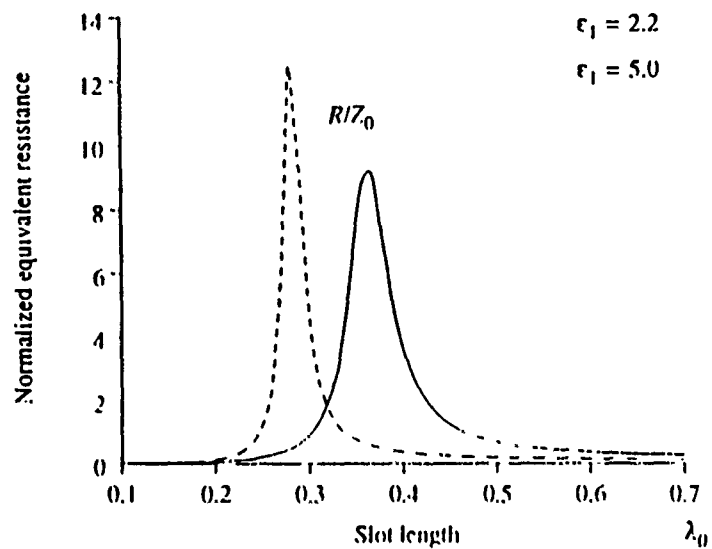


Figure 8-2. Normalized resistance of a 50Ω microstrip fed slot.  
 $h = 0.02\lambda_0$  and  $w_s = 0.01\lambda_0$ .

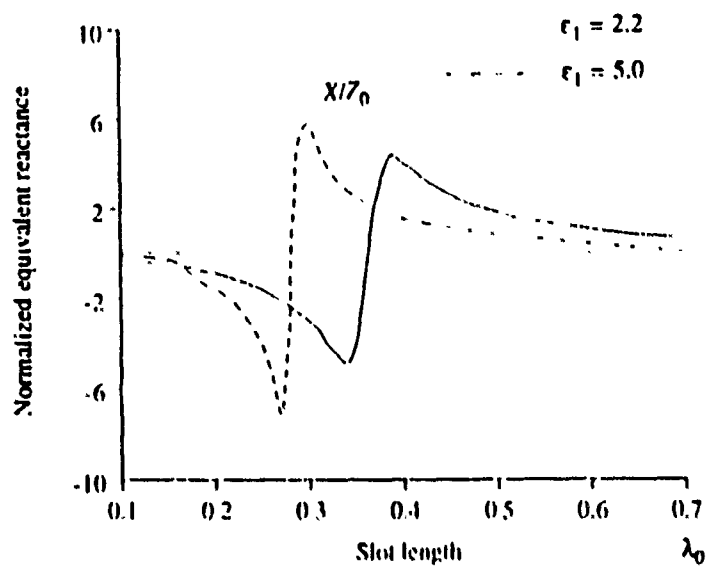


Figure 8-3. Normalized reactance of a 50Ω microstrip fed slot.  
 $h = 0.02\lambda_0$  and  $w_s = 0.01\lambda_0$ .



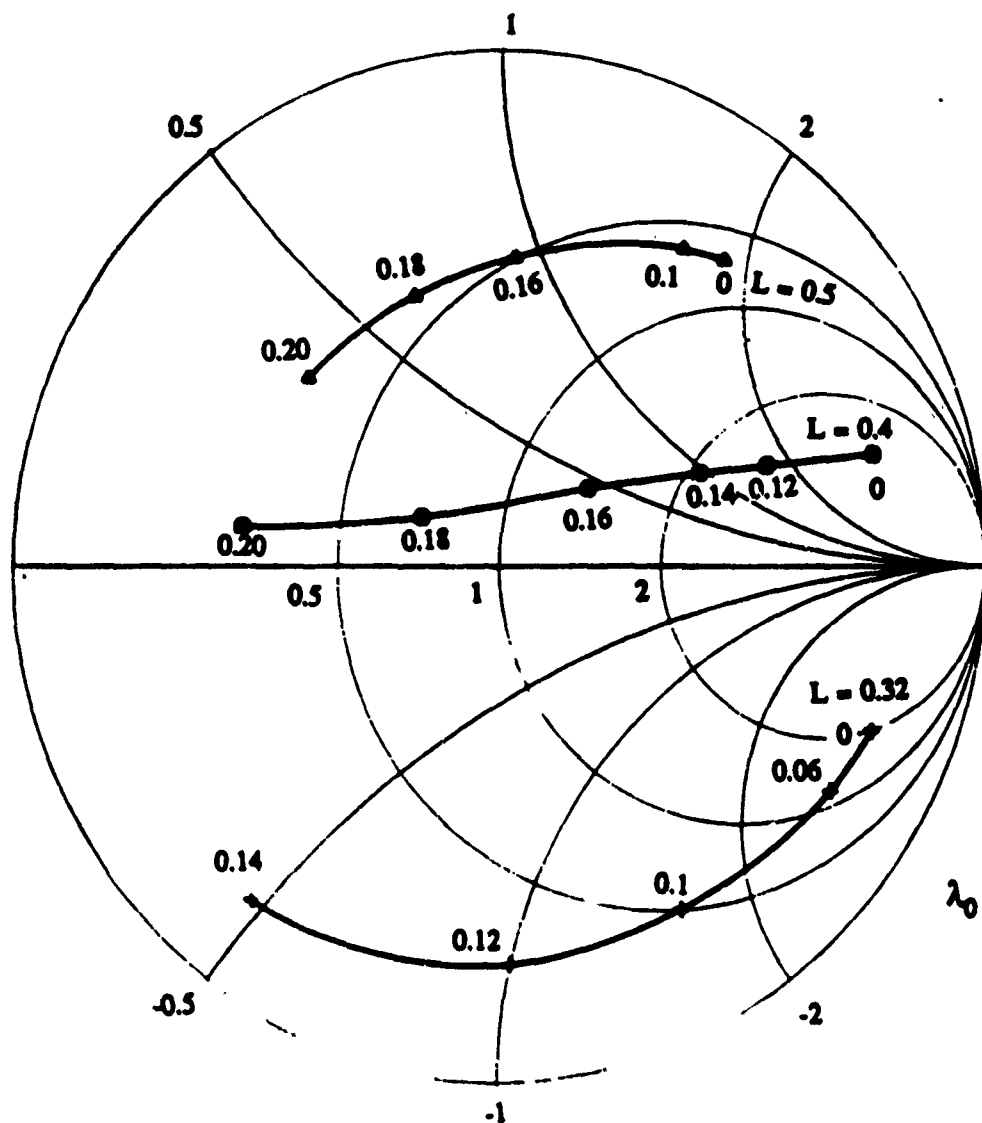


Figure 8-4. Smith chart plot of the impedance of a microstrip fed slot versus offset.

$\epsilon_1 = 2.2$ ,  $h = 0.02\lambda_0$ ,  $w_s = 0.01\lambda_0$  and  $w_m = 3.125h$ .

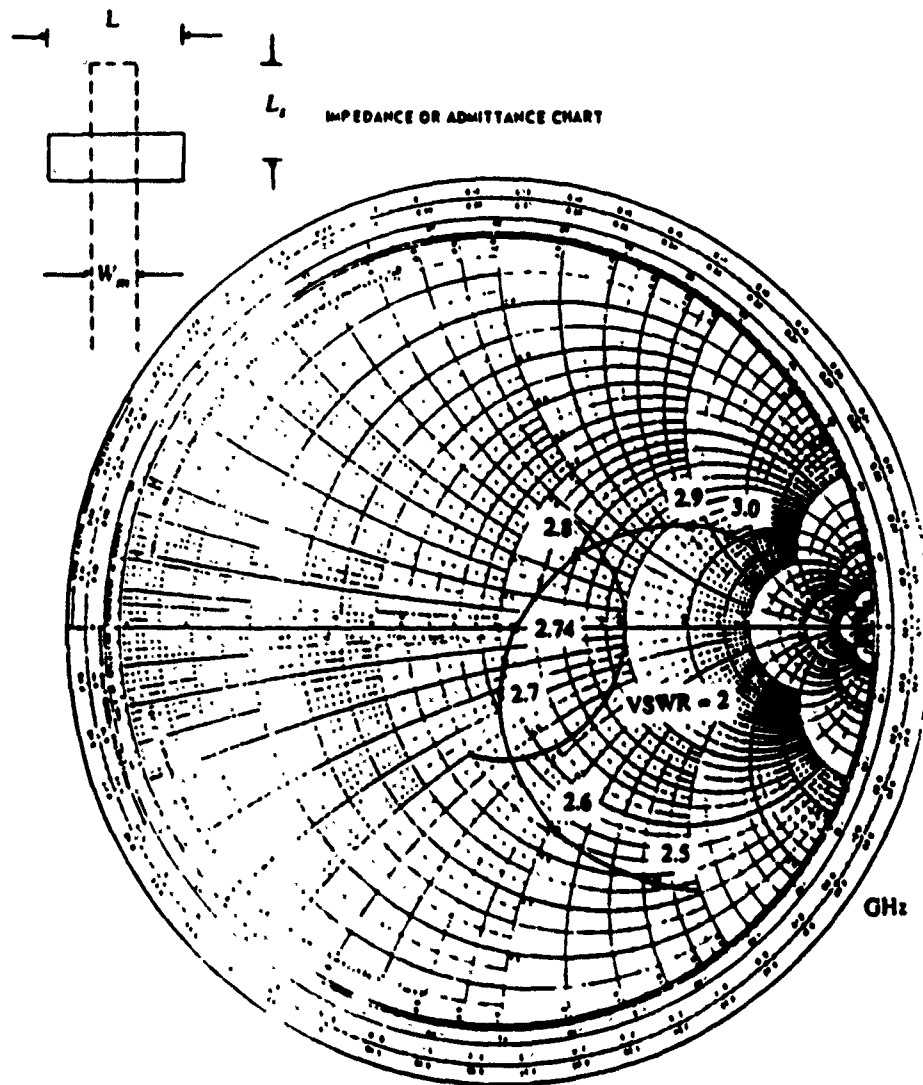


Figure 8-5. Input impedance of a stub-tuned slot fed by a microstripline.

$\epsilon_r = 2.2$ ,  $d = 0.2032$  cm,  $W_m = 0.635$  cm,  $W_s = 0.1016$  cm,  $L = 4.0$  cm  
and stub length = 0.22 cm.

The input impedance of a stub-tuned slot obtained from information above the reflection coefficient in the microstrip line is shown in Fig. 8-5 as a function of frequency. It is seen that the bandwidth is mainly determined by the tuning stub since the resistance is quite insensitive to the frequency. Therefore, to increase the bandwidth, the stub length should be chosen such that at the resonant frequency the change of stub impedance with frequency is as small as possible. Another way to increase bandwidth is to control the device parameters such that resonance occurs even without the tuning stub. Fig. 8-5 shows a typical example for this design where the bandwidth is 6% with a stub length  $\simeq 0.02\lambda_0$ . The bandwidth will also increase if the slot width is enlarged.

### 8.3. A Slot Line Fed Dipole

A new feeding structure for printed dipole antennas is shown in Fig. 8-6, where a slot line is etched in the ground plane, and excites a printed dipole through proximity coupling. In order that the slot line be an effective waveguiding structure, the substrate permittivity should be large ( $> 10$ ) to confine energy along the slot. The equivalent circuit of the dipole seen by the slot line is a shunt element. An example of this result as a function of dipole length with GaAs substrate ( $\epsilon_1 = 12.8$ ) is shown in Fig. 8-7. It is observed that the admittance changes more quickly with antenna length than for printed slots. The equivalent admittance of a dipole as a function of frequency is shown in Fig. 8-8 for a substrate with  $\epsilon_1 = 12$ . It is observed that the admittance changes drastically for a small change of frequency. This antenna structure is inherently narrow band. Another problem is that the efficiency of the antenna

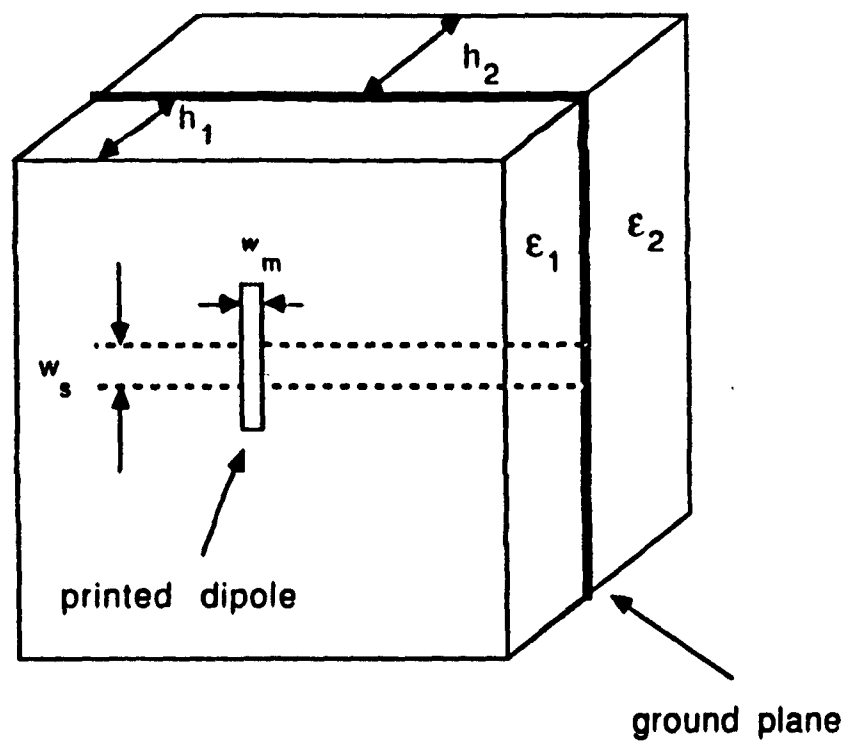


Figure 8-6. A slot line fed printed dipole.  
Dipole length:  $L$ .

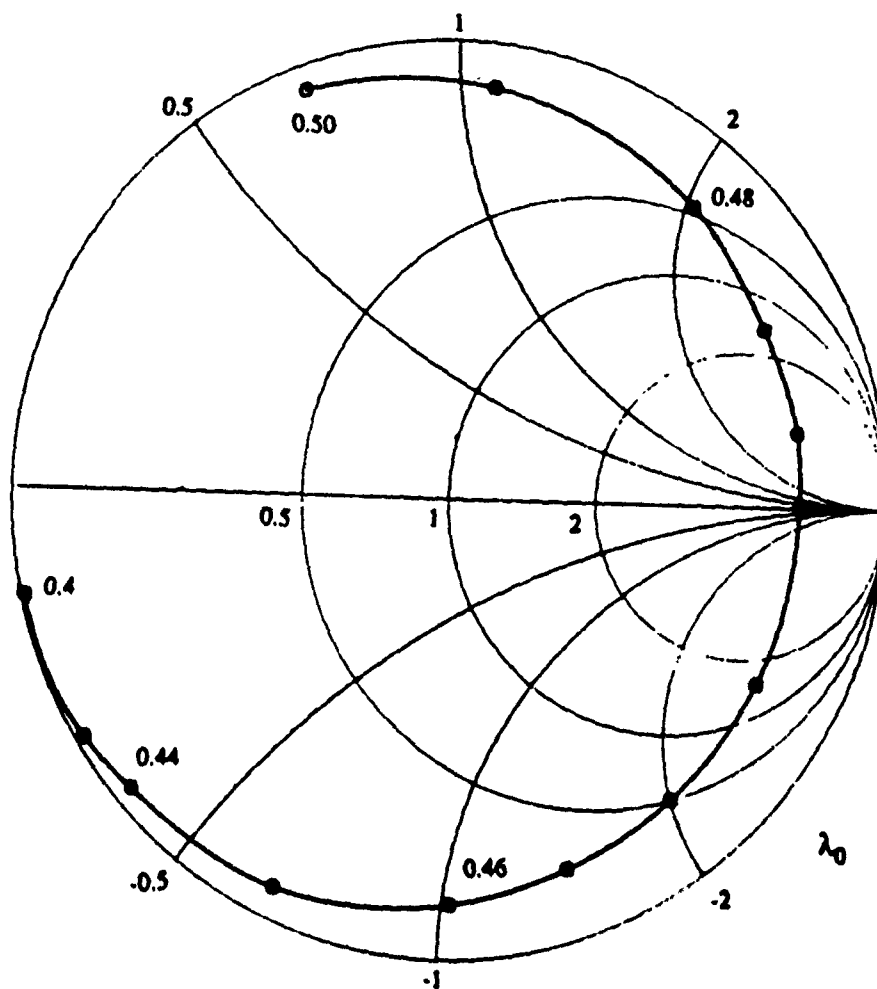


Figure 8-7. Normalized admittance of a slot line fed dipole  
versus dipole length.  $\epsilon_1 = 12.8$ ,  $h = 0.02\lambda_0$ ,  $w_s = 0.01\lambda_0$  and  $w_m = h$ .

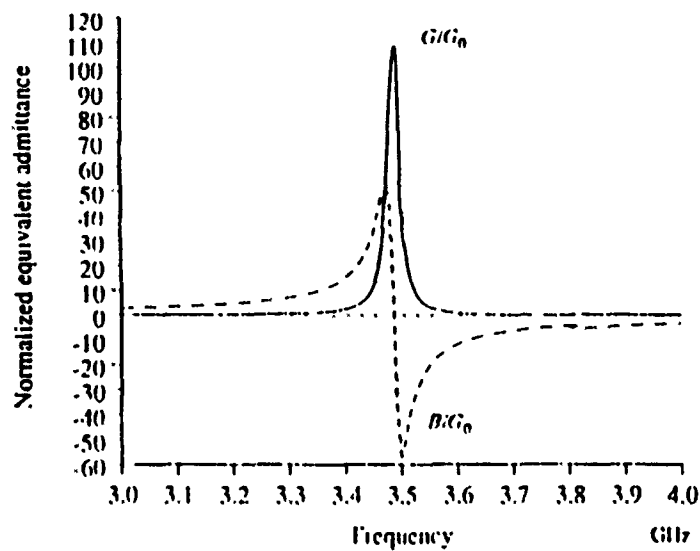


Figure 8.8 Normalized admittance of a slot line fed dipole versus frequency.

$\epsilon_1 = 12$ ,  $h = 0.121$  in,  $w_1 = 0.562h$ ,  $w_m = h$  and  $L = 1.6$  cm.

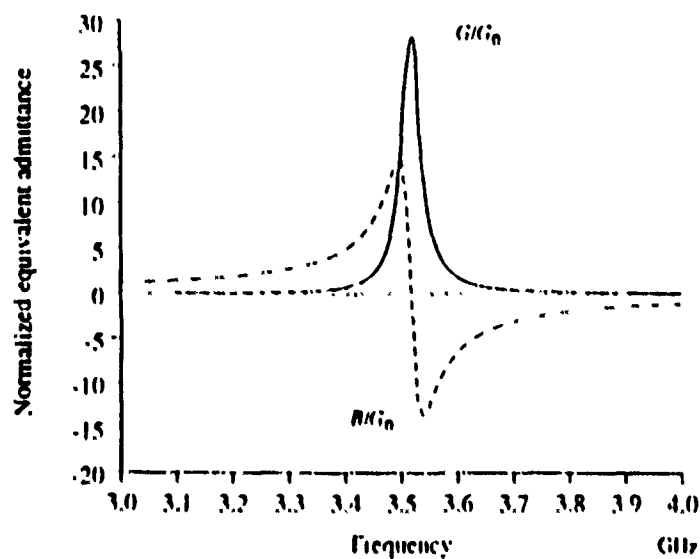


Figure 8.9. Normalized admittance of a slot line fed dipole versus frequency.

$\epsilon_1 = 2.54$ ,  $\epsilon_2 = 12$ ,  $h_1 = h_2 = 0.121$  in,  $w_1 = 0.562h$ ,  $w_m = h_1$  and  $L = 3$  cm.

is small for a large substrate permittivity. To overcome these disadvantages, dipoles can be printed in a low permittivity substrate and at the same time a high permittivity substrate can be used on the other side of the ground plane to confine energy near the slot line. This type of slot line sandwich structure has been discussed in Chap. IV. Another advantage of this structure is that, for monolithic applications, active devices can be made on a GaAs substrate and isolated from the antenna elements by a ground plane. This type of architecture can reduce spurious radiation due to active devices. An example of the results of the equivalent admittance of a dipole in a two-side slot line structure is shown in Fig. 8-9. The results are for the case when the dipole is printed on the substrate with  $\epsilon_1 = 2.54$ , while the other substrate is  $\epsilon_2 = 12$ . From the results in Figs. 8-8 and 8-9, it is seen that bandwidth is indeed improved by using a slotline sandwich. It should also be mentioned that the radiation and surface wave losses due to the feedline may also be reduced by using a slot line sandwich.

#### 8.4. An EMC Transverse Dipole

A dipole that is electromagnetically coupled to microstrip, but oriented transverse to the microstrip, as shown in Fig. 8-10, is one of the printed antenna feeding structures proposed by Oltman [56]. One of the features of this EMC transverse dipole is the light coupling between the dipole and the microstrip line. Therefore, it is fairly well suited for radiating element in large antenna array. A theoretical and experimental investigation of this EMC transverse dipole has been reported in [77].

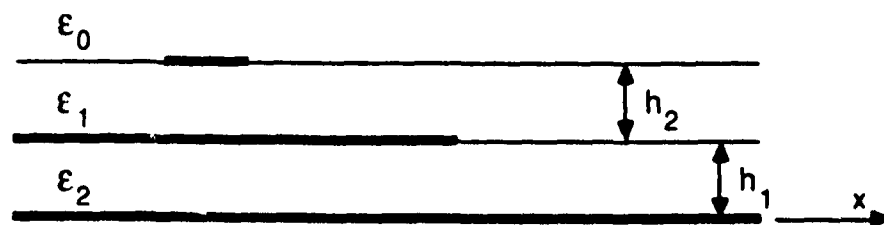
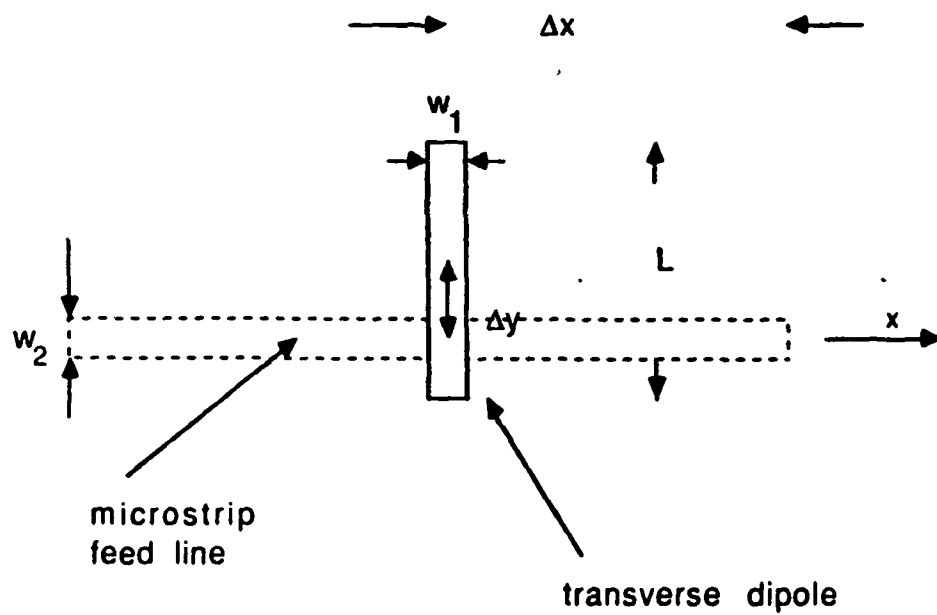


Figure 8-10. The electromagnetically coupled transverse dipole.



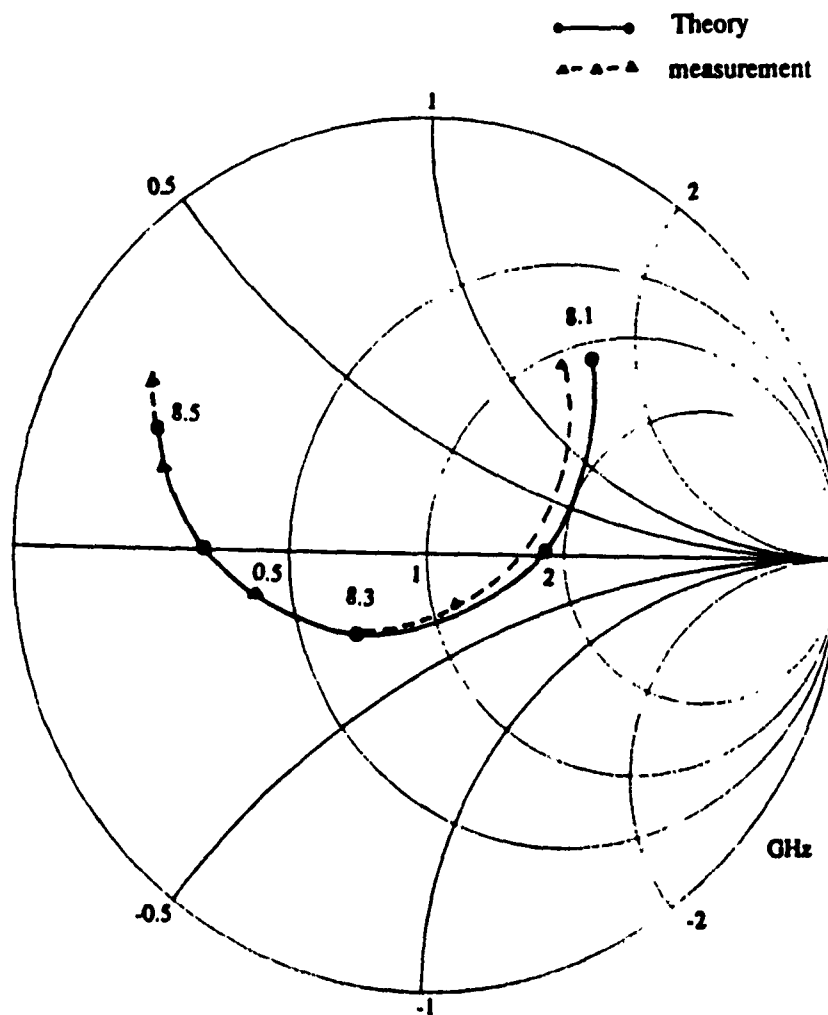


Figure 8-11. Comparison between theoretical and experimental results for the input impedance of an EMC transverse dipole.

$\epsilon_1 = 2.17$ ,  $\epsilon_2 = 2.17$ ,  $h_1 = h_2 = 0.8$  mm,  $w_1 = 1$  mm,  $w_2 = 2.2$  mm,  
 $\Delta x = 0$ ,  $\Delta y = 4.5$  mm and  $L = 12.4$  mm.

In the next chapter, array designs of this antenna architecture will be discussed. In order to check the analysis of this work, the result of the present analysis is compared against the experimental results presented in [77]. The comparison is shown in Fig. 8-11. It is found that the agreement is quite satisfactory.

### **8.5. A Microstrip Fed Slot Coupled Dipole**

A common problem for the antenna architectures discussed in the last few sections is that the feed line and radiating elements are on the same side of the ground plane, and spurious radiation due to the transmission line can not be eliminated completely. In millimeter wave applications, feed line radiation may cause severe cross polarization. A nice way to alleviate this difficulty is to use a two-sided structure, as shown in Fig. 8-12, where any radiation due to the feeding network and active devices is isolated from the antenna by a ground plane [85], [86]. The dipole is actually fed by a secondary source, namely a slot in the ground plane. This type of aperture-coupled antenna architecture seems to be a promising candidate in millimeter wave monolithic phased array applications. Since the combination of a slot and a dipole provides sufficient degrees of freedom, the dipole is centered to the slot and the slot is centered to the microstrip line. Also, since the main radiation comes from the dipole, the slot length can be chosen far below its resonant length. The equivalent circuit of a slot coupled dipole seen by the microstrip line is a series element. An example of this equivalent circuit as a function of dipole length for two different slot lengths is shown in Fig. 8-13. It is observed that

the increase of slot length will decrease the dipole length to obtain resonance. This is because when the dipole length decreases, resonance will be due to the resonance of the slot, whereas when the slot length decreases, the resonance will be due to the resonance of a center-fed dipole. It is also observed that the resonant resistance is larger for larger slot length.

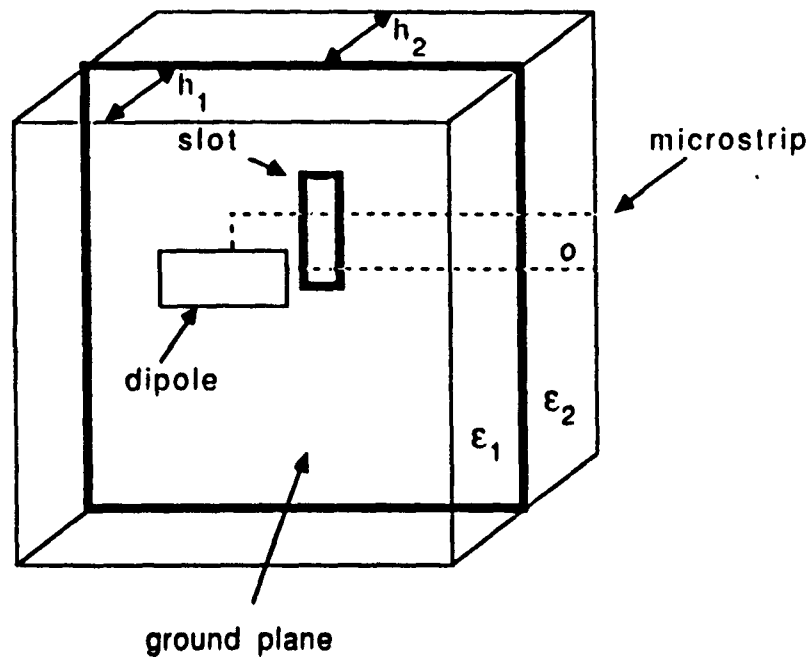


Figure 8-12. A microstrip fed slot coupled dipole.

Microstrip line width:  $w_m$ , slot length:  $L_s$ ,  
slot width:  $w_s$ , dipole length:  $L_d$  and  
dipole width:  $w_d$

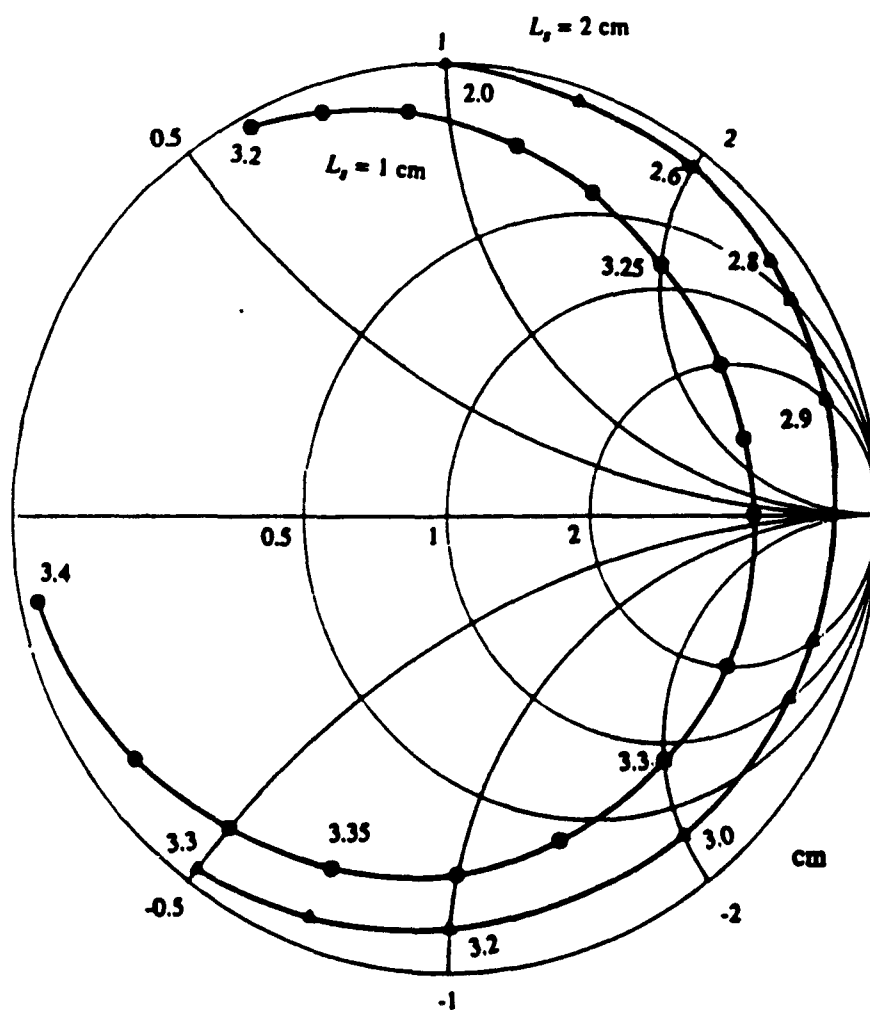


Figure 8-13. Normalized impedance of a microstrip fed slot coupled dipole versus dipole length.  $\epsilon_1 = \epsilon_2 = 2.54$ ,  $f = 3$  GHz,  $h_1 = h_2 = 1.6$  mm,  $w_s = 1$  mm,  $w_m = 4.45$  mm,  $w_d = h_1$ .

## **Chapter IX**

### **Design of Transversely Fed EMC Microstrip Dipole Arrays Including Mutual Coupling**

#### **9.1 Introduction**

Oltman introduced a class of electromagnetically coupled (EMC) dipole antennas [81], [56]. The advantages of EMC dipoles are greater bandwidth, higher efficiency and more easily matched to the feed lines, when compared to classically fed printed antennas. Based on the transmission line circuit model, Oltman and Huebner [56] built a longitudinal EMC dipole array. Later, Elliott and Stern developed a rigorous design theory to include the effects of mutual coupling which successfully predicted the array performance [59], [60]. An efficient way to obtain the design curves was reported later [42], [87] based on solving a Pocklington type integral equation using the method of moments. The EMC collinear dipole is ideally suited to a corporate feed, and elements of this type can be arranged in circular as well as rectangular grids.

Another dipole antenna of the Oltman type is the EMC transverse dipole, as shown in Fig. 9-1, where a dipole is oriented transverse to an embedded microstrip line. A string of these dipoles above a common microstrip line becomes a linear array. Depending on dipole spacing, one can obtain standing wave arrays or traveling wave arrays. A family of these linear arrays becomes a planar array. Current excitation on the dipole is governed by the amount

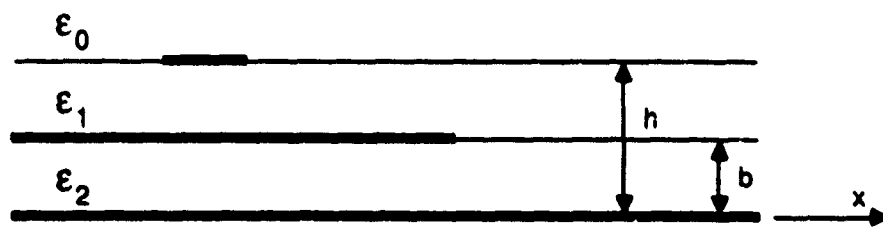
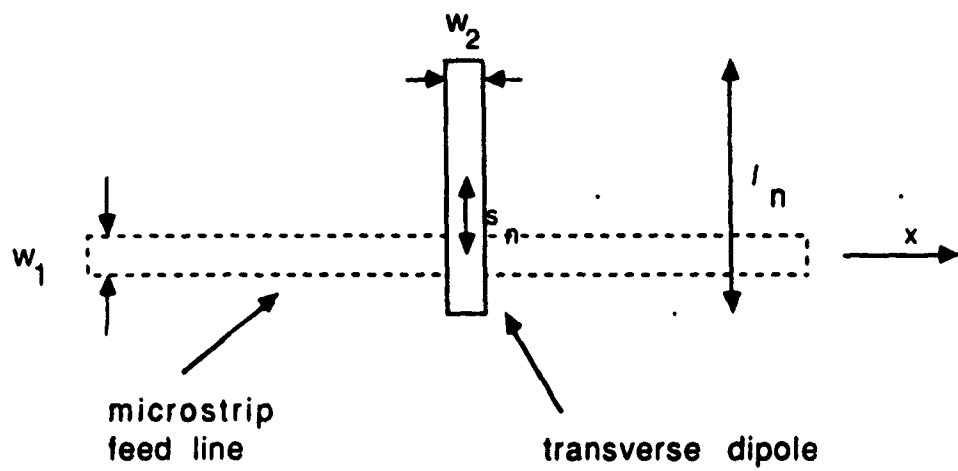


Figure 9-1. The electromagnetically coupled transverse dipole.

of offset and the dipole length. If the dipole straddles symmetrically, no excitation of the dipole occurs. Light coupling from line to dipole can be achieved through a slight lateral displacement of the dipole from its balance position. Because of this light coupling, large arrays are feasible [88].

Both theoretical and experimental studies of the EMC transverse dipole are reported recently [77]. In this chapter, a design technique which includes mutual coupling is developed for the EMC transverse dipole arrays. Two design equations will be introduced in Section 9.2. The methods for generating design curves will be discussed in Section 9.3. A design example will be given in Section 9.4 together with the experimental results. A numerical verification of the design by solving the boundary value problem of the whole array system will also be provided.

## 9.2. Two Design Equations.

For the transverse EMC dipole under consideration, it can be shown from image theory that the scattering off the dipole is symmetric. In other words, the forward and backward scattering coefficients are the same. Therefore, in terms of the transmission line equivalent circuit, the dipole can be approximated as a shunt element with respect to the feed [61]. Each dipole in the array environment can then be modelled as a two port network and the whole system is a linear bilateral network [59]. Therefore, one can write

$$I_n = \sum_{m=1}^N V_n Y_{mn} \quad (9.1)$$



as a set of equations connecting the transmission line mode voltages and currents at each reference port [61]. The active admittance of each dipole seen by the feed line can be defined from Eq. 9.1 by

$$\begin{aligned} Y_n^a &= \frac{I_n}{V_n'} \\ &= Y_{nn} + Y_n^b \end{aligned} \quad (9.2)$$

where

$$Y_n^b = \sum_{m=1}^N, \left( \frac{V_m'}{V_n'} \right) Y_{mn}, \quad (9.3)$$

with the prime on  $\sum$  indicating the term  $n = m$  is excluded.  $Y_{nn}$  is the self-admittance and  $Y_n^b$  is referred to as the mutual admittance due to the mutual coupling between each dipole. Since a linear system is assumed, the current in each dipole can be written as

$$\frac{I_n^{rad}}{V_n'} = \frac{I_{nn}}{V_n'} + \sum_{m=1}^N, \frac{I_{mn}}{V_n'} \quad (9.4)$$

where  $I_{nn}$  is the current of the  $n$ th dipole for a given mode voltage without the presence of other dipoles and  $I_{mn}$  is the current of the  $n$ th dipole due to the current in the  $m$ th dipole. The isolated dipole current  $I_{nn}$  is a function of mode voltage, dipole length and offset which can further be written as

$$\frac{I_{nn}}{V_n'} = \frac{Y_{nn}}{f_n(s_n, l_n)} \quad (9.5)$$

where  $f_n(s_n, l_n)$  is a coefficient function relating the isolated dipole current to its self-admittance.

The two design equations can be summarized from the above derivations by

$$\frac{I_n^{rad}}{V_n} = \frac{Y_{nn}}{f_n} + \sum_{m=1}^N \frac{I_{mn}}{V_n} \quad (9.6)$$

and

$$Y_n^a = Y_{nn} + \sum_{m=1}^N \frac{V_m}{V_n} Y_{mn}. \quad (9.7)$$

It is noted that, for the EMC tranverse dipole, the current phase variation in an isolated dipole is quite large, typically 5 to 10 degrees; while, in contrast, the current due to mutual coupling has a small phase variation. Therefore, in the design, the coefficient function is not suitable for relating mutual current ( $I_{mn}$ ) and mutual admittance ( $Y_{mn}$ ). One can use the mutual current term ( $I_{mn}$ ) directly in Eq. 9.6.

The fundamental design problem is now obvious. For a given design goal (radiating current in each dipole  $I_n^{rad}$ ) one wishes to find N set of  $(s_n, l_n)$  such that not only Eq. 9.6 is satisfied but also the active admittance seen by each feed line is what was prescribed. The definition of the radiating current in each dipole may depend on the design goal. For example, if one wishes to design a specific pattern in the H plane (perpendicular to the dipole), the  $I^{rad}$

should be defined as the current collapsed in the feed line [61]. In other words,

$$I_n^{rad} = \int_0^{l_n} I_n(y) dy. \quad (9.8)$$

In the two design equations in Eqs. 9.6 and 9.7,  $Y_{nn}$ ,  $f_n$ ,  $I_{mn}/V_n$  and  $Y_{mn}$  can be determined by the method of moments. This issue will be discussed in the next section.

Suppose that all four functions are known. Further computations are still required to find the dipole lengths and offsets. Since only relative currents in the dipoles are meaningful, one can arbitrarily choose a dipole, say the  $n$ th, with length  $l_n$  and offset  $s_n$ . For the moment, assume that no mutual coupling exists such that the left hand side of Eq. 9.6 can be determined according to the design goal (desired currents in the dipoles). One now can use the first design equation (Eq. 9.6) to find  $N-1$  dipole lengths and offsets. This procedure requires that a two-variable nonlinear equation be solved  $N-1$  times. To avoid the stability and solvability problem of this nonlinear equation, the conjugate gradient method [89] can be used to provide optimized solutions. Even if the above procedures are completed, a few iterations by changing the dipole length or offset of the first selected dipole are required to provide the prescribed input impedance. Now the design data is what one should obtain if no mutual coupling exists. To include the effect of mutual coupling, one can use the present design data to compute the mutual admittance and mutual currents and go back to the two design equations repeating the above iter-

ations. The whole procedure is iterated until the convergence of the design data is found.

### 9.3. Discussion of the Method of Moments Solution

In order to make an accurate design possible, information about the interaction between dipoles as well as dipole coupling to the feed line is required. The method of moments provides a rigorous and accurate solution. Integral equations for the EMC transverse dipole can be written as

$$E_x(x, y) = \iint G_{xx} J_x^{(1)}(x', y') dx' dy' + \iint G_{xy} J_y^{(2)}(x', y') dx' dy' \quad (9.9)$$

and

$$E_y(x, y) = \iint G_{yx} J_x^{(1)}(x', y') dx' dy' + \iint G_{yy} J_y^{(2)}(x', y') dx' dy' \quad (9.10)$$

where  $J_x^{(1)}(x', y')$  is the current in the microstrip line and  $J_y^{(2)}(x', y')$  is the current in the dipole. The functions  $G_{xx}$ ,  $G_{xy}$ ,  $G_{yx}$  and  $G_{yy}$  are the dyadic Green's function components. A nice way of modeling the feed line is to use a finite but long microstrip line with a  $\delta$ -gap generator placed far from the line-dipole coupling region [42], [43]. When the combination of piecewise sinusoidal and Maxwell current basis functions is used in the method of moments [42], [43] followed by the Galerkin procedure, the matrix equations

$$[Z_{mn}][I_n] = [E_n] \quad (9.11)$$

can be obtained. The excitation column vector  $E$  has components  $E_k = -1$  when the  $\delta$  gap source is located at the center of the  $k$ th basis function, and  $E_n = 0$  anywhere else. The impedance matrix elements are in the form of

$$Z_{mn} = \int_0^{\pi/2} \int_0^\infty [(k^2 - \lambda_x^2) f(\lambda) + \lambda_x^2 h(\lambda)] \bar{J}_n(\lambda_x, \lambda_y) \bar{J}_m(\lambda_x, \lambda_y) \cos(\lambda_x \Delta x) \cos(\lambda_y \Delta y) d\lambda d\phi \quad (9.12)$$

when the  $m$ th and the  $n$ th basis functions are both on the dipole or on the line, and

$$Z_{mn} = \int_0^{\pi/2} \int_0^\infty \lambda_x \lambda_y [f(\lambda) - h(\lambda)] \bar{J}_n(\lambda_x, \lambda_y) \bar{J}_m(\lambda_x, \lambda_y) \sin(\lambda_x \Delta x) \sin(\lambda_y \Delta y) d\lambda d\phi, \quad (9.13)$$

otherwise. The functions  $\bar{J}_n(\lambda_x, \lambda_y)$  and  $\bar{J}_m(\lambda_x, \lambda_y)$  are the Fourier transforms of the expansion and testing functions respectively.  $(\Delta x, \Delta y)$  is the displacement vector of two basis function centers,

$$\lambda_x = \lambda \cos \phi \quad (9.14)$$

and

$$\lambda_y = \lambda \sin \phi. \quad (9.15)$$

The function  $f(\lambda)$  and  $h(\lambda)$  are related to the Hertz potential described in Chap. II. The unknown currents in the feed line or the dipole can be obtained by matrix inversion. As a result, one can use the unimode transmission line theory to deduce the circuit information from the method of moments solution of the current in the feed line. This procedure involves finding the current maxi-

mum, minimum and their positions. Detailed procedures of this are shown in [42]. It is noted that in order to find the dipole equivalent admittance, the dipole can be placed a half electrical wave length from the line end such that the stub admittance will not be included in the input admittance observed by the feed line.

One of the features of using  $\delta$  gap source is that the mode voltage of the line changes with the change of the dipole length or offset; therefore care must be taken to find this mode voltage, since as shown in Eq. 9.6, dipole current is proportional to the mode voltage and only their ratio is useful in the design.

Another feature of using the moment method in the array design is that the information about the currents in the dipoles can be obtained from the numerical process. This aspect is particularly helpful, since one can use the dipole current directly to design for the desired excitation instead of using the equivalent circuit of the dipoles. This will be discussed further in the next section. Other issues in this array design are how the mutual coupling information can be separated from that of the self term and how this can be achieved without involving the whole system at the same time. In order to solve these problems, certain assumptions are necessary. It is assumed that the self admittance and self current to mode voltage ratio will not change with or without the presence of other dipoles, and that the mutual coupling between any two dipoles is unaffected by the rest. These two assumptions are good if mutual coupling is not too strong [61], which is usually true for practical arrays.

The method of computing mutual coupling of dipoles individually fed by a microstrip line has been discussed in [87]. One of the features of the array considered here is that the dipoles are series fed by transverse microstrip lines. The computation of mutual coupling in this case requires a different approach from [87]. To find the mutual coupling information, one can consider two dipoles fed by a microstrip line and follow a similar numerical method as for an isolated dipole case except for the additional computation of dipole to dipole reaction. An asymptotic extraction technique together with point source approximation has been developed in [44] to compute efficiently and accurately the reaction of two dipoles. After the matrix inversion, the solution of the current in the line or dipoles provide the total active admittance as well as active currents of the dipoles. For the  $n$ th and  $m$ th dipole with resonant spacing, the method of moments allows one to compute the total active admittance

$$\begin{aligned} Y_{tot}^a &= Y_n^a + Y_m^a \\ &= Y_{nn} + Y_{mm} \mp 2Y_{mn} \end{aligned} \quad (9.16)$$

The - or + signs depend on whether the dipole spacing is an odd or even integer of a half guide wavelength. From Eq. 9.16, if the self admittance of each dipole is known, the mutual admittance can be determined. The active currents in the dipole  $I_n^a$  and  $I_m^a$  can also be obtained numerically and can be described as

$$\frac{I_n^a}{V_n} = \frac{I_{nn}}{V_n} + \frac{I_{mn}}{V_n} \quad (9.17)$$

and

$$\frac{I_m^a}{V_m} = \frac{I_{mm}}{V_m} + \frac{I_{mn}}{V_m}. \quad (9.18)$$

From Eqs. 9.17 and 9.18 together with the information of the current excited in an isolated dipole, the mutual current ( $I_{mn}$ ) can be obtained.

#### 9.4. A Design Example

The previous discussion of the design theory applies either to a linear or a planar array. Here, a seven elements standing wave linear array will be designed to illustrate the design technique. The geometry is shown in Fig. 9-2. A sum pattern in the H-plane with a -20 dB side lobe level was prescribed for this array. The printed dipoles are series fed by a 50  $\Omega$  microstrip line embedded in the middle of the substrate of thickness 0.16 mm and permittivity 2.17. The design frequency is 8.3 GHz and element spacing is chosen to be one guide wavelength. All dipoles have the same width of 1 mm and the offsets and lengths are to be found. The design curves for the self admittance  $Y_{nn}$  and the coefficient function  $f_n$  as a function of offset and length obtained from the method of moments solution are shown in Figs. 9-3 and 9-4 respectively. It is found that, for the EMC transverse dipole, many basis functions are required to obtain adequate convergence. To obtain each data point, 19 expansion modes are used in the dipole and piecewise sinusoidal modes of size of 0.04 guide wavelength are used in the line. It is observed from Fig. 9-4 that for different dipole offsets and lengths, the phase of  $f_n$  is not a constant.



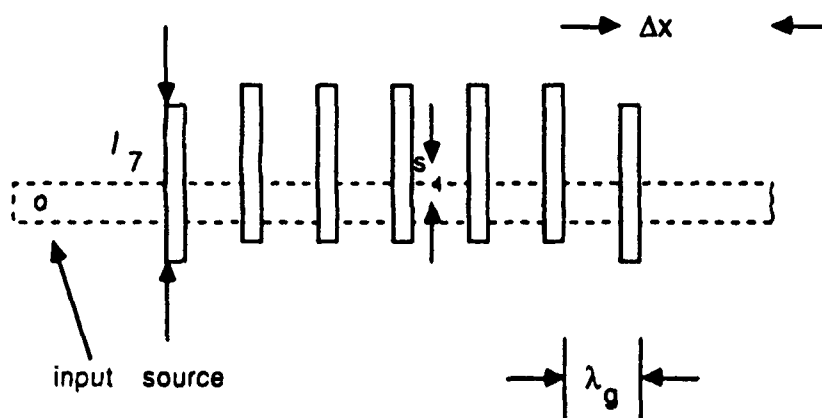


Figure 9-2. A seven element linear standing wave array.  
Elements are spaced by a guide wave length.

This implies that even for resonant spacing, to have in-phase excitation, the dipole can not be self resonant. To obtain a perfect match, the stub length  $\Delta x$  in Fig. 9-2 can be suitably adjusted to tune out the total active susceptance.

The sampled data are used to construct the data bank such that for a given offset and length the function value can be obtained through a two dimensional interpolation routine. Mutual coupling between two dipoles is a function of dipole lengths and offsets for a fixed spacing. It is found that mutual coupling is not sensitive to a small change of dipole length. Also from the results of no mutual coupling, it is found that the lengths of all the dipoles are different within 0.2%. Therefore, in the mutual coupling computation, the dipole lengths are fixed. The mutual admittance and mutual current as a function of offsets for one guide wavelength spacing and fixed dipole length are shown in Figs. 9-5 and 9-6 respectively. A similar procedure can be followed for a two wavelength spacing, and so on. As a result, the interpolation or extrapolation method can provide the mutual coupling information for any dipole spacing.

The design data after a few iterations, including the self and mutual admittances are shown in Table I. The element spacing is 23.6 mm and  $\Delta x = 11$  mm. It is seen that the mutual admittance is more than 25% of the total active admittance. Therefore, it is concluded that even at one wave length spacing, the effect of mutual coupling should not be ignored. To provide a confident check of the design data, the method of moments is applied to the seven element linear array. The results of active admittance and current in each dipole are shown in Table II together with the results from the

synthesis technique. It is observed that the current amplitude agrees within 1 to 2% and the phase agrees in  $\pm 1$  degree. The admittance comparison is also good.

The antenna array was built on a 10-in square Duroid board [90]. The measured return loss from the feed line is shown in Fig. 9-7. The bandwidth of this array is about 3.75%. The frequency for a perfect match is found to be 8.14 GHz which deviates 160 MHz (2%) from the design frequency. This result is rather good, considering that this array is very sensitive to the tolerances of the device parameters. Both the desired and measured radiation patterns in H-plane are shown in Fig. 9-8. It is observed that the main beam as well as the first side lobe agree well with the design criteria. Other side lobes in the measured pattern are a little too high, which is probably due to the finite size of the ground plane.

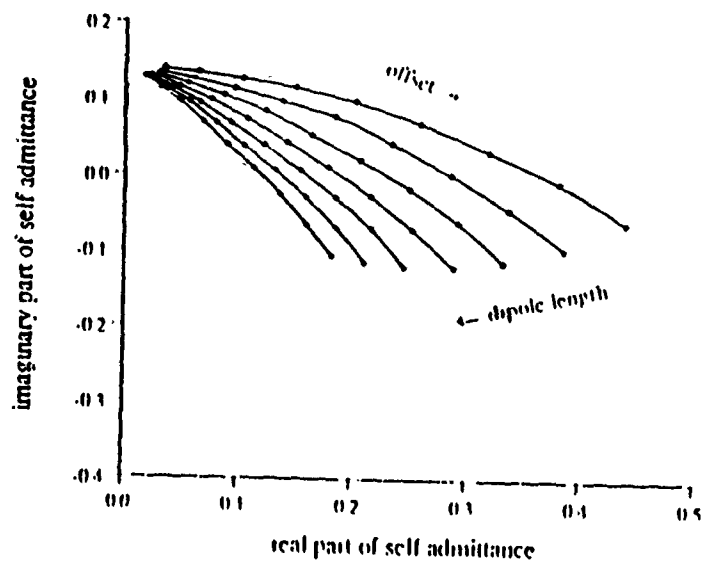


Figure 9-3. Self admittance of the dipole versus offset  $s$  and length  $l$ .

$$s = 0.32(k-1) \times 0.12 \text{ mm}, k = 1, 2, \dots, 9.$$

$$l = 12.6(n-1) \times 0.025 \text{ mm}, n = 1, 2, \dots, 7.$$

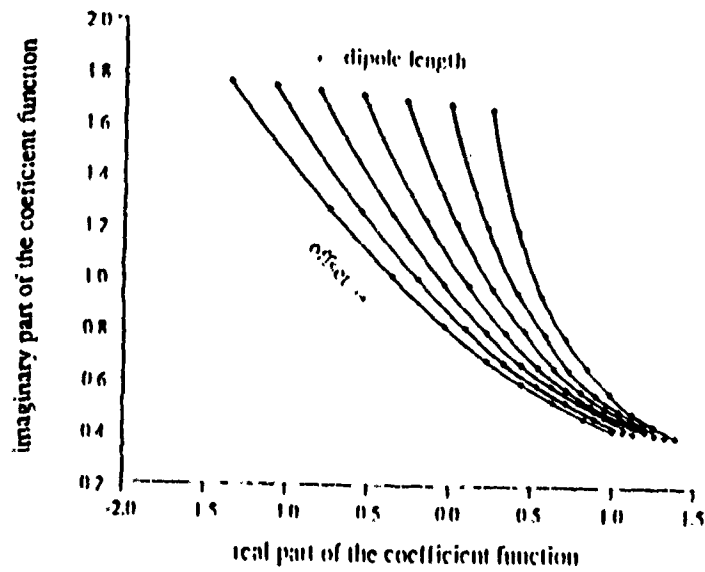


Figure 9-4. Coefficient function of the dipole versus offset  $s$  and length  $l$ .

$$s = 0.32(k-1) \times 0.12 \text{ mm}, k = 1, 2, \dots, 9.$$

$$l = 12.6(n-1) \times 0.025 \text{ mm}, n = 1, 2, \dots, 7.$$

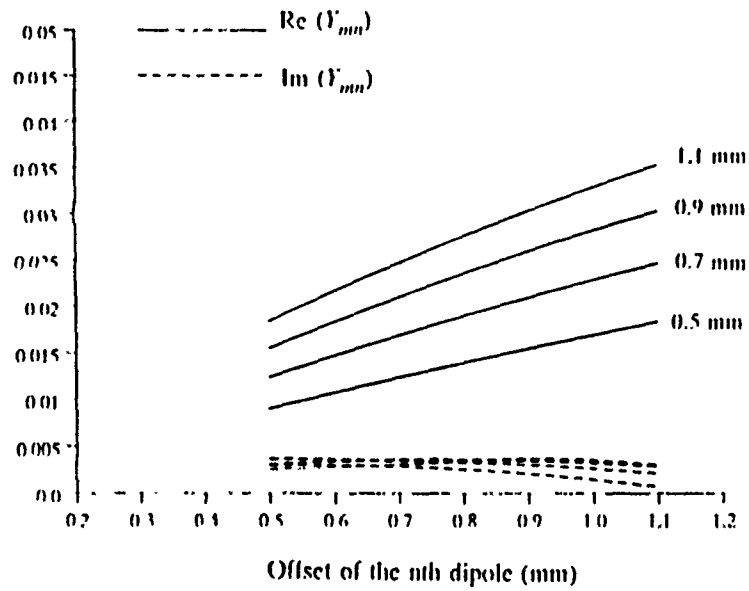


Figure 9-5. Mutual admittance of two dipoles versus their offsets.  
Element spacing is one guided wavelength and  $l = 12.7$  mm.

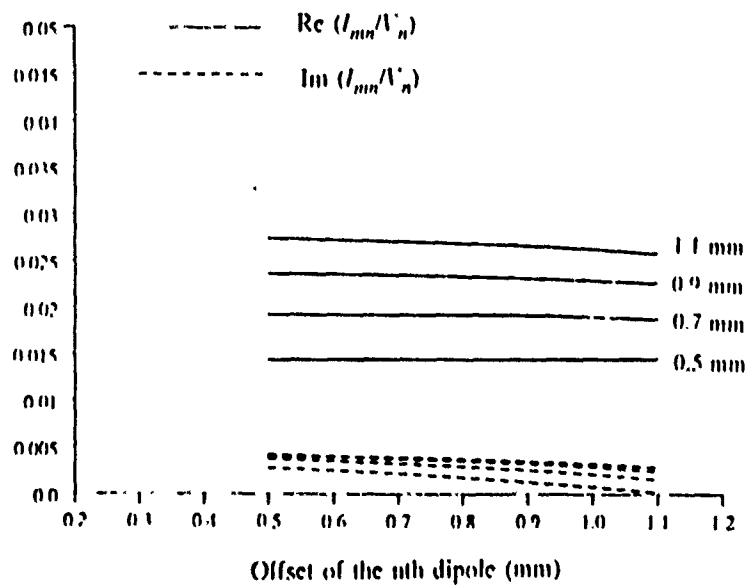


Figure 9-6. Mutual current of two dipoles versus their offsets.  
Element spacing is one guided wavelength and  $l = 12.7$  mm.

TABLE I

Design data of a seven element linear array				
No.	offset in mm	dipole length in mm	$Y_{nn}$	$Y_{mutual}$
1	0.5697	12.723	$0.0580 + j\ 0.0934$	$0.015 + j\ 0.003$
2	0.7425	12.743	$0.0825 + j\ 0.0519$	$0.038 + j\ 0.006$
3	0.9467	12.716	$0.1450 + j\ 0.0020$	$0.053 + j\ 0.006$
4	1.0200	12.703	$0.1769 - j\ 0.0235$	$0.060 + j\ 0.005$
5	0.9467	12.716	$0.1450 + j\ 0.0020$	$0.053 + j\ 0.006$
6	0.7425	12.743	$0.0825 + j\ 0.0519$	$0.038 + j\ 0.006$
7	0.5697	12.723	$0.0580 + j\ 0.0934$	$0.015 + j\ 0.003$

$Y_{in} = 1.02 + j0.002$  (result from iterations)

$Y_{in} = 1.08 + j0.006$  (result from I.E.S.)

TABLE II

Design check through an integral equation solution (I.E.S.)		
No.	desired current	I.E.S. current
1	$1.0000 < 0.0$	$1.0000 < 0.0$
2	$1.2751 < 0.0$	$1.264 < -1.2$
3	$1.6810 < 0.0$	$1.650 < -0.2$
4	$1.8351 < 0.0$	$1.824 < 1.4$
5	$1.6810 < 0.0$	$1.654 < 0.4$
6	$1.2751 < 0.0$	$1.266 < -0.8$
7	$1.0000 < 0.0$	$0.999 < 0.8$

The unit of the phase of current is in degree

yang 2 17/2/88 S1: dB-LOSS

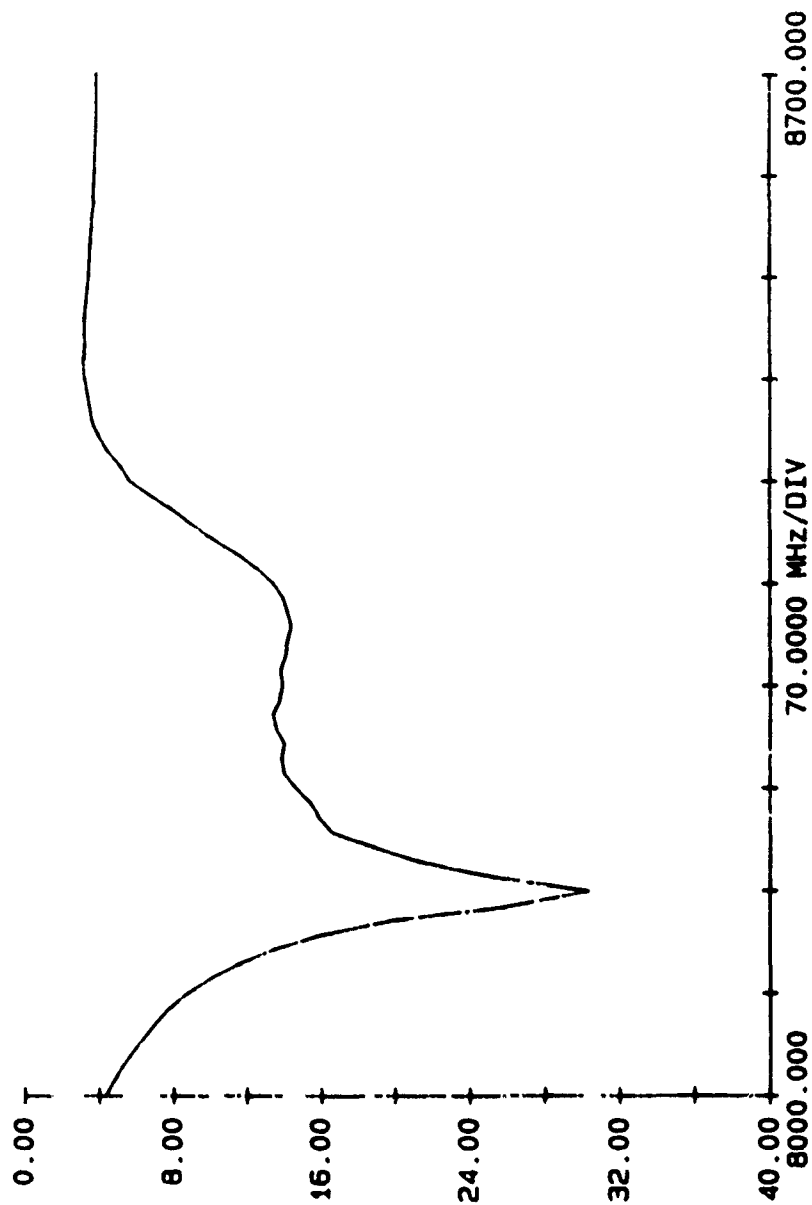


Figure 9-7. Measured return loss of the designed antenna array.

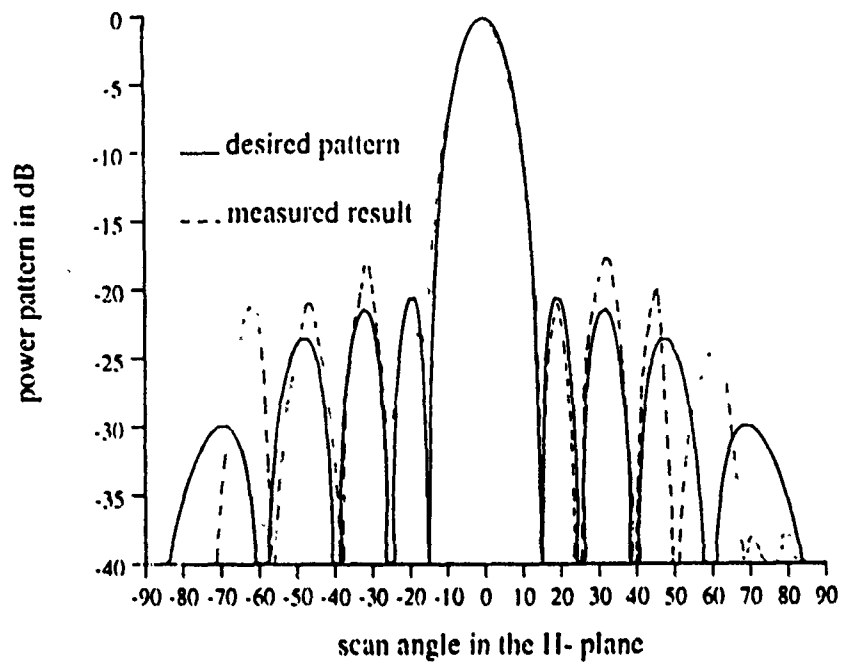


Figure 9-8. Comparison between the desired and measured antenna pattern in the H-plane.



## Chapter X

### Conclusion

In this dissertation, a generalized frequency dependent method has been developed to characterize integrated circuit discontinuities and printed circuit antennas. The analysis has taken into account all the physical effects including radiation, surface waves and higher order modes. The method of moments has been used to solve coupled integral equations. In the procedure, a mode expansion mechanism using the combination of the entire domain traveling wave modes and the piecewise sinusoidal subdomain modes has been developed. This scheme is particularly useful for the analysis of coupled infinite lines.

The geometries of microstrip open-end and gap discontinuities in two layer structures are analyzed. The fringing effect and radiation and surface wave losses as a function of various device parameters are studied. The results of this study have been obtained through a careful convergence test and compared against the quasi-static results in low frequency range with excellent agreement. A short-end slot line discontinuity in a one-side or a sandwiched structure is also studied. The advantages of using a slot line sandwich have been demonstrated.

Line to line transitions which are increasingly important in VLSI and monolithic circuits, have been investigated. The transition circuits studied include microstrip-slot line transition, proximity coupled collinear and trans-

verse microstrip transitions. The analysis of microstrip-slot line transition which includes the coupling between microstrip and slot line, reveals the versatility of the developed numerical methods. The analysis can be easily implemented in a computer aided design of both microstrip circuits and slot line circuits. The analysis of proximity coupled microstrip transition has shown that these transitions are broadband and provide a wide range of coupling coefficients, and have potential importance in the design of microwave filters and couplers. The experiment for the case of a transverse transition has been performed to verify the analysis.

The method for characterizing integrated circuit discontinuities is general enough to analyze a class of printed circuit antenna feeding structures. These structures include a microstrip fed slot, a slot line fed dipole, an EMC transverse dipole and a microstrip fed slot coupled dipole. The main features and potential applications for each antenna architecture in monolithic phase arrays have been discussed.

Design techniques and procedures for microstrip dipole arrays transversely fed by proximity coupled microstrip lines have been presented. Two design equations which include the effects of mutual coupling are developed and the corresponding design curves are obtained by a rigorous integral equation solution. A seven element standing wave linear array has been designed to illustrate the developed design procedures. The design data is checked by a complete integral equation solution of the array with excellent agreement. The radiation pattern and input impedance measurements are also compared with theory.

The integrated circuit components studied in this dissertation are either isolated line discontinuities or proximity coupled transition from line to line. The circuit components are slender strips or slots in rectangular shape. These considerations lead to the approximation of a one current component in the strip and a one electric field component in the slot. This simplified analysis has greatly reduced the CPU time without losing desired accuracy. With a straightforward (but tedious) modification of the present analysis which considers both current or field components in the circuit, one is able to characterize microstrip and slot junction discontinuities. The extension of the present research to coplanar waveguide or coplanar coupled line is also possible. The analysis of the printed antenna elements can be used directly to design monolithic antenna arrays without considering mutual coupling. The method of incorporating mutual coupling in the array designs has also been demonstrated with an EMC transverse dipole array as an example.

## REFERENCES

1. C. Mead and L. Lonway, Introduction to VLSI systems, Addison-Wesley Publishing Company, 1980.
2. P.R. Gray and R.G. Meyer, Analysis and design of analogy Integrated John Wiley & Sons, Inc., 1984.
3. S.M. Sze, Physics of semiconductor devices Wiley, 1981.
4. R.A. Pucel, "Design consideration for monolithic microwave circuits" IEEE Trans. on Microwave Theory and Technique, Vol. MTT-29, no. 6, pp. 513-534, June 1981.
5. D. Ch'en and D.R. Decker, "MMIC's the next generation of microwave components," Microwave Journal, pp. 67-78, May 1980.
6. E. Mahel and R.W. Wacker, "GaAs integrated microwave circuits," IEEE Trans. on Microwave Theory and Technique, Vol. MTT-16, no. 5, pp. 451-454, July 1968.
7. Leo Young and H. Sobol, Advances in Microwaves, Academic Press, 1974.
8. E.J. Denlinger, "A frequency dependent solution for microstrip transmission lines," IEEE Trans. on Microwave Theory and Technique, Vol. MTT-19, no. 1, pp. 30-39, Jan. 1971.
9. T. Itoh and R.J. Mittra, "Spectral domain approach for calculating the dispersion characteristics of microstrip lines," IEEE Trans. on Microwave Theory and Technique, Vol. MTT-21, pp. 496-499, 1973.
10. R.H. Jansen, "Unified user-oriented computation of shielded covered and open planar microwave and millimeter wave transmission lines," IEE J. Microwave Opt. Acoust. Vol. MOA-3, pp. 14-22, 1979.
11. A. Nakatani and N.G. Alexopoulos, "Toward a generalized Algorithm for the modeling of the dispersive properties of integrated circuit structures on anisotropic substrates," IEEE Trans. on Microwave Theory and Technique, Vol. MTT-33, pp. 1436-1441, Dec. 1985.
12. H. Ermert, "Guided modes and radiation characteristics of covered microstrip lines," A.E.U. Band-30, pp. 65-70, Jan. 1976.

13. G.H. Robinson and James L. Allen, "Slotline application to miniature ferrite devices," IEEE Trans. on Microwave Theory and Technique, Vol. MTT-17, no. 12, pp. 1097-1101, Dec. 1969.
14. E.A. Mariani, C.P. Heinzman, J.P. Agrios and S.B. Cohn, "Slot line Characteristics," IEEE Trans. on Microwave Theory and Technique, Vol. MTT-17, no. 12, pp. 1091-1096, Dec. 1969.
15. R.H. Jansen, "Computer-aided design of hybrid and monolithic microwave integrated circuits- state of arts, problems and trends", Invited paper for the Proceedings of 13th European microwave conference, pp.67-75, 1983.
16. K.C. Gupta, R. Garg and I.J. Bahl, Microstrip lines and slotlines Dedham, MA: Artech House, 1979.
17. M. Maeda, "Analysis of gap in microstrip transmission lines" IEEE Trans. on Microwave Theory and Technique, Vol. MTT-20, no. 6, pp. 390-396, June 1972.
18. P. Benedek and P. Silvester, "Equivalent capacitance for microstrip gap and steps," IEEE Trans. on Microwave Theory and Technique, Vol. MTT-20, no. 11, pp. 729-733, Nov 1972.
19. R. H. Jansen, "Hybrid mode analysis of end effects of planar microwave and millimeter wave transmission line", Proc. IEE, pt. H, vol. 128, pp. 77-86, 1981.
20. N. H. L. Koster and R. H. Jansen. "The equivalent circuit of the asymmetrical series gap in microstrip and suspended-substrate line," IEEE Trans. Microwave Theory and Technique, vol. MTT-30, pp. 1273-1279, Dec. 1986.
21. R. H. Jansen and N. H. L. Koster, "A unified CAD basis for the frequency dependent characterization of strip, slot and coplanar MIC components," Proc. 11th Eur. Microwave Conf., 1981, pp. 682-687.
22. R. H. Jansen, "The spectral domain approach for microwave integrated circuits," (Invited paper), IEEE Trans. Microwave Theory and Technique, vol. MTT-33, pp. 1043-1056, Oct. 1985.
23. H-Y. Yang and N.G. Alexopoulos, "Characterization of the finline step discontinuity on anisotropic substrates," IEEE Trans. on Microwave Theory and Technique, Vol. MTT-35, no. 11, pp. 956-963, Nov. 1987.

24. P. B. Katchi and N. G. Alexopoulos, "Frequency-dependent characteristics of microstrip discontinuities in millimeter wave integrated circuits," *IEEE Trans. on Microwave Theory and Technique*, vol. MTT-33, no. 10, pp. 1029-1035, Oct. 1985.
25. R. W. Jackson and D. M. Pozar, "Full wave analysis of microstrip open-end and gap discontinuities," *IEEE Trans. on Microwave Theory and Technique*, vol. MTT-33, no. 10, pp. 1036-1042, Oct. 1985.
26. R. W. Jackson, "Considerations in the use of coplanar waveguide for millimeter wave integrated circuits," *IEEE Trans. on Microwave Theory and Technique*, vol. MTT-47, no. 12, Dec. 1986.
27. H-Y. Yang and N.G. Alexopoulos, "A dynamic model for microstrip-slotline transition and related structures," *IEEE Trans. on Microwave Theory and Technique*, Vol. MTT-36, no. 2, pp. 286-293, Feb. 1988.
28. K.R. Carver and J.W. Mink, "Microstrip antenna technology" *IEEE Trans. on Antennas and Propagation*, vol. AP-29, no. 1, pp. 2-24, Jan. 1981.
29. R.J. Mailloux, J.F. McIlvanna and N.P. Kernweis, "Microstrip array technology," *IEEE Trans. on Antennas and Propagation*, vol. AP-29, no. 1, pp. 25-37, Jan. 1981.
30. G.A. Deschamps, "Microstrip microwave antennas," presented at the 3rd USAF Symp. on antennas, 1953.
31. R.E. Munson, "Conformal microstrip antennas and microstrip phased arrays," *IEEE Trans. on Antennas and Propagation*, vol. AP-22, no. 1, pp. 74-77, Jan. 1974.
32. A.G. Derneryd, "Linear microstrip array antennas," *Chalmer Univ. Technol., Goteborg, Sweden, Tech. Rep. TR 7505*, Oct. 1975.
33. Y.T. Lo, D. Solomon and W.F. Richards, "Theory and experiment on microstrip antennas," *IEEE Trans. on Antennas and Propagation*, vol. AP-27, no. 2, pp. 137-145, Feb. 1979.
34. W.F. Richards and Y.T. Lo, "An improved theory for microstrip antennas and applications," in *Dig. Int. Symp. Antennas Propagat. Soc.*, Seattle, WA, June 1979, pp. 113-116.

35. W.F. Richards, Y.T. Lo, P. Simon and D.D. Harrison, "Theory and applications of microstrip antennas," In Pro. Workshop Printed Circuit Antenna Tech., New Mexico State Univ. Las Cruces, Oct. 1979, pp.11; 1-8.
36. W.F. Richards and Y.T. Lo and D.D. Harrison, "An improved theory for microstrip antennas and applications," IEEE Trans. on Antennas and Propagation, vol. AP-29, no. 1, pp. 38-46, Jan. 1981.
37. T. Itoh and W. Menzel, "A full-wave analysis method for open microstrip structures," IEEE Trans. on Antennas and Propagation, vol. AP-29, no. 1, pp. 63-67, Jan. 1981.
38. I.E. Rana, On the theory and design of printed antenna arrays, Ph.D. dissertation, Univ. of California, Los Angeles, 1979.
39. I. E. Rana and N. G. Alexopoulos, "Current distribution and input impedance of printed dipoles," IEEE Trans. on Antennas Propagat., vol. AP-29, pp. 99-106, Jan. 1981.
40. D. M. Pozar, "Input impedance and mutual coupling of rectangular microstrip antennas," IEEE Trans. on Antennas Propagat., vol. AP-30, pp. 1191-1196, Nov. 1982.
41. D. M. Pozar, "Improved computational efficiency for the moment method solution of printed dipoles and patches," Electromagnetics, vol. 3, no. 3-4, pp. 299-309, July-Dec. 1983.
42. P. B. Katchi and N. G. Alexopoulos, "On the modeling of Electromagnetic coupled microstrip antennas- the printed strip dipole," IEEE Trans. on Antennas and Propagation, vol. AP-32, no. 11, pp. 1179-1186, Nov. 1984.
43. D.R. Jackson and N.G. Alexopoulos, "Analysis of planar strip geometries in a substrate-superstrate configuration," IEEE Trans. on Antennas and Propagation, vol. AP-34, no. 12, pp. 1430-1438, Dec. 1986.
44. D.R. Jackson and N.G. Alexopoulos, "An Asymptotic extraction technique for evaluating Sommerfeld-type integral," IEEE Trans. on Antennas and Propagation, vol. AP-34, no. 12, pp. 1467-1470, Dec. 1986.
45. N.G. Alexopoulos, P.B. Katchi and D.B. Rutledge, "Substrate optimization for integrated circuit antennas", IEEE Trans. Microwave theory and technique, Vol. MTT-31, pp. 550-557, July 1983.

46. P.B. Katchi and N.G. Alexopoulos, "On the effects of substrate thickness and permittivity on printed circuit antennas", IEEE Trans. Antennas Propagat., Vol.AP-31, pp. 34-39, Jan. 1983.
47. D.B. Rutledge, D.P. Neikirk and D.P. Kasilingam, "Integrated circuit antennas", Infrared and millimeter waves, Vol. 10, part 2 (K.J. Button, ed.), New York, Academic Press, pp. 1-90 1983.
48. D.M. Pozar, "Consideration for millimeter wave printed antennas", IEEE Trans. Antenna Propagat., Vol. AP-31, pp.740-747, SEP. 1983.
49. N.G. Alexopoulos and D.R. Jackson, "Fundamental superstrate (cover) effects on printed circuit antennas," IEEE Trans. Antennas Propagat., vol. AP-32, pp. 807-816, Aug. 1984.
50. N.G. Alexopoulos, D.R. Jackson and P.B. Katchi, "Criteria for nearly omnidirectional radiation patterns for printed antennas," IEEE Trans. Antennas Propagat., vol. AP-33, pp 195-205, Feb. 1985.
51. N.G. Alexopoulos and D.R. Jackson, "Gain enhancement methods for printed circuit antennas," IEEE Trans. Antennas Propagat., vol. AP-33, pp. 976-987, Sep. 1985.
52. D.R. Jackson and N.G. Alexopoulos, "Microstrip dipoles on electrically thick substrates," International Journal of infrared and millimeter waves, vol. 7, no. 1 pp. 1-26, 1986.
53. N. G. Alexopoulos, D. R. Jackson and P. B. Katchi, "Criteria for nearly omnidirectional radiation patterns for printed antennas," IEEE Trans. on Antennas Propagat., vol. AP-33, pp. 195-205, Feb. 1985.
54. H-Y. Yang and N.G. Alexopoulos, "Gain enhancement methods for printed circuit antennas through multiple superstrates," IEEE Trans. on Antennas and Propagation, Vol. AP-35, no. 7, pp.860-863, July 1987.
55. H-Y. Yang and N.G. Alexopoulos, "Generation of nearly hemispherical and high gain azimuthally symmetric pattern with printed circuit antennas," IEEE Trans. on Antennas and Propagation, Vol. AP-35, no. 8, pp.972-976, August, 1987.
56. H.G. Oltman and D.A. Huebner, "Electromagnetically coupled microstrip dipoles," IEEE Trans. on Antennas and Propagation, Vol. AP-29, no. 1, pp.151-157, Jan. 1981.
57. P.B. Katchi, "A generalized solution of a class of printed circuit antennas," Ph.D. Dissertation, UCLA 1984.



58. D.R. Jackson, "Fundamental superstrate(cover) effects on printed circuit antennas" Ph.D. Dissertation, UCLA 1985.
59. R.S. Elliott and G.J. Stern, "The design of microstrip dipole arrays including mutual coupling, part I:theory," IEEE Trans. on Antennas and Propagation, Vol. AP-29, no. 9, pp.757-760, Sep. 1981.
60. G.J. Stern and R.S. Elliott, "The design of microstrip dipole arrays including mutual coupling, part II:experiment," IEEE Trans. on Antennas and Propagation, Vol. AP-29, no. 9, pp.761-765, Sep. 1981.
61. R.S. Elliott, Antenna theory and design, Prentice-Hall, Inc., 1981.
62. A. Sommerfeld, Partial Differential Equations, New York: Academic, 1941, Vol. VI.
63. R.F. Harrington, Field computation by moment method, New York: Macmillan, 1968.
64. E. Zauderer, Partial differential equations of applied mathematics, New York: John Wiley & Sons, Inc, 1983.
65. P. Benedek and P. Silvester, "Equivalent capacitance of microstrip open circuit," IEEE Trans. on Microwave Theory and Technique, Vol. MTT-20, pp. 511-516, May 1972.
66. O. Fordham, Two layer microstrip transmission lines, Master Thesis, UCLA 1987.
67. E.H. Newman and D. Forrai, "Scattering from a microstrip patch," IEEE Trans. on Antennas and Propagation, Vol. AP-35, no 3, pp. 245-251, Mar. 1987.
68. The microwave Engineer's Handbook and Buyers' Guide. New York: Horizon House, p. 72, Feb. 1969.
69. S.B. Cohn, "Slot line-- and alternative transmission medium for integrated circuits," Presented at the G-MTT Symposium, May 1968.
70. S.B. Cohn, "Slotline on a dielectric substrate," IEEE Trans. on Microwave Theory and Technique, Vol. MTT-17, pp. 768-778, Dec. 1969.
71. B. Schiek, "Hybrid Branchline Couplers-- a useful new class of directional couplers," IEEE Trans. on Microwave Theory and Technique, Vol. MTT-22, pp. 864-869, July 1974.

72. E.A. Mariani and J. P. Agrios, "Slot-line filters and couplers," IEEE Trans. on Microwave Theory and Technique, Vol. MTT-18, pp. 1089-1095, Dec. 1970.
73. T. Itoh and R. Mittra, "Dispersion characteristics of slotlines," Electro. Lett., Vol. 7, pp.364-365, 1971.
74. J.B. Knorr and J. Saenz, "End effect in a shorted slot," IEEE Trans. on Microwave Theory and Technique, Vol. MTT-21, pp. 579-581, May. 1973.
75. J. B. Knorr, "Slot-line transitions," IEEE Trans. on Microwave Theory and Technique, vol. MTT-22, no. 5, pp. 548-554, May 1974.
76. D. Chambers, S. B. Cohn, E. G. Cristol and F. Young, "Microwave active network synthesis," Stanford Resr. Inst., Semiannual Report, June 1970.
77. P. Lepeltier, J.M. Floe'h and J. Citerne, "Complete and rigorous analysis of the electromagnetically coupled transverse microstrip dipole," Electronics Letters, Vol. 23, No. 16, pp. 822-824, July 1987.
78. P. Lepeltier, J.M. Floe'h, J. Citerne and D. Martin, "On the excitation microstrip line parasitic radiation observed in printed antennas - The EMC dipole," IEEE Antenna and Propagation Society International symposium, pp. 814-818, Blacksburg, June 1987.
79. I.J. Bahl and P. Bhartia, Microstrip antennas, Dedham, MA: Artech House, 1980.
80. R.E. Collin, Field Theory of Guided Waves, New York: McGraw Inc. 1960.
81. H.G. Oltman, "Electromagnetically coupled microstrip dipole antenna elements," Presented at the Proc. 8th European Microwave Conference, Paris, France, Sep. 1978.
82. Y. Yoshimura, "A microstripline slo antenna," IEEE Trans. on Microwave Theory and Techniques, Vol. MTT-20, pp. 760-762, Nov. 1972.
83. B.N. Das and K.K. Joshi, "Impedance of a radiating slot in the ground plane of a microstripline," IEEE Trans. on Antennas and Propagation, Vol. AP-30, no. 9, pp. 922-926, Sep. 1982.

84. D.M. Pozar, "A reciprocity method of analysis for printed slot and slot-coupled microstrip antennas," IEEE Trans. on Antennas and Propagation, Vol. AP-34, no. 12, pp. 1439-1446, Dec. 1986.
85. D.M. Pozar, "A microstrip antenna aperture coupled to a microstrip line," Electronics Lett., Vol 21, pp. 49-50, Jan, 1985.
86. P.L. Sullivan and D.H. Schaubert, "Analysis of an aperture-coupled microstrip antennas," IEEE Trans. on Antennas and Propagation, Vol. AP-34, no. 8. pp. 977-984, Aug. 1986.
87. P. B. Katchi, "A generalized method for the evaluation of mutual coupling in microstrip arrays," IEEE Trans. on Antennas and Propagation, vol. AP-35, no. 2, pp. 125-133, Feb. 1987.
88. R.S. Elliott, Private Communication.
89. M. Aoki, Introduction to optimization techniques. Macmillan, New York, 1971.
90. P. Lepeltier, Private Communication.

## Appendix A

The pertinent parameters in Eqs. 2.9-2.14 are expressed as

$$f_0(\lambda) = n_2^2 \left[ \frac{q_2 \cosh q_2(z_s - b)}{\mu_2} + \frac{q_1 \sinh q_2(z_s - b)}{\mu_1 \tanh q_1 b} \right] \quad (A.1)$$

$$h_0(\lambda) = \left[ \frac{(1 - n_2^2)}{\mu_2} f_0(\lambda) A_1(\lambda) + \frac{n_2^2}{\mu_2} q_2 (n_2^2 - n_1^2) A_2(\lambda) \right] \quad (A.2)$$

$$f_1(\lambda) = \frac{n_2^2}{n_1^2 \sinh q_1 b} \left[ q \sinh q_2(h - z_s) + \frac{q_2 \cosh q_2(h - z_s)}{\mu_2} \right] \quad (A.3)$$

$$h_1(\lambda) = \frac{\mu_1}{\mu_2} [f_1(\lambda) A_3(\lambda) \tanh q_1 b (n_2^2 - n_1^2) + \operatorname{sech} q_1 b q_2 (1 - n_2^2) f_0(\lambda)] \quad (A.4)$$

for  $b \leq z \leq z_s$

$$f_2(\lambda) = A_4(\lambda) \sinh q_2(z - b) + A_5(\lambda) \cosh q_2(z - b) \quad (A.5)$$

for  $z_s \leq z \leq h$ ,  $f_2(\lambda)$  is similar to Equation (A.5) except  $z$  and  $z_s$  are interchanged due to the reciprocity.

$$h_2(\lambda) = (n_2^2 - n_1^2) A_5(\lambda) A_6(\lambda) + (1 - n_2^2) A_7(\lambda) A_8(\lambda) \quad (A.6)$$

$$A_1(\lambda) = q_2 n_1^2 \cosh q_2(h - b) + \frac{\mu_1}{\mu_2} q_1 n_2^2 \tanh q_1 b \sinh q_2(h - b) \quad (A.7)$$

$$A_2(\lambda) = q \sinh q_2(h - z_s) + \frac{q_2}{\mu_2} \cosh q_2(h - z_s) \quad (A.8)$$

$$A_3(\lambda) = q \varepsilon_2 \sinh q_2(h - b) + q_2 \cosh q_2(h - b) \quad (A.9)$$

$$A_4(\lambda) = \frac{q_1 \cosh q_2(h - z_s)}{\mu_1 \tanh q_1 b} + \frac{\mu_2 q_1 q \sinh q_2(h - z_s)}{\mu_1 q_2 \tanh q_1 b} \quad (A.10)$$

$$A_5(\lambda) = q \sinh q_2(h - z_s) + \frac{q_2}{\mu_2} \cosh q_2(h - z_s) \quad (A.11)$$

$$A_6(\lambda) = \frac{q n_2^2 \sinh q_2(h - z)}{\mu_2} + q_2 \cosh q_2(h - z) \quad (A.12)$$

$$A_7(\lambda) = \frac{q_2 \cosh q_2(z_s - h)}{\mu_2} + \frac{q_1 \sinh q_2(z_s - b)}{\mu_1 \tanh q_1 b} \quad (A.13)$$

$$A_8(\lambda) = q_2 n_1^2 \cosh q_2(z - b) + \frac{\mu_1}{\mu_2} q_1 n_2^2 \sinh q_2(z - b) \tanh q_1 b \quad (A.14)$$

## Appendix B

The pertinent parameters in Eqs. 2.28-2.33 are expressed as

$$f'_0(\lambda) = \varepsilon_1 q_2 \frac{\sinh q_1 z_s}{\sinh q_1 b} \quad (B.1)$$

$$h'_0(\lambda) = \frac{f'_0(\lambda)}{\mu_2} [(1 - n_2^2) n_1^2 B_1(\lambda) + (n_2^2 - n_1^2) B_2(\lambda)] \quad (B.2)$$

for  $z_s \leq z \leq b$

$$f'_1(\lambda) = \frac{\mu_2 \sinh q_1 z_s}{\mu_1 \sinh^2 q_1 b} B_3(\lambda) \sinh q_1 z + \frac{\sinh q_1 z_s \sinh q_1 (b - z)}{q_1 \sinh q_1 b} D_e(\lambda) \quad (B.3)$$

for  $0 \leq z \leq z_s$ ,  $f'_1(\lambda)$  is similar to Eq. (B.3) except  $z$  and  $z_s$  are interchanged due to the reciprocity.

$$h'_1(\lambda) = \frac{\varepsilon_2 f'_0(\lambda) \sec q_1 b}{\varepsilon_1 q_2 n_2^2} [(n_1^2 - n_2^2) B_2(\lambda) B_4(\lambda) + q_2^2 n_1^2 (1 - n_2^2)] \quad (B.4)$$

$$f'_2(\lambda) = \frac{f'_0(\lambda)}{q_2 \varepsilon_2} [q \sinh q_2 (h - z) + \frac{q_2 \cosh q_2 (h - z)}{\mu_2}] \quad (B.5)$$

$$h'_2(\lambda) = \frac{f'_0(\lambda)}{n_2^2 q_2} [(n_2^2 - n_1^2) B_2(\lambda) B_5(\lambda) + q_2 n_1^2 (1 - n_2^2) B_6(\lambda)] \quad (B.6)$$

$$B_1(\lambda) = q_2 \cosh q_2 (h - b) + \frac{\varepsilon_2}{\varepsilon_1} q_1 \tanh q_1 b \sinh q_2 (h - b) \quad (B.7)$$

$$B_2(\lambda) = \mu_2 q \sinh q_2 (h - b) + q_2 \cosh q_2 (h - b) \quad (B.8)$$

$$B_3(\lambda) = q \sinh q_2(h - b) + \frac{q_2}{\mu_2} \cosh q_2(h - b) \quad (B.9)$$

$$B_4(\lambda) = q_2 \cosh q_2(h - b) + q\varepsilon_2 \sinh q_2(h - b) \quad (B.10)$$

$$B_5(\lambda) = q_2 \cosh q_2(h - z) + q\varepsilon_2 \sinh q_2(h - z) \quad (B.11)$$

$$B_6(\lambda) = q_2 \cosh q_2(z - b) + \frac{\varepsilon_2}{\varepsilon_1} q_1 \tanh q_1 b \sinh q_2(z - b) \quad (B.12)$$

## Appendix C

The pertinent parameters in Equations (2.85)-(2.90) are expressed as

$$f_{m0}(\lambda) = \frac{\mu_1 n_1^2 n_2^2 q_2}{\mu_2 \cosh q_1 b} \quad (C.1)$$

$$h_{m0}(\lambda) = q_2 \sinh q_2 (h - b) C_1(\lambda) + q_2^2 \cosh q_2 (h - b) C_2(\lambda) \quad (C.2)$$

$$f_{m1}(\lambda) = \frac{e^{-q_1 z}}{q_1} + (1 - \tanh q_1 b)(C_3(\lambda) + C_4(\lambda)) \quad (C.3)$$

$$h_{m1}(\lambda) = \frac{q_1}{\sinh q_1 b \cosh q_1 b} \left[ \frac{q_2^2 n_1^2 (1 - n_2^2)}{\mu_2} + C_5(\lambda) C_6(\lambda) \right] \quad (C.4)$$

$$f_{m2}(\lambda) = \frac{q f_{m0}(\lambda)}{q_2} C_7(\lambda) \quad (C.5)$$

$$h_{m2}(\lambda) = \frac{\mu_1}{\mu_2 \cosh q_1 b} C_8(\lambda) C_6(\lambda) + n_1^2 (1 - n_2^2) \frac{q_2}{\mu_2} C_9(\lambda) \quad (C.6)$$

$$C_1(\lambda) = \frac{q_1 n_1^2 (1 - n_2^2)}{\sinh q_1 b} + \frac{\mu_1 q n_2^2 (n_2^2 - n_1^2)}{\mu_2^2 \cosh q_1 b} \quad (C.7)$$

$$C_2(\lambda) = \frac{\mu_1 n_2^2 (1 - n_1^2)}{\mu_2 \cosh q_1 b} \quad (C.8)$$

$$C_3(\lambda) = \sinh q_2 (h - b) \left( \mu_1 \varepsilon_2^2 q - \frac{n_1^2 q_2^2}{q_1} \right) \quad (C.9)$$



$$C_4(\lambda) = \cosh q_2(h - b)(\mu_1 \varepsilon_2 q_2 - \frac{n_1^2 \varepsilon_2 q_2 q}{q_1}) \quad (C.10)$$

$$C_5(\lambda) = \frac{q_2 \cosh q_2(h - b)}{\mu_2} + q \sinh q_2(h - b) \quad (C.11)$$

$$C_6(\lambda) = (n_2^2 - n_1^2)[q_2 \cosh q_2(h - b) + q \varepsilon_2 \sinh q_2(h - b)] \quad (C.12)$$

$$C_7(\lambda) = \frac{q_2 \cosh q_2(h - z)}{n_2^2 q} + \frac{\sinh q_2(h - z)}{\mu_1} \quad (C.13)$$

$$C_8(\lambda) = \frac{q_2 \cosh q_2(h - z)}{\mu_2} + q \sinh q_2(h - z) \quad (C.14)$$

$$C_9(\lambda) = \frac{q_1 \sinh q_2(z - b)}{\sinh q_1 b} + \frac{\mu_1 q_2 \cosh q_2(z - b)}{\mu_2 \cosh q_1 b} \quad (C.15)$$

## Appendix D

The asymptotic extraction technique discussed in Section III of Chap. III, requires the computation of the following integral

$$E_{mn} = \frac{30}{j\epsilon_{eff}} \int_{-w/2}^{w/2} \int_{-w/2}^{w/2} \int_{-d_1}^{d_1} \int_{-d_1}^{d_1} J(y) J(y') f_0(x) f_0(x') \left[ \left( \frac{\partial}{\partial x^2} + k_e^2 \right) \frac{e^{-jk_e R}}{R} \right] dx dx' dy dy' \quad (D.1)$$

where

$$f_0(x) = \frac{\sin k_{e1}(d_1 - |x|)}{\sin k_{e1}d_1}, \quad (D.2)$$

$$R = \sqrt{(x - x' + nd_1 - md_1)^2 + (y - y')^2}, \quad (D.3)$$

$$k_e = \sqrt{\epsilon_{eff}}, \quad (D.4)$$

and  $J(y)$  is shown in Eq. (3.5). The quadruple integral in Eq. D.1 can be further reduced to a double integral with integrand containing the Fresnel functions if  $k_e = k_{e1}$ . Since the integration range is usually small, the integration converges quite easily.

## Appendix E

The dominant term of the asymptotic form of Eq. 3.30 is

$$E = \frac{120k_mk_e}{j\pi\epsilon_{eff}} \int_0^{\pi/2} \int_A^\infty \frac{F_1^2(\lambda_y)}{\lambda_x^2 - k_m^2} (\cos \lambda_x d_1 - \cos k_e d_1) \cos \lambda_x n d_1 d\lambda d\phi \quad (E.1)$$

E when transformed back to Fourier domain can be expressed as

$$E = 0.5 E_1(d_1 + nd_1) + 0.5 E_1(d_1 - nd_1) - \cos k_e d_1 E_1(nd_1) \\ + 0.5 E_2(d_1 + nd_1) + 0.5 E_2(d_1 - nd_1) - \cos k_e d_1 E_2(nd_1) \quad (E.2)$$

where

$$E_1(\alpha) = \int_A^\infty F_1^2(\lambda_y) d\lambda_y \int_0^\infty \frac{\cos \lambda_x \alpha}{(\lambda_x^2 - k_m^2) \sqrt{\lambda_x^2 + \lambda_y^2}} d\lambda_x, \quad (E.3)$$

$$E_2(\alpha) = \int_0^A F_1^2(\lambda_y) d\lambda_y \int_{\lambda_x}^\infty \frac{\cos \lambda_x \alpha}{(\lambda_x^2 - k_m^2) \sqrt{\lambda_x^2 + \lambda_y^2}} d\lambda_x \quad (E.4)$$

and

$$\lambda_x = \sqrt{A^2 - \lambda_y^2} \quad (E.5)$$

The integrations in Eqs. E.3 and E.4 both converge. however, in order to obtain more accurate and efficient computation, further analysis may be required. For the  $\lambda_x$  integration in Eq. E.3, the integration contour in a complex plane can be deformed (referring to Fig. E-1) along the branch cut. This will help the integration decay exponentially when the cos argument is not zero.

Using the branch cut integration and a secant transformation,  $E_1(\alpha)$  can be written as

$$E_1(\alpha) = \int_A^\infty F_1^2(\lambda_y) d\lambda_y \int_0^{\pi/2} \frac{e^{-\lambda_y \sec \theta \alpha} \cos \theta}{\lambda_y^2 + k_m^2 \cos^2 \theta} d\theta \quad (E.6)$$

The convergence of the  $\lambda_x$  integration in Eq. E.4 can be improved for  $\alpha \neq 0$  by deforming the integration contour in the complex plane. The new contour is shown in Fig. E-2. The final form of the integration in Eq. E.4 can be written as

$$E_2(\alpha) = \frac{Re}{2} \int_0^A F_1^2(\lambda_y) d\lambda_y j e^{j\alpha \sqrt{A^2 - \lambda_y^2}} \int_0^\infty \frac{e^{-\alpha u} du}{(\lambda^2(u) - k_m^2) \sqrt{\lambda_y^2 + \lambda^2(u)}} \quad (E.7)$$

where

$$\lambda(u) = \sqrt{A^2 - \lambda_y^2} + ju \quad (E.8)$$

It should be noted that the singularities in either Eq. E.1 or E.2 are ignored since, as pointed out in Chap. III, these singularities are removable.

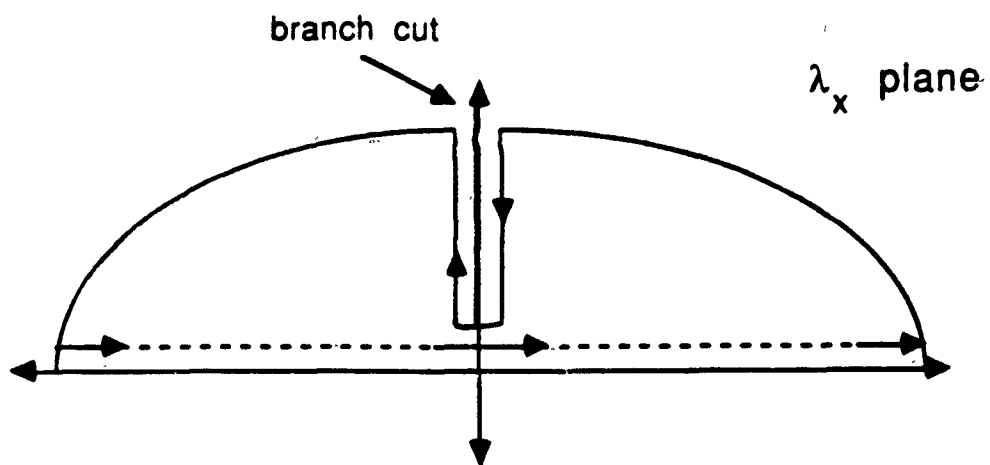


Figure E-1. Integration contour of Eq. E.3.

branch point at  $j\lambda_y$

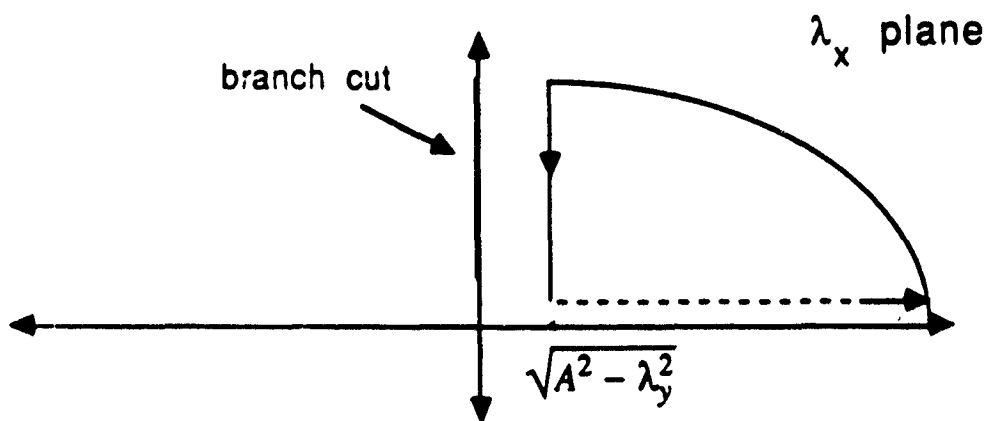


Figure E-2. Integration contour of Eq. E.4.

# A RIGOROUS DISPERSIVE CHARACTERIZATION OF MICROSTRIP CROSS AND TEE JUNCTIONS †

Shih-Chang Wu, Hung-Yu Yang and Nicolaos G. Alexopoulos

Electrical Engineering Department  
University of California, Los Angeles  
Los Angeles, CA 90024

**Abstract**— A full-wave spectral-domain analysis is applied to the characterization of multi-port microstrip discontinuities. This approach employs the moment method to find the currents in the microstrip circuits and subsequently, the scattering parameters of the junctions. In this approach, all the physical effects are considered, including radiation and surface waves. The numerical results for a tee and a cross junction are presented and agree well with the quasi-static values at low frequencies. The  $S$  parameters of a tee junction are further compared against the measured results with excellent agreement. The utilization of a shaped T-junction as a broad-band equal-power divider is also discussed.

## I. Introduction:

The full-wave analysis which deals with microstrip discontinuities in an open geometry has been applied to a variety of problems. This approach based on the moment method solution of an exact integral equation involves the computation of a continuous plane wave spectrum such that the effects of radiation, surface waves and the higher-order modes are included. This full-wave analysis has been applied to microstrip open-ends and gaps [1-3], steps [4], and bends [5-7].

From the review of the past work, one finds the full wave analysis up to now is limited to two-port structures. In this paper, a full-wave analysis up to four ports is presented. The spectral domain dyadic Green's functions are adopted in electric-field integral equations (EFIE) to handle double-layer substrate problems. Both longitudinal and transverse current components on the microstrip are taken into account and are the solution of the method of moments. In Section II, the method of moments formulation of the EFIE is briefly outlined. Mode expansion utilizing the combination of semi-infinite line modes on transmission lines and piecewise sinusoidal basis functions on the vicinity of the discontinuity are also discussed. In Section III, numerical results of the scattering parameters of various microstrip discontinuities such as basic tee and cross junctions as well as a shaped T-junction are discussed and

compared with available measurements and quasi-static results.

## II. Analysis:

Microstrip discontinuities can be looked upon, from a circuit point of view, as  $N$  transmission lines ( $N$  ports) jointed in a common region. The modeling involves finding the current distribution not only in the junction region but also in the  $N$  semi-infinite microstrip transmission lines. The approach to solve the problem is based on the moment method solution of the exact integral equations.

A generic four-port microstrip discontinuity is presented in Fig. 1. Four semi-infinite microstrip transmission lines which extend to  $\pm \infty$  in  $x$  or  $y$  direction are jointed in a common block (dash line box in Fig. 1). The widths of these four transmission lines are not necessary the same. The planar configuration of the microstrip discontinuity inside the common block is a state of the art to design the desired performance of this junction in a specified frequency range.

For microstrip junction problems, the concept of a module can be used. A module encloses the region at or near the junction where higher order modes are generated. The region otherwise consists of purely uniform transmission lines. The currents inside the module are expanded in terms of piecewise sinusoidal basis functions, while the currents outside the module are uniform transmission line currents (semi-infinite mode SIM).

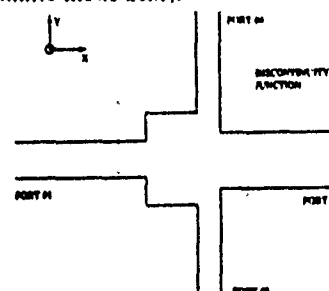


Fig. 1 A generic structure of a four port microstrip discontinuity

†This research was supported by U.S. Army Research Grant DAAL 03-86-K-0090

If a local coordinate system is used at each line and the excitation is in the  $n^{th}$  port, then away from the junctions, the current in the  $n^{th}$  port, with longitudinal component oriented in  $x$  direction, is

$$J_x^{T_n} = (e^{-j\zeta_n \beta_n x_n} - \Gamma_n e^{j\zeta_n \beta_n x_n}) f_n(y_n), \quad (1)$$

while the current in the  $p^{th}$  port in  $x$  direction, with  $p \neq n$ , is

$$J_x^{T_p} = -\frac{\zeta_p}{\zeta_n} \Gamma_p e^{-j\zeta_p \beta_p x_p} f_p(y_p). \quad (2)$$

In addition, the current in the  $q^{th}$  port in  $y$  direction is

$$J_y^{T_q} = -\frac{\zeta_q}{\zeta_n} \Gamma_q e^{-j\zeta_q \beta_q y_q} f_q(x_q). \quad (3)$$

$\zeta_k$  is a sign index function of  $k^{th}$  port.

$$\zeta_k = \begin{cases} +1 & ; k^{th} \text{ line extends to } +\infty \text{ in } x \text{ or } y \text{ direction} \\ -1 & ; k^{th} \text{ line extends to } -\infty \text{ in } x \text{ or } y \text{ direction} \end{cases} \quad (4)$$

where  $k$  could be  $p, q$  or  $n$ .  $f_k$  and  $\beta_k$  are the pre-calculated current transverse dependence and the propagation constant on the  $k^{th}$  microstrip transmission line, respectively. It is noted that, in terms of scattering parameters,  $\Gamma_k$  is  $S_{kn}$ . This aspect describes a unique feature of the approach.

The basis function of the module is chosen as a piecewise sinusoidal (PWS) function in the longitudinal direction (the direction of current flow) and a pulse function in the transverse direction. Mathematically, the current inside the module can be expressed as

$$J^{module} = \left[ \sum_{n=1}^N I_x^n g_x^n(x) h_y^n(y) \right] \hat{x} + \left[ \sum_{m=1}^M I_y^m h_x^m(x) g_y^m(y) \right] \hat{y} \quad (5)$$

The closed form of the Fourier transform of the basis function can be found.

A nearly Galerkin method is applied to transform the integral equations into a matrix equation. Inside the module, the testing functions are in the same form as the current basis functions. The testing function for the semi-infinite line, which is chosen as a piecewise sinusoidal function in direction of current flow and with the same transverse dependence as the transmission line current, is applied adjacent to the module. Finally, the matrix equation is in the form of

$$\begin{bmatrix} [Z_{nn}^{xx}] & [Z_{nn}^{xy}] & [Z_{T_{1,2}}^{xx}] & [Z_{T_{3,4}}^{xx}] \\ [Z_{nn}^{yx}] & [Z_{nn}^{yy}] & [Z_{T_{1,2}}^{yx}] & [Z_{T_{3,4}}^{yx}] \\ [Z_{T_{1,2}}^{xx}] & [Z_{T_{1,2}}^{xy}] & [Z_{T_{1,2}}^{T_{1,2}}] & [Z_{T_{3,4}}^{T_{1,2}}] \\ [Z_{T_{3,4}}^{xx}] & [Z_{T_{3,4}}^{xy}] & [Z_{T_{1,2}}^{T_{3,4}}] & [Z_{T_{3,4}}^{T_{3,4}}] \end{bmatrix} \begin{bmatrix} [I_x^n] \\ [I_y^m] \\ [\Gamma_x^{1,2}] \\ [\Gamma_y^{3,4}] \end{bmatrix} = \begin{bmatrix} [V_{in}^x] \\ [V_{in}^y] \\ [V_{in}^{T_{1,2}}] \\ [V_{in}^{T_{3,4}}] \end{bmatrix} \quad (6)$$

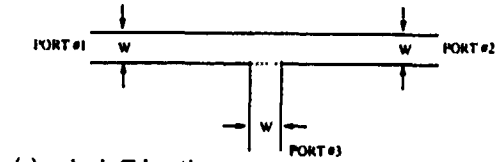
Each element in the submatrices of  $[Z]$  and  $[V_{in}]$  is the reaction between the basis function and the testing function and is in the form of a double integration in a spectral domain. The superscripts in  $[Z]$  indicate the orientations of the corresponding testing and basis functions; and the subscripts represent their locations. For instance,

$$Z_{nm}^{yx} = \frac{1}{r_0} \iint \tilde{G}_{yx}(k_x, k_y) X_x^n(k_x) Y_x^m(k_y) X_y^{m'}(k_x) Y_y^{n'}(k_y) dk_x dk_y \quad (7)$$

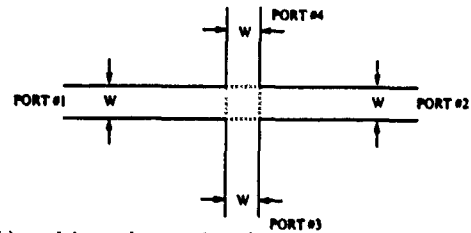
is the reaction between the basis function  $I_x^n$  (current in the  $x$  direction), with the testing function  $I_y^{m'}$  (current in the  $y$  direction).  $[V_{in}]$  is in the same mathematical form as  $[Z]$  except that the basis function is the semi-infinite mode of the incident wave.

### III. Results and Discussions:

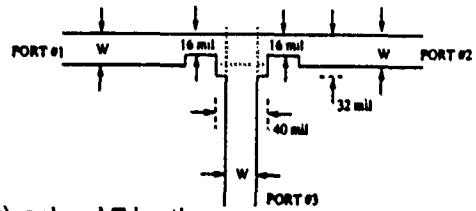
In this research, several microstrip discontinuities are analyzed by the method described above. The data generated by TOUCHSTONE version 1.7, which are essentially quasi-static results, are also presented for comparison.



(a). a basic T-junction



(b). a right angle cross junction



(c). a shaped T-junction



(d). the substrate structure

Fig. 2 Layout of a variety of junctions

A basic T-junction with three identical semi-infinite transmission lines is shown Fig. 2(a). The numerical results shown in Fig. 3 and 4 are converged within 0.2dB in magnitude and  $2.5^\circ$  in phase. The results of the magnitude of the scattering coefficients are compared against with measurements [8] and the quasi-static values (TOUCHSTONE data), and are shown in Fig. 3. It is seen that the present full-wave results are in excellent agreement with the measured data, but agree well only in the low frequency range with the TOUCHSTONE results. In the high frequency region, the unequal power transmitted on S21 and S31 observed in both theory and measurement is more significant than what TOUCHSTONE predicts. It is noted that the TOUCHSTONE results are from a quasi-static analysis, which are not as accurate at high frequencies. The full-wave results and the TOUCHSTONE results for the phase of S33 are also compared and are shown in Fig. 4. Good agreement is found below 10 GHz, but more than  $45^\circ$  discrepancy is found at 24 GHz in this particular case.

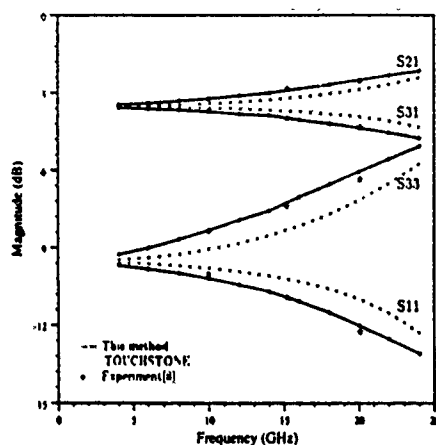


Fig. 3 Magnitude of S parameters of a basic T-junction ( $\epsilon_r = 9.9$ ,  $h = 25$  mil,  $w = 24$  mil)

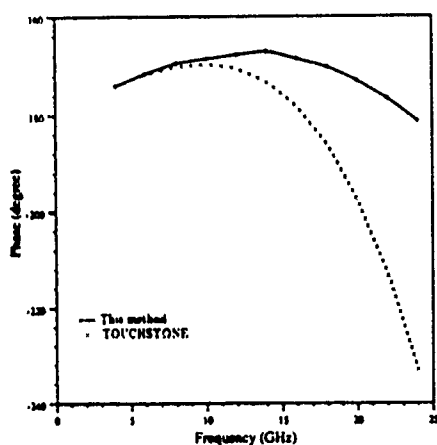


Fig. 4 Phase of S33 of a basic T-junction ( $\epsilon_r = 9.9$ ,  $h = 25$  mil,  $w = 24$  mil)

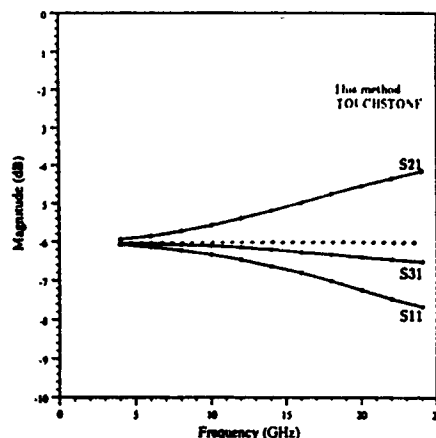


Fig. 5 Magnitude of S parameters of a right angle crossing junction ( $\epsilon_r = 10.2$ ,  $h = 25$  mil,  $w = 24$  mil)  
Note that in TOUCHSTONE  $|S11| \approx |S21| \approx |S31|$

A symmetrical cross junction is shown in Fig. 2(b), where two identical transmission lines are crossed at a right angle. With the same numerical convergence criteria as in a basic T-junction, the magnitudes of scattering coefficients are shown in Fig. 5. TOUCHSTONE predicts equal power distribution for a cross junction in a wide frequency range; however, the results of this study indicate there is an unequal power distribution for the cross junction. The phenomenon of unequal power distribution is more significant for higher frequencies. From a distributed circuit point of view, this phenomenon is obvious since port II and port III are not symmetric and the current tends to go straight through the cross junction. For a quasi-static calculation, the cross junction is like two wires jointing together and in terms of the lumped circuit concept, the power distributed in each port is certainly identical.

The problem for a basic junction is that the power transmission distributed in each port is usually restricted. For example, in a basic T-junction, there is always more power transmitted in port II than in port III, and the reflection coefficient increases as the frequency increases. In order to make the circuit design more flexible, modified or compensated discontinuities are usually used [9]. A shaped T-junction shown in Fig. 2(c) is an example of this modification. In the present full-wave analysis, the advantage of using piecewise sinusoidal basis functions can be seen in this particular application. By using piecewise sinusoidal basis functions inside the module, the shape of the junction can be quite flexible in the modeling. The design of a shaped T-junction shown in Fig. 2(c) is intended for equal-power transmission in ports II and III and small reflection coefficient at port III. If the difference of the transmitted power for ports II and III is required to be less than 0.5 dB,



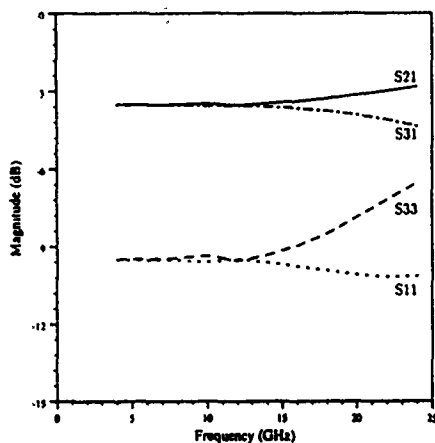


Fig. 6 Magnitude of  $S$  parameters of a shaped T-junction ( $\epsilon_r = 10.2$ ,  $h = 25$  mil,  $w = 24$  mil)

the results in Fig. 6 show that equal power transmission is very broad band (from D.C. up to 16 GHz). In comparison, for a basic T-junction, equal power transmission only valid up to 6 GHz. Besides,  $S_{33}$  of a shaped T-Junction is usually a few dB lower than that of a basic T-junction.

#### IV. Conclusion:

A full wave analysis of a multi-port network is carried out by the moment method. It has the capability of analyzing four-port irregular shaped junctions. The results for a tee and a cross junctions are presented and found in good agreement with the quasi-static results at low frequencies. An example of using a shaped T-junction to improve the performance of a basic T-junction was given. This example also illustrated the flexibility and the CAD potential of the full-wave analysis presented in this paper. The computed results are further compared against the measured data for a tee junction. The comparison shows excellent agreement.

#### Acknowledgement:

The authors wish to thank Professor Ingo Wolff and his colleagues for providing the measured T-junction results.

## References

- [1] P.B. Katehi and N.G. Alexopoulos, "Frequency-dependent characteristics of microstrip discontinuities in millimeter wave integrated circuits," *IEEE Trans. on Microwave Theory and Techniques*, Vol. MTT-33, pp.1029-1035, Oct. 1985.
- [2] R.W. Jackson and D. M. Pozar, "Full wave analysis of microstrip open-end and gap discontinuities," *IEEE Trans. on Microwave Theory and Techniques*, Vol. MTT-33, pp.1036-1042, Oct. 1985.
- [3] H.Y. Yang, N.G. Alexopoulos and D.R. Jackson, "Microstrip open-end and gap discontinuities in a substrate-superstrate structure," *IEEE Trans. on Microwave Theory and Techniques*, Vol. MTT-37, pp.1542-1546, Oct. 1989.
- [4] R.W. Jackson, "Full-wave, finite element analysis of irregular microstrip discontinuities," *IEEE Trans. on Microwave Theory and Techniques*, Vol. MTT-37, pp. 81-89, Jan. 1989.
- [5] J.R. Mosig, "Arbitrarily shaped microstrip structures and their analysis with a mixed potential integral equation," *IEEE Trans. on Microwave Theory and Techniques*, Vol. MTT-36, pp. 314-323, Feb. 1988.
- [6] A. Skrivervik and J.R. Mosig, "Equivalent circuits of microstrip discontinuities including radiation effects," 1989 IEEE MTT-S International Microwave Symposium Digest, pp. 1147-1150.
- [7] W.P. Harokopus and P.B. Katehi, "An accurate characterization of open microstrip discontinuities including radiation losses," 1989 IEEE MTT-S International Microwave Symposium Digest, pp. 231-234.
- [8] I. Wolff, private communication
- [9] M. Dydyk, "Master the T-junction and sharpen your MIC designs," *Microwaves*, pp.184-186, May 1977.

# A Generalized Method for the Distinction of Radiation and Surface-Wave Losses in Microstrip Discontinuities<sup>†</sup>

T.S. Horng, S.C. Wu, H.Y. Yang, and N.G. Alexopoulos

Electrical Engineering Department, University of California, Los Angeles  
Los Angeles, CA 90024

## Abstract

A generalized method for calculating both radiation and surface-wave losses is developed for microstrip discontinuities. The losses are determined by a rigorous Poynting vector analysis where the current distribution over the entire microstrip discontinuities is a result of a full-wave moment method solution. It is found that above a certain frequency, the surface-wave loss becomes more important than the radiation loss. A self-consistency check of the results based on power conservation is also presented.

## Introduction

Radiation and surface waves are unavoidable physical effects of microstrip discontinuities associated with an open structure. In recent years, a full-wave analysis that includes these physical effects has been developed for various microstrip discontinuities [1-5]. Although both radiation and surface waves are included, the analysis only provides the total losses. One still can not distinguish the percentage of power losses due to radiation and due to surface waves. The full-wave analysis employs the moment method to find the currents in the microstrip circuits and subsequently, the circuit parameters of the discontinuities. From an antenna

point of view, once the currents in a conductor are known, the time-harmonic fields can be computed. From the theory of printed circuit antennas [6], the radiated space waves are spherical waves in the hemisphere above the substrate; while surface waves are cylindrical waves guided along the planar direction of the substrate and decay exponentially toward the free space. The power due to radiation and surface waves can therefore be computed separately through a rigorous Poynting vector analysis. In this work, radiation and surface-wave losses for several types of microstrip discontinuities are investigated. These discontinuities include open-end, right-angle bend, rectangular patch and overlay electromagnetically coupled (EMC) lines.

## Analysis

In the integral equation formulations, all field components can be expressed in terms of the dyadic Green's functions and the current components. Therefore, the current distribution over an entire discontinuity can be treated as a basic block [7] for this analysis. The radiation loss can be calculated by integrating the Poynting vector over an infinite plane (shown in Fig. 1) in the free space above the entire microstrip circuits. The expression is written as

$$P_{ra} = \frac{1}{2} R_0 \iint_{\Sigma} (\vec{E} \times \vec{H}^*) \cdot \vec{ds} \quad (1)$$

<sup>†</sup> This research was supported under U.S. Army Research Office Grant DAAL 03-86-k-0090

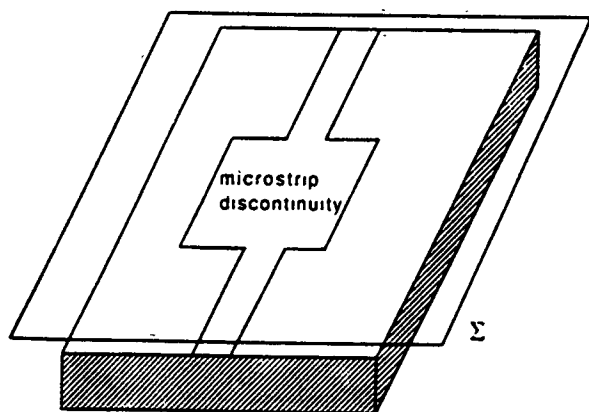


Fig. 1. Integration plane for calculating radiation loss.

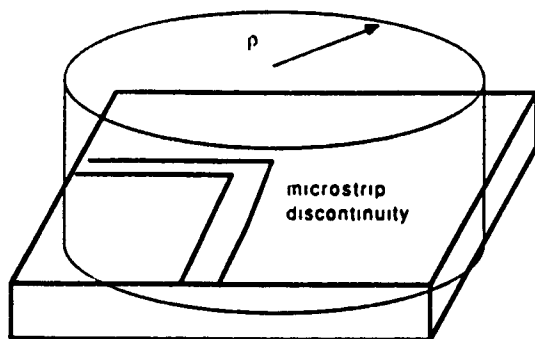


Fig. 2. Integration cylinder for calculating surface-wave loss.

Frequency (GHz)	Total Power	Reflected Power	Transmitted Power	Radiation Loss	Surface-wave Loss
20	1.001	0.134	0.822	0.022	0.023
21	0.997	0.153	0.787	0.027	0.030
22	1.001	0.172	0.755	0.033	0.041
23	1.005	0.193	0.719	0.039	0.054
24	1.007	0.208	0.678	0.048	0.073

Table 1. Power conservation check for right-angle bend discontinuity.  
(Parameters are the same as those in Fig. 4.)

Surface waves can be obtained from the residues of the Fourier integrals in the spectral domain approach. With the characteristics that surface waves propagate along the surface, the surface-wave loss can be found by integrating the Poynting vector over a cylinder (shown in Fig. 2) of large radius  $\rho$ . The expression of the surface-wave power is

$$P_{su} = \int_0^\infty \int_0^{2\pi} \frac{1}{2} R_c (\vec{E}_{res} \times \vec{H}_{res}^*) \cdot \hat{\rho} \rho d\phi dz \quad (2)$$

## Numerical Results and Discussions

Due to power conservation, the summation of each power should be equivalent to the incident power. An example of this check is shown in Table I. The incident power is normalized to 1. Due to power conservation, total power which is the summation of reflected, transmitted, radiated and surface-wave power should be equal to 1. The result in Table I shows excellent agreement.

Figs. 3-5 show the percentage of radiation loss, surface-wave loss, and total power loss as a function of frequency for open-end, right-angle bend, and overlay electromagnetically coupled lines respectively. It is seen that the losses due to both radiation and surface waves increase with frequency. At low frequencies, the losses are mainly due to radiation. When the frequency increases, surface-wave loss increases faster than the radiation loss. Above a certain frequency, the surface-wave loss is more significant than the radiation loss. Fig. 6 shows the power distributions of a rectangular patch antenna. It can be seen that the maximum radiation efficiency is about 65% in a very narrow band around 7.2GHz with about 10% surface wave loss and 25% return loss.

## Conclusions

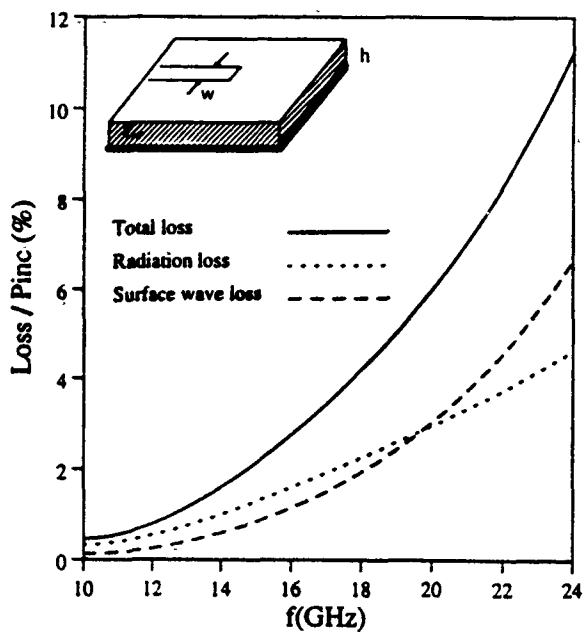


Fig. 3. Power losses versus frequency for open-end discontinuity.  
( $\epsilon_r = 10.2$ ,  $w = 24\text{mil}$ ,  $h = 25\text{mil}$ )

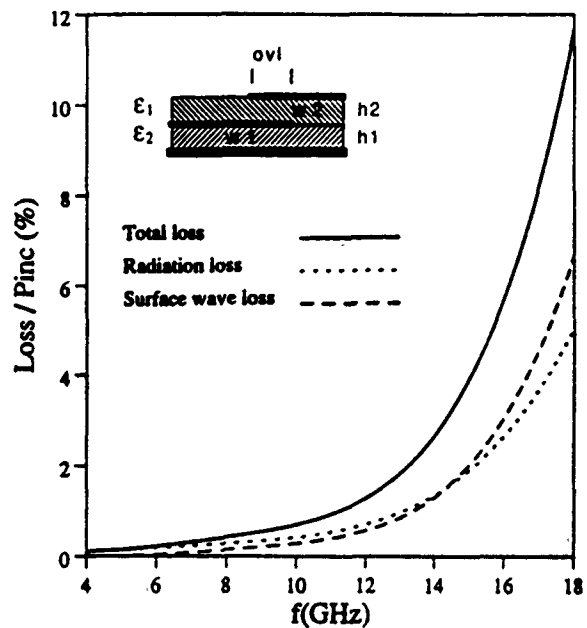


Fig. 5. Power losses versus frequency for overlay EMC lines.  
( $\epsilon_r = 2.2$ ,  $\epsilon_r = 10.2$ ,  $h_1 = 25\text{mil}$ ,  $h_2 = 25\text{mil}$ ,  
 $w_1 = 42\text{mil}$ ,  $w_2 = 76\text{mil}$ ,  $ovl = 83\text{mil}$ )

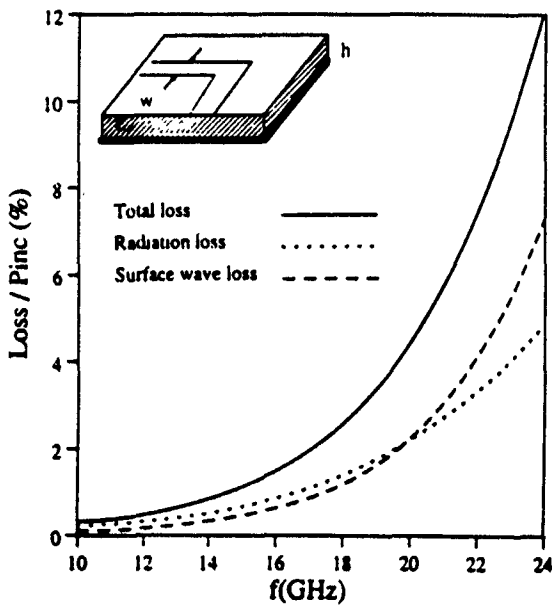


Fig. 4. Power losses versus frequency for right-angle bend discontinuity.  
( $\epsilon_r = 10.2$ ,  $w = 24\text{mil}$ ,  $h = 25\text{mil}$ )

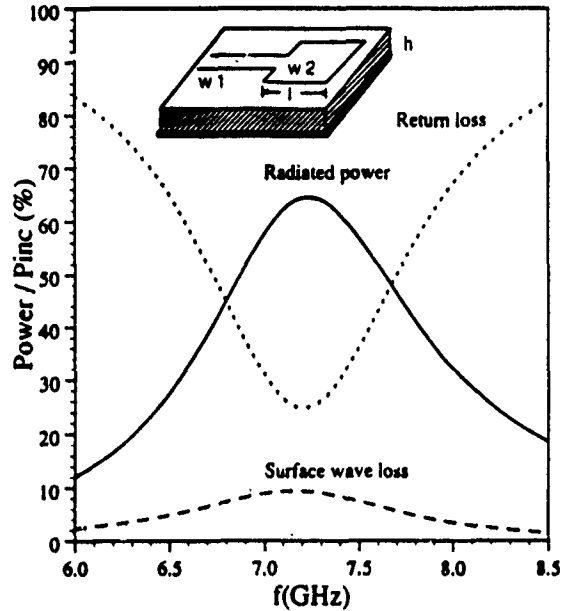


Fig. 6. Power distributions versus frequency for a rectangular patch antenna.  
( $\epsilon_r = 2.33$ ,  $w_1 = 50\text{mil}$ ,  $h = 62\text{mil}$ ,  $w_2 = 500\text{mil}$ ,  $l = 500\text{mil}$ )

A generalized method to distinguish power losses due to radiation and surface waves is presented. This method should aid in CAD for minimizing power losses launched into radiated space waves and surface waves from arbitrary microstrip discontinuities and maximizing the radiation efficiency for arbitrary patch antennas. Power loss mechanism in other types of microstrip discontinuities, such as gap, step and stubline will be easily implemented in this analysis.

## References

- [1] P.B. Katehi and N.G. Alexopoulos, "Frequency Dependent Characteristics of Microstrip Discontinuities in Millimeter-Wave Integrated Circuits," *IEEE Trans. on Microwave Theory and Techniques*, Vol. MTT-33, pp. 1029-1035, Oct. 1985.
- [2] H.Y. Yang and N.G. Alexopoulos, "Basic building block for high frequency interconnects: theory and experiment," *IEEE Trans. on Microwave Theory and Techniques*, Vol. MTT-36, pp. 1258-1264, Aug. 1988.
- [3] R.W. Jackson and D.M. Pozar, "Full-wave analysis of microstrip open-end and gap discontinuities," *IEEE Trans. on Microwave Theory and Techniques*, Vol. MTT-33 pp. 1036-1042, Oct. 1985.
- [4] A. Skrivervik and J.R. Mosig, "Equivalent circuits of microstrip discontinuities including radiation effects," 1989 *IEEE MTT-S International Microwave Symposium Digest*, pp. 1147-1150.
- [5] W.P. Harokopus and P.B. Katehi, "An accurate characterization of open microstrip discontinuities including radiation losses," 1989 *IEEE MTT-S International Microwave Symposium Digest*, pp. 231-234.
- [6] N.G. Alexopoulos and D.R. Jackson, "Fundamental superstrate (cover) effects on printed circuit antennas," *IEEE Trans. on Antennas and Propagation*, Vol. AP-32, pp. 807-816, Aug. 1984.
- [7] S.C. Wu, H.Y. Yang and N.G. Alexopoulos, "A rigorous dispersive characterization of microstrip cross and tee junctions," *IEEE MTT-S International Microwave Symposium*, to be published.

**UNIVERSITY OF CALIFORNIA**

**Los Angeles**

**LINE-TO-LINE TRANSITIONS IN THREE LAYER  
SHIELDED MICROSTRIPS**

**A thesis submitted in partial satisfaction of the  
requirements for the degree  
Master of Science in Electrical Engineering**

**By**

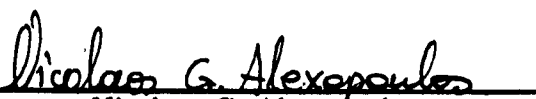
**Tzyy-Sheng Horng**

**1990**

The thesis of Tzyy-Sheng Horng is approved.

  
Robert S. Elliott

  
Yahya Rahmat-Samii

  
Nicolaos G. Alexopoulos,  
Committee Chair


University of California, Los Angeles

1990

The thesis of Tzyy-Sheng Horng is approved.

  
Robert S. Elliott

  
Yahya Rahmat-Samii

  
Nicolaos G. Alexopoulos,  
Committee Chair

University of California, Los Angeles

1990



## **Dedication**

**To my parents**

## Table of Contents

List of figures .....	v
List of Tables .....	vii
Acknowledgements .....	viii
Abstract .....	ix
I     Introduction .....	1
II    The dispersion characteristics of three layer shielded microstrip lines ..	4
2.1   Green's function for three layer shielded microstrips .....	4
2.2   Integral equations for calculating propagation constants .....	8
2.3   Spectral domain calculation of characteristic impedance .....	13
2.4   Numerical results and discussions .....	15
III   Full wave analysis of shielded microstrip line-to-line transitions .....	30
3.1   Green's function formulation and the method of moments .....	30
3.2   Numerical results and discussions .....	38
3.3   Power conservation check .....	46
IV    Conclusions .....	52
References .....	53
Appendix A .....	55
Appendix B .....	59
Appendix C .....	61
Appendix D .....	63

## List of Figures

Fig. 2.1	An electric Hertzian dipole in a three layer shielded structure ....	4
Fig. 2.2	Expansion functions .....	11
Fig. 2.3	Shielded microstrip lines .....	16
Fig. 2.4	Characteristics of a single line versus permittivity .....	18
Fig. 2.5	Characteristics of a single line versus strip-width .....	19
Fig. 2.6	Characteristics of a single line versus strip-offset .....	20
Fig. 2.7	Characteristics of a single line versus normalized frequency .....	21
Fig. 2.8	Characteristics of symmetric coupled lines versus strip-offset ....	23
Fig. 2.9	Characteristics of asymmetric coupled lines versus normalized frequency .....	24
Fig. 2.10	Current distributions of asymmetric coupled lines .....	25
Fig. 2.11	Characteristics of symmetric coupled lines in comparison with Ref[13] .....	26
Fig. 2.12	Characteristics of asymmetric coupled lines in comparison with Ref[15] .....	27
Fig. 3.1	Edge-coupled line-to-line transition .....	31
Fig. 3.2	Overlay-coupled line-to-line transition .....	32
Fig. 3.3	Overlay coupled-to-single line-to-line transition .....	33
Fig. 3.4	Layout of expansion modes for longitudinal currents and transverse currents .....	35
Fig. 3.5	$ \Gamma $ versus overlap for the configuration of Fig. 3.1 .....	39
Fig. 3.6	$ T $ versus overlap for the configuration of Fig. 3.1 .....	39
Fig. 3.7	$ \Gamma $ versus overlap for the configuration of Fig. 3.2 .....	40
Fig. 3.8	$ T $ versus overlap for the configuration of Fig. 3.2 .....	40

Fig. 3.9	$ \Gamma $ versus overlap for even-mode excitation (configuration Fig. 3.3) .....	41
Fig. 3.10	$ T $ versus overlap for even-mode excitation (configuration Fig. 3.3) .....	41
Fig. 3.11	$ \Gamma $ versus overlap for odd-mode excitation (configuration Fig. 3.3) .....	42
Fig. 3.12	$ T $ versus overlap for odd-mode excitation (configuration Fig. 3.3) .....	42
Fig. 3.13	Magnitude of $\Gamma$ and $T$ versus frequency (configuration Fig. 3.2) .....	45
Fig. 3.14	Phase of $\Gamma$ and $T$ versus frequency (configuration Fig. 3.2) .....	45

## **List of Tables**

<b>Table 2.1</b>	<b>Characteristics of two layer symmetric coupled lines in comparison with the quasistatic results Ref[12]</b>	<b>29</b>
<b>Table 3.1</b>	<b>Power conservation check for the configuration of Fig. 3.1</b>	<b>48</b>
<b>Table 3.2</b>	<b>Power conservation check for the configuration of Fig. 3.2</b>	<b>49</b>
<b>Table 3.3</b>	<b>Power conservation check for the configuration of Fig. 3.3 (even-mode excitation)</b>	<b>50</b>
<b>Table 3.4</b>	<b>Power conservation check for the configuration of Fig. 3.3 (odd-mode excitation)</b>	<b>51</b>

## **Acknowledgements**

I would like to express my gratitude to Professor N.G. Alexopoulos for his support and guidance during this research.

I would also like to thank Dr. H.Y. Yang for his many helpful insights and technical discussions.

Finally I would thank Professors R.S. Elliott and Y. Rahmat-Samii for serving in the committee.

**ABSTRACT OF THE THESIS**

**LINE-TO-LINE TRANSITIONS IN THREE LAYER**

**SHIELDED MICROSTRIPS**

by

**Tzyy-Sheng Horng**

**Master of Science in Electrical Engineering**

**University of California, Los Angeles, 1990**

**Professor Nicolaos G. Alexopoulos, Chair**

This thesis is mainly composed of two parts. The first part is to determine the frequency-dependent characteristics of microstrip lines in a three layer shielded structure. Numerical results given in this part include the propagation constant, characteristic impedance and transverse dependence of longitudinal and transverse currents of both microstrip single and coupled lines for a variety of dielectric configurations. The second part is to analyze the behavior of several types of microstrip line-to-line transitions. The methodology employs a moment method procedure where the combination of subdomain expansion modes and entire domain microstrip modes is used. The transitions studied include edge-coupled lines, overlay-coupled lines and coupled-to-single lines. A power conservation check based on a rigorous Poynting vector analysis is also used to determine the accuracy of the numerical convergence.

# **Chapter I**

## **Introduction**

Shielded microstrips are commonly encountered in microwave and millimeter integrated circuits. The advantages include relatively low losses and fairly high Q-factor as compared with open microstrips[1]. Many applications such as high directivity directional couplers and broadband filters have been realized in shielded structures[2][3]. In antenna applications, shielded microstrips can provide nice features when used to feed a linear array of slots in the outer conductor wall[4]. For sufficiently low frequencies, the quasi-static theory can be employed to characterize shielded microstrip lines and their discontinuities reasonably well[5]-[8]. However, as the frequency increases, the deviation from quasi-static behavior becomes significant and a more rigorous full-wave analysis is necessary.

To calculate accurately the dispersion characteristics of shielded microstrip lines, the spectral-domain analysis proposed by Itoh and Mittra[9] is numerically simpler and more efficient than the conventional space-domain techniques. This method allows one to convert convolutions into algebraic equations in the Green's function formulation; thus avoiding the necessity of the evaluation of complicated integrals. Since the strip-width and strip-offset are comparable to the waveguide dimensions, the transverse current component should not be neglected and a complete dyadic Green's function is required. After deriving the spectral-domain Green's function for a three layer shielded structure, boundary conditions on the strips are employed to obtain integral equations. As a result, the propagation constant and current distributions on the strips can be determined by the method



of moments. An impedance definition using power and total currents are chosen to describe the exchange of power with TEM lines [10]. Once the current distributions on the strips are found, the six field components can be obtained and the characteristic impedance can be calculated through performing the surface integral of the Poynting vector in the propagating direction.

Based on the analysis described in Chapter II, the computer program developed for calculating the dispersion characteristics of shielded microstrip lines can offer the capacity to analyze the shielded microstrip single and coupled lines with arbitrary strip-width and strip-offset, while only limited results in some special cases were reported by a few authors [12]-[15].

Several types of shielded microstrip line-to-line transitions are also studied in this thesis as the important building blocks for high frequency inter-connects. Applications in mm-wave integrated circuits include high-pass filter, multiplexers and directional couplers. Losch [17] has designed a broadband highpass filter in realization of an overlay-coupled line transition based on a quasi-static formulation. A more rigorous full-wave analysis for coupled line filters associated with the open structure has been discussed by Katehi [18] for an edge-coupled transition and by Yang and Alexopoulos [20] for an overlay-coupled transition. In [20] a spectral-domain approach by expanding the current in the coupled line section with a combination of entire domain and subdomain modes is used. This mode expansion mechanism seems to be the most efficient and fruitful by far. For the advantage of preventing unnecessary interaction and radiation loss, a waveguide housing is sometimes more practical to the real circuit design. In Chapter III, a full-wave moment method is used to characterize shielded line-to-line transitions. The transitions including edge-coupled lines, overlay-coupled lines and

coupled-to-single lines are investigated.

For shielded microstrip transitions, the incident power should be equal to the summation of reflected power, transmitted power and some losses coupled to the higher order modes and the multi-layered waveguide modes. With proper waveguide dimensions, the losses coupled to the higher order modes and the multi-layered waveguide modes can be removed. Therefore, a power conservation among the incident, reflected and transmitted powers can be checked to determine the numerical accuracy. In Chapter III, the scattering coefficients are obtained through the method of moments. However, due to the different characteristic impedance between the feedline and the parasitic coupled line, these coefficients can't contain the information of power conservation. With the characteristic impedance obtained through the Poynting vector analysis described in Chapter II, the reflected power associated with the feedline and the transmitted power associated with the parasitic coupled line can be normalized respectively by the product of the characteristic impedance and the square of the absolute value of scattering coefficient for each line.

The results of power distributions and scattering coefficients of line-to-line transitions can identify the properties and applications of each transition.

## Chapter II

### The Dispersion Characteristics of Three Layer

#### Shielded Microstrip Lines

##### 2.1 Green's Function for Three Layer Shielded Microstrips

In this section, the dyadic Green's function for an electric Hertzian dipole embedded in a three layer shielded structure is derived in a spectral domain. The geometry shown in Fig. 2.1 contains three different dielectric layers with permittivity  $\epsilon_1, \epsilon_2, \epsilon_3$ , and thickness  $h_1, h_2, h_3$  respectively. The permeability in each region is assumed  $\mu_0$ , the free space permeability. The total thickness is  $b$  and the distance between two sidewalls is  $a$ . The dipole, oriented in the planar( $x$  or  $z$ ) direction, is located either at  $y = h_1$  or at  $y = h_1 + h_2$ .

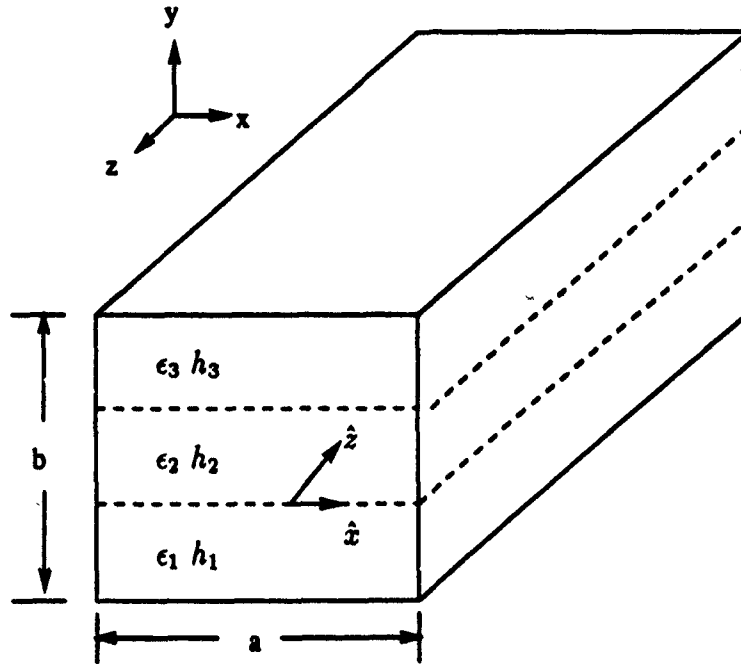


Fig. 2.1 An electric Hertzian dipole in a three layer shielded structure.

Instead of deriving the fields directly, the Green's function is more easily obtained from a Hertz potential  $\vec{\Pi}$  which satisfies the differential equations

$$\nabla^2 \vec{\Pi}_{(i)} + k_i^2 \vec{\Pi}_{(i)} = 0, \quad (2.1)$$

where subscript  $i$  identifies different dielectric layers,  $i = 1, 2, 3$ . The boundary conditions at each interface for a dipole oriented in the  $z$  direction and located at  $x = x_1', y = h_1, z = 0$  are  
at  $y = h_1 + h_2$ ,

$$k_3^2 \Pi_{3z} = k_2^2 \Pi_{2z}, \quad (2.2)$$

$$j\omega\epsilon_3 \frac{\partial \Pi_{3z}}{\partial y} - j\omega\epsilon_2 \frac{\partial \Pi_{2z}}{\partial y} = 0, \quad (2.3)$$

$$\epsilon_3 \Pi_{3y}^z = \epsilon_2 \Pi_{2y}^z, \quad (2.4)$$

$$\frac{\partial \Pi_{3y}^z}{\partial y} - \frac{\partial \Pi_{2y}^z}{\partial y} = \frac{\partial \Pi_{2z}}{\partial z} - \frac{\partial \Pi_{3z}}{\partial z}, \quad (2.5)$$

and at  $y = h_1$ ,

$$k_2^2 \Pi_{2z} = k_1^2 \Pi_{1z}, \quad (2.6)$$

$$j\omega\epsilon_2 \frac{\partial \Pi_{2z}}{\partial y} - j\omega\epsilon_1 \frac{\partial \Pi_{1z}}{\partial y} = -\delta(x - x_1')\delta(z), \quad (2.7)$$

$$\epsilon_2 \Pi_{2y}^z = \epsilon_1 \Pi_{1y}^z, \quad (2.8)$$

$$\frac{\partial \Pi_{2y}^z}{\partial y} - \frac{\partial \Pi_{1y}^z}{\partial y} = \frac{\partial \Pi_{1z}}{\partial z} - \frac{\partial \Pi_{2z}}{\partial z}. \quad (2.9)$$

When the dipole is oriented in  $x$  direction, the boundary conditions are  
at  $y = h_1 + h_2$ ,

$$k_3^2 \Pi_{3x} = k_2^2 \Pi_{2x}, \quad (2.10)$$

$$j\omega\epsilon_3 \frac{\partial \Pi_{3x}}{\partial y} - j\omega\epsilon_2 \frac{\partial \Pi_{2x}}{\partial y} = 0, \quad (2.11)$$

$$\epsilon_3 \Pi_{3y}^x = \epsilon_2 \Pi_{2y}^x, \quad (2.12)$$

$$\frac{\partial \Pi_{3y}^x}{\partial y} - \frac{\partial \Pi_{2y}^x}{\partial y} = \frac{\partial \Pi_{2x}}{\partial x} - \frac{\partial \Pi_{3x}}{\partial x}, \quad (2.13)$$

and at  $y = h_1$ ,

$$k_2^2 \Pi_{2x} = k_1^2 \Pi_{1x}, \quad (2.14)$$

$$j\omega\epsilon_2 \frac{\partial \Pi_{2x}}{\partial y} - j\omega\epsilon_1 \frac{\partial \Pi_{1x}}{\partial y} = -\delta(x - x'_1)\delta(z), \quad (2.15)$$

$$\epsilon_2 \Pi_{2y}^z = \epsilon_1 \Pi_{1y}^z, \quad (2.16)$$

$$\frac{\partial \Pi_{2y}^z}{\partial y} - \frac{\partial \Pi_{1y}^z}{\partial y} = \frac{\partial \Pi_{1x}}{\partial x} - \frac{\partial \Pi_{2x}}{\partial x}, \quad (2.17)$$

where  $\vec{\Pi}_i = \Pi_{ix}\hat{x} + \Pi_{iy}\hat{y} + \Pi_{iz}\hat{z}$ ,  $\Pi_{iy} = \Pi_{iy}^x + \Pi_{iy}^z$  and  $k_i$  is equal to  $\omega\sqrt{\epsilon_i\mu_0}$ .

By matching the boundary conditions that the tangential electric fields are zero at  $x = 0, x = a, y = 0$  and  $y = b$ , the two-dimensional Fourier transform of the Hertz potential in each region can be defined as,

in region 3,

$$\Pi_{3x}(x, y, z) = \frac{1}{2\pi a} \sum_{n=-\infty}^{\infty} \int_{-\infty}^{\infty} A_x \sinh q_3(b-y) \sin \alpha_n x e^{-j\beta z} d\beta, \quad (2.18)$$

$$\Pi_{3x}(x, y, z) = \frac{1}{2\pi a} \sum_{n=-\infty}^{\infty} \int_{-\infty}^{\infty} A_x \sinh q_3(b-y) \cos \alpha_n x e^{-j\beta z} d\beta, \quad (2.19)$$

$$\Pi_{3y}^z(x, y, z) = \frac{1}{2\pi a} \sum_{n=-\infty}^{\infty} \int_{-\infty}^{\infty} A'_x \cosh q_3(b-y) \sin \alpha_n x e^{-j\beta z} d\beta, \quad (2.20)$$

$$\Pi_{3y}^x(x, y, z) = \frac{1}{2\pi a} \sum_{n=-\infty}^{\infty} \int_{-\infty}^{\infty} A'_x \cosh q_3(b-y) \cos \alpha_n x e^{-j\beta z} d\beta, \quad (2.21)$$

in region 2,

$$\Pi_{2x}(x, y, z) = \frac{1}{2\pi a} \sum_{n=-\infty}^{\infty} \int_{-\infty}^{\infty} (B_x \sinh q_2 y + C_x \cosh q_2 y) \sin \alpha_n x e^{-j\beta z} d\beta, \quad (2.22)$$

$$\Pi_{2x}(x, y, z) = \frac{1}{2\pi a} \sum_{n=-\infty}^{\infty} \int_{-\infty}^{\infty} (B_x \sinh q_2 y + C_x \cosh q_2 y) \cos \alpha_n x e^{-j\beta z} d\beta, \quad (2.23)$$

$$\Pi_{2y}^z(x, y, z) = \frac{1}{2\pi a} \sum_{n=-\infty}^{\infty} \int_{-\infty}^{\infty} (B'_x \sinh q_2 y + C'_x \cosh q_2 y) \sin \alpha_n x e^{-j\beta z} d\beta, \quad (2.24)$$

$$\Pi_{2y}^x(x, y, z) = \frac{1}{2\pi a} \sum_{n=-\infty}^{\infty} \int_{-\infty}^{\infty} (B'_x \sinh q_2 y + C'_x \cosh q_2 y) \cos \alpha_n x e^{-j\beta z} d\beta, \quad (2.25)$$

and in region 1,

$$\Pi_{1z}(x, y, z) = \frac{1}{2\pi a} \sum_{n=-\infty}^{\infty} \int_{-\infty}^{\infty} D_z \sinh q_1 y \sin \alpha_n x e^{-j\beta z} d\beta, \quad (2.26)$$

$$\Pi_{1x}(x, y, z) = \frac{1}{2\pi a} \sum_{n=-\infty}^{\infty} \int_{-\infty}^{\infty} D_x \sinh q_1 y \cos \alpha_n x e^{-j\beta z} d\beta, \quad (2.27)$$

$$\Pi_{1y}^z(x, y, z) = \frac{1}{2\pi a} \sum_{n=-\infty}^{\infty} \int_{-\infty}^{\infty} D'_z \cosh q_1 y \sin \alpha_n x e^{-j\beta z} d\beta, \quad (2.28)$$

$$\Pi_{1y}^x(x, y, z) = \frac{1}{2\pi a} \sum_{n=-\infty}^{\infty} \int_{-\infty}^{\infty} D'_x \cosh q_1 y \sin \alpha_n x e^{-j\beta z} d\beta, \quad (2.29)$$

where  $q_i = \sqrt{\alpha_n^2 + \beta^2 - k_i^2}$  and  $\alpha_n = \frac{n\pi}{a}$ . The coefficients  $A_z, A'_z, B_z, B'_z, \dots, D'_x$  are determined by substituting Eqs. [2.18]-[2.29] into Eqs. [2.2]-[2.17]. The results are listed in Appendix A.

The lateral electromagnetic fields in region  $i$  are related to the Hertz potential through

$$E_{iz} = k_i^2 \Pi_{iz} + \frac{\partial}{\partial x} \left( \frac{\partial \Pi_{iz}}{\partial x} + \frac{\partial \Pi_{iy}}{\partial y} + \frac{\partial \Pi_{iz}}{\partial z} \right), \quad (2.30)$$

$$E_{iy} = k_i^2 \Pi_{iy} + \frac{\partial}{\partial y} \left( \frac{\partial \Pi_{iz}}{\partial x} + \frac{\partial \Pi_{iy}}{\partial y} + \frac{\partial \Pi_{iz}}{\partial z} \right), \quad (2.31)$$

$$E_{iz} = k_i^2 \Pi_{iz} + \frac{\partial}{\partial z} \left( \frac{\partial \Pi_{iz}}{\partial x} + \frac{\partial \Pi_{iy}}{\partial y} + \frac{\partial \Pi_{iz}}{\partial z} \right), \quad (2.32)$$

$$H_{iz} = j\omega\epsilon_i \left( \frac{\partial \Pi_{iz}}{\partial y} - \frac{\partial \Pi_{iy}}{\partial z} \right), \quad (2.33)$$

$$H_{iy} = j\omega\epsilon_i \left( \frac{\partial \Pi_{iz}}{\partial z} - \frac{\partial \Pi_{iz}}{\partial x} \right), \quad (2.34)$$

and

$$H_{iz} = j\omega\epsilon_i \left( \frac{\partial \Pi_{iy}}{\partial x} - \frac{\partial \Pi_{iz}}{\partial y} \right). \quad (2.35)$$

Taking the two-dimensional Fourier transform of the electric field components in Eqs. [2.30]-[2.32], the spectral-domain dyadic Green's function at each

interface is then obtained as follows

$$\tilde{E}_{1x}(y = h_1) = \tilde{G}_{11xx} \cos \alpha_n x \cos \alpha_n x'_1 + \tilde{G}_{11xz} \cos \alpha_n x \sin \alpha_n x'_1, \quad (2.36)$$

$$\tilde{E}_{1z}(y = h_1) = \tilde{G}_{11xz} \sin \alpha_n x \sin \alpha_n x'_1 + \tilde{G}_{11xx} \sin \alpha_n x \cos \alpha_n x'_1, \quad (2.37)$$

$$\tilde{E}_{1x}(y = h_1 + h_2) = \tilde{G}_{21xx} \cos \alpha_n x \cos \alpha_n x'_1 + \tilde{G}_{21xz} \cos \alpha_n x \sin \alpha_n x'_1, \quad (2.38)$$

$$\tilde{E}_{1z}(y = h_1 + h_2) = \tilde{G}_{21xz} \sin \alpha_n x \sin \alpha_n x'_1 + \tilde{G}_{21xx} \sin \alpha_n x \cos \alpha_n x'_1. \quad (2.39)$$

For a dipole oriented in the planar direction and located at  $x = x'_2, y = h_1 + h_2$  and  $z = 0$ , the expressions for the dyadic Green's function are the same except replacing  $\epsilon_1, h_1, x'_1$  by  $\epsilon_3, h_3, x'_2$ , respectively. The expressions are

$$\tilde{E}_{2x}(y = h_1) = \tilde{G}_{12xx} \cos \alpha_n x \cos \alpha_n x'_2 + \tilde{G}_{12xz} \cos \alpha_n x \sin \alpha_n x'_2, \quad (2.40)$$

$$\tilde{E}_{2z}(y = h_1) = \tilde{G}_{12xz} \sin \alpha_n x \sin \alpha_n x'_2 + \tilde{G}_{12xx} \sin \alpha_n x \cos \alpha_n x'_2, \quad (2.41)$$

$$\tilde{E}_{2x}(y = h_1 + h_2) = \tilde{G}_{22xx} \cos \alpha_n x \cos \alpha_n x'_2 + \tilde{G}_{22xz} \cos \alpha_n x \sin \alpha_n x'_2, \quad (2.42)$$

$$\tilde{E}_{2z}(y = h_1 + h_2) = \tilde{G}_{22xz} \sin \alpha_n x \sin \alpha_n x'_2 + \tilde{G}_{22xx} \sin \alpha_n x \cos \alpha_n x'_2. \quad (2.43)$$

In Eqs. [2.36]-[2.43] the functions  $\tilde{E}_{i\hat{u}}$  are defined as

$$E_{i\hat{u}}(x, y = y_i, z) = \frac{1}{2\pi a} \sum_{n=-\infty}^{\infty} \int_{-\infty}^{\infty} \tilde{E}_{\hat{u}}(\alpha_n, \beta, x, x') e^{-j\beta(z-z')} d\beta \quad (2.44)$$

and the spectral-domain Green's functions  $\tilde{G}_{ij\hat{u}_1\hat{u}_2}$  can be found in Appendix B.

## 2.2 Integral Equations for Calculating Propagation Constants

By superposition, the total electric fields due to the currents on the microstrips are

$$\tilde{E}(x, y, z) = \iint \tilde{\mathcal{C}}_E^{\text{m}}(x, y, z; x', z') \cdot \tilde{J}(x', z') dx' dz', \quad (2.45)$$

where the spatial domain dyadic Green's function is equivalent to

$$\overline{\overline{G}}_E(x, y, z; x', z') = \frac{1}{2\pi a} \sum_{n=-\infty}^{\infty} \int_{-\infty}^{\infty} \overline{\overline{G}}(\alpha_n, \beta, y) \begin{pmatrix} \sin \alpha_n x \\ \cos \alpha_n x \end{pmatrix} \begin{pmatrix} \sin \alpha_n x' \\ \cos \alpha_n x' \end{pmatrix} e^{-j\beta(z-z')} d\beta. \quad (2.46)$$

The spectral-domain dyadic Green's functions  $\overline{\overline{G}}$  at each interface are expressed in Appendix B. For microstrip lines located at  $y = h_1$  and  $h_1 + h_2$ , the currents on strips are traveling along the  $z$ -axis with propagation constants  $\beta_p$  and can be written as

$$\vec{J}_1(x', y', z') = (J_{1tx}(x')\hat{x} + J_{1tz}(x')\hat{z})e^{-j\beta_p z'} \quad (2.47)$$

and

$$\vec{J}_2(x', y', z') = (J_{2tx}(x')\hat{x} + J_{2tz}(x')\hat{z})e^{-j\beta_p z'}, \quad (2.48)$$

respectively. With the boundary conditions that tangential electric fields are zero on the strips, the integral equations can be obtained by substituting Eqs. [2.47], [2.48] into Eqs. [2.45],[2.46]. For each  $(x, z)$  on the microstrips, these integral equations are

$$\begin{bmatrix} E_{1x}(x, y = h_1, z) \\ E_{1z}(x, y = h_1, z) \\ E_{2x}(x, y = h_1 + h_2, z) \\ E_{2z}(x, y = h_1 + h_2, z) \end{bmatrix} = \frac{1}{a} e^{-j\beta_p z} \sum_{n=-\infty}^{\infty} \overline{\overline{G}}_1(\alpha_n, \beta_p, x) \begin{bmatrix} \int J_{1tx}(x') \sin \alpha_n x' dx' \\ \int J_{1tz}(x') \cos \alpha_n x' dx' \\ \int J_{2tx}(x') \sin \alpha_n x' dx' \\ \int J_{2tz}(x') \cos \alpha_n x' dx' \end{bmatrix} \\ = \begin{bmatrix} 0 \\ 0 \\ 0 \\ 0 \end{bmatrix}, \quad (2.49)$$



where

$$\overline{\tilde{G}}_1 = \begin{bmatrix} \tilde{G}_{11zz} \sin \alpha_n x & \tilde{G}_{11xz} \sin \alpha_n x & \tilde{G}_{12zz} \sin \alpha_n x & \tilde{G}_{12xz} \sin \alpha_n x \\ \tilde{G}_{11xz} \cos \alpha_n x & \tilde{G}_{11xx} \cos \alpha_n x & \tilde{G}_{12xz} \cos \alpha_n x & \tilde{G}_{12xx} \cos \alpha_n x \\ \tilde{G}_{21zz} \sin \alpha_n x & \tilde{G}_{21xz} \sin \alpha_n x & \tilde{G}_{22zz} \sin \alpha_n x & \tilde{G}_{22xz} \sin \alpha_n x \\ \tilde{G}_{21xz} \cos \alpha_n x & \tilde{G}_{21xx} \cos \alpha_n x & \tilde{G}_{22xz} \cos \alpha_n x & \tilde{G}_{22xx} \cos \alpha_n x \end{bmatrix}. \quad (2.50)$$

The method of moments can be used here to solve the integral equations accurately for propagation constants  $\beta_p$  and simultaneously obtain a good approximation of the actual current distributions. A proper choice[16] of expansion functions to satisfy the asymptotic requirement of the current distribution near the edge is

$$J_{itz}(x'_i) = \sum_{m=1}^{N_s} A_m J_{itz}^m(x'_i) \quad m = 1, 2, \dots, N_s \quad (2.51)$$

and

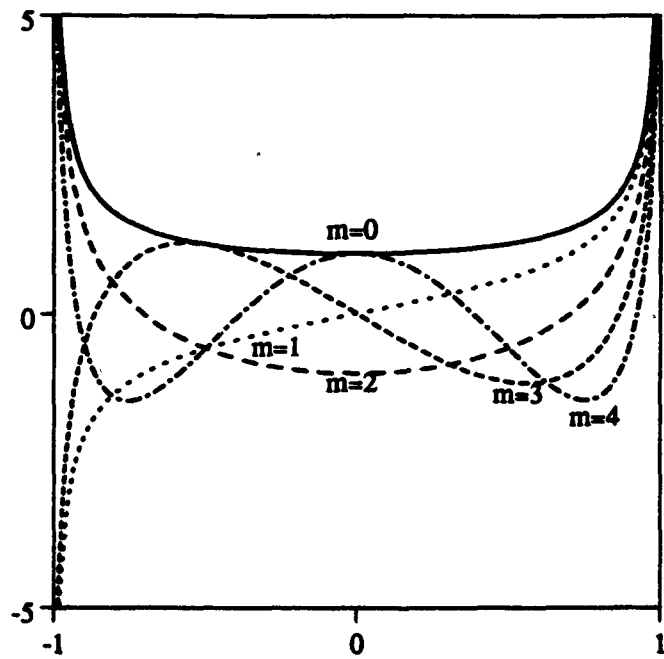
$$J_{itz}(x_i) = \sum_{m=1}^{N_s} B_m J_{itz}^m(x_i) \quad m = 1, 2, \dots, N_s, \quad (2.52)$$

where

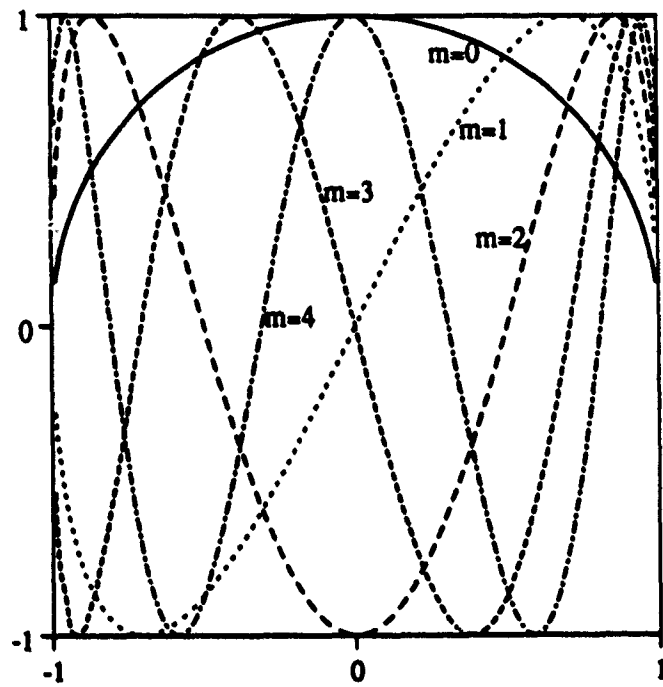
$$J_{itz}^m(x'_i) = \frac{T_{m-1}\left(\frac{2x'_i}{w_i}\right)}{\frac{\pi w_i}{2} \sqrt{1 - \left(\frac{2x'_i}{w_i}\right)^2}}, \quad (2.53)$$

$$J_{itz}^m(x_i) = \frac{U_{m-1}\left(\frac{2x_i}{w_i}\right) \sqrt{1 - \left(\frac{2x_i}{w_i}\right)^2}}{\frac{\pi w_i}{2}}, \quad (2.54)$$

and  $x'_i = x' - \delta_i$ .  $\delta_i$  and  $w_i$  are strip-offset and strip-width, respectively, associated with microstrip  $i$ . The functions  $T_m$  and  $U_m$  are Chebyshev polynomials of the first and second kinds, respectively. These expansion functions [2.53],[2.54] are shown in Fig. 2.2. Following the Galerkin procedure applied in the spectral domain, electric fields in Eq. [2.49] are tested with the expansion functions  $J_{itz}^m e^{j\beta_p z}$  and  $J_{itz}^m e^{j\beta_p z}$ . This results in a set of linear equations. These linear equations, when



(a)  $J_{tz}^m$



(b)  $J_{tx}^m$

Fig. 2.2 Expansion functions

expressed in matrix form, are

$$\bar{Z}(\beta) \begin{bmatrix} A_m \\ B_m \end{bmatrix} = 0, \quad (2.55)$$

where

$$\bar{Z}(\beta) = \begin{bmatrix} [Z_{11zz}] & [Z_{11zx}] & [Z_{12zz}] & [Z_{12zx}] \\ [Z_{11xz}] & [Z_{11xx}] & [Z_{12xz}] & [Z_{12xx}] \\ [Z_{21zz}] & [Z_{21zx}] & [Z_{22zz}] & [Z_{22zx}] \\ [Z_{21xz}] & [Z_{21xx}] & [Z_{22xz}] & [Z_{22xx}] \end{bmatrix}. \quad (2.56)$$

The matrix elements in each submatrix are in the general form of

$$Z_{ij\hat{u}_1\hat{u}_2}^{m\ k}(\beta) = \sum_{n=-\infty}^{\infty} \tilde{G}_{ij\hat{u}_1\hat{u}_2}(\alpha_n, \beta) \tilde{J}_{i\hat{u}_1}^m \tilde{J}_{j\hat{u}_2}^k, \quad (2.57)$$

where  $\tilde{J}$  is defined as

$$\tilde{J}_{iz}^m = \int_{-\frac{w_i}{2}}^{\frac{w_i}{2}} J_{iz}^m(x'_i) \sin \alpha_n(x'_i + \delta_i) dx'_i, \quad (2.58)$$

$$\tilde{J}_{ix}^m = \int_{-\frac{w_i}{2}}^{\frac{w_i}{2}} J_{ix}^m(x'_i) \cos \alpha_n(x'_i + \delta_i) dx'_i. \quad (2.59)$$

With the Bessel function identities

$$J_n(z) j^n \pi = \int_{-1}^1 \frac{e^{jzx} T_n(x)}{\sqrt{1-x^2}} dx \quad (2.60)$$

and

$$\frac{J_{n+1}(z)}{z} (n+1) j^n \pi = \int_{-1}^1 U_n(x) \sqrt{1-x^2} e^{jzx} dx, \quad (2.61)$$

Eqs. [2.58],[2.59] can be further expressed in closed forms, which are

$$\begin{aligned} \tilde{J}_{iz}^m &= \cos \alpha_n \delta_i I_m \left[ j^{m-1} J_{m-1} \left( \frac{\alpha_n w_i}{2} \right) \right] \\ &+ \sin \alpha_n \delta_i R_e \left[ j^{m-1} J_{m-1} \left( \frac{\alpha_n w_i}{2} \right) \right] \end{aligned} \quad (2.62)$$

and

$$\begin{aligned} \tilde{J}_{ix}^m &= \cos \alpha_n \delta_i R_e \left[ j^{m-1} m J_m \left( \frac{\alpha_n w_i}{2} \right) \frac{2}{\alpha_n w_i} \right] \\ &- \sin \alpha_n \delta_i I_m \left[ j^{m-1} m J_m \left( \frac{\alpha_n w_i}{2} \right) \frac{2}{\alpha_n w_i} \right]. \end{aligned} \quad (2.63)$$

In solving Eq. [2.55] to obtain the coefficients  $A_m$  and  $B_m$ , the determinant should be set to zero for non-trivial solutions. Therefore, the matrix elements [2.57] can be evaluated numerically for any  $\beta$  and the values which force the determinant of  $\bar{Z}$  to zero are the propagation constants. In other words, the propagation constant  $\beta_p$  must satisfy the characteristic equation

$$\det \bar{Z}(\beta_p) = 0. \quad (2.64)$$

### 2.3 Spectral Domain Calculation of Characteristic Impedance

Once the current distributions are obtained, the characteristic impedance of three layer shielded microstrip lines can be calculated using the ratio of average power to half of the square of the total longitudinal current[10]. The formula of the characteristic impedance, for a single line, is

$$Z_c = \frac{2P_{av}}{I_z^2}, \quad (2.65)$$

while for symmetric coupled lines, is

$$Z_c = \frac{2P_{av}}{I_{z1}^2 + I_{z2}^2} = \frac{P_{av}}{I_{z1}^2}. \quad (2.66)$$

The average power is the surface integral of the  $z$  component of the Poynting vector

$$P_{av} = \frac{1}{2} \text{Re} \int_0^a \int_0^b (\vec{E} \times \vec{H}^*) \cdot \hat{z} dy dx. \quad (2.67)$$

It is noted that the axial currents of asymmetric coupled lines  $I_{z1}$  and  $I_{z2}$  are not the same. Therefore, in order that the definition of characteristic impedance be useful, the formula described in [11] can be used:

$$Z_{pi} = \frac{2P_{av}^{pi}}{I_{zpi}^2} = \frac{\text{Re} \int_0^a \int_0^b (\vec{E}_{pi} \times \vec{H}_{pi}^*) \cdot \hat{z} dy dx}{I_{zpi}^2}, \quad (2.68)$$

where  $P_{av}^{pi}$  and  $I_{zpi}$  are respectively the average partial power and axial current associated with the microstrip  $i$  for the mode  $p$ . In the above,  $\vec{E}_{pi}$  is the total electric field and  $\vec{H}_{pi}$  is the magnetic field generated by the current on the microstrip  $i$ . With similar approach in deriving Eq. [2.49], the transverse components of electromagnetic fields in region  $i$  can be expressed as

$$E_{ix}(x, y, z) = \frac{1}{a} e^{-j\beta_p z} \sum_{n=-\infty}^{\infty} \vec{E}_x^i(\alpha_n, \beta_p, y) \cos \alpha_n x \begin{bmatrix} \int J_{1tx}(x') \sin \alpha_n x' dx' \\ \int J_{1tx}(x') \cos \alpha_n x' dx' \\ \int J_{2tx}(x') \sin \alpha_n x' dx' \\ \int J_{2tx}(x') \cos \alpha_n x' dx' \end{bmatrix}, \quad (2.69)$$

$$E_{iy}(x, y, z) = \frac{1}{a} e^{-j\beta_p z} \sum_{n=-\infty}^{\infty} \vec{E}_y^i(\alpha_n, \beta_p, y) \sin \alpha_n x \begin{bmatrix} \int J_{1tx}(x') \sin \alpha_n x' dx' \\ \int J_{1tx}(x') \cos \alpha_n x' dx' \\ \int J_{2tx}(x') \sin \alpha_n x' dx' \\ \int J_{2tx}(x') \cos \alpha_n x' dx' \end{bmatrix}, \quad (2.70)$$

$$H_{ix}(x, y, z) = \frac{1}{a} e^{-j\beta_p z} \sum_{n=-\infty}^{\infty} \vec{H}_x^i(\alpha_n, \beta_p, y) \sin \alpha_n x \begin{bmatrix} \int J_{1tx}(x') \sin \alpha_n x' dx' \\ \int J_{1tx}(x') \cos \alpha_n x' dx' \\ \int J_{2tx}(x') \sin \alpha_n x' dx' \\ \int J_{2tx}(x') \cos \alpha_n x' dx' \end{bmatrix}, \quad (2.71)$$

and

$$H_{iy}(x, y, z) = \frac{1}{a} e^{-j\beta_p z} \sum_{n=-\infty}^{\infty} \vec{H}_y^i(\alpha_n, \beta_p, y) \cos \alpha_n x \begin{bmatrix} \int J_{1tx}(x') \sin \alpha_n x' dx' \\ \int J_{1tx}(x') \cos \alpha_n x' dx' \\ \int J_{2tx}(x') \sin \alpha_n x' dx' \\ \int J_{2tx}(x') \cos \alpha_n x' dx' \end{bmatrix}, \quad (2.72)$$

where

$$\vec{E}_x^i = \begin{bmatrix} \tilde{E}_{i1xx} & \tilde{E}_{i1xz} & \tilde{E}_{i2xx} & \tilde{E}_{i2xz} \end{bmatrix}, \quad (2.73)$$

$$\vec{E}_y^i = \begin{bmatrix} \tilde{E}_{i1yx} & \tilde{E}_{i1yz} & \tilde{E}_{i2yx} & \tilde{E}_{i2yz} \end{bmatrix}, \quad (2.74)$$

$$\vec{\bar{H}}_x = \begin{bmatrix} \tilde{H}_{i1xx} & \tilde{H}_{i1yx} & \tilde{H}_{i2xx} & \tilde{H}_{i2yx} \end{bmatrix}, \quad (2.75)$$

and

$$\vec{\bar{H}}_y = \begin{bmatrix} \tilde{H}_{i1yz} & \tilde{H}_{i1yx} & \tilde{H}_{i2yz} & \tilde{H}_{i2yx} \end{bmatrix}. \quad (2.76)$$

Substituting Eqs. [2.69]-[2.72] into Eq. [2.67], one can proceed the integration with respect to  $x$  to yield

$$P_i = \frac{1}{4a} \hat{z} \cdot \sum_{n=-\infty}^{\infty} \left( \int_{h_i} \begin{bmatrix} \vec{\bar{E}}_x \\ \vec{\bar{E}}_y \end{bmatrix} dy \begin{bmatrix} \int J_{1tx}(x') \sin \alpha_n x' dx' \\ \int J_{1tx}(x') \cos \alpha_n x' dx' \\ \int J_{2tx}(x') \sin \alpha_n x' dx' \\ \int J_{2tx}(x') \cos \alpha_n x' dx' \end{bmatrix} \right) \times \left( \int_{h_i} \begin{bmatrix} \vec{\bar{H}}_x \\ \vec{\bar{H}}_y \end{bmatrix} dy \begin{bmatrix} \int J_{1tx}(x') \sin \alpha_n x' dx' \\ \int J_{1tx}(x') \cos \alpha_n x' dx' \\ \int J_{2tx}(x') \sin \alpha_n x' dx' \\ \int J_{2tx}(x') \cos \alpha_n x' dx' \end{bmatrix} \right)^*, \quad (2.77)$$

where  $P_i$  is the average power in region  $i$ . The integration over  $y$  can be also solved in closed form and the results are shown in Appendix C.

The average partial power  $P_{av}^i$  can be calculated in a similar way by considering only  $J_{itx}$  and  $J_{itz}$  in Eqs. [2.71],[2.72].

## 2.4 Numerical Results and Discussions

The shielded microstrip lines considered in this analysis are shown in Figs. 2.3(a)-(d) where infinitesimally thin strips and the ground plane are assumed to be perfect conductors. It is also assumed that the substrate material is lossless. The propagation constant associated with these structures can be deter-

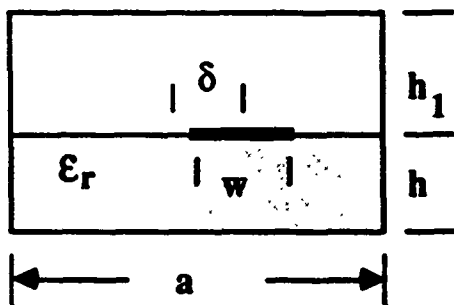


Fig. 2.3(a) Two layer single line

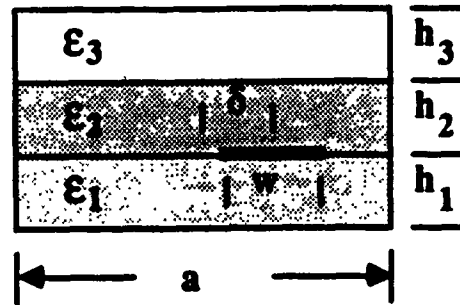


Fig. 2.3(b) Three layer single line

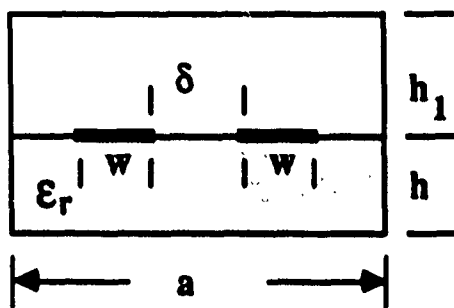


Fig. 2.3(c) Symmetric coupled lines

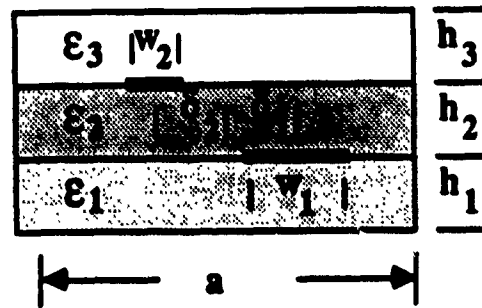


Fig. 2.3(d) Asymmetric coupled lines

Fig. 2.3 Shielded microstrip lines

mined by solving Eq. [2.64] and the approximated current distributions can be obtained simultaneously. The longitudinal current distribution is normalized such that its integration over the entire strip-width is equal to unity. The transverse current distribution is also normalized in relative magnitude compared to the longitudinal current distribution. Once both current distributions are known, one can solve the six field components, and therefore the characteristic impedance can be computed through a power-current definition. The dispersion characteristics for both single and coupled lines are evaluated numerically and their dependence on dielectric constant, strip-width, strip-offset and frequency will be discussed in this section.

Dispersion characteristics for the single-line configuration are shown in Figs. 2.4-2.7. In Fig. 2.4, the dispersion characteristics are computed for various dielectric constants. It is seen that the increase in permittivity increases the propagation constant and decreases the characteristic impedance, regardless of which layer the strip is located. Fig. 2.5 shows the variation of dispersion characteristics with the strip-width. As the width increases, the transverse current density also increases and the longitudinal current distribution becomes more oscillatory. Both propagation constant and characteristic impedance drop significantly as the width is close to the distance between two sidewalls. Fig. 2.6 shows the dispersion characteristics as a function of the strip-offset. The transverse current distribution increases asymmetrically with the increase of strip-offset  $\delta$ . Both propagation constant and characteristic impedance decrease with the increase of strip-offset  $\delta$ . Fig. 2.7 shows the frequency behavior of a single line. The behavior of the current distributions is similar to the dependence on strip-width because the strip-width becomes electrically wider as the frequency increases. Both propagation constant and characteristic impedance increase with frequency



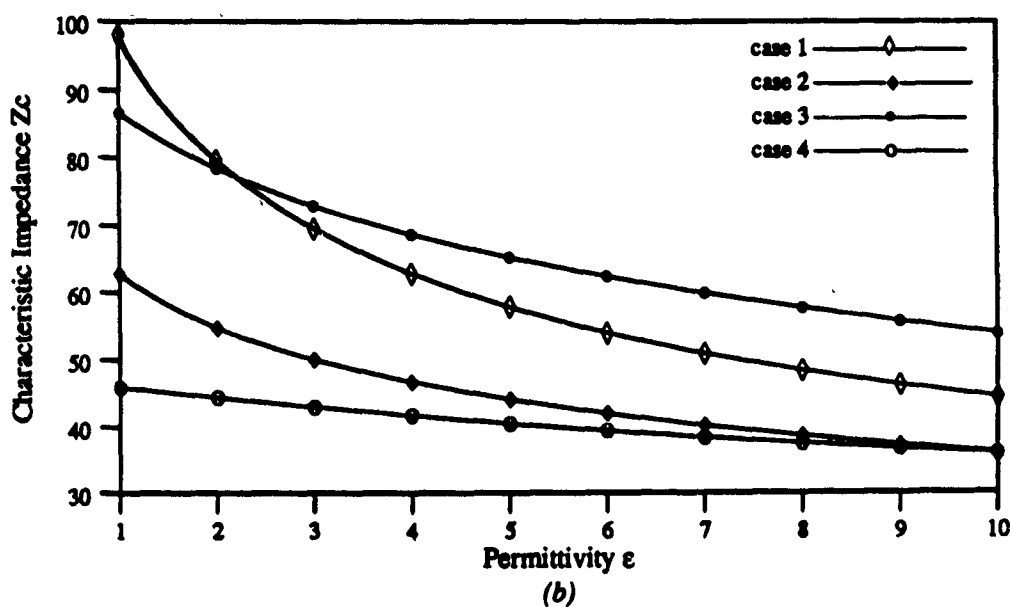
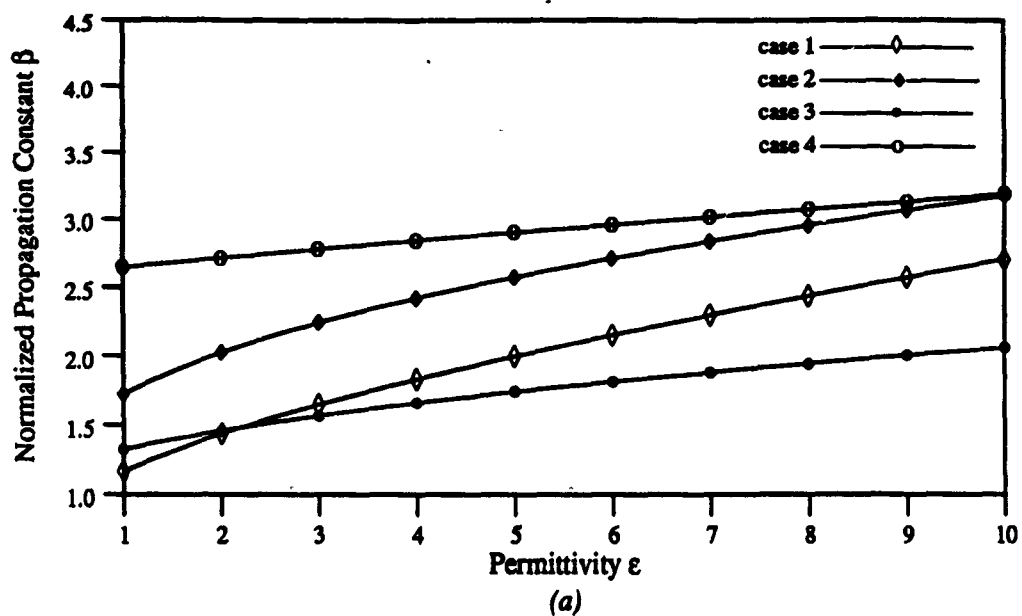


Fig. 2.4 Characteristics of a single line for the configuration of Fig. 2.3(b).

(a) Normalized propagation constant versus permittivity  $\epsilon$ .

(b) Characteristic impedance versus permittivity  $\epsilon$ .

Case 1:  $\epsilon_2 = 2.2, \epsilon_1 = \epsilon_3 = \epsilon$ , Case 2:  $\epsilon_2 = 10.2, \epsilon_1 = \epsilon_3 = \epsilon$ ,

Case 3:  $\epsilon_1 = \epsilon_3 = 2.2, \epsilon_2 = \epsilon$ , Case 4:  $\epsilon_1 = \epsilon_3 = 10.2, \epsilon_2 = \epsilon$ ,

$h_1 = h_2 = h_3 = 0.02\lambda_0, \frac{w}{h_1} = 1, \frac{a}{h_1} = 10, \delta = 0$  for all cases.

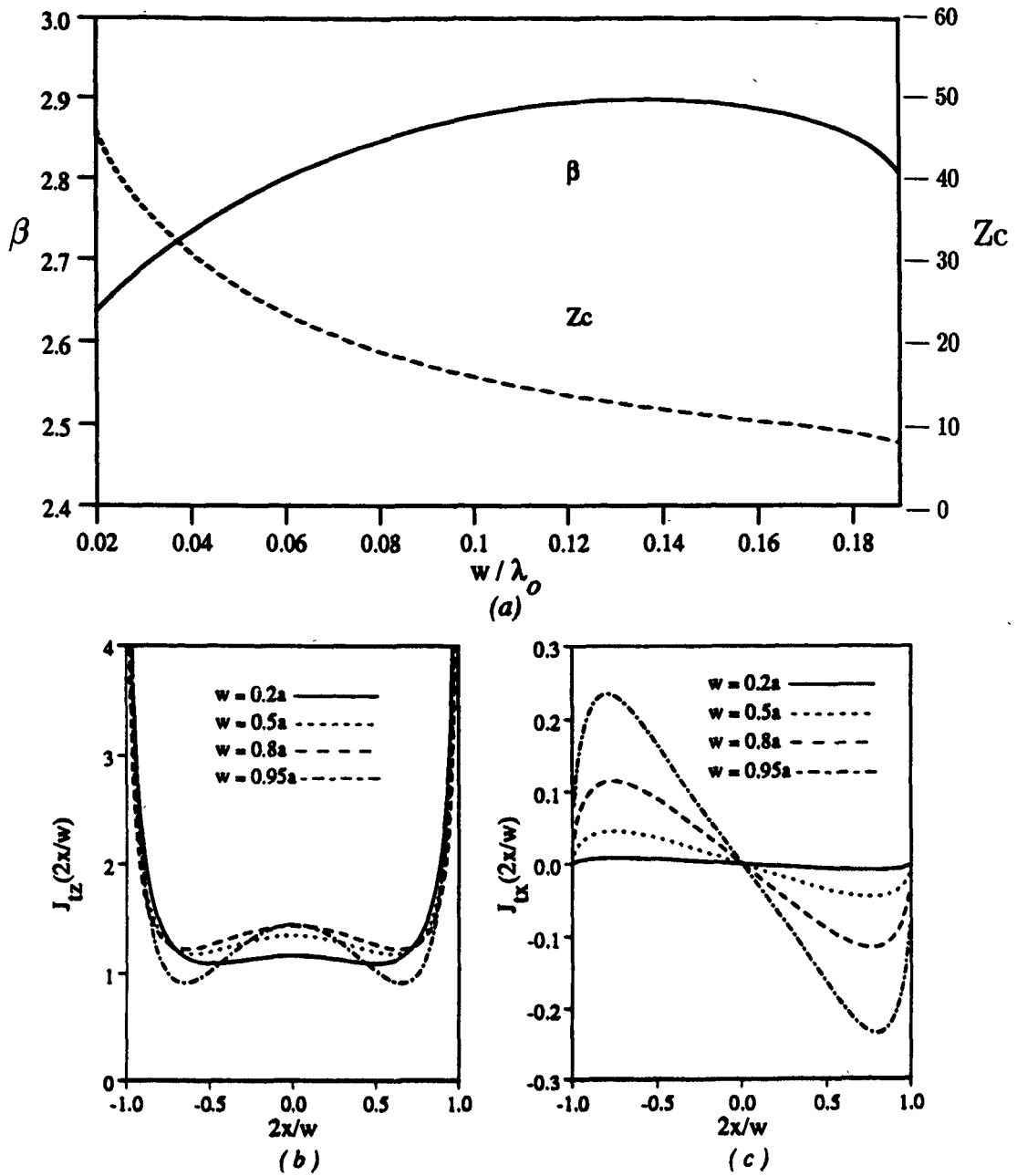


Fig. 2.5 Characteristics of a single line for the configuration of Fig. 2.3(a).  
 (a) Normalized propagation constant and characteristic impedance versus strip-width. (b) Normalized longitudinal current density versus strip position. (c) Relative transverse current density versus strip position.  
 $\epsilon_r = 10.2, h = 0.02\lambda_0, \frac{\xi}{h} = 0.0, \frac{h_1}{h} = 2.0, \frac{a}{h} = 10.0$

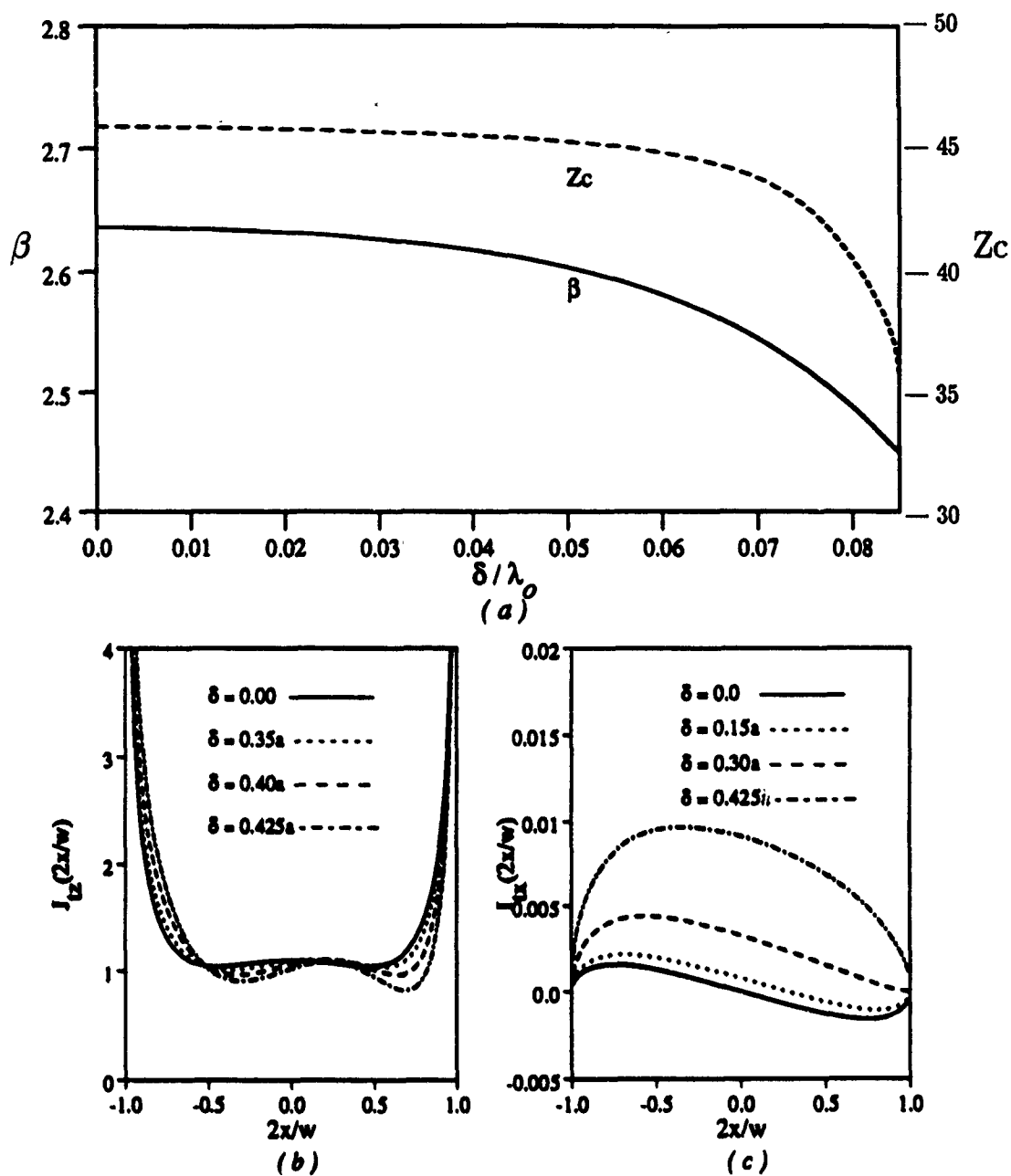


Fig. 2.6 Characteristics of a single line for the configuration of Fig. 2.3(a).  
 (a) Normalized propagation constant and characteristic impedance versus strip-offset. (b) Normalized longitudinal current density versus strip position. (c) Relative transverse current density versus strip position.  
 $\epsilon_r = 10.2$ ,  $h = 0.02\lambda_0$ ,  $\frac{w}{\lambda} = 1.0$ ,  $\frac{a}{\lambda} = 2.0$ ,  $\frac{g}{\lambda} = 10.0$

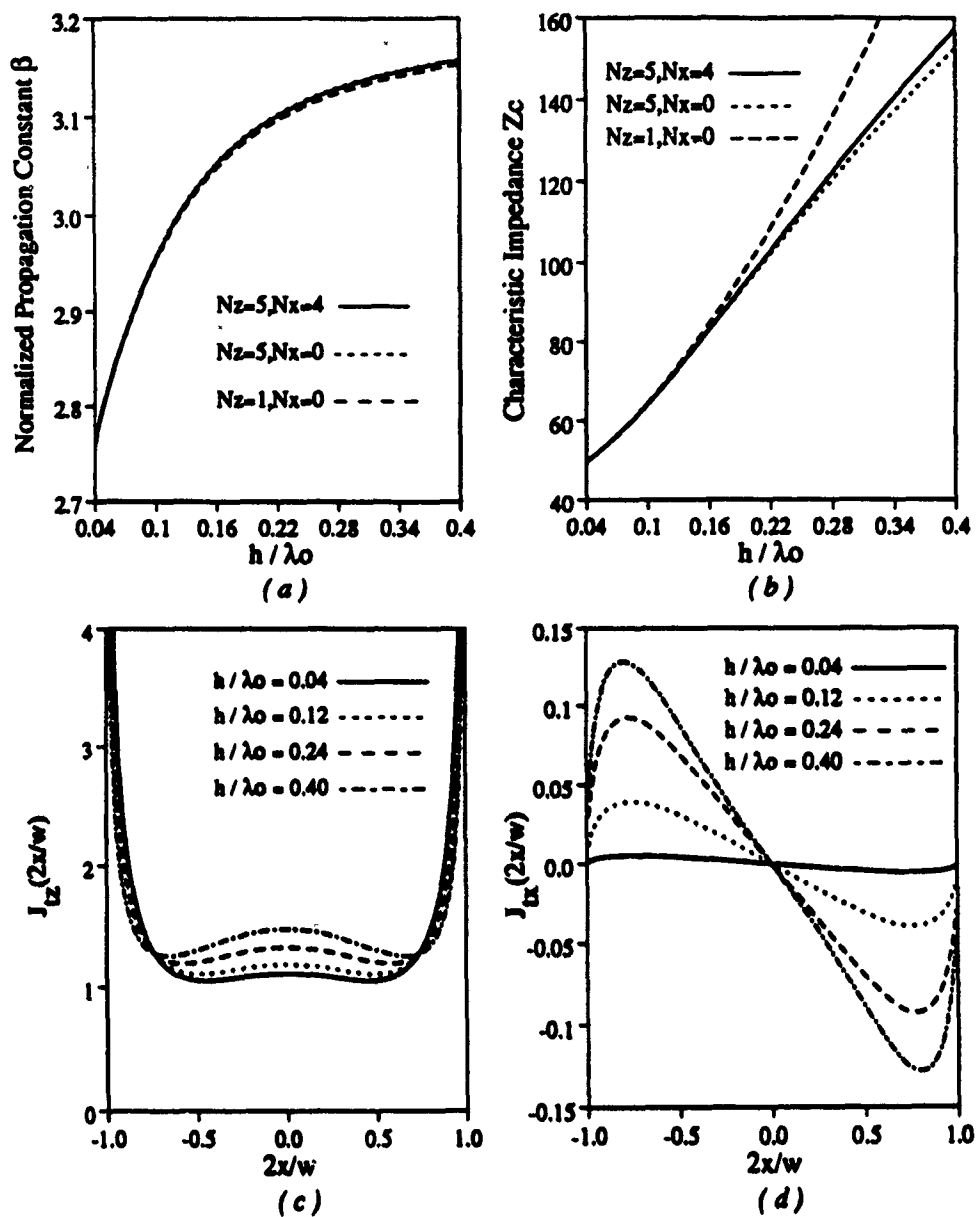


Fig. 2.7 Characteristics of a single line for the configuration of Fig. 2.3(a).

(a) Normalized propagation constant versus normalized frequency.

(b) Characteristic impedance versus normalized frequency.

(c) Normalized longitudinal current density versus strip position.

(d) Relative transverse current density versus strip position.

$$\epsilon_r = 10.2, \frac{w}{h} = 1.0, \frac{f}{k} = 0.0, \frac{A_1}{k} = 2.0, \frac{g}{k} = 10.0$$

in this case. The number of expansion functions used to calculate propagation constant is much less sensitive than that used to calculate the characteristic impedance.

Figs. 2.8-2.12 show the dispersion characteristics for coupled lines. In Fig. 2.8, two dominant modes, even-mode and odd-mode of symmetric coupled lines are shown as a function of the strip-offset  $\delta$  and are compared with the results of a single line in some special cases. The even-mode for  $\delta = 0$  corresponds to the dominant mode of a single line with the strip-width twice wide, while the odd-mode corresponds to the dominant mode of a single line with an electric wall at  $x = \frac{a}{2}$ . The comparison shows good agreement. Fig. 2.9 shows the dispersion characteristics of asymmetric coupled lines for two independent modes. Mode 1, which is similar to the odd mode of the symmetric coupled lines, has slower phase velocity than mode 2 and its effective dielectric constant is close to 2.2. This indicates that the fields are confined in the middle layer. On the other hand, mode 2, similar to the even-mode of symmetric coupled lines, has larger phase velocity. This implies the fields around lines are less confined. Both modes are not strongly dispersive. Fig. 2.10 shows the current distributions on each strip for both modes.

The spectral-domain analysis provides unique features in calculating the dispersion characteristics of shielded microstrip lines. However, care must be taken on the choice of the basis functions for numerical convergence and efficiency. The actual unknown current distributions can be approximated reasonably well if a proper choice of expansion functions is made. Fig. 2.11 shows the comparison with the theoretical results published by Krage and Haddad [13] for the symmetric coupled lines. Good agreement is found if the same number of the expansion

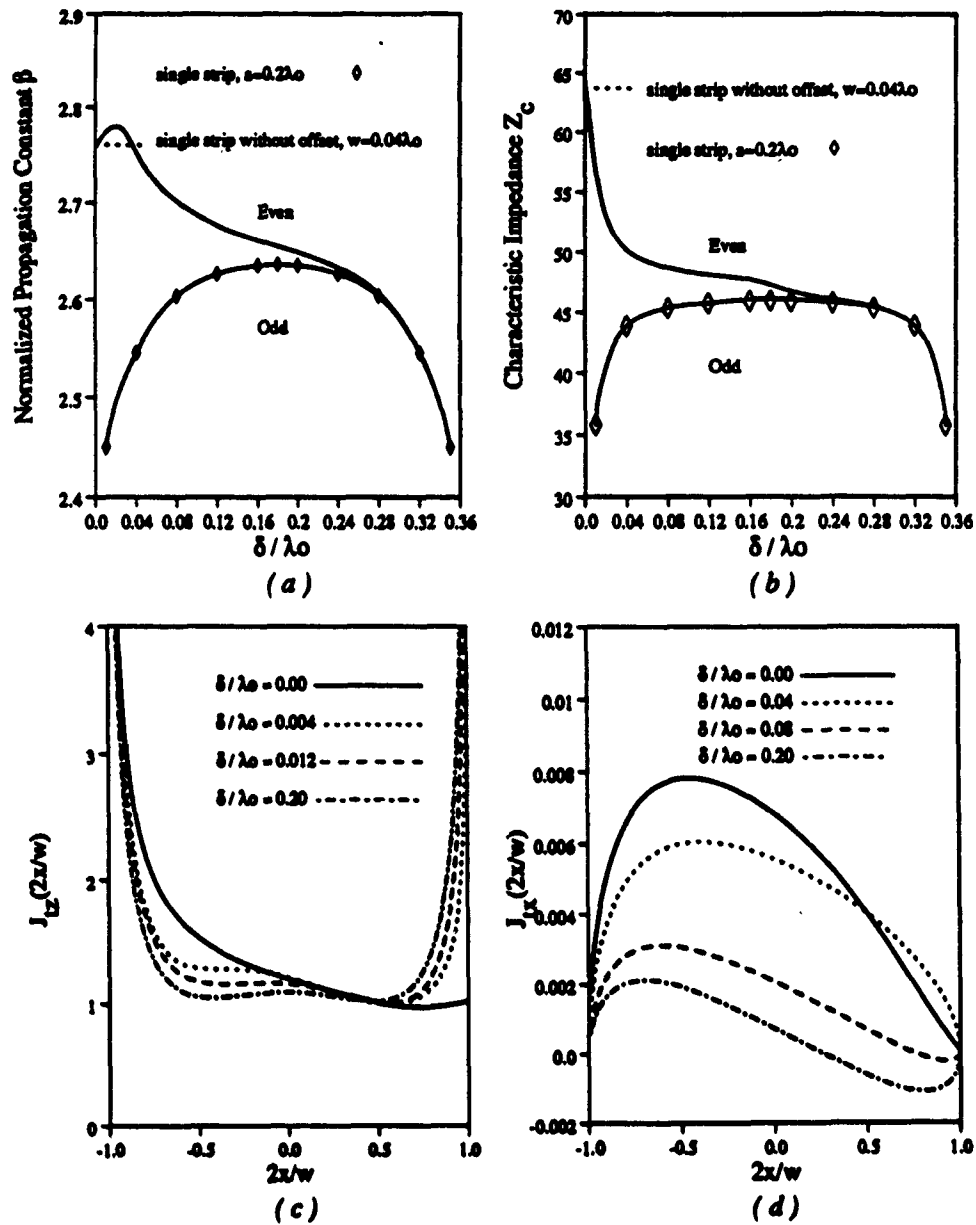


Fig. 2.8 Characteristics of symmetric coupled lines. (Fig. 2.3(c))  
 (a) Normalized propagation constant versus strip-offset.  
 (b) Characteristic impedance versus strip-offset.  
 (c) Even-mode longitudinal current density versus strip position.  
 (d) Even-mode transverse current density versus strip position.  
 $\epsilon_r = 10.2$ ,  $h = 0.02\lambda_0$ ,  $\frac{h}{\lambda} = 2.0$ ,  $\frac{w}{\lambda} = 1.0$ ,  $\frac{s}{\lambda} = 20.0$

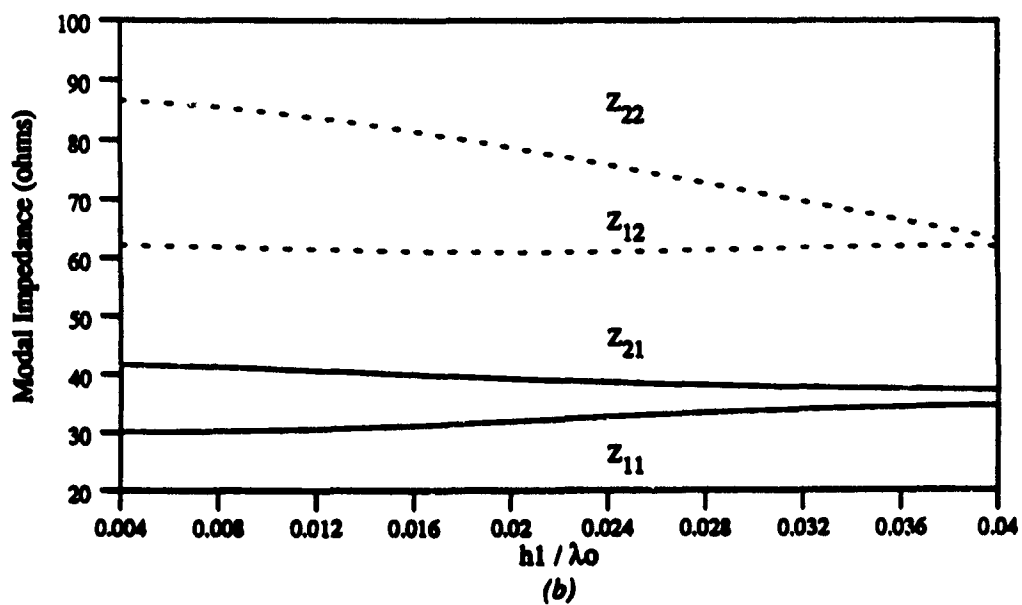
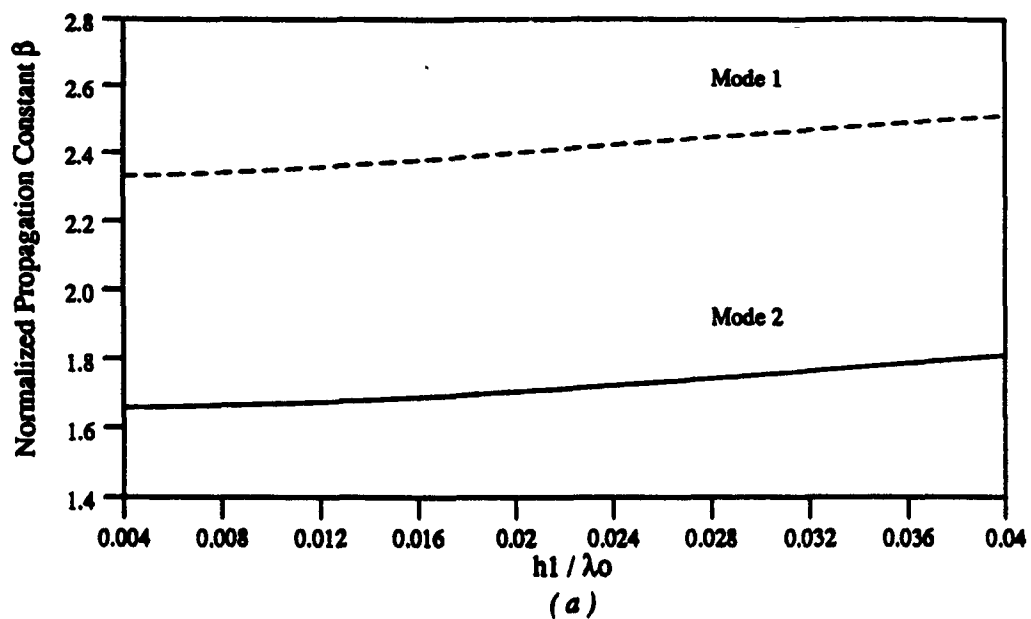


Fig. 2.9 Characteristics of asymmetric coupled lines. (Fig. 2.3(d))

(a) Normalized propagation constant versus normalized frequency.

(b) Modal impedance versus normalized frequency.

$$\epsilon_1 = 2.2, \epsilon_2 = 10.2, \epsilon_3 = 1.0, \frac{h_2}{h_1} = 1.0, \frac{h_3}{h_1} = 1.0, \\ \frac{b_1}{h_1} = 1.0, \frac{b_2}{h_1} = 0.5, \frac{b_3}{h_1} = 1.0, \frac{b_4}{h_1} = 1.5, \frac{b}{h} = 10.0$$

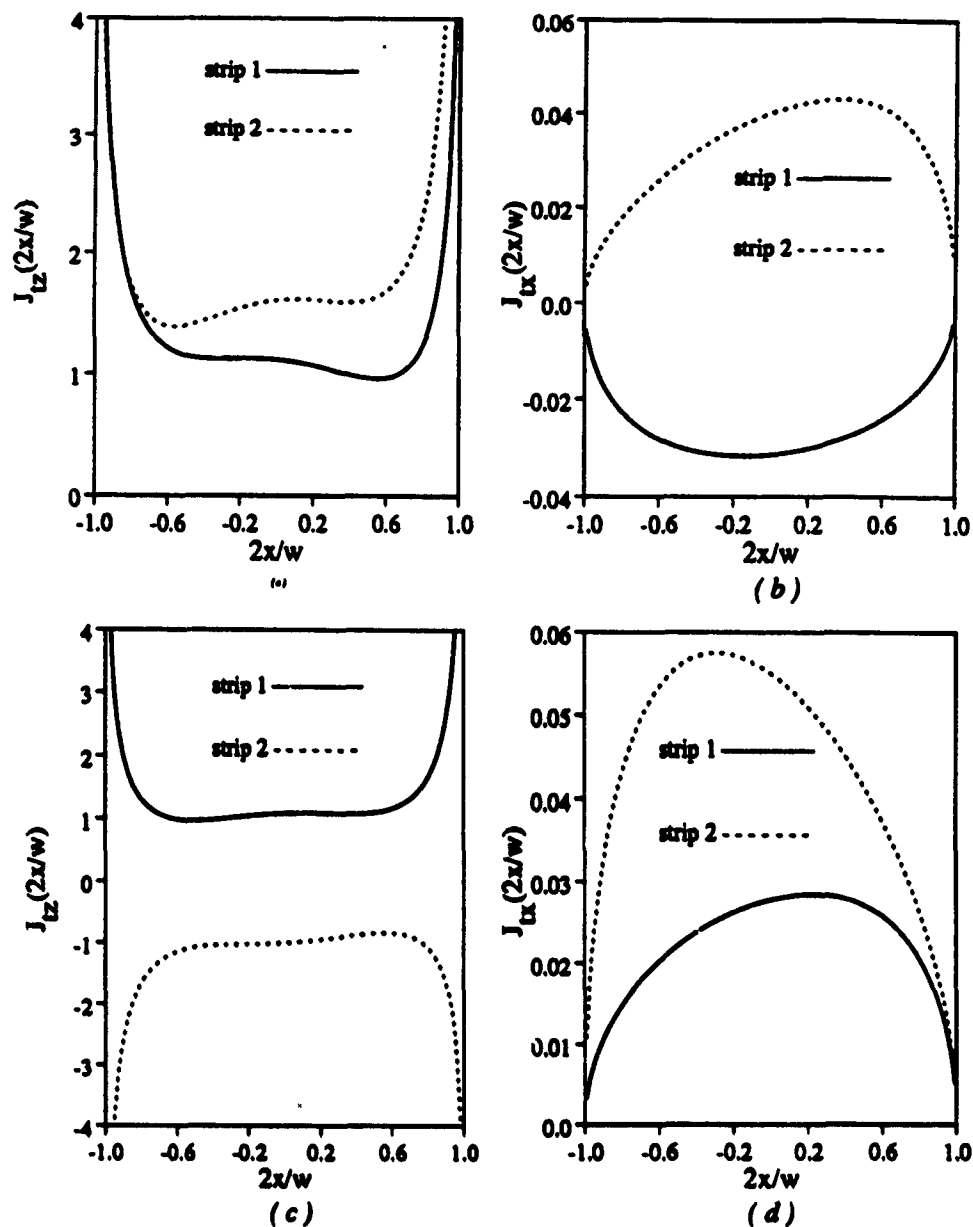


Fig. 2.10 Current distributions of asymmetric coupled lines. (Fig. 2.3(d))  
 (a) Normalized longitudinal current density versus strip position. (mode 2)  
 (b) Relative transverse current density versus strip position. (mode 2)  
 (c) Normalized longitudinal current density versus strip position. (mode 1)  
 (d) Relative transverse current density versus strip position. (mode 1)  
 $\epsilon_1 = 2.2, \epsilon_2 = 10.2, \epsilon_3 = 1.0, \frac{\lambda_2}{\lambda_1} = 1.0, \frac{\lambda_3}{\lambda_1} = 1.0, \frac{\epsilon_1}{\lambda_1} = 1.0, \frac{\epsilon_2}{\lambda_1} = 0.5,$   
 $\frac{\lambda_2}{\lambda_1} = 1.0, \frac{\lambda_3}{\lambda_1} = 1.5, \frac{\epsilon}{\lambda} = 10.0$



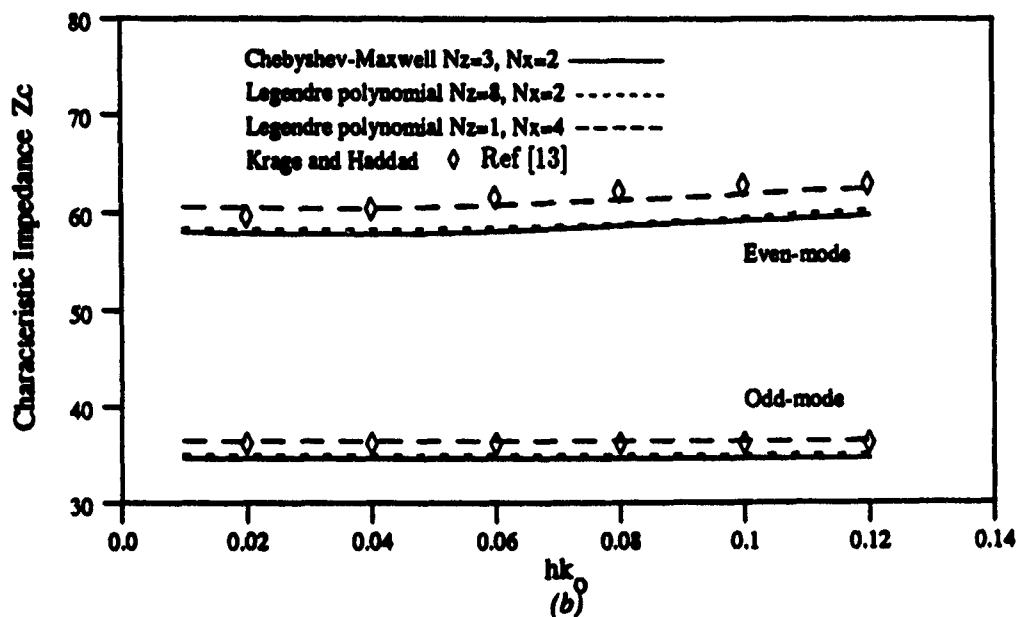
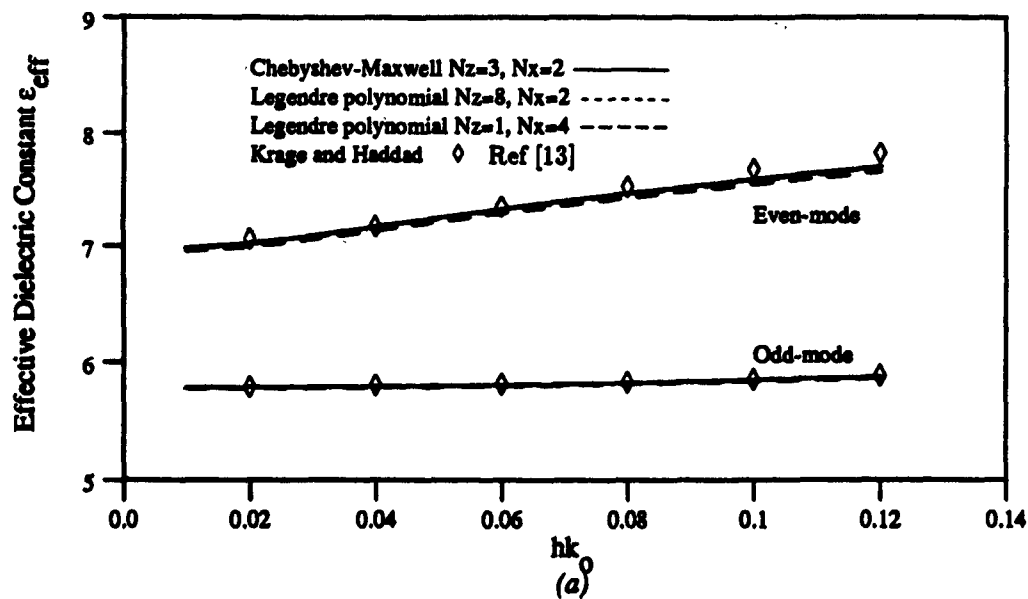


Fig. 2.11 Characteristics of symmetric coupled lines. (Fig. 2.3(c))

(a) Effective dielectric constant versus normalized frequency.

(b) Characteristic impedance versus normalized frequency.

$\epsilon_r = 10.$ ,  $\frac{A}{k} = 2.$ ,  $\frac{b}{k} = 0.4$ ,  $\frac{w}{k} = 1.$ ,  $\frac{g}{k} = 20.$

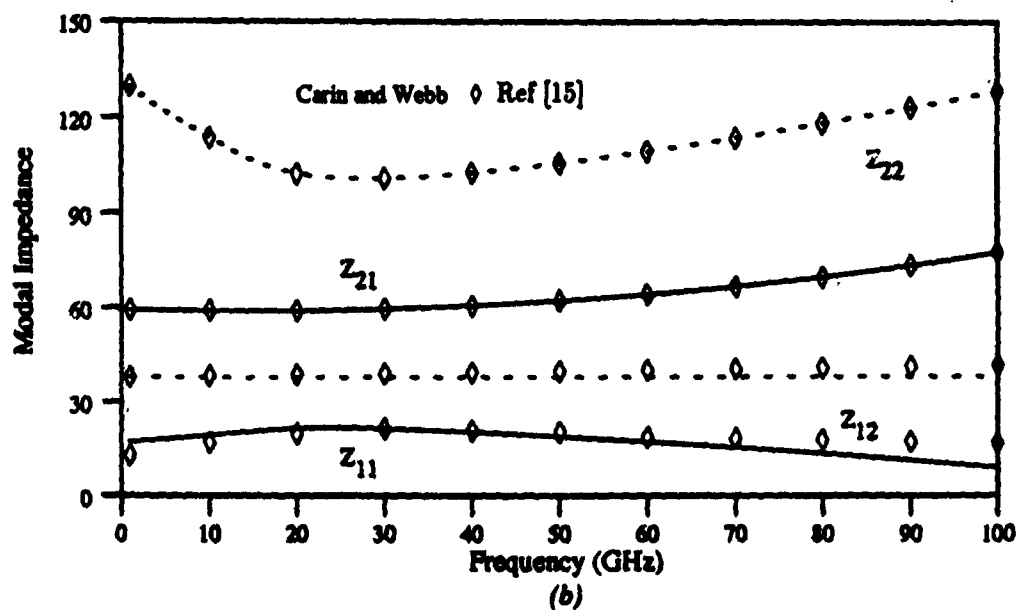
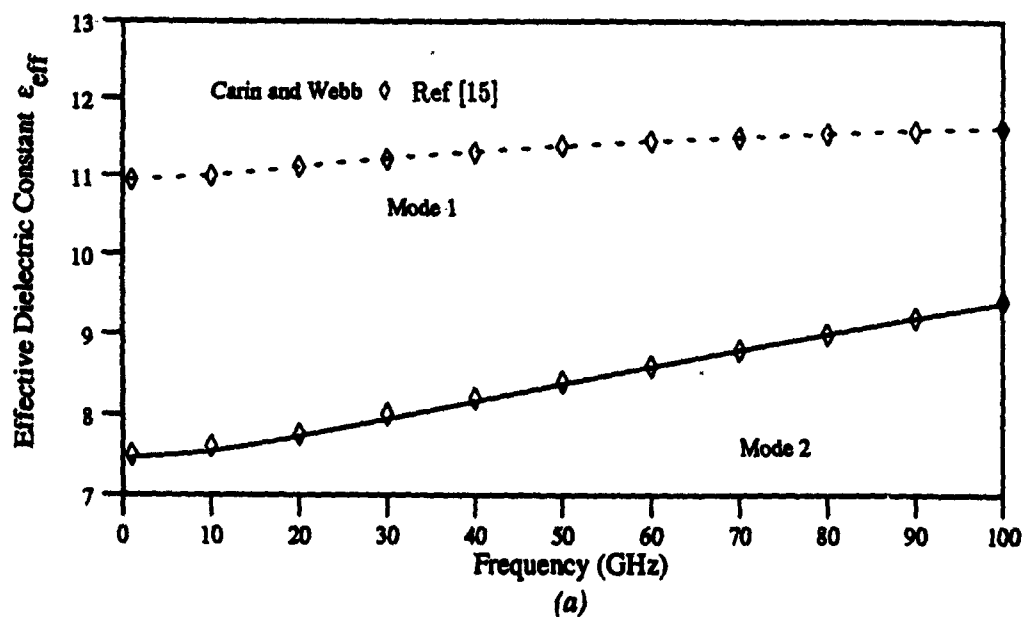


Fig. 2.12 Characteristics of asymmetric coupled lines. (Fig. 2.3(d))

(a) Effective dielectric constant versus frequency.

(b) Modal impedance versus frequency.

$\epsilon_1 = 12, \epsilon_2 = 12, \epsilon_3 = 1, h_1 = h_2 = 127\mu m, \frac{h_1}{\lambda_1} = 198,$   
 $\frac{h_2}{\lambda_1} = 2, \frac{h_3}{\lambda_1} = 2, \frac{w_1}{\lambda_1} = 1, \frac{w_2}{\lambda_1} = 1, \frac{g}{\lambda_1} = 200$

functions ( first four Legendre polynomials for expanding the longitudinal current density and one sinusoidal function for expanding the transverse current density) is used. By increasing the number to 8 for the longitudinal current density and to 2 for the transverse current density, the curves are much close to those using the expansion functions in Eqs. [2.53],[2.54] with only three expansion functions for the longitudinal current density and two for the transverse current density. The comparison between this analysis and the quasi-static results[12] at low frequencies are shown in Table 2.1 for symmetric coupled lines with different strip-offsets. The comparison shows good agreement. Fig. 2.12 shows the comparison for asymmetric coupled lines with the results published recently by Carin and Webb[15]. The dyadic Green's function used in [15] doesn't consider the fact that the tangential electric field on both sidewalls is zero and is treated as a good approximation only when the distance between the two sidewalls is large compared to the strip-width.

Geometrical parameters: $\epsilon_r = 9.5, h = 0.004\lambda_0, h_1 = 9h, w = h, \delta = 0$					
O D D	$\delta/h$	$v_{ph}$	$v_{ph}$ Ref [12]	$Z_c$	$Z_c$ Ref [12]
	0.05	0.431	0.434	19.09	23.50
	0.25	0.427	0.429	31.37	32.50
	1.00	0.419	0.419	41.68	42.00
	2.00	0.411	0.412	45.80	46.00
E V E N	$\delta/h$	$v_{ph}$	$v_{ph}$ Ref [12]	$Z_c$	$Z_c$ Ref [12]
	0.05	0.383	0.384	65.64	65.60
	0.25	0.381	0.383	61.89	62.00
	1.00	0.380	0.382	54.67	55.00
	2.00	0.384	0.386	50.99	51.00

Table. 2.1 Characteristics of two layer symmetric coupled lines in comparison with the quasi-static results Ref [12].

## Chapter III

### Full Wave Analysis of Shielded Microstrip

#### Line-To-Line Transitions

##### 3.1 Green's Function Formulation and the Method of Moments

Several types of shielded line-to-line transitions as shown in Figs. 3.1-3.3 are investigated. The methodology applied here is in analogy to that reported in [19],[20] by expanding the currents in the coupled line section with a combination of entire domain and subdomain modes, however, the spectral-domain Green's function and the numerical procedure are very much different. Since the strip-offset and strip-width are comparable to the waveguide dimensions, the transverse current component should not be neglected and a complete dyadic Green's function for an enclosed multi-layer structure is required in the integral equation formulation. The derivation of integral equations for overlay-coupled lines is similar to that of Eq. [2.49] except the currents on strips should be

$$\begin{aligned}\vec{J}_1(x', y', z') &= J_{1tz}(x')(J_{11z}^s(z') + J_{11z}^s(z'))\hat{z} \\ &+ J_{1tx}(x')(J_{11x}^s(z') + J_{11x}^s(z'))\hat{x}\end{aligned}\quad (3.1)$$

and

$$\begin{aligned}\vec{J}_2(x', y', z') &= J_{2tz}(x')(J_{21z}^s(z') + J_{21z}^s(z'))\hat{z} \\ &+ J_{2tx}(x')(J_{21x}^s(z') + J_{21x}^s(z'))\hat{x},\end{aligned}\quad (3.2)$$

where

$$J_{11z}^s = (e^{-j\beta_{p1}z'} - \Gamma e^{-j\beta_{p1}z'})U(-z'), \quad (3.3)$$

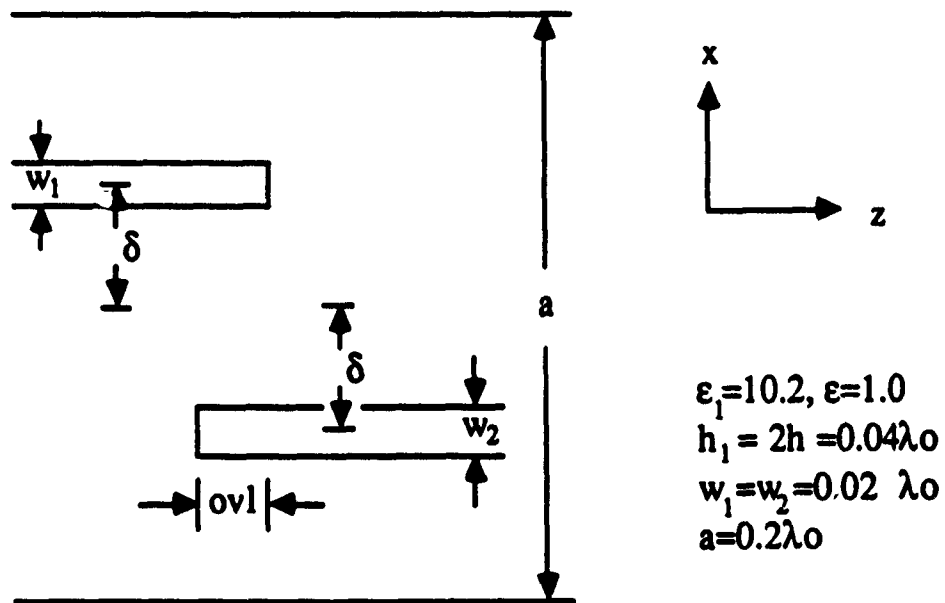
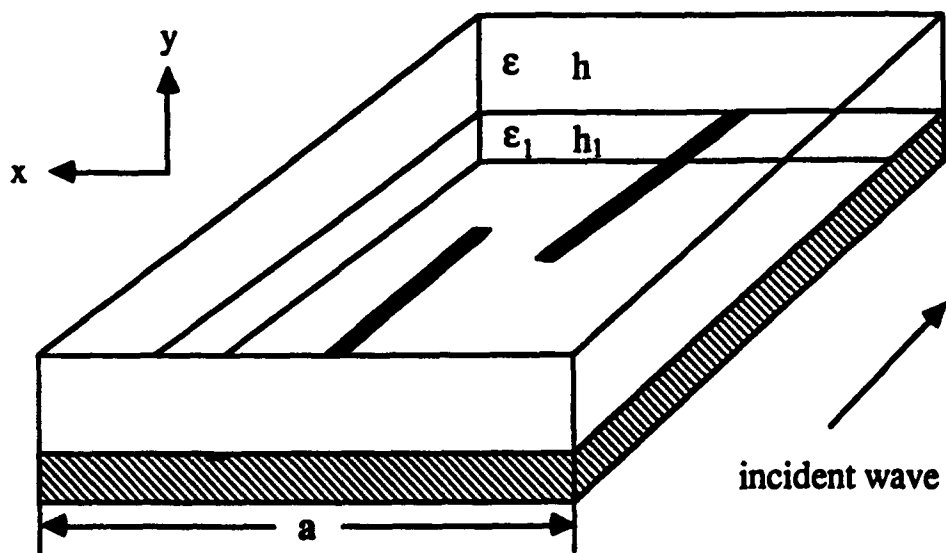


Fig. 3.1 Edge coupled line-to-line transition

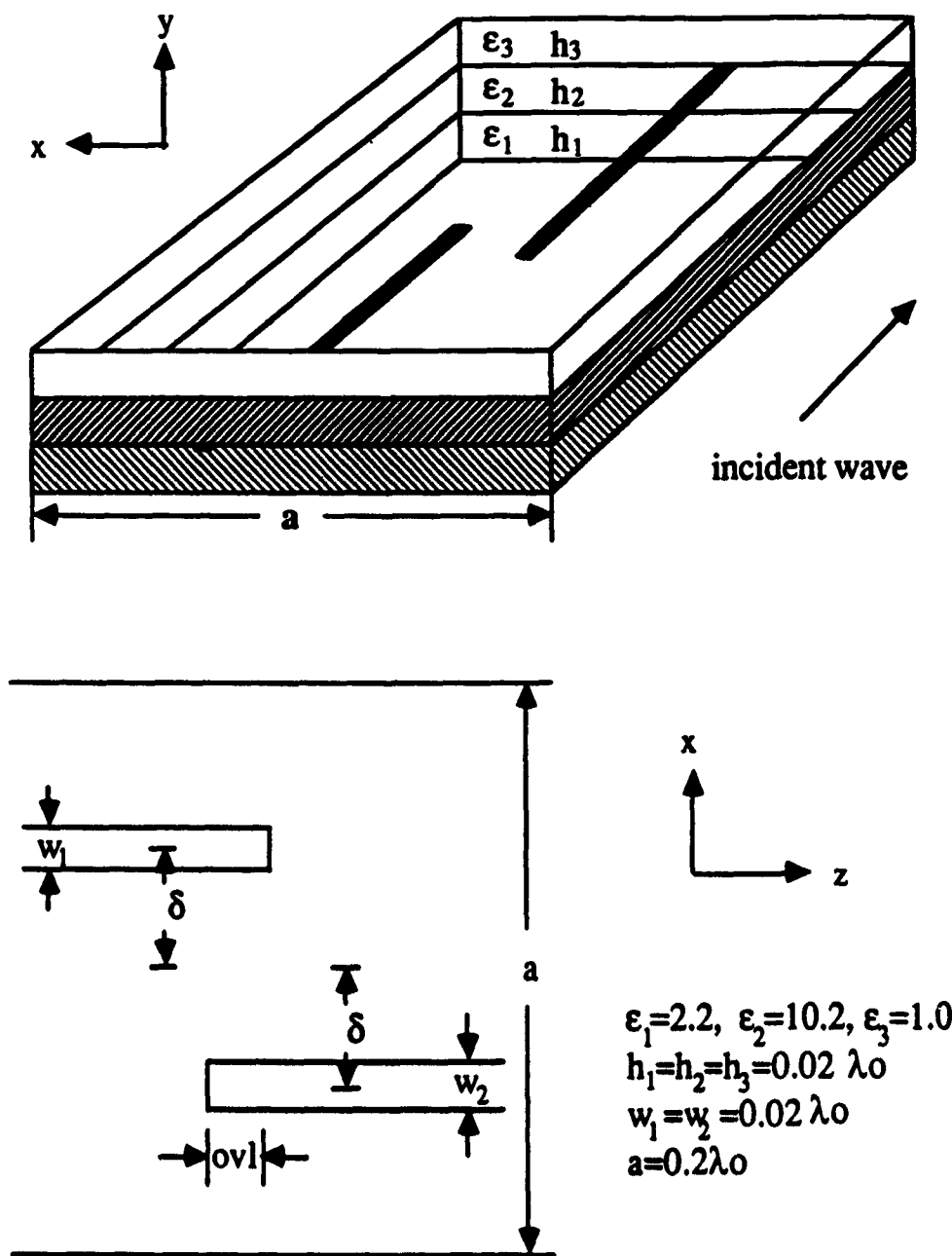
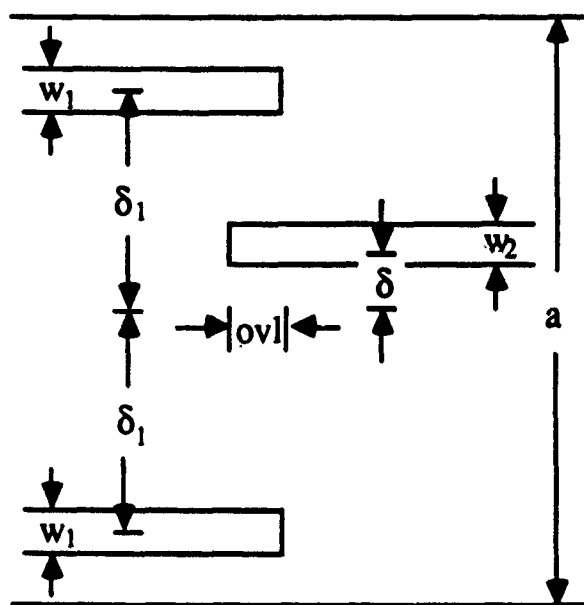
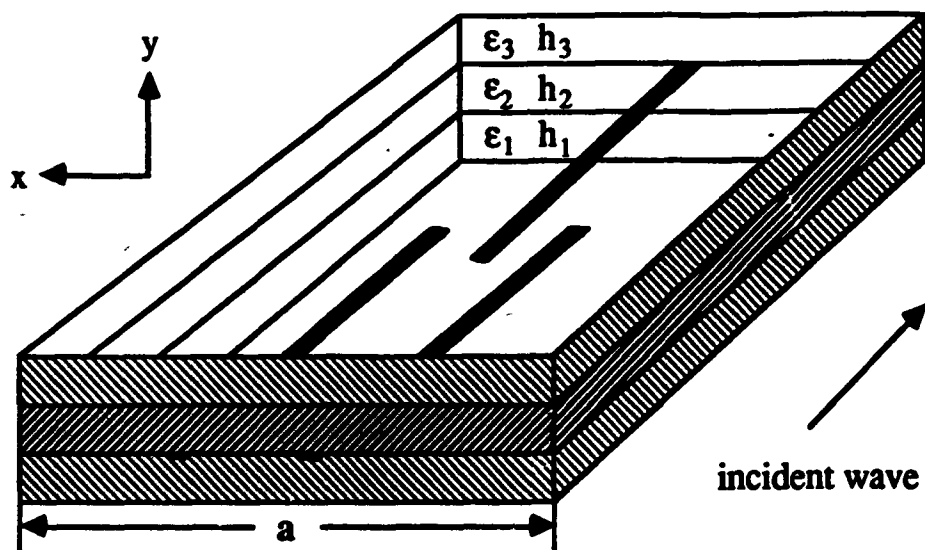


Fig. 3.2 Overlay coupled line-to-line transition



$$\begin{aligned}\epsilon_1 &= 2.2, \epsilon_2 = 10.2, \epsilon_3 = 2.2 \\ h_1 &= h_2 = h_3 = 0.02 \lambda_0 \\ w_1 &= w_2 = 0.02 \lambda_0 \\ a &= 0.2 \lambda_0 \\ \delta_1 &= 0.1 a\end{aligned}$$

Fig. 3.3 Overlay coupled-to-single line transition



$$J_{1lx}^e = \sum_{n=1}^N I_{1x}^n f_{1x}^n(z'), \quad (3.4)$$

$$J_{1lx}^e = J_{1lx}^s, \quad (3.5)$$

$$J_{1lx}^s = \sum_{m=1}^M I_{1x}^m f_{1x}^m(z'), \quad (3.6)$$

$$J_{2lx}^e = (Te^{-j\beta_{p2}z'})U(z' + ovl), \quad (3.7)$$

$$J_{2lx}^s = \sum_{n=1}^N I_{2x}^n f_{2x}^n(z'), \quad (3.8)$$

$$J_{2lx}^e = J_{2lx}^s, \quad (3.9)$$

$$J_{2lx}^s = \sum_{m=1}^M I_{2x}^m f_{2x}^m(z'), \quad (3.10)$$

and

$$U(x) = \begin{cases} 1 & ; \text{if } x > 0 \\ 0 & ; \text{otherwise.} \end{cases} \quad (3.11)$$

$ovl$  is the overlap of the two microstrip lines. Superscripts  $e$  and  $s$  represent the entire domain modes and the subdomain modes respectively. The transverse dependence  $J_{iix}$  and propagation constants  $\beta_{pi}$  are parameters with respect to the entire domain modes of the microstrip  $i$  and can be obtained through the analysis in Chapter II. The combination of a piecewise-sinusoidal(PWS) function and a pulse function is used as subdomain mode and is defined from the end of each line(shown in Fig. 3.4). These modes are

$$f_{is}^m(z) = \begin{cases} \frac{\sin k_{si}(d-|z-z_m|)}{\sin k_{si}d} & ; \text{for } |z-z_m| \leq d \\ 0 & ; \text{otherwise} \end{cases} \quad (3.12)$$

and

$$f_{is}^m(z) = \begin{cases} \frac{1}{2} & ; \text{for } |z-z_m| \leq \frac{d}{2} \\ 0 & ; \text{otherwise} \end{cases}, \quad (3.13)$$

where  $d$  is the half-length of the PWS function and also the width of pulse function.  $z_m$  is the center associated with each expansion function. The parameter  $k_{si}$  can be chosen quite flexibly within 0 to  $\frac{\pi}{2d}$ . A nice feature of the combination

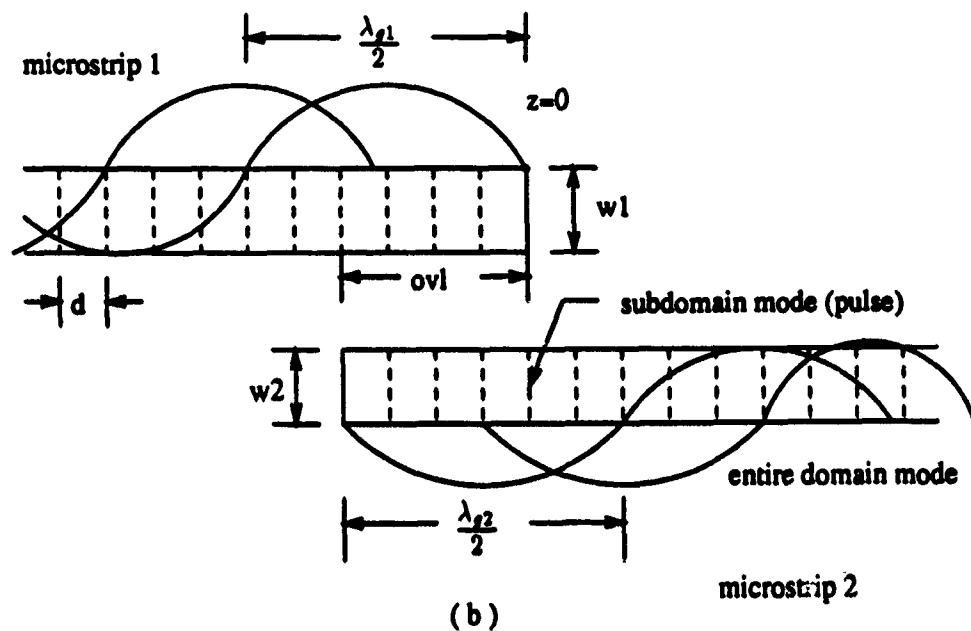
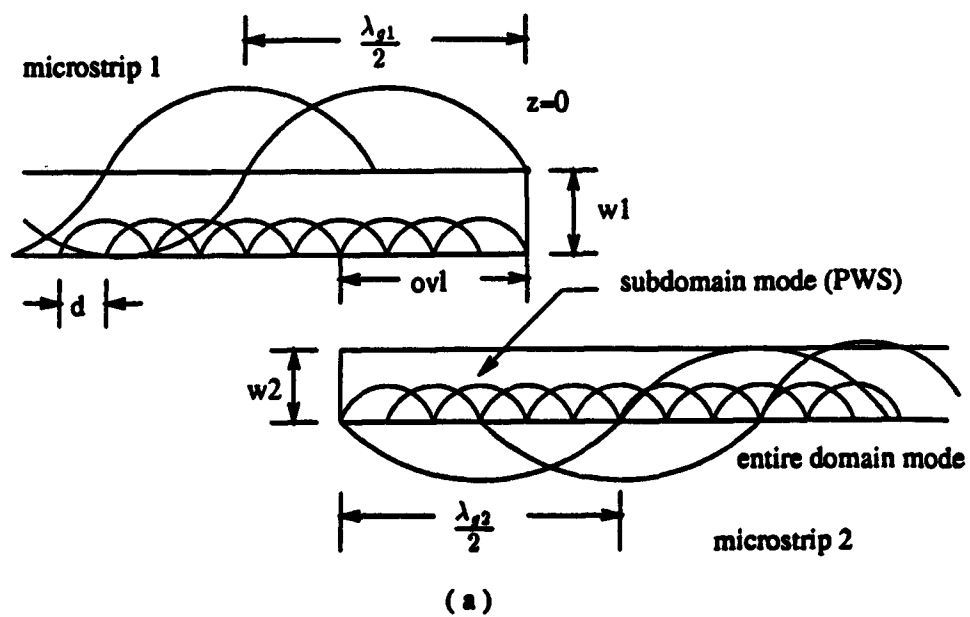


Fig. 3.4 Layout of expansion modes for  
 (a) longitudinal currents and  
 (b) transverse currents

of subdomain and entire domain modes is that when the method of moments is applied, the quantities of interest,  $\Gamma$  and  $T$ , are directly obtained by matrix inversion. Besides, the dimension of the impedance matrix is relatively small, typically  $< 40$ . The integral equation using the above currents can be expressed as

$$\begin{bmatrix} E_{1z}(x, y = h_1, z) \\ E_{1x}(x, y = h_1, z) \\ E_{2z}(x, y = h_1 + h_2, z) \\ E_{2x}(x, y = h_1 + h_2, z) \end{bmatrix} = \frac{1}{2\pi a} \sum_{n=-\infty}^{\infty} \int_{-\infty}^{\infty} e^{-j\beta z} \overline{G}_1(\alpha_n, \beta, x) \begin{bmatrix} \tilde{J}_{1tz}(\tilde{J}_{1lz}^e + \tilde{J}_{1lz}^s) \\ \tilde{J}_{1tx}(\tilde{J}_{1lx}^e + \tilde{J}_{1lx}^s) \\ \tilde{J}_{2tz}(\tilde{J}_{2lz}^e + \tilde{J}_{2lz}^s) \\ \tilde{J}_{2tx}(\tilde{J}_{2lx}^e + \tilde{J}_{2lx}^s) \end{bmatrix} d\beta$$

$$= \begin{bmatrix} 0 \\ 0 \\ 0 \\ 0 \end{bmatrix}, \quad (3.14)$$

where

$$\tilde{J}_{itz} = \int_0^a J_{itz}(x') \sin \alpha_n x' dx', \quad (3.15)$$

$$\tilde{J}_{itx} = \int_0^a J_{itx}(x') \cos \alpha_n x' dx', \quad (3.16)$$

$$\tilde{J}_{uz}^e = \int_{-\infty}^{\infty} J_{uz}^e(z') e^{j\beta z'} dz', \quad (3.17)$$

$$\tilde{J}_{uz}^s = \int_{-\infty}^{\infty} J_{uz}^s(z') e^{j\beta z'} dz', \quad (3.18)$$

and  $\overline{G}_1$  is expressed in Eq. [2.50].

Using a Galerkin's procedure in the method of moments, the testing functions chosen as  $J_{itz}(x)f_{iz}^k(z)$  are applied to the integral equations 3.14. The x-directed currents of entire domain modes are neglected in comparison with the z-directed currents of entire domain modes. This results in  $2M+2N+2$  linear

equations with  $2M+2N+2$  unknowns. These linear equations, when expressed in matrix form, are

$$\begin{bmatrix} [Z_{11ss}] & [Z_{11se}^{ref}] & [Z_{12ss}] & [Z_{12se}^{tra}] \\ [Z_{21ss}] & [Z_{21se}^{ref}] & [Z_{22ss}] & [Z_{22se}^{tra}] \end{bmatrix} \begin{bmatrix} [I_{1s}] \\ -\Gamma \\ [I_{2s}] \\ T \end{bmatrix} = \begin{bmatrix} [Z_{11se}^{inc}] \\ [Z_{21se}^{inc}] \end{bmatrix}, \quad (3.19)$$

where each submatrix  $[Z_{ijss}]$ , due to the presence of both x and z directed currents, contains 4 submatrices as

$$[Z_{ijss}] = \begin{bmatrix} [Z_{ijssxx}] & [Z_{ijssxz}] \\ [Z_{ijsszx}] & [Z_{ijsszz}] \end{bmatrix} \quad (3.20)$$

and submatrix  $[I_{js}]$  and  $[Z_{ijse}^p]$  (superscript p identifies the entire domain modes *ref*, *tra*, and *inc*), contain two submatrices as

$$[I_{js}] = \begin{bmatrix} [I_{js}] \\ [I_{jx}] \end{bmatrix} \quad (3.21)$$

and

$$[Z_{ijse}^p] = \begin{bmatrix} [Z_{ijse}^p] \\ [Z_{ijse}^p] \end{bmatrix}. \quad (3.22)$$

Each element in these submatrices represents the reaction of different basis functions. For instance, the elements of  $[Z_{12ssxx}]$  are the reaction between x-directed currents of subdomain mode associated with microstrip 1 and z-directed currents of subdomain mode associated with microstrip 2. The elements of  $[Z_{11se}^{ref}]$  are the reaction between x-directed currents of subdomain modes associated with microstrip 1 and z-directed currents of reflected propagating mode. These subdomain modes are either PWS functions or pulse functions. The entire domain modes are composed of the reflected mode, transmitted mode, and incident mode which are distinguished by the abbreviation *ref*, *tra*, and *inc*, respectively. The

computation of each element requires both infinite summation and integration in the spectral domain and their expressions are in the general forms of

$$Z_{ijss\hat{u}_1\hat{u}_2}^{kl} = \sum_{n=-\infty}^{\infty} \int_{-\infty}^{\infty} \tilde{G}_{ij\hat{u}_1\hat{u}_2}(\alpha_n, \beta) \tilde{J}_{it\hat{u}_1}(\alpha_n) \tilde{J}_{jt\hat{u}_2}(\alpha_n) \tilde{f}_{i\hat{u}_1}^k(\beta) \tilde{f}_{j\hat{u}_2}^l(\beta) d\beta \quad (3.23)$$

and

$$Z_{ij\hat{u}_e}^{kp} = \sum_{n=-\infty}^{\infty} \int_{-\infty}^{\infty} \tilde{G}_{ij\hat{u}_e}(\alpha_n, \beta) \tilde{J}_{it\hat{u}}(\alpha_n) \tilde{J}_{jt\hat{u}}(\alpha_n) \tilde{f}_{i\hat{u}}^k(\beta) \tilde{J}_{j\hat{u}}^p(\beta) d\beta, \quad (3.24)$$

where  $\tilde{f}_{i\hat{u}}^k$  and  $\tilde{J}_{j\hat{u}}^p$  are Fourier transform of the longitudinal dependence of the  $k$ th subdomain mode and entire domain mode  $p$  respectively. The spectral-domain expressions of longitudinal dependence for both subdomain and entire domain modes can be found in Appendix D.

The analysis for other line-to-line transitions are similar to that for overlay coupled lines. For edge-coupled lines the  $y$  dependence of currents associated with the parasitic coupled line should be the same as that associated with the feedline. For coupled-to-single lines the entire domain modes in the feedlines should be discussed separately due to the existence of two different modes (even-mode and odd-mode).

### 3.2 Numerical Results and Discussions

Numerical results for line-to-line transitions including reflection and transmission coefficients as a function of the overlap and line-offset are shown in Figs. 3.5-3.12. It is found that the bandwidth, defined as the frequency range between two cut-off frequencies, is approximately  $\frac{\lambda_{pe}}{2}$  and the maximum coupling occurs around  $ovl = \frac{(n+\frac{1}{2})\lambda_{pe}}{2}$  with a wide frequency-insensitive range. This implies that the transitions are broad-band and are very useful in many MMIC applications. These phenomena can be explained empirically by a quasi-static analysis of symmetric coupled lines. For two coupled lines, the impedance matrix [21] is

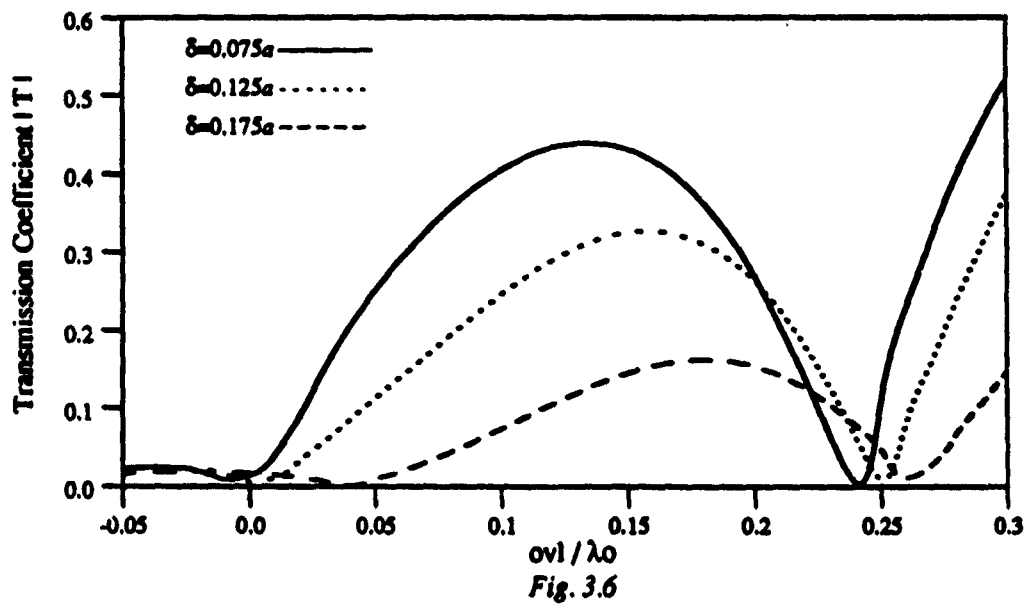
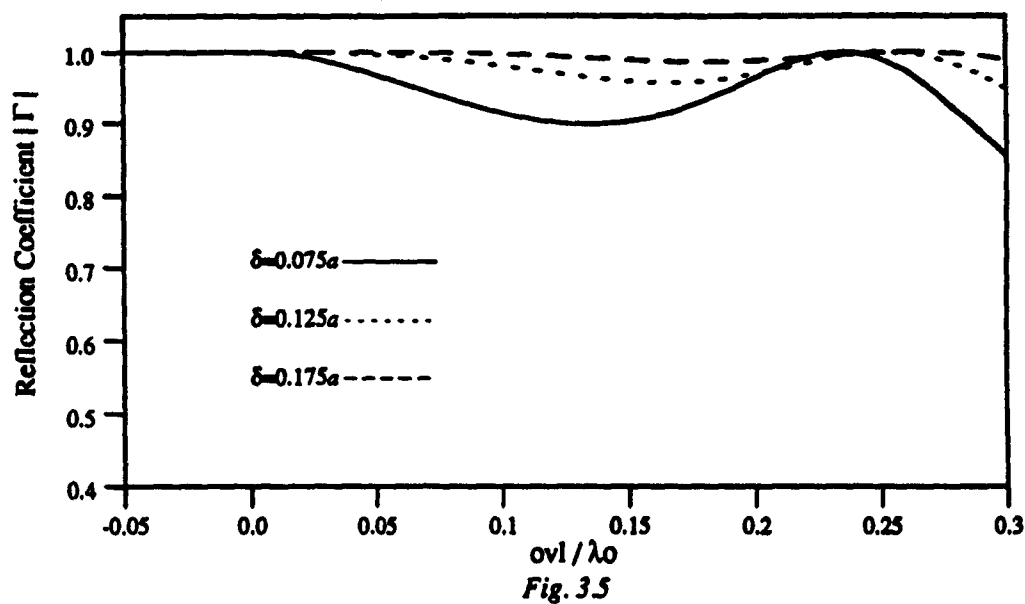


Fig. 3.5  $|\Gamma|$  versus overlap for the configuration of Fig. 3.1

Fig. 3.6  $|T|$  versus overlap for the configuration of Fig. 3.1

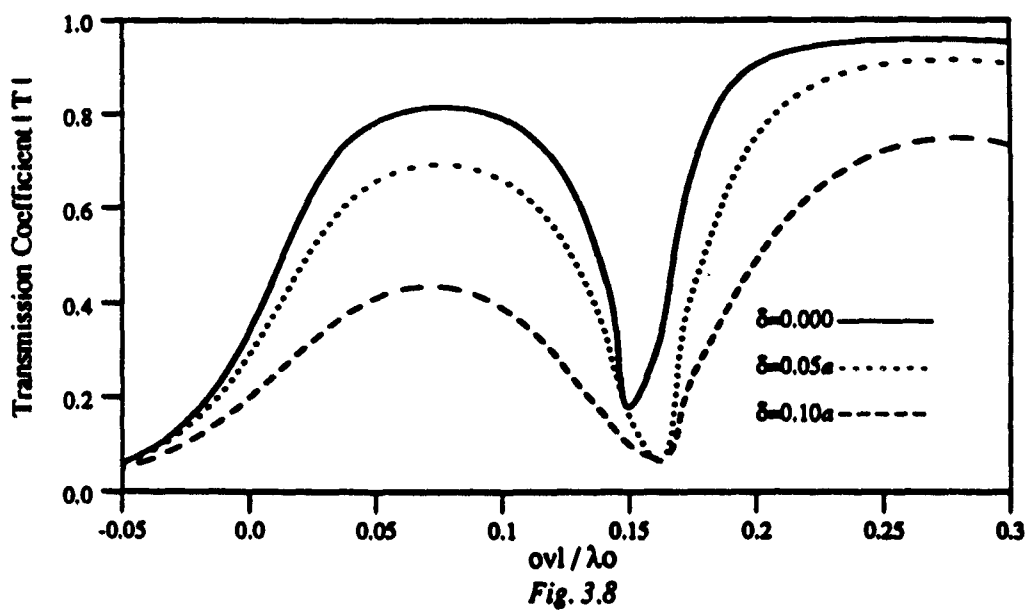
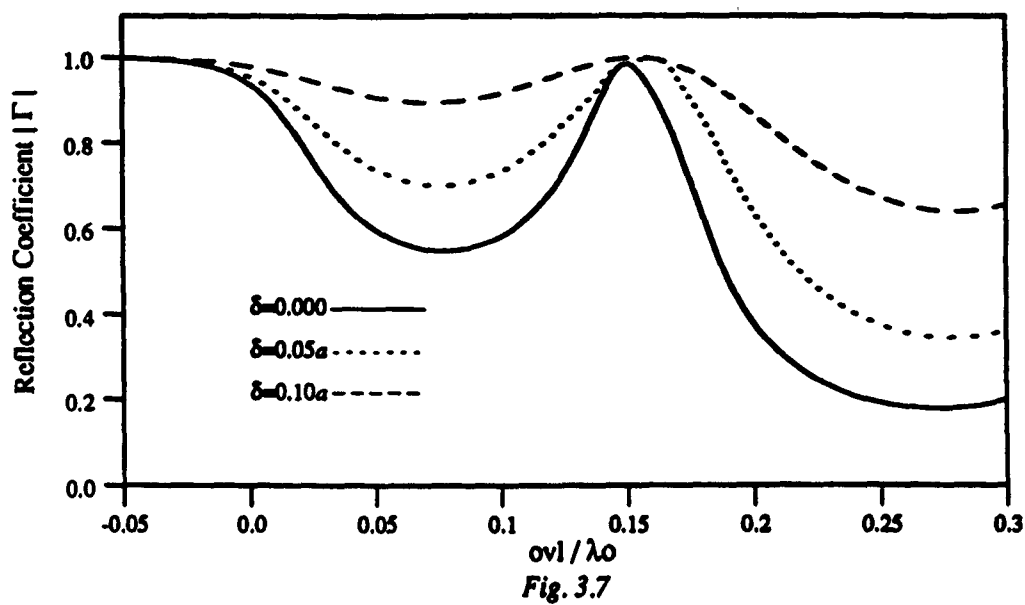


Fig. 3.7  $|\Gamma|$  versus overlap for the configuration of Fig. 3.2

Fig. 3.8  $|T|$  versus overlap for the configuration of Fig. 3.2

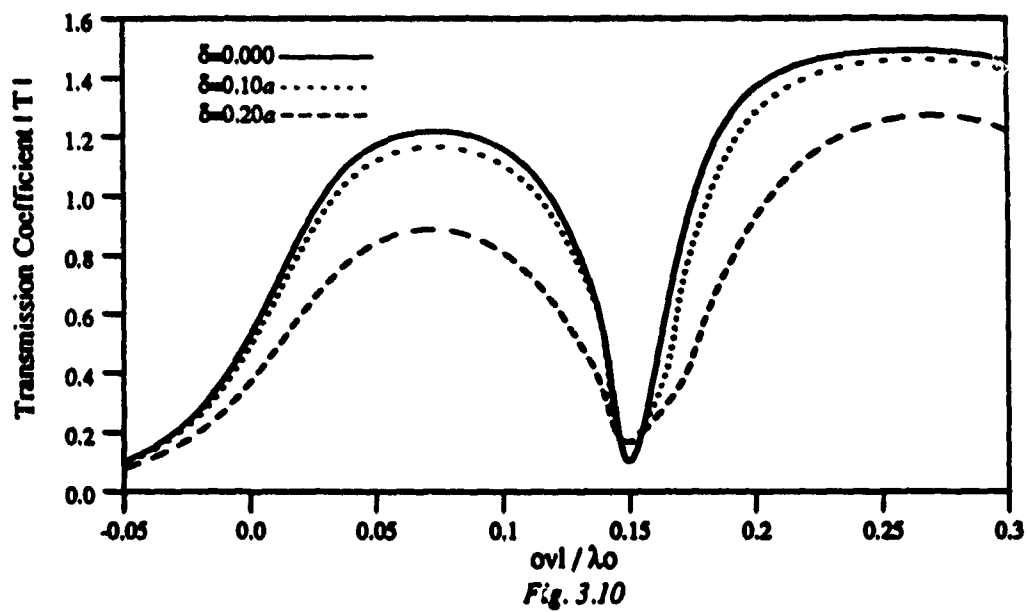
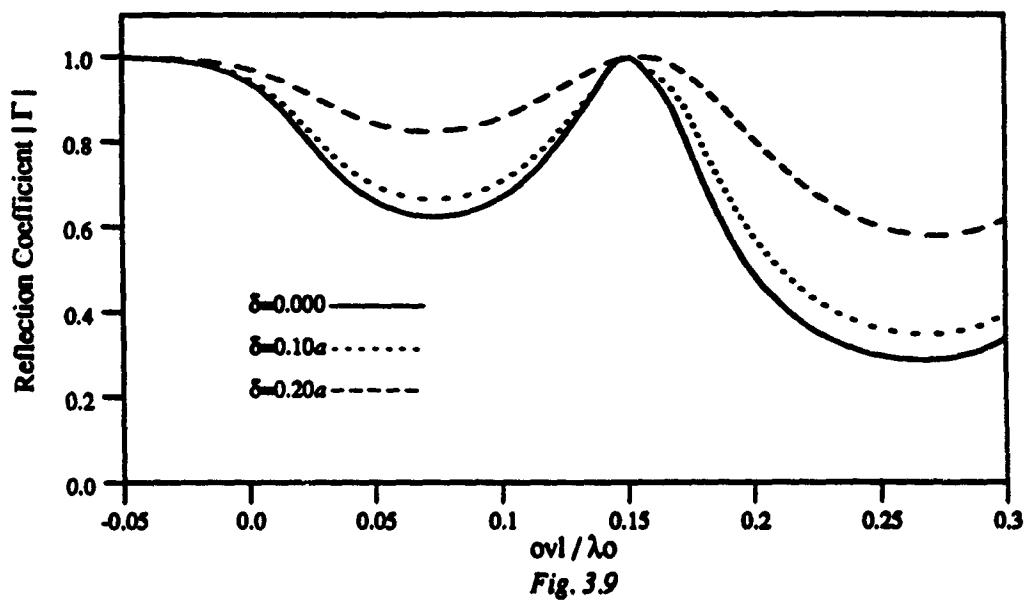


Fig. 3.9  $|\Gamma|$  versus overlap for even-mode excitation.  
(configuration Fig. 3.3)

Fig. 3.10  $|T|$  versus overlap for even-mode excitation.  
(configuration Fig. 3.3)



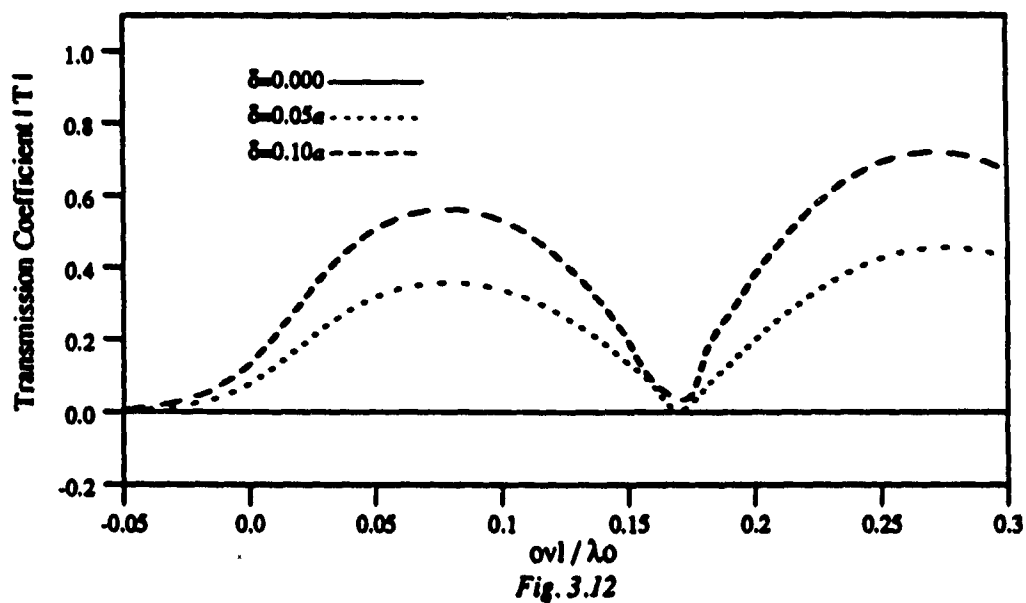
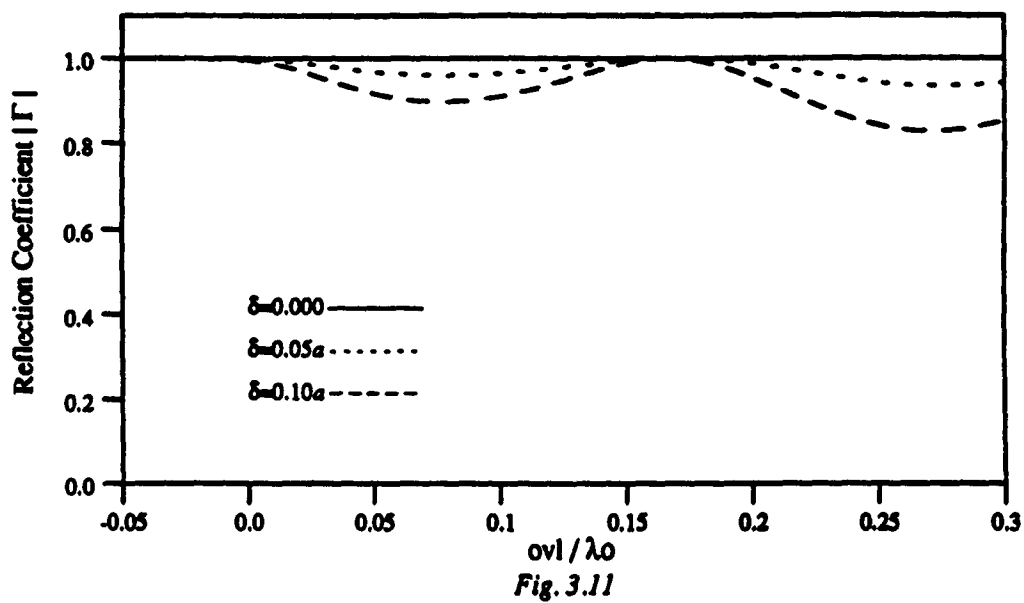


Fig. 3.11  $|\Gamma|$  versus overlap for odd-mode excitation.  
(configuration Fig. 3.3)

Fig. 3.12  $|T|$  versus overlap for odd-mode excitation.  
(configuration Fig. 3.3)

$$Z_{11} = Z_{22} = -j\frac{1}{2}(Z_{ce} \cot \theta_e + Z_{co} \cot \theta_o) \quad (3.25)$$

and

$$Z_{12} = Z_{21} = -j\frac{1}{2}(Z_{ce} \csc \theta_e - Z_{co} \csc \theta_o), \quad (3.26)$$

where

$$\theta_e = \frac{2\pi}{\lambda_{ge}} ovl \quad (3.27)$$

and

$$\theta_o = \frac{2\pi}{\lambda_{go}} ovl. \quad (3.28)$$

$Z_{ce}$  and  $Z_{co}$  represent respectively even-mode and odd-mode characteristic impedance associated with the coupled line section. The scattering matrix can be found from the impedance matrix. As a result the reflection and transmission coefficients are obtained:

$$\Gamma = \frac{Z_{11}^2 - Z_{12}^2 - Z_c^2}{(Z_{11} + Z_c)^2 - Z_{12}^2}, \quad (3.29)$$

$$T = \frac{2Z_{12}}{(Z_{11} + Z_c)^2 - Z_{12}^2}, \quad (3.30)$$

where  $Z_c$  is the characteristic impedance of feedline and the parasitic coupled line.

From Eq. [3.30], the cut-off condition occurs at  $Z_{12} = 0$ . That is

$$\frac{Z_{ce}}{Z_{co}} = \frac{\sin \theta_e}{\sin \theta_o} \quad (3.31)$$

For the general case  $Z_{ce} \gg Z_{co}$ , the solution is approximated to

$$ovl \simeq \frac{n\lambda_{go}}{2} \quad n = 0, 1, 2, 3, \dots \quad (3.32)$$

Since the fields of the odd-mode associated with the coupled line section in an overlay configuration are mostly confined in the middle layer, the effective dielectric constant of the odd-mode is approximately equal to the dielectric constant of the middle layer. Therefore, the overlap for cut-off is about:

$$ovl = \frac{1}{2\sqrt{\epsilon_2}} \quad (3.33)$$

For edge coupled lines, the fields associated with odd-mode are spread in the two dielectric layers. Therefore, the relative guided wavelength is approximately equal to the mean value of the guided wavelength with respect to each dielectric layer. Assuming these two dielectric layers with permittivity  $\epsilon_u$ , and  $\epsilon_d$  respectively, the overlap for transmission cut-off is about:

$$ovl = \frac{1}{2\sqrt{\frac{\epsilon_u + \epsilon_d}{2}}} \quad (3.34)$$

Figs. 3.5-3.8 show that the coupling efficiency is better in overlay line-to-line transition than in edge coupled line-to-line transition. This indicates the former constitutes a promising element in realization of millimeter wave high-pass filter. Figs. 3.9-3.12 show the results for the case of an overlay coupled-to-single microstrip transition. It is seen that the even-mode coupling depends less on the strip-offset of parasitic coupled line, as compared with single-line coupling. It is also noted that the even-mode of coupled lines can couple energy to a centered parasitic microstrip line while the odd-mode can not. This may find applications in a phase detector.

The frequency response of an overlay coupled microstrip transition is shown in Figs. 3.13-3.14. The geometrical parameters are specially designed in the coupled line section where the line-width is much larger than the spacing between two lines. It is seen that, in a wide frequency range, the coupling coefficients are almost independent of frequency. In addition, it is possible to couple more than 95% of the total power through the discontinuity. This geometry (so called suspended stripline) may be very useful due to these two excellent characteristics.

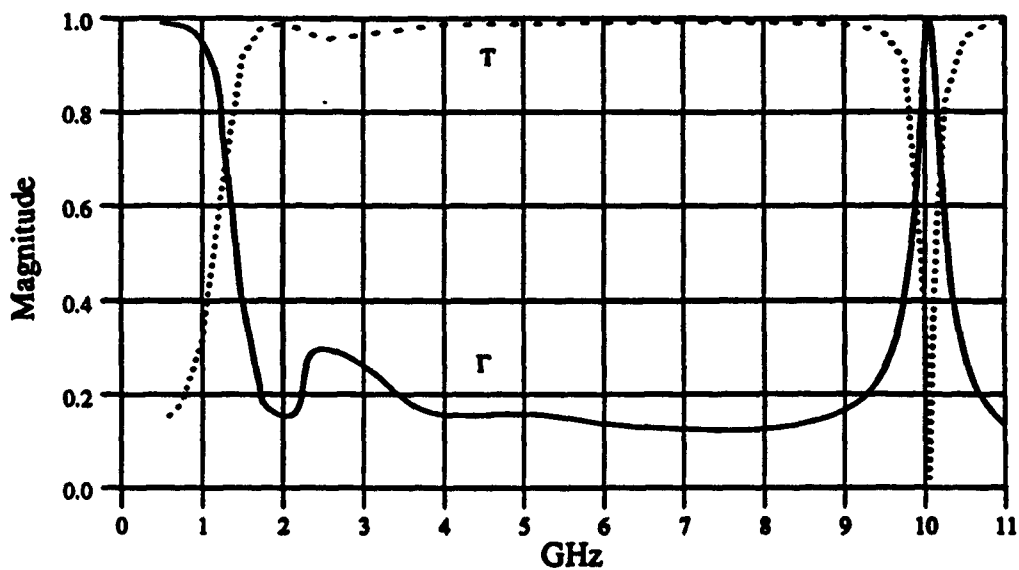


Fig. 3.13



Fig. 3.14

Fig. 3.13 Magnitude of  $\Gamma$  and  $T$  versus frequency.

Fig. 3.14 Phase of  $\Gamma$  and  $T$  versus frequency.

$\epsilon_1 = \epsilon_3 = 1, \epsilon_2 = 10.2, h_1 = h_3 = 70\text{mil}, h_2 = 10\text{mil}, w_1 = w_2 = 50\text{mil},$   
 $\delta_1 = \delta_2 = 0, \text{ovl} = 185\text{mil}, a = 500\text{mil},$  (configuration Fig. 3.2)

In the present computations of the above transition problems, entire domain modes of 3 guided wavelengths long and 9-18 subdomain modes for both pulse and piecewise sinusoidal functions are used in each microstrip line. The numerical results obtained are within 1% convergence accuracy. The power conservation is also checked in each case and will be discussed in next section.

### 3.3 Power Conservation Check

For shielded microstrip transitions, the convergence of the moment method solutions is very sensitive to the type and number of expansion function chosen. Power conservation provides a nice way of checking the accuracy of the solutions. According to the configurations in Figs. 3.1-3.3, the incident power should be equal to the summation of reflected power, transmitted power and some losses coupled to the higher order modes and the multi-layered waveguide modes. These higher order modes and multi-layered waveguide modes correspond respectively to the zeros and poles of the characteristic equation 2.64[22]. Moreover, all of the higher order modes and multi-layer waveguide modes have cut-off frequency while the dominant mode is zero cut-off[23]. That is to say, by choosing the relatively smaller waveguide dimensions or lower frequencies, one can allow only dominant mode propagating in the shielded structure. In this analysis to characterize the shielded line-to-line transitions, the waveguide dimensions are restricted to allow only dominant mode for each line. Therefore, the relation of power conservation for line-to-line transitions can be simply written as

$$P_{inc} = P_{ref} + P_{tra}, \quad (3.35)$$

where  $P_{inc}$ ,  $P_{ref}$  and  $P_{tra}$  represent incident, reflected and transmitted power, respectively. With the reflection and transmission coefficients obtained by the method of moments in Sec. 3.1 and the characteristic impedance obtained by the

Poynting vector analysis in Sec. 2.3. The reflected power associated with the feedline and transmitted power associated with the parasitic coupled line can be normalized respectively by the product of the characteristic impedance and the square of the absolute value of the scattering coefficient for each line. Thus, the relation of power conservation can be expressed in terms of scattering coefficients and characteristic impedance as follows:

$$|\Gamma|^2 + \frac{Z_{c2}}{Z_{c1}}|T|^2 = 1, \quad (3.36)$$

where  $Z_{c1}$  and  $Z_{c2}$  are the characteristic impedance of the feedline and the parasitic coupled line, respectively. For coupled-to-single configuration, the relation is slightly different due to different definition of characteristic impedance for symmetric coupled lines. The relation is

$$|\Gamma|^2 + \frac{Z_{c2}}{2Z_{ce,o}}|T|^2 = 1, \quad (3.37)$$

where  $Z_{ce}$  and  $Z_{co}$  are characteristic impedance of even-mode and odd-mode, respectively.

The conservation check for Figs. 3.5-3.12 are shown in Table 3.1~3.4 respectively. It is seen that the error in each case is within 1%. This confirms the excellent accuracy of the numerical results of both the frequency-dependent characteristic impedance and the moment method solutions.

Microstrip 1

$$\delta_1 = 0.075a$$

$$\beta_{p1} = 2.634$$

$$Z_{c1} = 45.90$$

Microstrip 2

$$\delta_2 = 0.075a$$

$$\beta_{p2} = 2.634$$

$$Z_{c2} = 45.90$$

<i>ovl</i>	$ \Gamma ^2 + \frac{Z_{c2}}{Z_{c1}} T ^2$	<i>ovl</i>	$ \Gamma ^2 + \frac{Z_{c2}}{Z_{c1}} T ^2$
-0.05	1.000	0.13	1.000
-0.03	1.000	0.15	1.000
-0.01	1.000	0.17	1.000
0.01	1.000	0.19	1.000
0.03	1.000	0.21	1.000
0.05	1.000	0.23	1.000
0.07	1.000	0.25	1.000
0.09	1.000	0.27	1.000
0.11	1.000	0.29	1.000

Table. 3.1 Power conservation check for the configuration of Fig. 3.1. Both  $|\Gamma|$  and  $|T|$  are the same as those in Fig. 3.5 and Fig. 3.6.

Microstrip 1

$$\delta_1 = 0.000$$

$$\beta_{p1} = 1.946$$

$$Z_{c1} = 55.90$$

Microstrip 2

$$\delta_2 = 0.000$$

$$\beta_{p2} = 1.907$$

$$Z_{c2} = 59.00$$

$ovl$	$ \Gamma ^2 + \frac{Z_{c2}}{Z_{c1}} T ^2$	$ovl$	$ \Gamma ^2 + \frac{Z_{c2}}{Z_{c1}} T ^2$
-0.05	1.000	0.13	0.997
-0.03	1.000	0.15	0.999
-0.01	1.001	0.17	1.004
0.01	1.003	0.19	1.003
0.03	1.004	0.21	1.002
0.05	1.003	0.23	1.001
0.07	1.001	0.25	1.000
0.09	1.001	0.27	1.000
0.11	0.999	0.29	0.999

Table. 3.2 Power conservation check for the configuration of Fig. 3.2. Both  $|\Gamma|$  and  $|T|$  are the same as those in Fig. 3.7 and Fig. 3.8.



Microstrip 1a and 1b

$$\delta_1 = 0.100a$$

$$\beta_{p1} = 1.950$$

$$Z_{c1} = 63.80$$

Microstrip 2

$$\delta_2 = 0.000$$

$$\beta_{p2} = 2.072$$

$$Z_{c2} = 53.60$$

<i>ovl</i>	$ \Gamma ^2 + \frac{Z_{c2}}{2Z_{c1}} T ^2$	<i>ovl</i>	$ \Gamma ^2 + \frac{Z_{c2}}{2Z_{c1}} T ^2$
-0.05	1.000	0.13	1.001
-0.03	1.000	0.15	1.002
-0.01	1.000	0.17	1.002
0.01	1.000	0.19	1.001
0.03	1.000	0.21	1.002
0.05	1.002	0.23	1.005
0.07	1.003	0.25	1.002
0.09	1.002	0.27	1.000
0.11	1.001	0.29	1.003

Table. 3.3 Power conservation check for the configuration of Fig. 3.3. Both  $|\Gamma|$  and  $|T|$  are the same as those in Fig. 3.9 and Fig. 3.10.

Microstrip 1a and 1b

$$\delta_1 = 0.100a$$

$$\beta_{p1} = 2.291$$

$$Z_{c1} = 45.30$$

Microstrip 2

$$\delta_2 = 0.100a$$

$$\beta_{p2} = 2.075$$

$$Z_{c2} = 53.60$$

<i>ovl</i>	$ \Gamma ^2 + \frac{Z_{c2}}{2Z_{c1}} T ^2$	<i>ovl</i>	$ \Gamma ^2 + \frac{Z_{c2}}{2Z_{c1}} T ^2$
-0.05	1.000	0.13	1.005
-0.03	1.000	0.15	1.005
-0.01	1.000	0.17	1.003
0.01	1.000	0.19	1.001
0.03	1.000	0.21	1.000
0.05	1.000	0.23	1.000
0.07	1.000	0.25	1.002
0.09	1.001	0.27	1.005
0.11	1.003	0.29	1.007

Table. 3.4 Power conservation check for the configuration of Fig. 3.3. Both  $|\Gamma|$  and  $|T|$  are the same as those in Fig. 3.11 and Fig. 3.12.

## Chapter IV

### Conclusions

An efficient method has been presented in Chapter II for obtaining the dispersion properties of three layer shielded microstrip lines. This method, which is based on a hybrid mode analysis followed by the method of moments has a number of unique features. Numerical results given include the propagation constant, characteristic impedance, transverse dependence of longitudinal and transverse current distributions for both single and coupled microstrip lines with arbitrary strip-width and strip-offset. The dispersion characteristics and their dependence on various geometrical parameters have also been presented. This method is general and can be easily extended to the multiconductor case. The choice of expansion functions is carefully made for improving numerical efficiency. Good agreement is shown in comparison with other available data.

In Chapter III, a full-wave analysis is proposed to develop a generalized dynamic model for several types of shielded microstrip line-to-line transitions. The results obtained from the method of moments are checked by power conservation with error within 1%. The results presented also show excellent properties in some transitions and may find promising applications in MMIC coupler and filter designs.

## References

- [1] T.C. Edwards, *Foundations for Microstrip Circuit Design*. Chichester, NY: Wiley, 1983.
- [2] M. Aikawa, "Microstrip line directional couplers with tight coupling and high directivity," *Electronics and Communications in Japan*, Vol. J60-B, no. 4, pp. 253-259, April, 1977.
- [3] J.E. Dean and J.D. Rhodes, "Design of MIC broadband contiguous multiplexers," in 1980 IEEE MTT-S International Microwave Symposium Digest, pp. 147-149.
- [4] P.K. Park, "Theory, analysis, and design of a new type of strip-fed slot array," PH.D. Dissertation, UCLA 1979.
- [5] H.A. Wheeler, "Transmission-line properties of parallel strip separated by a dielectric board," *IEEE Trans. on Microwave Theory and Techniques*, Vol. MTT-13, pp. 172-185, Mar. 1965.
- [6] T.G. Bryant and J.A. Weiss, "Parameters of microstrip transmission lines and of coupled pairs of microstrip lines," *IEEE Trans. on Microwave Theory and Techniques*, Vol. MTT-16, pp. 1021-1027, Dec. 1968.
- [7] M.K. Krage and G.I. Haddad, "Characteristics of coupled microstrip transmission lines-II: Evaluation of coupled-line parameters," *IEEE Trans. on Microwave Theory and Techniques*, Vol. MTT-18, pp. 222-228, Apr. 1970.
- [8] K.C. Gupta, R. Gary and I.J. Bahl, *Microstrip Lines and Slotlines*. Dedham, MA: Artech House, 1979.
- [9] T. Itoh and R. Mittra, "A technique for computing dispersion characteristics of shielded microstriplines," *IEEE Trans. on Microwave Theory and Techniques*, Vol. MTT-21, pp. 896-898, Oct. 1974.
- [10] J.B. Knorr and A. Tufekcioglu, "Spectral-domain calculation of microstrip characteristic impedance," *IEEE Trans. on Microwave Theory and Techniques*, Vol. MTT-23, pp. 725-728, Sept. 1975.
- [11] R.H. Jansen, "Unified user-oriented computation of shielded, covered and open planar microwave and millimeter-wave transmission-line characteristics," *Microwaves, Opt. and Acous.*, Vol. 3, pp. 14-22, Jan. 1979.
- [12] S.V. Judd, I. Whiteley, R.J. Clowes and D.C. Rickard, "An analytical method for calculating microstrip transmission line parameters," *IEEE Trans. on Microwave Theory and Techniques*, Vol. MTT-18, pp. 78-87, Feb. 1970.

- [13] M.K. Krage and G.I. Haddad, "Frequency-dependent characteristics of microstrip transmission lines," *IEEE Trans. on Microwave Theory and Techniques*, Vol. MTT-20, pp. 678-686, Oct. 1972.
- [14] A. Nakatani and N.G. Alexopoulos, "Toward a generalized algorithm for the modeling of dispersive properties of integrated circuit structures on anisotropic substrates," *IEEE Trans. on Microwave Theory and Techniques*, Vol. MTT-33, pp. 1436-1441, Dec. 1985.
- [15] L. Carin and K.J. Webb, "An equivalent circuit model for terminated hybrid-mode multiconductor transmission lines," *IEEE Trans. on Microwave Theory and Techniques*, Vol. MTT-37, pp. 1784-1793, Nov. 1989.
- [16] E. El-sharawy and R.W. Jackson, "Coplanar waveguide and slot line on magnetic substrates: analysis and experiment," *IEEE Trans. on Microwave Theory and Techniques*, vol. MTT-36, pp. 1071-1078, June 1988.
- [17] L.E. Losch, "Design Procedure for inhomogeneous coupled line sections," *IEEE Trans. on Microwave Theory and Techniques*, Vol. MTT-36, pp. 1186-1190, July 1988.
- [18] P.B. Katehi, "Radiation losses in MM-wave open microstrip filters," *Electromagnetics*, vol. 7, pp. 137-152, 1987.
- [19] H.Y. Yang and N.G. Alexopoulos, "A dynamic model for microstrip-slotline transition and related structure," *IEEE Trans. on Microwave Theory and Techniques*, Vol. MTT-36, pp. 286-293, Feb. 1988.
- [20] H.Y. Yang and N.G. Alexopoulos, "Basic building blocks for high frequency interconnects: theory and experiment," *IEEE Trans. on Microwave Theory and Techniques*, Vol. MTT-36, pp. 1258-1264, Aug. 1988.
- [21] G.I. Zysman and A.K. Johnson, "Coupled transmission line networks in an inhomogeneous dielectric medium," *IEEE Trans. on Microwave Theory and Techniques*, vol. MTT-17, pp. 753-759, Oct. 1969.
- [22] C.J. Railton and T. Rozzi, "Complex modes in boxed microstrip," *IEEE Trans. on Microwave Theory and Techniques*, Vol. MTT-36, pp. 865-874, May 1988.
- [23] E. Yamashita and K. Atsuki, "Analysis of microstrip-like transmission lines by nonuniform discretization of integral equations," *IEEE Trans. on Microwave Theory and Techniques*, Vol. MTT-24, pp. 195-200, Apr. 1976.

## Appendix A

The pertinent coefficients in Eqs. [2.18]~[2.29] are expressed as

$$A_z = \frac{-j\omega\mu_o \sin \alpha_n x'_1}{k_o^2 \text{Den1}} \left( \frac{\epsilon_2}{\epsilon_3} \sinh q_1 h_1 \right) \quad (\text{A.1})$$

$$A'_z = \frac{-j\omega\mu_o \sin \alpha_n x'_1}{k_o^2 \text{Den1 Den2}} \begin{pmatrix} -j\beta \frac{q_1}{q_2} \epsilon_2 \left( \frac{\epsilon_2}{\epsilon_3} - 1 \right) \sinh q_1 h_1 \sinh q_2 h_2 f_{21} \\ -j\beta \epsilon_1 \left( \frac{\epsilon_2}{\epsilon_3} - 1 \right) \cosh q_1 h_1 \cosh q_2 h_2 f_{21} \\ +j\beta \epsilon_1 \left( \frac{\epsilon_2}{\epsilon_1} - 1 \right) \cosh q_1 h_1 f_{11} \end{pmatrix} \quad (\text{A.2})$$

$$B_z = \frac{-j\omega\mu_o \sin \alpha_n x'_1}{k_o^2 \text{Den1}} \begin{pmatrix} -\frac{q_1}{q_2} \sinh q_1 h_1 \cosh q_2 (h_1 + h_2) \cosh q_3 h_3 \\ -\sinh q_1 h_1 \sinh q_2 (h_1 + h_2) \sinh q_3 h_3 \end{pmatrix} \quad (\text{A.3})$$

$$C_z = \frac{-j\omega\mu_o \sin \alpha_n x'_1}{k_o^2 \text{Den1}} \begin{pmatrix} \frac{q_1}{q_2} \sinh q_1 h_1 \sinh q_2 (h_1 + h_2) \cosh q_3 h_3 \\ + \sinh q_1 h_1 \cosh q_2 (h_1 + h_2) \sinh q_3 h_3 \end{pmatrix} \quad (\text{A.4})$$

$$B'_z = \frac{-j\omega\mu_o \sin \alpha_n x'_1}{k_o^2 \text{Den1 Den2}} \begin{pmatrix} -j\beta \frac{q_1}{q_2} (\epsilon_2 - \epsilon_3) f_{21} \\ \cdot \sinh q_1 h_1 \cosh q_2 h_1 \cosh q_3 h_3 \\ -j\beta \left( \frac{q_1 q_2}{\epsilon_2} - \epsilon_1 \right) f_{21} \\ \cdot \cosh q_1 h_1 \sinh q_2 h_1 \cosh q_3 h_3 \\ -j\beta (\epsilon_3 - \frac{q_1 q_2}{\epsilon_2}) f_{11} \\ \cdot \cosh q_1 \sinh q_2 (h_1 + h_2) \cosh q_3 h_3 \\ -j\beta \frac{q_1}{q_2} (\epsilon_2 - \epsilon_1) f_{11} \\ \cdot \cosh q_1 h_1 \cosh q_2 (h_1 + h_2) \sinh q_3 h_3 \end{pmatrix} \quad (\text{A.5})$$

$$C'_z = \frac{-j\omega\mu_0}{k_0^2} \frac{\sin \alpha_n x'_1}{\text{Den1 Den2}} \begin{pmatrix} j\beta \frac{\epsilon_2}{\epsilon_3} (\epsilon_2 - \epsilon_3) f_{21} \\ \cdot \sinh q_1 h_1 \sinh q_2 h_1 \cosh q_3 h_3 \\ + j\beta (\frac{\epsilon_1 \epsilon_3}{\epsilon_2} - \epsilon_1) f_{21} \\ \cdot \cosh q_1 h_1 \cosh q_2 h_1 \cosh q_3 h_3 \\ + j\beta (\epsilon_3 - \frac{\epsilon_1 \epsilon_3}{\epsilon_2}) f_{11} \\ \cdot \cosh q_1 \cosh q_2 (h_1 + h_2) \cosh q_3 h_3 \\ + j\beta \frac{\epsilon_2}{\epsilon_3} (\epsilon_2 - \epsilon_1) f_{11} \\ \cdot \cosh q_1 h_1 \sinh q_2 (h_1 + h_2) \sinh q_3 h_3 \end{pmatrix} \quad (\text{A.6})$$

$$D_z = \frac{-j\omega\mu_0}{k_0^2} \frac{\sin \alpha_n x'_1}{\text{Den1}} \begin{pmatrix} \frac{\epsilon_2}{\epsilon_1} \frac{\epsilon_3}{\epsilon_2} \cosh q_3 h_3 \sinh q_2 h_2 \\ + \frac{\epsilon_2}{\epsilon_1} \sinh q_3 h_3 \cosh q_2 h_2 \end{pmatrix} \quad (\text{A.7})$$

$$D'_z = \frac{-j\omega\mu_0}{k_0^2} \frac{\sin \alpha_n x'_1}{\text{Den1 Den2}} \begin{pmatrix} j\beta \frac{\epsilon_2}{\epsilon_3} \epsilon_2 (\frac{\epsilon_2}{\epsilon_1} - 1) \sinh q_3 h_3 \sinh q_2 h_2 f_{11} \\ + j\beta \epsilon_3 (\frac{\epsilon_2}{\epsilon_1} - 1) \cosh q_3 h_3 \cosh q_2 h_2 f_{11} \\ - j\beta \epsilon_3 (\frac{\epsilon_2}{\epsilon_3} - 1) \cosh q_3 h_3 f_{21} \end{pmatrix} \quad (\text{A.8})$$

$$A_z = \frac{-j\omega\mu_0}{k_0^2} \frac{\cos \alpha_n x'_1}{\text{Den1}} \left( \frac{\epsilon_2}{\epsilon_3} \sinh q_1 h_1 \right) \quad (\text{A.9})$$

$$A'_z = \frac{-j\omega\mu_0}{k_0^2} \frac{\cos \alpha_n x'_1}{\text{Den1 Den2}} \begin{pmatrix} -\alpha_n \frac{\epsilon_2}{\epsilon_3} \epsilon_2 (\frac{\epsilon_2}{\epsilon_3} - 1) \sinh q_1 h_1 \sinh q_2 h_2 f_{21} \\ -\alpha_n \epsilon_1 (\frac{\epsilon_2}{\epsilon_3} - 1) \cosh q_1 h_1 \cosh q_2 h_2 f_{21} \\ + \alpha_n \epsilon_1 (\frac{\epsilon_2}{\epsilon_3} - 1) \cosh q_1 h_1 f_{11} \end{pmatrix} \quad (\text{A.10})$$

$$B_z = \frac{-j\omega\mu_0}{k_0^2} \frac{\cos \alpha_n x'_1}{\text{Den1}} \begin{pmatrix} -\frac{\epsilon_2}{\epsilon_3} \sinh q_1 h_1 \cosh q_2 (h_1 + h_2) \cosh q_3 h_3 \\ - \sinh q_1 h_1 \sinh q_2 (h_1 + h_2) \sinh q_3 h_3 \end{pmatrix} \quad (\text{A.11})$$

$$C_z = \frac{-j\omega\mu_0}{k_0^2} \frac{\cos \alpha_n x'_1}{\text{Den1}} \begin{pmatrix} \frac{\epsilon_2}{\epsilon_3} \sinh q_1 h_1 \sinh q_2 (h_1 + h_2) \cosh q_3 h_3 \\ + \sinh q_1 h_1 \cosh q_2 (h_1 + h_2) \sinh q_3 h_3 \end{pmatrix} \quad (\text{A.12})$$

$$B'_x = \frac{-j\omega\mu_o}{k_o^2} \frac{\cos \alpha_n x'_1}{Den1 Den2} \begin{pmatrix} -\alpha_n \frac{q_1}{q_2} (\epsilon_2 - \epsilon_3) f_{21} \\ \cdot \sinh q_1 h_1 \cosh q_2 h_1 \cosh q_3 h_3 \\ -\alpha_n \left( \frac{\epsilon_1 \epsilon_3}{\epsilon_2} - \epsilon_1 \right) f_{21} \\ \cdot \cosh q_1 h_1 \sinh q_2 h_1 \cosh q_3 h_3 \\ -\alpha_n \left( \epsilon_3 - \frac{\epsilon_1 \epsilon_3}{\epsilon_2} \right) f_{11} \\ \cdot \cosh q_1 \sinh q_2 (h_1 + h_2) \cosh q_3 h_3 \\ -\alpha_n \frac{q_1}{q_2} (\epsilon_2 - \epsilon_1) f_{11} \\ \cdot \cosh q_1 h_1 \cosh q_2 (h_1 + h_2) \sinh q_3 h_3 \end{pmatrix} \quad (A.13)$$

$$C'_z = \frac{-j\omega\mu_o}{k_o^2} \frac{\cos \alpha_n x'_1}{Den1 Den2} \begin{pmatrix} \alpha_n \frac{q_1}{q_2} (\epsilon_2 - \epsilon_3) f_{21} \\ \cdot \sinh q_1 h_1 \sinh q_2 h_1 \cosh q_3 h_3 \\ +\alpha_n \left( \frac{\epsilon_1 \epsilon_3}{\epsilon_2} - \epsilon_1 \right) f_{21} \\ \cdot \cosh q_1 h_1 \cosh q_2 h_1 \cosh q_3 h_3 \\ +\alpha_n \left( \epsilon_3 - \frac{\epsilon_1 \epsilon_3}{\epsilon_2} \right) f_{11} \\ \cdot \cosh q_1 \cosh q_2 (h_1 + h_2) \cosh q_3 h_3 \\ +\alpha_n \frac{q_1}{q_2} (\epsilon_2 - \epsilon_1) f_{11} \\ \cdot \cosh q_1 h_1 \sinh q_2 (h_1 + h_2) \sinh q_3 h_3 \end{pmatrix} \quad (A.14)$$

$$D_z = \frac{-j\omega\mu_o}{k_o^2} \frac{\cos \alpha_n x'_1}{Den1} \begin{pmatrix} \frac{\epsilon_2 q_1}{\epsilon_1 q_2} \cosh q_3 h_3 \sinh q_2 h_2 \\ + \frac{\epsilon_2}{\epsilon_1} \sinh q_3 h_3 \cosh q_2 h_2 \end{pmatrix} \quad (A.15)$$

$$D'_z = \frac{-j\omega\mu_o}{k_o^2} \frac{\cos \alpha_n x'_1}{Den1 Den2} \begin{pmatrix} \alpha_n \frac{q_1}{q_2} \epsilon_2 \left( \frac{\epsilon_2}{\epsilon_1} - 1 \right) \sinh q_3 h_3 \sinh q_2 h_2 f_{11} \\ + \alpha_n \epsilon_3 \left( \frac{\epsilon_2}{\epsilon_1} - 1 \right) \cosh q_3 h_3 \cosh q_2 h_2 f_{11} \\ - \alpha_n \epsilon_3 \left( \frac{\epsilon_2}{\epsilon_1} - 1 \right) \cosh q_3 h_3 f_{21} \end{pmatrix} \quad (A.16)$$

where



$$Den1 = \epsilon_2 \begin{pmatrix} q_1 \cosh q_1 h_1 \cosh q_2 h_2 \sinh q_3 h_3 \\ + \frac{q_1 q_3}{q_2} \cosh q_1 h_1 \sinh q_2 h_2 \cosh q_3 h_3 \\ + q_3 \sinh q_1 h_1 \cosh q_2 h_2 \cosh q_3 h_3 \\ + q_2 \sinh q_1 h_1 \sinh q_2 h_2 + \sinh q_3 h_3 \end{pmatrix} \quad (A.17)$$

$$Den2 = \begin{pmatrix} \epsilon_3 q_1 \sinh q_1 h_1 \cosh q_2 h_2 \cosh q_3 h_3 \\ + \epsilon_2 \frac{q_1 q_3}{q_2} \sinh q_1 h_1 \sinh q_2 h_2 \sinh q_3 h_3 \\ + \frac{\epsilon_1 \epsilon_3}{\epsilon_2} q_2 \cosh q_1 h_1 \sinh q_2 h_2 \cosh q_3 h_3 \\ + \epsilon_1 q_3 \cosh q_1 h_1 \cosh q_2 h_2 \sinh q_3 h_3 \end{pmatrix} \quad (A.18)$$

$$f_{11} = \sinh q_1 h_1 \cosh q_2 h_2 \sinh q_3 h_3 + \frac{q_3}{q_2} \sinh q_1 h_1 \sinh q_2 h_2 \cosh q_3 h_3 \quad (A.19)$$

$$f_{22} = \frac{q_1}{q_2} \cosh q_1 h_1 \sinh q_2 h_2 \sinh q_3 h_3 + \sinh q_1 h_1 \cosh q_2 h_2 \sinh q_3 h_3 \quad (A.20)$$

$$f_{12} = \sinh q_1 h_1 \sinh q_3 h_3 \quad (A.21)$$

$$f_{21} = \sinh q_1 h_1 \sinh q_3 h_3 \quad (A.22)$$

## Appendix B

The spectral-domain dyadic Green's function in Eqs. [2.36]~[2.43] is

$$G_{11zz} = \frac{-j\omega\mu_o}{k_o^2} \left[ \frac{k_2^2 - \beta^2}{Den1} f_{11} + \frac{\beta^2}{Den1 Den2} (f_{11} \cdot f_3 + f_{21} \cdot f_6) \right] \quad (B.1)$$

$$G_{11xx} = \frac{-j\omega\mu_o}{k_o^2} \left[ \frac{k_2^2 - \alpha_n^2}{Den1} f_{11} + \frac{\alpha_n^2}{Den1 Den2} (f_{11} \cdot f_3 + f_{21} \cdot f_6) \right] \quad (B.2)$$

$$G_{11xz} = \frac{\omega\mu_o}{k_o^2} \left[ \frac{-\alpha_n\beta}{Den1} f_{11} + \frac{\alpha_n\beta}{Den1 Den2} (f_{11} \cdot f_3 + f_{21} \cdot f_6) \right] \quad (B.3)$$

$$G_{11zx} = -G_{11xz} \quad (B.4)$$

$$G_{12zz} = \frac{-j\omega\mu_o}{k_o^2} \left[ \frac{k_2^2 - \beta^2}{Den1} f_{12} + \frac{\beta^2}{Den1 Den2} (f_{12} \cdot f_3 + f_{22} \cdot f_6) \right] \quad (B.5)$$

$$G_{12xx} = \frac{-j\omega\mu_o}{k_o^2} \left[ \frac{k_2^2 - \alpha_n^2}{Den1} f_{12} + \frac{\alpha_n^2}{Den1 Den2} (f_{12} \cdot f_3 + f_{22} \cdot f_6) \right] \quad (B.6)$$

$$G_{12xz} = \frac{\omega\mu_o}{k_o^2} \left[ \frac{-\alpha_n\beta}{Den1} f_{12} + \frac{\alpha_n\beta}{Den1 Den2} (f_{12} \cdot f_3 + f_{22} \cdot f_6) \right] \quad (B.7)$$

$$G_{12zx} = -G_{12xz} \quad (B.8)$$

$$G_{22zz} = \frac{-j\omega\mu_o}{k_o^2} \left[ \frac{k_2^2 - \beta^2}{Den1} f_{22} + \frac{\beta^2}{Den1 Den2} (f_{22} \cdot f_3 + f_{12} \cdot f_4) \right] \quad (B.9)$$

$$G_{22xx} = \frac{-j\omega\mu_o}{k_o^2} \left[ \frac{k_2^2 - \alpha_n^2}{Den1} f_{22} + \frac{\alpha_n^2}{Den1 Den2} (f_{22} \cdot f_3 + f_{12} \cdot f_4) \right] \quad (B.10)$$

$$G_{22xz} = \frac{\omega\mu_o}{k_o^2} \left[ \frac{-\alpha_n\beta}{Den1} f_{22} + \frac{\alpha_n\beta}{Den1 Den2} (f_{22} \cdot f_3 + f_{12} \cdot f_4) \right] \quad (B.11)$$

$$G_{22zx} = -G_{22xz} \quad (B.12)$$

$$G_{21zz} = G_{12zz} \quad (B.13)$$

$$G_{21xx} = G_{12xx} \quad (B.14)$$

$$G_{21xz} = G_{12xz} \quad (B.15)$$

$$G_{21zx} = G_{12zx} \quad (B.16)$$

where  $Den1, Den2, f_{11}, f_{12}, f_{21}, f_{22}$  are listed in Appendix A, the functions  $f_3, f_4, f_5,$

and  $f_6$  are expressed as follows:

$$\begin{aligned} f_3 = & -\epsilon_3 q_1 \left( \frac{\epsilon_2}{\epsilon_3} - 1 \right) \sinh q_1 h_1 \cosh q_2 h_2 \cosh q_3 h_3 \\ & - \frac{\epsilon_1 \epsilon_3}{\epsilon_2} q_2 \left( \frac{\epsilon_2}{\epsilon_3} - 1 \right) \cosh q_1 h_1 \sinh q_2 h_2 \cosh q_3 h_3 \end{aligned} \quad (\text{B.17})$$

$$\begin{aligned} f_5 = & -\epsilon_1 q_3 \left( \frac{\epsilon_2}{\epsilon_1} - 1 \right) \cosh q_1 h_1 \cosh q_2 h_2 \sinh q_3 h_3 \\ & - \frac{\epsilon_1 \epsilon_3}{\epsilon_2} q_2 \left( \frac{\epsilon_2}{\epsilon_1} - 1 \right) \cosh q_1 h_1 \sinh q_2 h_2 \cosh q_3 h_3 \end{aligned} \quad (\text{B.18})$$

$$f_4 = -\epsilon_1 q_3 \left( \frac{\epsilon_2}{\epsilon_1} - 1 \right) \cosh q_1 h_1 \sinh q_3 h_3 \quad (\text{B.19})$$

$$f_6 = -\epsilon_3 q_1 \left( \frac{\epsilon_2}{\epsilon_3} - 1 \right) \sinh q_1 h_1 \cosh q_3 h_3 \quad (\text{B.20})$$

## Appendix C

The average power in each region is expressed as

$$P_1 = \frac{1}{4a} \sum_{n=-\infty}^{\infty} [\check{E}_{1x} \check{H}_{1y}^* f_{1ss} - \check{E}_{1y} \check{H}_{1x}^* f_{1cc}] \quad (C.1)$$

$$P_2 = \frac{1}{4a} \sum_{n=-\infty}^{\infty} \left[ \begin{aligned} &(\check{E}_{2xs} \check{H}_{2ys}^* - \check{E}_{2ys} \check{H}_{2xs}^*) f_{2ss} \\ &+ (\check{E}_{2xs} \check{H}_{2yc}^* - \check{E}_{2ys} \check{H}_{2xc}^*) f_{2sc} \\ &+ (\check{E}_{2xc} \check{H}_{2ys}^* - \check{E}_{2yc} \check{H}_{2xs}^*) f_{2cs} \\ &+ (\check{E}_{2xc} \check{H}_{2yc}^* - \check{E}_{2yc} \check{H}_{2xc}^*) f_{2cc} \end{aligned} \right] \quad (C.2)$$

$$P_3 = \frac{1}{4a} \sum_{n=-\infty}^{\infty} [\check{E}_{3x} \check{H}_{3y}^* f_{3ss} - \check{E}_{3y} \check{H}_{3x}^* f_{3cc}] \quad (C.3)$$

where

$$\check{E}_{1x} = (k_1^2 - \alpha_n^2) D_x + \alpha_n q_1 (D'_z + D'_x) - j\beta \alpha_n D_z \quad (C.4)$$

$$\check{E}_{1y} = (k_1^2 + q_1^2) (D'_z + D'_x) - \alpha_n q_1 D_x - j q_1 \beta D_z \quad (C.5)$$

$$\check{H}_{1x} = j\omega \epsilon_1 q_1 D_z - \omega \epsilon_1 \beta (D'_z + D'_x) \quad (C.6)$$

$$\check{H}_{1y} = \omega \epsilon_1 \beta D_x - j\omega \epsilon_1 \alpha_n D_z \quad (C.7)$$

$$\check{E}_{2xs} = (k_2^2 - \alpha_n^2) B_x + \alpha_n q_2 (C'_z + C'_x) - j\beta \alpha_n \beta_z \quad (C.8)$$

$$\check{E}_{2xc} = (k_2^2 - \alpha_n^2) C_x + \alpha_n q_2 (B'_z + B'_x) - j\beta \alpha_n C_z \quad (C.9)$$

$$\check{E}_{2ys} = (k_2^2 + q_2^2) (B'_z + B'_x) - \alpha_n q_2 C_x - j q_1 \beta C_z \quad (C.10)$$

$$\check{E}_{2yc} = (k_2^2 + q_2^2) (C'_z + C'_x) - \alpha_n q_2 B_x - j q_1 \beta B_z \quad (C.11)$$

$$\check{H}_{2xs} = j\omega \epsilon_2 q_2 C_x - \omega \epsilon_2 \beta (B'_z + B'_x) \quad (C.12)$$

$$\check{H}_{2xc} = j\omega \epsilon_2 q_2 B_x - \omega \epsilon_2 \beta (C'_z + C'_x) \quad (C.13)$$

$$\check{H}_{2ys} = \omega \epsilon_2 \beta B_x - j\omega \epsilon_2 \alpha_n B_z \quad (C.14)$$

$$\check{H}_{2yc} = \omega\epsilon_2\beta C_x - j\omega\epsilon_2\alpha_n C_z \quad (C.15)$$

$$\check{E}_{3x} = (k_3^2 - \alpha_n^2)A_x - \alpha_n q_3(A'_x + A'_x) - j\beta\alpha_n A_z \quad (C.16)$$

$$\check{E}_{3y} = (k_3^2 + q_3^2)(A'_x + A'_x) + \alpha_n q_3 A_x + j q_3 \beta A_z \quad (C.17)$$

$$\check{H}_{3x} = -j\omega\epsilon_3 q_3 A_x - \omega\epsilon_3 \beta(A'_x + A'_x) \quad (C.18)$$

$$\check{H}_{3y} = \omega\epsilon_3 \beta A_x - j\omega\epsilon_3 \alpha_n A_z \quad (C.19)$$

and

$$f_{1ss} = Sgn_i \left[ -\frac{1}{2}h_1 + \frac{1}{4q_1} \sinh 2q_1 h_1 \right] \quad (C.20)$$

$$f_{1cc} = \left[ \frac{1}{2} + \frac{1}{4q_1} \sinh 2q_1 h_1 \right] \quad (C.21)$$

$$f_{2ss} = Sgn_i \left[ -\frac{1}{2}h_2 + \frac{1}{4q_2} (\sinh 2q_2 (h_1 + h_2) - \sinh 2q_2 h_1) \right] \quad (C.22)$$

$$f_{2sc} = \left[ \frac{1}{4q_2} (\cosh 2q_2 (h_1 + h_2) - \cosh 2q_2 h_1) \right] \quad (C.23)$$

$$f_{2cs} = Sgn_i \left[ \frac{1}{4q_2} (\cosh 2q_2 (h_1 + h_2) - \cosh 2q_2 h_1) \right] \quad (C.24)$$

$$f_{2cc} = \left[ \frac{1}{2}h_2 + \frac{1}{4q_2} (\sinh 2q_2 (h_1 + h_2) - \sinh 2q_2 h_1) \right] \quad (C.25)$$

$$f_{3ss} = Sgn_i \left[ -\frac{1}{2}h_3 + \frac{1}{4q_3} \sinh 2q_3 h_3 \right] \quad (C.26)$$

$$f_{3cc} = \left[ \frac{1}{2}h_3 + \frac{1}{4q_3} \sinh 2q_3 h_3 \right] \quad (C.27)$$

$Sgn_i$  is equal to 1 as  $q_i$  is real and equal to -1 as  $q_i$  is imaginary. The functions  $A_k \sim D_k$  and  $A'_k \sim D'_k$  can be found in Appendix A.

## Appendix D

The Fourier transform of longitudinal dependence of both subdomain modes and entire domain modes are as follows:

$$\tilde{f}_{iz}^m = \frac{2k_{ei}(\cos k_{ei}d - \cos \beta d)}{\sin k_{ei}d(\beta^2 - k_{ei}^2)} e^{j\beta z_m} \quad (D.1)$$

$$\tilde{f}_{iz}^m = \frac{\sin \frac{\beta d}{2}}{\frac{\beta d}{2}} e^{j\beta z_m} \quad (D.2)$$

$$\tilde{J}_{11\hat{u}}^{*ref}(\beta) = (e^{-j\frac{\beta\pi}{2\beta_{p1}}} + j) \int_{-\infty}^0 \sin \beta_{p1} z e^{j\beta z} dz \quad (D.3)$$

$$\tilde{J}_{21\hat{u}}^{*tra}(\beta) = (e^{j\frac{\beta\pi}{2\beta_{p2}}} + j) \int_{-\infty}^0 \sin \beta_{p2} z e^{-j\beta z} dz \quad (D.4)$$

$$\tilde{J}_{11\hat{u}}^{*inc}(\beta) = (e^{-j\frac{\beta\pi}{2\beta_{p1}}} - j) \int_{-\infty}^0 \sin \beta_{p1} z e^{j\beta z} dz \quad (D.5)$$

where

$$\int_{-\infty}^0 \sin \beta_{pi} z e^{\mp j\beta z} dz = \frac{\beta_{pi}}{\beta^2 - \beta_{pi}^2} + j\pi [\delta(\beta \pm \beta_{pi}) - \delta(\beta \mp \beta_{pi})] \quad (D.6)$$

**END  
FILMED**

**DATE:** 1-9/

**DTIC**